# Processus physiques et chimiques en failles sismiques : exemples de failles actives et exhumées

Silvia Mittempergher

UNIVERSITÀ
DEGLI STUDI
DI PADOVA

**Sede Amministrativa: Università degli Studi di Padova**

Sede Consorziata: Université de Grenoble

Dipartimento di Geoscienze

SCUOLA DI DOTTORATO DI RICERCA IN SCIENZE DELLA TERRA

CICLO XXIV

# Physico-chemical processes in seismogenic faults: active and exhumed examples

**Direttore della Scuola :** Ch.mo Prof. Gilberto Artioli

**Supervisore** : Ch.mo Prof. Giulio Di Toro

Ch.mo Prof. Jean-Pierre Gratier

**Dottoranda** : Silvia Mittempergher

UNIVERSITÉ DE GRENOBLE

# THÈSE

Pour obtenir le grade de

## DOCTEUR DE L'UNIVERSITÉ DE GRENOBLE

Spécialité: **Terre solide**

Arrêté ministériel : 7 août 2006

Présentée par


## Silvia MITTEMPERGHER


Thèse dirigée par Prof. **Giulio DI TORO** et
Par Prof. **Jean Pierre GRATIER**

préparée au sein du **Laboratoire IsTerre** et **Dipartimento di Geoscienze (Université de Padoue)** dans **l'École Doctorale Terre, Univers, Environnement** et dans la **Scuola di dottorato in Scienze della Terra (Université de Padoue)**

# Physico-chemical processes in seismogenic faults: active and exhumed examples

Thèse soutenue publiquement le **4 avril 2012**,
devant le jury composé de:

**Prof. Daniel FAULKNER**
Professeur, Université de Liverpool, rapporteur
**Prof. Karen MAIR**
Professeur, Université de Oslo, rapporteur
**Prof. Giulio DI TORO**
Professeur, Université de Padoue, directeur
**Prof. Jean Pierre GRATIER**
Professeur, Université J. Fourier, Grenoble, directeur

# *Riassunto*

I processi chimici e fisici attivi nel ciclo sismico controllano l'evoluzione delle proprietà meccaniche delle zone di faglia, sia nel breve (durante un terremoto) che nel lungo periodo (il recupero delle proprietà elastiche delle rocce di faglia nel periodo intersismico). Studiare le rocce di faglia naturali è un mezzo per riconoscere i processi attivi nelle varie fasi del ciclo sismico. In questa tesi, vengono studiati campioni da due faglie sismogenetiche: la Faglia di San Andreas (California, USA), attiva, e la Faglia delle Gole Larghe (Alpi Meridionali, Italia), faglia sismogenetica esumata. La Faglia di San Andreas è stata perforata fino ad una profondità di 2.7 km, con il recupero campioni da profondità prossime agli ipocentri di terremoti di bassa intensità (M<3) registrati in questo tratto della faglia. Una sovrapposizione ciclica di strutture legate a presso-soluzione(*creep*), idrofratturazione e ancora presso-soluzione potrebbe confermare il modello secondo cui, in faglie mature e ricche in materiali argillosi come la Faglia di San Andreas, si possano formare delle sacche poco permeabili isolate in cui la pressione dei fluidi può aumentare a causa della continua compattazione del materiale di faglia, fino a superare la resistenza alla rottura della roccia. La faglia delle Gole Larghe è una faglia esumata che era attiva 30 Ma fa a 9 -11 km di profondità. La presenza di pseudotachiliti, fusi di frizione prodotti durante lo scivolamento sismico, testimonia l'attività sismica passata. Due argomenti sono stati affrontati: (i) l'evoluzione microstrutturale delle rocce cataclastiche associate alle pseudotachiliti all'aumentare della deformazione, per identificare i processi che possono portare alla nucleazione di instabilità frizionali nelle prime fasi di crescita di una faglia. (ii) L'origine dei fluidi nelle faglie sismogenetiche e nel processo di fusione per attrito. Nel caso della Faglia delle Gole Larghe, la formazione di un sistema di faglie cataclastiche consente l'ingresso di un fluido acquoso, di probabile origine profonda. La composizione isotopica delle psudotachiliti naturali è simile a quello di pseudotachiliti artificiali prodotte in condizioni anidre. La principale fonte di fluidi nelle pseudotachiliti è quindi la deidratazione dei minerali idrati della roccia incassante indotta dal calore di frizione prodotto dallo scivolamento cosismico.

# *Abstract*

The time recurrence of earthquakes is the result of the feedback between the tectonic loading and the evolution of fault strength during the seicmic cycle. This thesis aims to identify the chemical and physical processes in fault rocks from the modern seismogenic San Andreas Fault (California, USA) and the ancient seismogenic Gole Larghe Fault (Southern Alps, Italy). The San Andreas Fault was drilled to 2.7 km depth, and samples were extracted from the depth of nucleation of repeating microearthquakes. A cyclic recurrence of pressure-solution creep – hydrofracture - pressure solution creep supports the idea that isolated compartments of high fluid pressure might cause the nucleation of small to moderate size earthquakes, associated with the dominant creeping activity in this fault segment. The Gole Larghe Fault Zone was active 30 Ma ago at 9 – 11 km depth. The occurrence of pseudotachylytes witnesses its seismic behavior. Two topics were investigated: (i) The fabric evolution of cataclastic rocks with increasing deformation, to identify the processes potentially leading to the onset of unstable slip at the early stages of fault growth. (ii) The origin of fluids involved in seismic faulting and frictional melting. The formation of a cataclastic fault network allows the ingression of external hydrous fluids, probably of deep origin. The similar isotopic composition of natural pseudotachylytes and pseudotachylytes produced in dry conditions suggests that the fluid source is the dehydration of OH-bearing minerals in the wall rocks induced by coseismic frictional heating.



# *Résumé*

Les temps de récurrence des séismes résultent d'une interaction complexe entre le chargement tectonique de la faille et l'évolution dans le temps des propriétés rhéologiques et de transfert des roches de la faille. Les processus physiques et chimiques, activés pendant le cycle sismique, déterminent l'évolution des propriétés mécaniques des failles, à court terme (pendant un séisme) comme à long terme (en intersismique: récupération des propriétés mécaniques de la faille). L'étude des roches de failles naturelles permet d'identifier les processus actifs pendant les diverses phases des cycles sismiques. Durant cette thèse, des échantillons provenant de deux failles sismiques ont été étudiés: la Faille de San Andreas (Californie, USA), une faille active, et la faille de Gole Larghe (Alpes Méridionales, Italie), une faille exhumée. La Faille de San Andreas a été forée jusqu'à 3 km de profondeur. Les échantillons montrent une superposition de mécanismes de dissolution – cristallisation sous contrainte, de cataclase localisée, d'hydrofracturation et d'altération métamorphique. Ces processus sont compatibles avec la formation de poches de fluides dans des zones de faible perméabilité, où la pression de fluides augmente à cause de la compaction progressive de la gouge de faille, jusqu'à la rupture. La faille de Gole Larghe est une faille exhumée, qui a préservé des pseudotachylites (roches fondues par la chaleur de friction lors du glissement sismique) formées à 9 - 11 km de profondeur il y a 30 millions d'années. Deux aspects sont traités: (i) l'évolution des microstructures des cataclasites associées aux pseudotachylites pour identifier les processus qui peuvent porter à la formation d'instabilités frictionnelles pendant les premières phases de croissance d'une faille; (ii) l'origine des fluides dans les failles sismiques et pendant la fusion par friction. La formation d'un système de failles à cataclasites permet la percolation d'un fluide aqueux de la profondeur. La composition isotopique des pseudotachylites (calculée sans la composante d'hydratation) est proche à celle des pseudotachylites reproduites expérimentalement au laboratoire (sans fluides). La principale source de fluides pendant la fusion par friction est donc la déshydratation des minéraux hydratés des roches autour de la faille.

# *Acknowledgements*

It will be difficult to acknowledge properly the many people who contributed in many ways to this work. I apologize in advance if I forgot somebody (and I did for sure!!).

First of all, thanks to all the people who helped me in collecting data in Padua, Rome, Pisa, Grenoble, Louisville, College Station: Leonardo Tauro, Elena Masiero (thin section preparation), Stefano Castelli (too many thin section scans and photomosaics!), Luca Peruzzo (SEM), Andrea Cavallo (FE-SEM and microprobe), Giuliana De Grandis (mineral separations), Ilaria Bedeschi (CHN analyses), Eric Levine (FTIR analyses), Jacek Jasinsky (TEM in Louisville), Brad Weymer and John Firth (SAFOD sample extraction).

A special thanks to Francois Renard, Mai-Linh Doan, Jafar Hadizadeh, Anne-Marie Boullier, Giorgio Pennacchioni, Federico Zorzi, Fabrizio Nestola, Richard Spiess, Luigi Dallai and Chiara Boschi to have been always available for discussions and for everything they taught me (or, at least, they tried…).

Thanks to all the people participating to the many trips to the Adamello, for doing such a great science, without forgetting a good radler at the Lobbia hut: Steve, Elena, Tom, André, Ashley, Andrea (thanks– K2 Way-Back are great), Nicolas, Stefan, Bob, Angela, Marie, Marieke.

Steve, besides being a tireless mate for mountain hiking, helped me a lot by hosting me in Rome, helping at the FESEM, revising my bad English and my confused ideas. Thanks!!!

A great thanks to my supervisors, Giulio and Jean Pierre, for being always available for discussing and for trying to put some order in my work. If they failed, it's only my fault! Giulio is one of the most amazing person I ever met, and it was an honor to work with him.

The people who shared the office with me during these years were so great! Fabio, I would never had got through winter 2010 without you. Michele F., thanks for your sense of humor. Virginie, thanks for your patience in listening to my disconnected sentences in French…

My family and my friends at have always supported my strange project of studying stones… Thanks to you all, and in particular to Michele for formatting the references (and for being exactly as he is).

# Table of contents

# Chapter 1. Introduction

## 1.1 Fluid enhanced physico-chemical processes in the seismic cycle

Slip on seismogenic faults is attained by a repetition of earthquakes, which occur at not predictable intervals and locations (Gilbert, 1909), and interseismic creep (e.g. afterslip, Johanson et al., 2006). The elastic rebound theory, formulated by Reid (1910) based on geodetic data from the San Francisco earthquake of 1906, formalizes the observations of Gilbert, by interpreting the earthquakes as the result of sudden relaxation of elastic strain, which was accumulated over a long period (centuries to millennia) by the steady motion of the regions on either side of the fault. If the cycle of loading - failure were regular, the time prediction of earthquakes would be possible, once the rate of tectonic loading and the fault strength were known (e.g., characteristic earthquakes: for a discussion about earthquake prediction and probabilistic forecasting, Jordan et al., 2011). Both stress loading of the fault and fault strength evolve in a complex way during time, and their interactions determine the complexity of the seismic cycle (Kanamori and Brodsky, 2004) (Figure 1). The complex behavior of faults depends on the interaction between:

(i) The rate of stress loading. Perturbations of the background tectonic loading might arise from static and dynamic stress changes due to slip on nearby faults (e.g., Stein, 1999; Gomberg et al., 2001; Johnson and Xiaoping, 2005), or by the mechanical effects of pore fluid migration (e.g. Miller et al., 2004).

(ii) The time dependent strength of the fault zones. Physical and chemical processes in the fault zone rocks control the short term (e.g., coseismic processes, velocity-dependent weakening and strengthening, Sone and Shimamoto, 2009; Di Toro et al., 2011) and long term fault strength (evolution of elastic properties of the fault zone with time, fault sealing, fault weakening processes: Blanpied et al., 1992a,b; Miller et al., 1996; Gratier et al., 2003; 2011; Jefferies et al., 2006; Smith et al., 2008; Collettini et al., 2009).

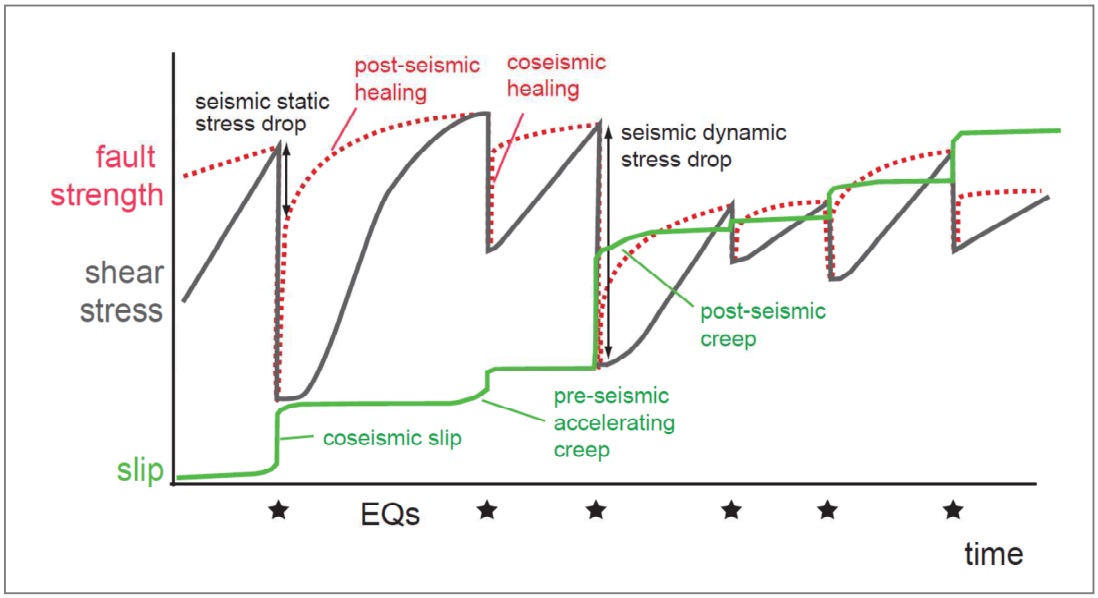


**FIGURE 1.1.** Fault failure occurs when the shear stress exceeds the fault strength. Both fault strength and loading stress evolve in time, and their feedback determines the irregular earthquake recurrence times. Pre-seismic accelerating creep might occur for some earthquakes. Post seismic creep might be as large as coseismic slip in some fault patches. This framework renders a physically-based earthquake forecasting model an extremely challenging task (from Di Toro et al., in press).

Understanding the processes controlling the evolution of the fault zone properties during the seismic cycle is a fundament for a physically-based probabilistic forecasting of earthquakes, and for determining the conditions which make a fault accommodate deformation by aseismic slip instead of seismically. Rocks which form in fault zones preserve the signatures of the processes affecting the fault rocks during the seismic cycle (e. g., Sibson, 1977; Smith et al., 2008). Earthquakes nucleate at depth in the crust: active earthquake sources can be accessed only by deep drilling of active fault zones and the depth of investigation is limited to the first 3km (e.g., Zoback et al., 2010; Boullier, 2011). The sources of the most intense earthquakes in the continental crust are located around 10 – 15 km depth (Scholz, 2002), and can be investigated only when faults are exhumed by tectonics (e.g. Sibson, 1977). In this thesis, physico-chemical processes occurring in natural fault zones have been investigated in two case studies: the active San Andreas Fault, in California, which was drilled to 3 km depth, and the Gole Larghe Fault zone, a seismogenic source exhumed from 10 km. Fluid-rock interactions have been found to be pervasive in both geological contexts. Fluids are crucial in controlling the physical properties of fault zones, as well as their mechanical behavior at the scale of the seismic cycle. The influx of fluids spans from mechanical effects on the nucleation, propagation,

arrest and recurrence of earthquakes, to the long term compositional and structural evolution of a fault zone.

### *1.1 Mechanical effects of fluids in fault zones*

The effective stresses acting in a fluid saturated medium is obtained by subtracting the pore pressure to the stress, following the concept developed in soil mechanics by Terzaghi (1943). Applied to fault mechanics, the Terzaghi's principle is a mechanism for lowering the strength of faults in presence of fluid pressure above the hydrostatic, as was firstly stated for thrust faults by Hubbert and Rubey (1959). Since then, this mechanism has been considered an explanation of many paradoxes of fault and earthquake mechanics, as (i) the low heat flow along active mature faults, such as the San Andreas Fault (Lachenbruch, 1980; Rice, 1992); (ii) the nucleation of earthquakes on unfavorably oriented faults (Sibson, 1990). Direct evidence of the effects of fluid pressure in fault stability comes from earthquakes induced by injection of fluids down boreholes (e.g., Zoback and Harjes, 1997), or by infilling of water reservoirs (e.g., Simpson et al., 1988). Geological evidence that fluid pressure higher than hydrostatic has been achieved periodically in the crust come from the widespread occurrence of veins in crustal rocks at different depths (Ramsay, 1980; Etheridge et al., 1984; Vannucchi, 2001). Shear zones in particular are recognized as preferential conduits for focused flow of overpressured fluids and mineralization (e.g., Sibson, 1987). Occurrence of multiple vein episodes in fault zones supports the idea that fluid pressure might vary during time in tectonic processes (e.g., Robert et al., 1995; Fagereng et al., 2010). How fluid pressure can be built-up and maintained in the different tectonic contexts is indeed a debated question. One of the hypothesis is that fluid overpressure might result from the sealing of some sectors of the fault zone (Byerlee, 1990). Fluids are also affecting coseismic processes, such as rupture stopping by rapid drops in fluid pressures in dilatational jogs (Sibson, 1985), or cause extreme coseismic fault weakening by thermal pressurization (e.g., Lachenbruch, 1980; Sibson, 1973; Brantut et al., 2008).

### *1.2 Chemical effects of fluids in fault zones*

Fluids exert influence on the fault zones by a variety of chemical effects, such as fluid-assisted retrograde mineral reactions, pressure-solution, crack healing and sealing, cementation, subcritical crack growth. All these effects are interrelated, in that they depend upon possibly thermally activated (endothermic and exothermic) chemical reactions between the rock and pore fluids, as well as the rate at which dissolved species are transported through the pore fluid (Hickman et al., 1995).

Retrograde metamorphism of fault rock minerals might result in long term weakening of the fault zone, when reaction products are weaker than the reactants. Some examples are the weakening of granite in fault zones due to alteration of feldspar to kaolinite (Evans, 1988), muscovite (Janecke and Evans, 1988) or, at shallower depth, to laumontite (Blenkinsop and Sibson, 1992). The abundance of clays in shallow mature fault gouge is interpreted as due to the preferential hydrolysis of feldspar to phyllosilicates in fault zones. An interesting case is the formation of the Mg-rich smectite clay saponite in fault rocks derived from the alteration of ultramafic protoliths, as found in SAFOD cores (Holdsworth et al., 2011; Moore and Rymer, 2012) and on other fault zones (Sone et al., 2012). The saponite is an extremely weak mineral (having coefficient of friction of 0.1), and its occurrence has been invoked as an explanation for creep at very low shear strength along the central section of the San Andreas Fault at shallow (< 5 km) depth (Lockner et al., 2011; Carpenter et al., 2011).

Pressure solution is a deformation mechanism occurring in rocks containing an intergranular fluid phase. Under a non-hydrostatic stress, localized dissolution occurs at grain boundaries which support the largest normal stress. Dissolution rate of minerals in an aqueous fluid is indeed higher where a crystal lattice is under high stress, due to the increase of chemical potential with pressure. The dissolved material can diffuse in the fluid, drawn by chemical potential gradients induced by stress differences, to sites of low solubility. Deposition of the dissolved material occurs then at free grain boundaries that are in contact with fluids. In natural fault zones, the minerals which precipitate at free grain boundaries are not necessarily the same which were dissolved, in response to local ambient (P - T) conditions and the chemical composition of the fluid (incongruent pressure solution). Fluid can also migrate to larger distances and deposit material in sites such as veins or strain shadows. Pressure solution processes are an effective mechanism for accommodating aseismic creep in crustal fault zones (e.g., Gratier et al., 2011). At the same time, they determine the long term strength of fault rocks, since mass transfer processes control the compositional and textural evolution of fault rocks, such the development of foliated rocks (e.g., Jefferies et al., 2006) and furnish chemical species which contribute to fracture sealing (e.g., Gratier et al., 2003). Due to pressure-solution processes, the less soluble species are passively concentrated along planar surfaces which are roughly perpendicular to the maximum principal stress. Compared with other rock forming minerals, the phyllosilicates have lower solubility in most crustal environments, and this makes foliation surfaces to be relatively enriched in aligned phyllosilicates; this fabric strongly

influences the frictional properties of faults, as friction along foliation surfaces has been proved to be much lower than the same material in an isotropic arrangement (Collettini et al., 2009).

### *1.3 Fluids in the seismic cycle: open questions*

The chemical and mechanical effects of fluids on faults are related with the various phases of the seismic cycle. Earthquake ruptures, causing pervasive fractures in the fault rocks ,as measured by seismic wave tomography on faults before and after earthquakes (e.g., Brenguier et al., 2008), and as observed in damaged zones of exhumed faults (e..g., Mitchell and Faulkner, 2009), enhance fault permeability. Fluid ingression in the fault zone boosts pressure-solution processes, which are likely to be more efficient between two successive earthquakes and to accommodate some deformation by post-seismic creep. Fracturing and cataclasis reduce the size of the distance of mass transfer between dissolution and precipitation sites, thus increasing the rate of pressure-solution. Sealing of fractures causes pressure-solution processes to be gradually less effective in accommodating creep, due to the increased distance of mass transfer. The fault zone recovers strength and the permeability decreases.

The cyclic evolution of permeability of fault zones has lead to the hypothesis that fluids, upon infiltrating after an earthquake, would be trapped due to the subsequent reduction in permeability by (i) sealing of fractures and (ii) compaction of cataclasites and fault gouge. Further reduction of pore spaces by creep and compaction of the fault gouge would allow the fluid pressure to raise until a new earthquake rupture would nucleate, and the cycle starts again (Blanpied et al., 1992; Sleep and Blanpied, 1992; Byerlee, 1993; Gratier et al., 2003; Faulkner and Rutter, 2001). This mechanism has been adduced to explain earthquakes along major, misoriented faults like the San Andreas fault. If the cycle of fluid trapping and pore pressure rise due to sealing and compaction of fault rocks is really applicable to natural faults, and to which extent, has not yet demonstrated by field evidences. For instance, is this mechanism active in the entire fault, or only in some fault zone compartments? And could this mechanism be efficient at hypocentral depths of major crustal earthquakes (10-15 km)?

Another effect of fluids in seismic fault networks is earthquake triggering by fluid redistribution and migration, as observed in seismic sequences of the Apennines in Italy (Miller et al., 2004; Chiarabba et al., 2009). Identifying the source of fluids, and thus the extent of fluid circulation in fault zones, might constrain at what depth and in which geological context such a mechanism can be active. From stable isotope studies, it has been observed that in deep-seated shear zones, fluids are

of local origin and the fluid-rock ratio is low. But in shallower and brittle fault networks, the opening of the system due to rupture propagation might allow ingression of external fluids and high fluid-rock ratios (e.g., Kerrich et al., 1984). The large extent of fluid circulation in brittle fault networks has been proved by geochemical studies in exhumed faults (e.g., Pili et al., 2002), which demonstrated, for instance, the flux of mantle derived fluids in the San Andreas fault system (Kennedy et al., 1997; Pili et al., 2011) and the infiltration of meteoric water in other faults (e.g., O'Hara and Sharp, 2001). Fluid infiltration in seismogenic faults would possibly be recorded by pseudotachylytes, quenched frictional melts which form coseismically. Stable isotope studies in deep seated pseudotachylytes demonstrated that, in those conditions, fluids embedded in pseudotachylytes were of local origin (Moecher and Sharp, 2004). If fluid ingression might trigger earthquake nucleation in other geological contexts, is still not constrained by geochemical evidence.

This thesis aims to contribute to the understanding some of the issues discussed above by integrating microstructural, geochemical and field studies on two case studies:

(i) The San Andreas Fault, which was drilled to 2.7 km depth and gives the unique opportunity to correlate fault microstructures to detailed in-situ measurements of the fault activity. The identification of a cyclic recurrence of pressure-solution creep, hydrofracture and pressure solution creep supports the idea that, in mature fault zones isolated compartments of high fluid pressure might cause low intensity seismicity, associated to the dominant creep activity (Chapter 2).

(ii) The Gole Larghe Fault Zone, an exhumed fault which was active at 9 – 11 km depth. The occurrence of pseudotachylytes allows to investigate the processes occurring at hypocentral depth of major earthquakes (Scholz, 2002). Two topics were investigated: (i) The fabric evolution of cataclastic rocks associated with pseudotachylytes with increasing deformation. This microstructural study aims to identify the (interseismic?) processes leading to the onset of unstable slip (Chapter 3). (ii) The origin of fluids involved in earthquakes nucleating at 9 – 11 km depth, where, potentially, meteoric fluids might be involved (Chapter 4).

# Chapter 2. Physico-chemical processes in the SAFOD phase 3 cores


## Abstract

*The San Andreas Fault Observatory at Depth (SAFOD) in Parkfield, central California, has been drilled through a fault segment that is actively deforming through creep and microearthquakes. Creeping is accommodated in two fault strands, the Southwest and Central Deforming Zones, embedded within a damaged zone of deformed shale and siltstone. During drilling, no pressurized fluids have been encountered, even though the fault zone acts as a permeability barrier to fluid circulation between the North American and Pacific plates. Microstructural analysis of sheared shales associated with calcite and anhydrite-bearing veins found in SAFOD cores collected at 1.5m from the Southwest Deforming Zone, suggests that transient increases of pore fluid pressure have occurred during the fault activity, causing mode I fracturing of the rocks. Such build-ups in fluid pressure may be related to permeability reduction during fault creep and pressure-solution processes, resulting in localized failure of small fault zone patches and providing a potential mechanism for the initiation of some of the microearthquakes registered in the SAFOD site.*



***This work was prepared in collaboration with Giulio Di Toro, Jean Pierre Gratier, Jafar Hadizadeh, Steven A. F. Smith, Richard Spiess and published as Mittempergher et al., GRL 2011.***


## 2.1 Introduction

The National Science Foundation granted EarthScope San Andreas Fault Observatory at Depth (SAFOD) in Parkfield offers the opportunity to correlate physical and chemical processes identified in core samples with high-resolution seismological and geophysical data (e.g., Zoback et al., 2010;

Jeppson et al., 2010; Bradbury et al., 2011). Such a complementary and multidisciplinary approach allows to reconstruct the deformation styles and the structure of the active San Andreas Fault (SAF). The SAFOD is located in the transition zone between the creeping segment of the SAF (to the north), and the southern "locked" segment, which lastly ruptured in the 1857 Mw7.8 Fort Tejon earthquake (Figure 1a). Near Parkfield, the SAF activity includes permanent creep at about 20 mm $yr^{-1}$ (Titus et al., 2006), microearthquakes (e.g. Nadeau and Johnson., 1998) and moderate (~M6) earthquakes that ruptured at fairly regular intervals between 1857 and 2004 (e.g. Bakun et al., 2005) south of the SAFOD site. The SAFOD main hole crosses the actively deforming SAF at ~2.7km of vertical depth, approximately 100 m above the hypocentral area of a cluster of repeating M2 earthquakes, which was one of the targets for drilling (Nadeau et al., 2004; Thurber et al., 2004; Zoback et al., 2010). In 2007, about 40 m of core was extracted parallel to the main hole, including a section that crosses the two actively creeping strands of the fault detected by borehole casing deformation, named Southwest Deforming Zone (SDZ) and Central Deforming Zone (CDZ) (Zoback et al., 2010).

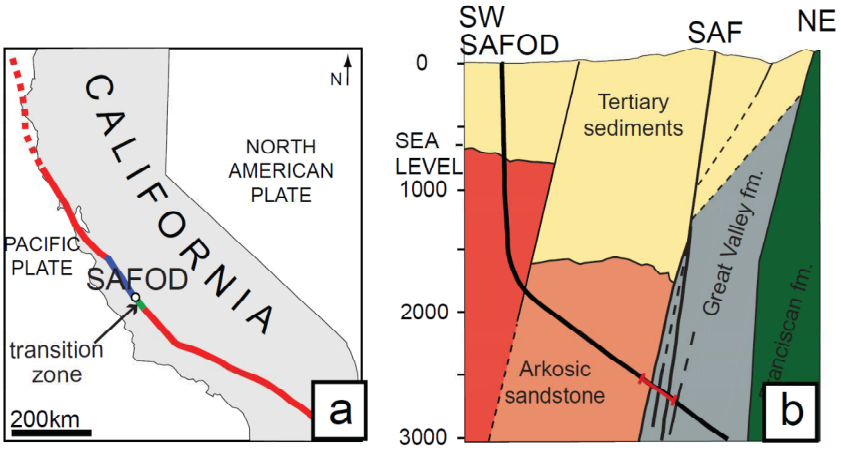


FIGURE 1. Geological setting. (a) Sketch of the SAFOD location in California. The SAF is in red (locked segments), blue (creeping section) and green (transition zone). (b) Schematic geological section of the SAFOD site, parallel to the borehole trajectory (thick black line) (Zoback et al., 2010).

Slip in the SAF occurs at much lower shear stress than expected based on laboratory friction of rock forming minerals (Brune et al., 1969), suggesting that it behaves as a weak fault in a strong crust (Rice, 1992); such a model is confirmed by down hole stress measurements and mechanical modeling (Hickman and Zoback, 2004; Chéry et al., 2004; Boness and Zoback, 2006). Pressurization of the fault core by pore fluids was one of the explanations suggested for the low strength of the SAF (Rice,

1992). Since no fluid pressure higher than hydrostatic has been detected during drilling (Zoback et al., 2010), the most convincing mechanisms remain the presence of intrinsically weak material within the actively creeping sections (saponite clays, Lockner et al., 2011; Carpenter et al., 2011) and the effect of stress driven pressure solution creep processes, which can explain the weak behavior of the SAF at temperature > 150 – 200°C, conditions where the saponite clays are not stable any more (Gratier et al., 2011). The study of the source mechanisms of repeating microearthquakes in Parkfield at depth of 2 - 5km reveals peak stress drops exceeding 50MPa (Imanishi and Ellsworth, 2006; Dreger et al., 2007), suggesting that relatively strong asperities exist within an otherwise weak fault zone.

### *2.1.1 The SAFOD borehole*

A 2.2 km deep vertical pilot hole was drilled in 2004 to collect preliminary geophysical and geological data to plan the successive phases of drilling through the SAF (Hickman et al., 2004 and references therein). The main hole was drilled in 2005 (Phases 1 and 2), in vertical direction down to 1500m depth, then inclined at about 50°, in order to intersect the SAF at high angle. The lithologies crossed during drilling were interpreted from the drill cuttings (Solum et al., 2006; Bradbury et al., 2007), and the mud gases were continuously analyzed (Wiersberg and Erzinger, 2008). Open hole geophysical logs were acquired during drilling and through wire line logging in the open hole (Baker-Atlas open hole logging). The formation resistivity, density, compensated neutron porosity, porosity, caliper, gamma ray signature and $V_P$ and $V_S$ were recorded along the main hole trajectory, from 3000m to 4000m MD (measured depth, along the main hole). The measurements were repeated in the cased hole in 2007, and the deformation registered by the 40 arm caliper tool allowed to localize the two actively creeping zones, lately named SDZ and CDZ (Zoback et al., 2010). The geophysical logs acquired in the SAFOD are available on the ICDP website (www.safod.icdp-online.org/), and the data were analyzed in Jeppson et al. (2010).

FIGURE 2 (next page). Open hole geophysical logs. (a) Open hole geophysical logs collected in 2005, before placing the hole casing. The locations of the low velocity, low resistivity zone is indicated in light gray. The rough location of the Phase 3 cores is indicated by black rectangles. (b) The caliper measurements in November 2007, with the zones of casing deformation highlighted in red ellipses.

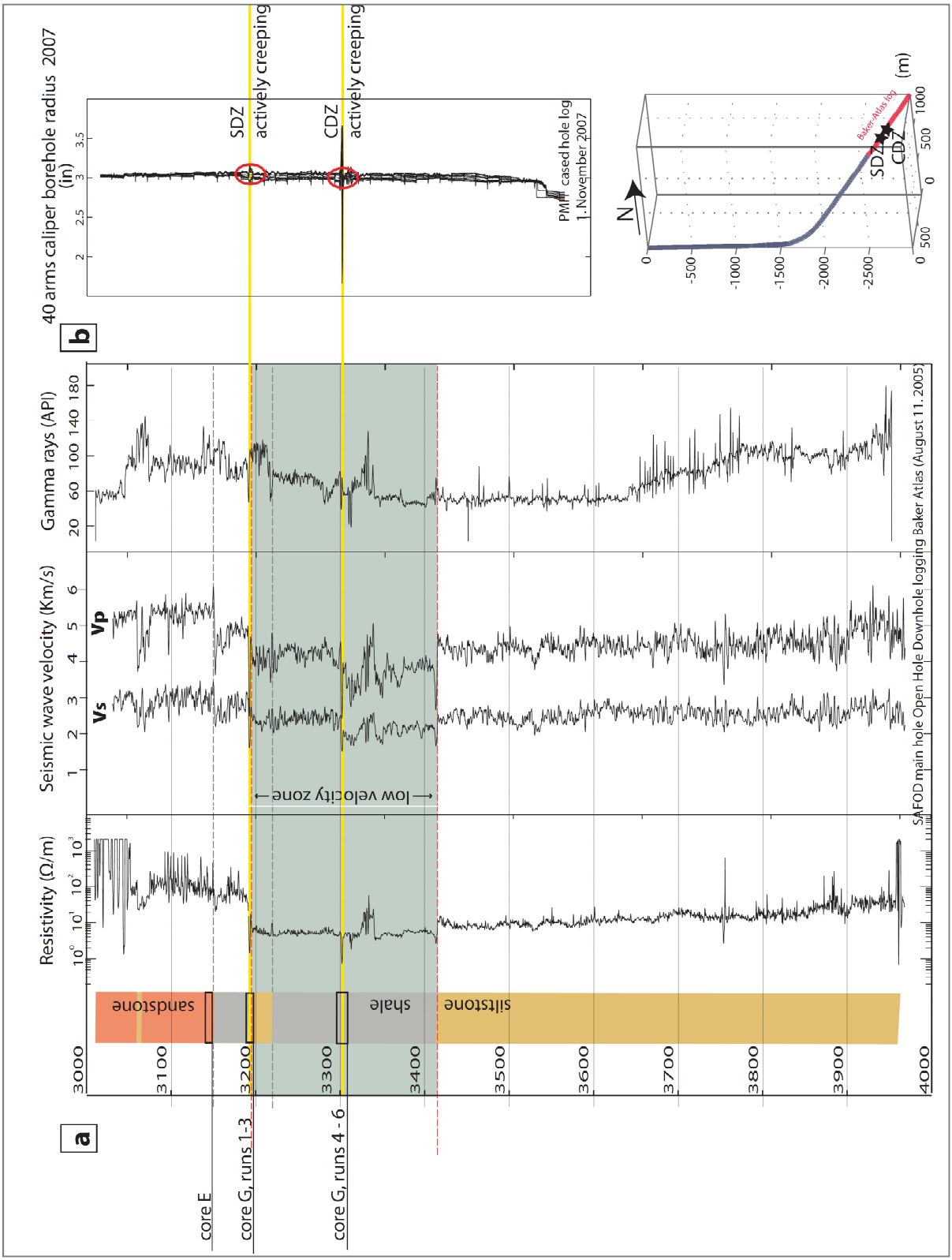
a
b
Resistivity (Ω/m)
Seismic wave velocity (Km/s)
Gamma rays (API)
Vp
Vs
low velocity zone
sandstone
shale
siltstone
core E
core G, runs 1-3
core G, runs 4 - 6
SAFOD main hole Open Hole Downhole logging Baker Atlas (August 11. 2005)
40 arms caliper borehole radius 2007 (in)
SDZ
actively creeping
CDZ
actively creeping
PMI cased hole log 1. November 2007
N
Baker-Atlas log
SDZ
CDZ
(m)

Combining drill cuttings interpretation and geophysical and geochemical logs, the downhole geology was reconstructed to plan the trajectories to extract continuous cores (Phase 3) (Figure 1b). The geological plate boundary has been crossed at about 3170m MD. It separates coarse arkosic sandstones (interpreted as the result of the erosion of Salinian granites of Paleocene – Eocene age (Springer et al., 2009)) to the south-west (Pacific plate) from shales – siltstones (interpreted as belonging to the Great Valley formation, Solum et al., 2006) to the north-east (North American plate). About 20m downhole from the geological plate boundary, a zone with seismic wave velocities ($V_P$ and $V_S$) 20-30% lower than the surrounding rocks and low resistivity extends for about 220 m (Figure 2). The low velocity zone is interpreted as the SAF damaged zone, and corresponds to an interval of foliated, clay-rich, sheared sedimentary rocks (Jeppson et al., 2010; Bradbury et al., 2011). Caliper measurements were repeated in 2007, revealing that the case of the hole was slightly deformed at 3192m MD and, more intensely at 3302 m MD (Figure 2c). The actively deforming zones have lower seismic velocities (both $V_P$ and $V_S$) than the surrounding rocks, lower resistivity and lower gamma ray intensity.

The Phase 3 cores were extracted from the geological plate boundary (Hole E) and across the two actively deformed zones (Hole G, Runs 1-3 across the SDZ and Hole G, Runs 4 - 6 across the CDZ). An accurate petrographical and microstructural description of the cores is presented by Holdsworth et al. (2011) and Bradbury et al. (2011). The main features of the Phase 3 cores are summarized in Figure 3, obtained by integrating our observations and data collected in published studies (Janssen et al., 2010; 2011; Holdsworth et al., 2011; Mittempergher et al., 2011; Bradbury et al., 2011; Gratier et al., 2011). The locations of the samples described in the next paragraphs are indicated by arrows.

### *2.1.2 Overview of the fault zone rocks*

The SAFOD cores revealed that the SAF is composed of different juxtaposed tectonic and lithological units, as many major fault zones in sedimentary units (e.g., subduction channels, Meneghini et al., 2009; Fagereng and Sibson, 2010). The SAF thus contains a mixture of materials with different stiffness, frictional properties, permeability and porosity, and mineral compositions (Bradbury et al., 2011). The deformation styles of these materials might be very different, and the combined creeping and microearthequake activity in the SAF is likely related with the different rheologies of the materials present within the fault zone.

FIGURE 3. Summary of the structures found in the SAFOD phase 3 cores. The cores below 3301m MD are not drawn, because no samples below the CDZ were examined in this study.

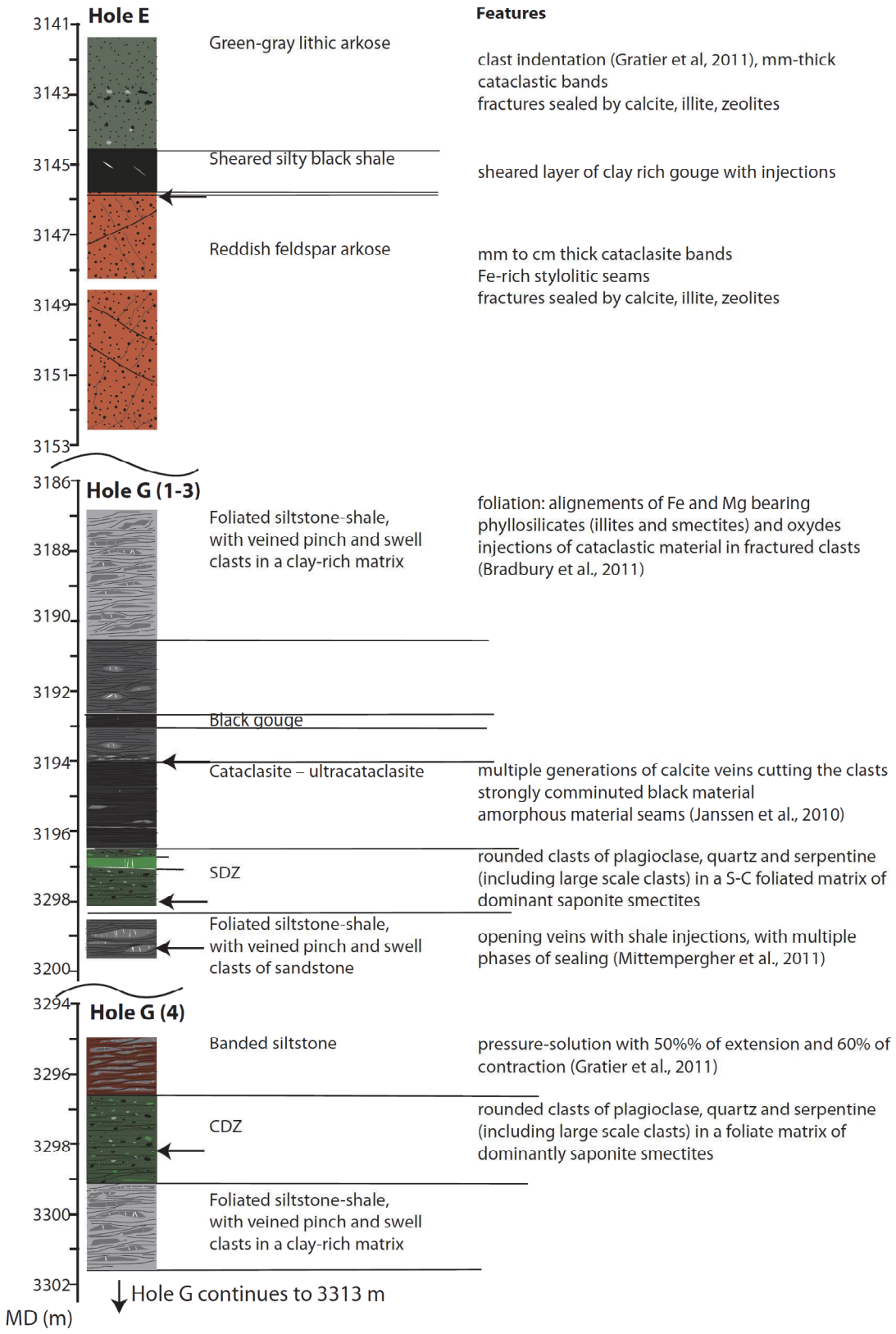
Hole E
3141
3143
3145
3147
3149
3151
3153
Green-gray lithic arkose
Sheared silty black shale
Reddish feldspar arkose
Features
clast indentation (Gratier et al, 2011), mm-thick cataclastic bands
fractures sealed by calcite, illite, zeolites
sheared layer of clay rich gouge with injections
mm to cm thick cataclasite bands
Fe-rich stylolitic seams
fractures sealed by calcite, illite, zeolites
3186
Hole G (1-3)
3188
3190
3192
3194
3196
3298
3200
Foliated siltstone-shale, with veined pinch and swell clasts in a clay-rich matrix
Black gouge
Cataclasite – ultracataclasite
SDZ
Foliated siltstone-shale, with veined pinch and swell clasts of sandstone
foliation: alignements of Fe and Mg bearing phyllosilicates (illites and smectites) and oxydes
injections of cataclastic material in fractured clasts (Bradbury et al., 2011)
multiple generations of calcite veins cutting the clasts
strongly comminuted black material
amorphous material seams (Janssen et al., 2010)
rounded clasts of plagioclase, quartz and serpentine (including large scale clasts) in a S-C foliated matrix of dominant saponite smectites
opening veins with shale injections, with multiple phases of sealing (Mittempergher et al., 2011)
3294
Hole G (4)
3296
3298
3300
3302
Banded siltstone
CDZ
Foliated siltstone-shale, with veined pinch and swell clasts in a clay-rich matrix
pressure-solution with 50%% of extension and 60% of contraction (Gratier et al., 2011)
rounded clasts of plagioclase, quartz and serpentine (including large scale clasts) in a foliate matrix of dominantly saponite smectites
Hole G continues to 3313 m
MD (m)

The SAF damaged zone (low velocity zone), is mainly composed of foliated siltstone shale, embedding elongated, pinch-and-swell clasts of more competent sandstone or siltstone (Figure3). The stiffer clasts are pervasively veined. Within the SAF damaged zone, different zones of shear localizations are present: (i) black gouge – cataclasite zones, which are not deforming, and (ii) two layers of foliated clay and serpentine rich gouge, which are actively creeping. The structure of the SAF low velocity zone contrasts strongly with the rock on the other side of the "geological" plate boundary, composed of relatively undeformed greenish sandstones and fractured reddish sandstones (Figure 3).

After introducing the analytical methods applied and the main characters of the deformation structures within the different domains of the SAF crosscut by the SAFOD Phase 3 cores, we will focus on the microstructural study of samples located at the interface between sheared shales and ribbons of sandstone with pervasive veining. We provide evidence of fracture opening in the presence of fluids and discuss mechanisms for permeability reduction and strength recovery after failure.

## 2.2 Analytical methods

The mineral composition has been determined by X-ray Powder Diffraction (XRPD). The data were obtained by step scanning using an automated diffractometer system (Philips X'Change) with incident- and diffracted-beam soller slit (0.04 rad.). The instrument was equipped with a curved graphite diffracted-beam monochromator and a gas proportional detector. Divergence and antiscatter slits of 1/2° were used so that the irradiated area could be confined to the sample at angles >10 °2theta. A receiving slit of 0.2 mm was used. A long fine focus Cu X-ray tube was operated at 40 kV and 30 mA. Diffraction pattern was obtained using a step interval of 0.02 °2theta with a counting time of 15 s. The scan was performed over the range 3–70° 2theta. The program High Score Plus (PANalytical) was used for phase identification and Rietveld refinement (Rietveld, 1967). The fine fraction was separated from the bulk powder and treated with ethylene glycol and heated to 200°C and 300°C for clay identification, following the methods described in Moore and Reynolds (1997).

Microchemical mapping was performed on polished thin sections with an Eagle III microfluorescence apparatus located at the Laboratoire de Géodynamique des Chaine Alpine (LGCA) of Grenoble (France). A grid of 256x200 spectra was acquired, with spacing of 55µm in x direction and 61µm in y direction. The fluorescence spectra acquisition was limited to the region of interest (ROI) of the following wavelength: FeK, TiK, MgK, AlK, CaK, NaK, SiK, KK and SK.

Microstructural investigations were performed on carbon-coated, polished thin sections with a field emission scanning electron microscope (FE-SEM) JSM6500F upgraded to version 7000 and equipped with an energy dispersive X-ray spectroscopy (EDS) analyzer with internal standards for quantitative chemical composition (Istituto Nazionale di Geofisica e Vulcanologia, Rome). Backscattered electron (BSE) images were collected at working distance of 10 mm and accelerating voltage of 10 kV; the BSE resolution in these conditions is 4 nm. The EDS electron beam spot size for analysis was 400 nm as estimated by means of Monte Carlo Method simulations.

The microtexture of calcite in veins was investigated by an optical microscope equipped with a Technosyn, 8200 MKII cathodoluminescence apparatus (Laboratoire de Géophysique Interne et Tectonophysique, Grenoble).

The EBSD patterns in calcite were acquired by a CamScan MX2500 SEM equipped with a tungsten filament (University of Padova) and indexed using Channel 5 software by HKL Technology. Indexing was accepted when at least six detected Kikuchi bands matched with those in the standard reflector file for calcite.

Microscopic and macroscopic fractures were discretized by tracing the digital image of the thin section. The discretized curves are composed of nodes, whose position is described by position vectors in a local reference frame;the nodes are connected by sub-equal segments, whose length is approximately 100-400 micron. To analyze the orientation data, we measured and recorded the orientation of each individualsegment and plotted all of the data on a rose diagram (Figure 2b), following the procedure of Griffith et al. (2010).

## 2.4 Observations

### *2.4.1 Deformed arkosic sandstone*

The reddish sandstones between 3146 and 3153m MD (along the core) are cut by pervasive fractures, cataclastic bands and Fe-rich pressure solution seams. The sandstones are composed mostly of quartz, albite and K-feldspar (microcline), with variable amounts of hematite, laumontite, analcime, clays (illite-smectite interlayers) and calcite (from semi-quantitative XRPD analysis). Cataclastic zones are strongly affected by pressure-solution mass transfer processes, as observed by the distribution of elements across the shear zones in XRF elemental maps Figure 4a, b. The cataclasite and the pressure-solution seams on one side of the fault are enriched in Fe, while Ca is preferentially found in calcite filled veins on the other side. Indentation of feldspar clasts is observed

within the cataclasite and in the surrounding rocks (Figure 4c,d). Intragranular fractures in quartz and feldspar grains are sealed by calcite and newly grown illite-smectite lamellae (Figure 4e, 5b). Clasts within the cataclasite layers have jagged outlines, indicative of dissolution due to fluid-rock interactions (Figure 5a).

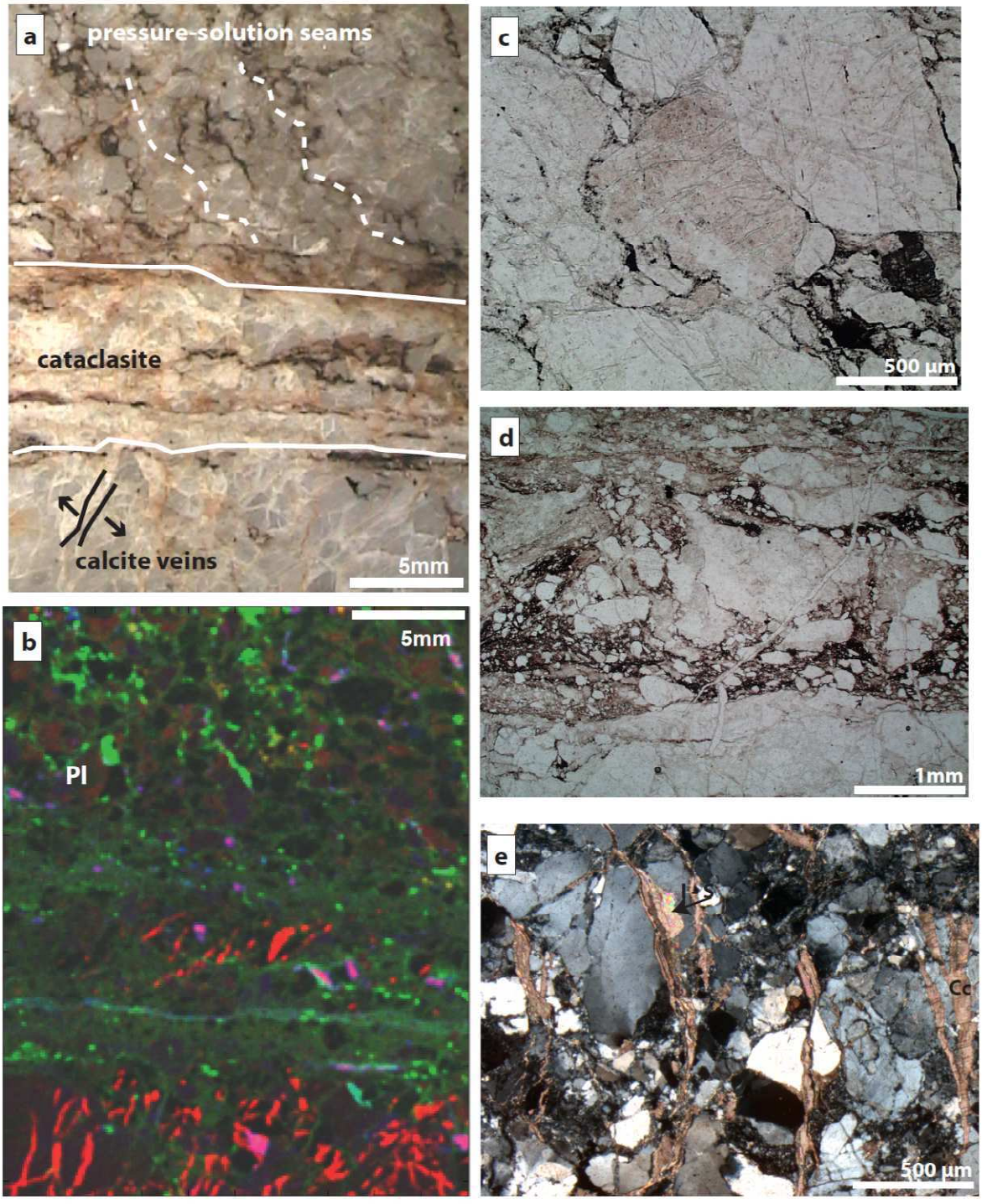

FIGURE 4 (previous page). Microstructures in the arkosic sandstone. (a) Reflected light image of a section across a cataclastic zone within the reddish arkosic sandstone. (b) Combination of X-Ray Fluorescence chemical maps of the area shown in (a): Red = Ca, Green = Fe, Blue = Ti. Green and blue layers indicate concentration of Fe and Ti oxides, red lines are veins sealed by calcite. Plagioclase (Pl) is dark red. (c) Detail of the sandstone outside the cataclastic zone, showing diffuse deformation structures as clast indentation and "radial" microcracking. (d) Detail of polimineralic clasts within the cataclasite zone, with indented boundaries. (e) Calcite and illite-bearing vein sealing the host sandstone.

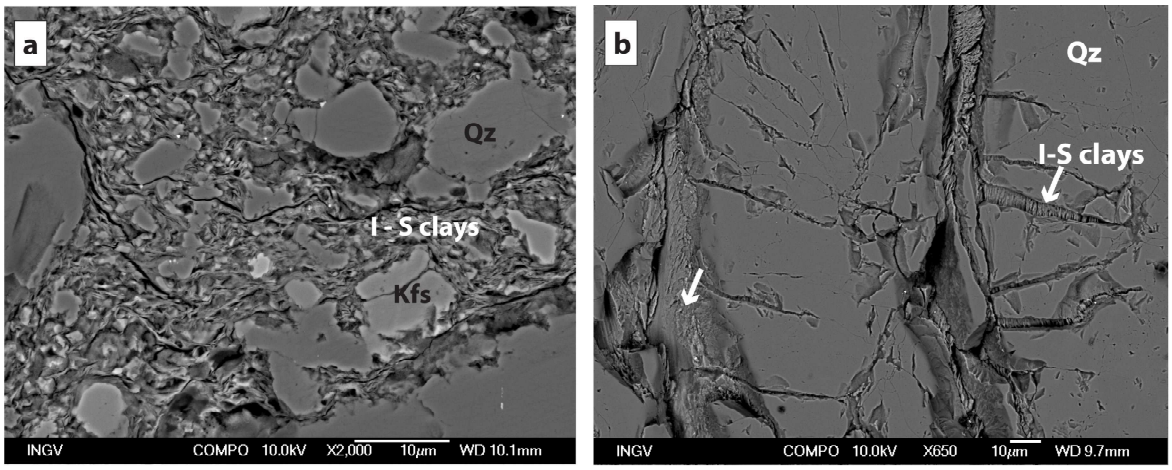


FIGURE 5. Scanning Electron images of the Arkose Sandostone. (a) SEM-BSE image of the cataclasite layer, with corroded clasts of quartz and K-feldspar in a matrix composed mainly of clays. (b) SEM-BSE image of a fractured quartz clast, with clay lamellae g filling the cracks.

### *2.4.1 Zones of shear localization*

Within the SAFOD phase 3 cores, there are two actively creeping shear zones (the CDZ and SDZ) and some inactive shear zones. Creeping shear zones have very different mineralogical composition and internal structure than the inactive shear zones. The rocks from the SDZ and CDZ contain serpentine, saponite, quartz, albite, chlorite and calcite (semi-quantitative XRPD analysis). The gouge in both CDZ and SDZ is made of rounded clasts of quartz, plagioclase, serpentine, chromium spinel, polimineralic veined cataclasites, suspended in a matrix of dominant Mg-rich clays (likely saponite from XRPD analysis). Calcite clasts are present as well. Except the spinel, clasts are strongly altered, with growth of Mg-rich clays in fractures and along the clast boundaries (Figure 6a). The clay rich matrix is pervasively foliated (Figure 6b). The foliation does not correspond to a chemical layering and there is apparently no difference in concentration of chemical elements (in this case, Mg) between clays in sites of stress concentration and in pressure shadows (Figure 7).

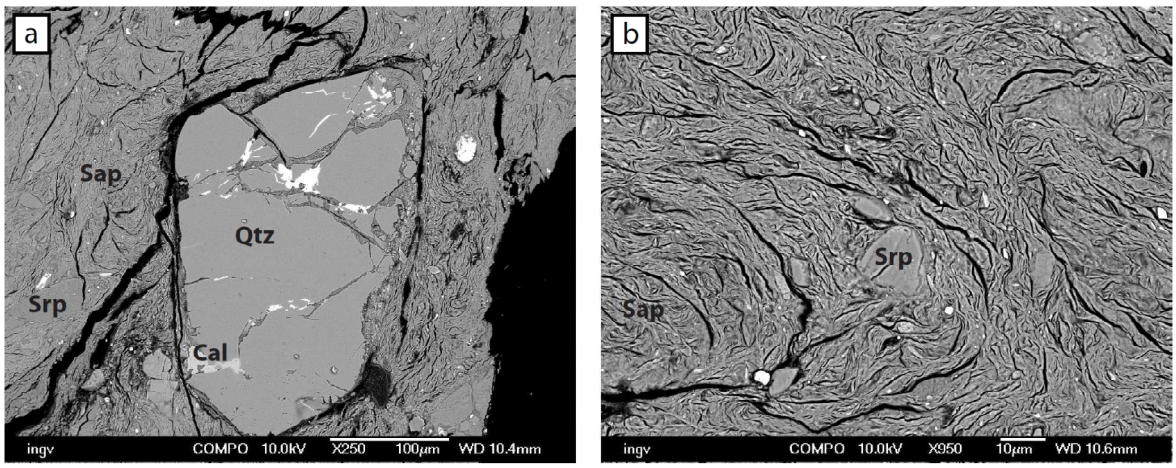


FIGURE 6. Microstructures from the Central Deforming Zone. (a) SEM BSE image of clast embedded in clay rich matrix, CDZ. Clay lamellae fill the fractures inside the clast. (b) SEM-BSE image of the foliated clay matrix, which is folded in this image.

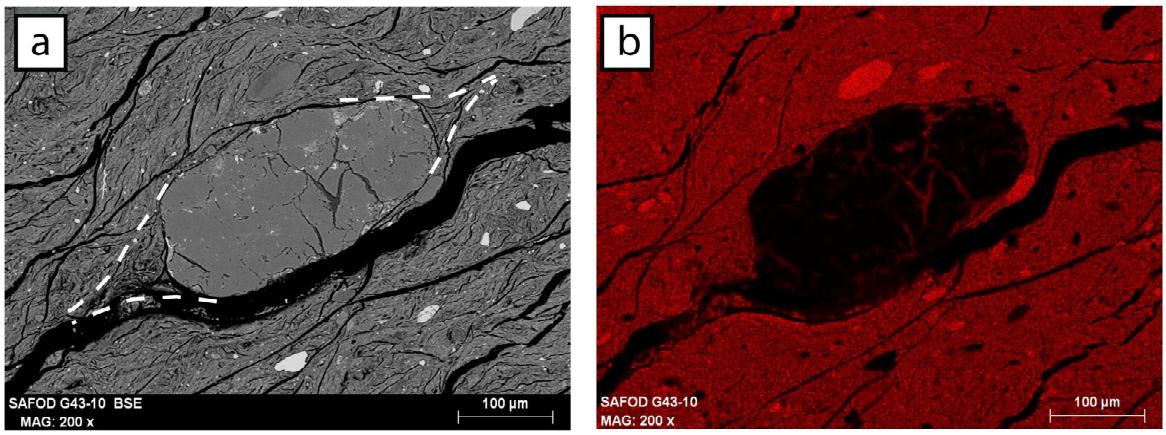


FIGURE 7. Energy dispersive X-ray spectroscopy (EDS) map from the Central Deforming Zone. (a) SEM BSE image (dashed lines limit the pressure shadows) and (b) EDS map of Mg over the same area.

An inactive shear zone is found between 3194 and 3196m MD, very close to the active SDZ. Within this interval, smears of amorphous material were found by TEM investigations (Janssen et al., 2010), and evidences of gouge injections are reported (Bradbury et al., 2011; Holdsworth et al., 2011). The bulk mineral composition is quartz, albite, K-feldspar (microcline), illite-smectites, calcite, chlorite and pyrite. The cataclasite is formed of elongated macroscopic clasts, cut by multiple generations of calcite veins. The fine grained matrix is composed of rounded clasts (comminuted quartz and feldspar, down to sub-micron size) and illite-smectite lamellae (Figure 8a). A

compositional layering is seen within the fine grained matrix of the cataclasite (Figure 8c). Notably, a domain of black, cohesive fault gouge is present below (downhole) the cataclastic layer with macroscopic clasts. The gouge is formed of intensely comminuted clasts (down to 200nm), mixed with clay lamellae (Figure 8b).

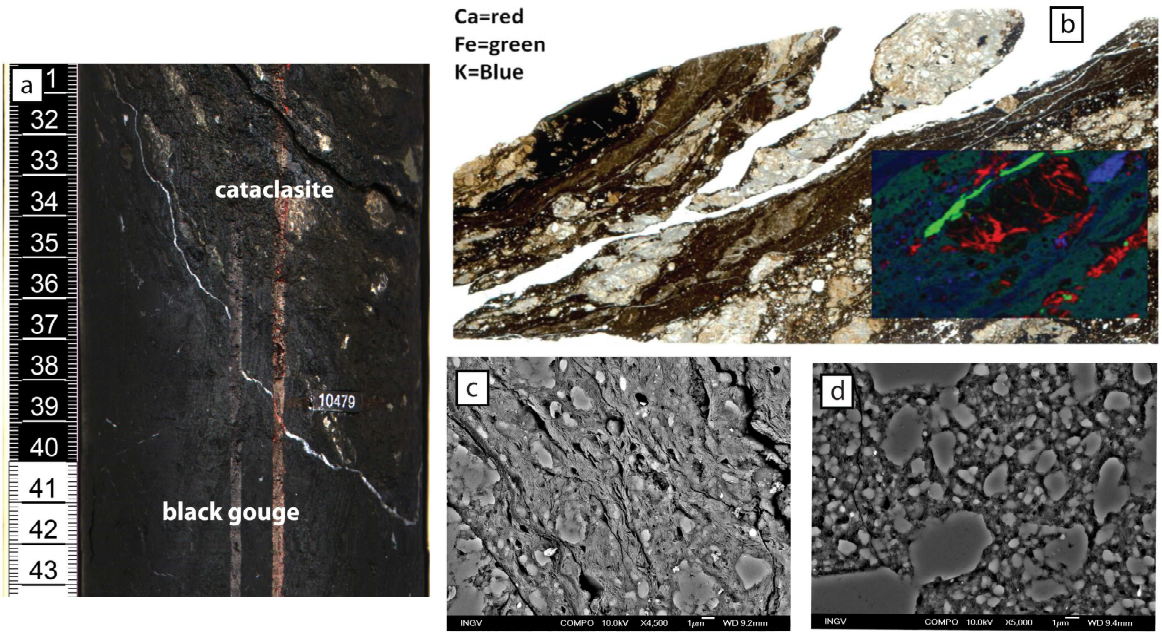


FIGURE 8. Microstructures from the cataclasite at 3194m (MD along the core). (a) Image of the core at the boundary between a foliated ctaclasite and black gouge. (b) Thin section scan of the foliated cataclasite layer at 3194 m, with superimposed chemical XRF map, highlighting the chemical banding between Fe-rich and K-rich gouge and Ca rich (veined) clasts. Image courtesy of Jafar Hadizadeh. (b) SEM-BSE image of a detail within a clay gouge layer in the foliated cataclasite. (c) SEM BSE image of detail of strongly comminuted black gouge found below the foliated cataclasite.

### *2.4.3 Veining and deformation in the foliated shales with embedded sandstone ribbons*

Here we report detailed observations on rocks sampled between 3298.5 and 3299.5 m MD (along the core), including sheared Fe-rich shales and veined sandstone ribbons (Figure 9). The phase III cores have been drilled along a trajectory parallel to that of the main hole, and we consider the attitude of the main hole axis as a reference to infer an approximate orientation of the sample. Using the foliation in the shale as reference plane and assuming that its attitude is roughly parallel to the SAF plane (Figure 9b, c), the veins are sub-vertical and make an angle of 40-100° clockwise with respect to the foliation plane (Figure 9b, c).

The sandstone in the studied core is medium grained (>500µm), composed of clasts of plagioclase, K-feldspar, quartz, mica and bioclasts and cemented by quartz. Pervasive macroscopic and microscopic veins in the sandstone are sealed by calcite and anhydrite; the veins crosscutting the boundary between sheared shale and sandstone are intruded by the shale (Figure 9c). The veins oriented at an acute angle to the shale foliation are extensional, while those roughly perpendicular to the shale foliation show extension with a component of sinistral shear (Figure 9c).

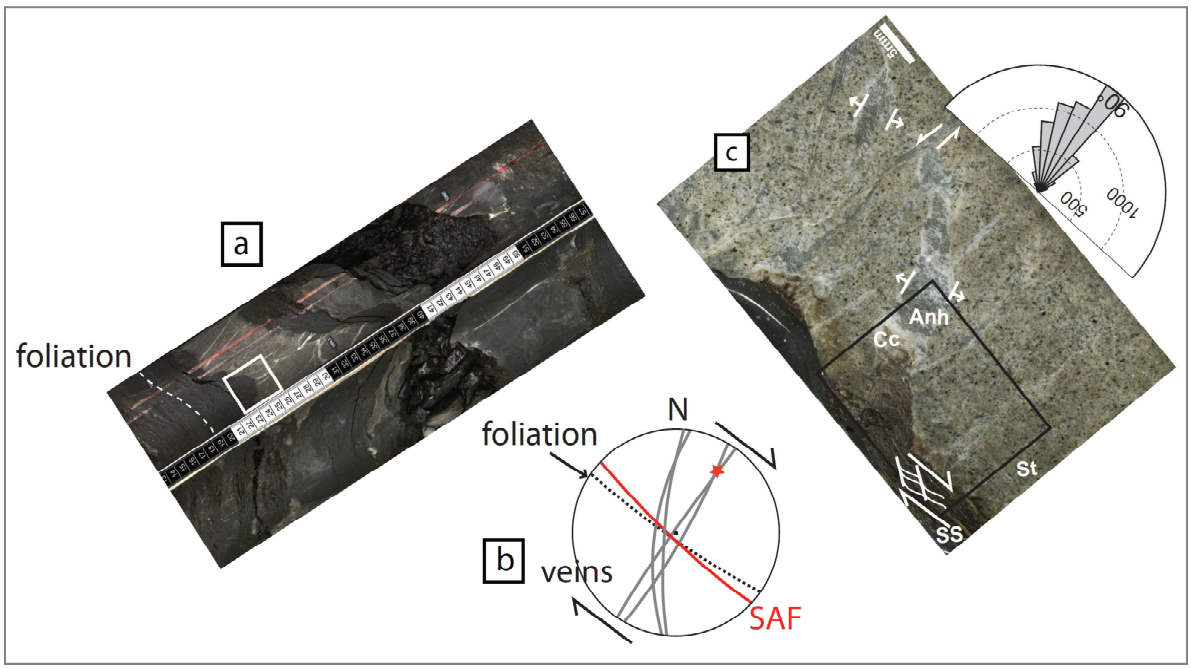


FIGURE 9. Sample of foliated shales with embedded sandstone ribbons: location and orientation. (a) The studied core section (image from http://www.earthscope.org/observatories/safod/). (b) Lower hemisphere stereoplot of great circles corresponding to the attitude of the SAF in Parkfield (red, datum from (Boness and Zoback, 2006)), the inferred attitude of the foliation surfaces in the studied core (dotted line) and the vein surfaces (gray). (c) Polished thin section, reflected light photomosaic (Cc: calcite, Anh: anhydrite, SS: sheared shale, St: sandstone). Inset: rose diagram of the orientation of the anhydrite-calcite veins, referred to the orientation of the foliation in the gouge; dashed lines contours the number of counted segments (see AM 1 for details of fracture counting). The black square is the area in Figure 10a.

The sheared shale is composed of illite and illite-smectite interlayers (altogether 48.9%), quartz (18.9%), albite (14.5%), K-feldspar (11.2%) and chlorite (4.9%), with minor calcite (1.1%) and pyrite (0.5%) (Rietveld XRPD quantitative analysis). The illite-smectite interlayers contain about 20% smectite. The sheared shale is foliated along clay-rich dissolution seams, bended toward the intrusion in the veins (XRF chemical map, Figure 10a). The material within the foliation surfaces have smaller

grain size and is depleted in Ca, Na, K, Si and enriched in Fe and Mg relative to the less deformed shale. This evolution is seen when comparing the foliation with the initial texture preserved within a strain shadow around a pyrite clast (Figure 10b). Locally the foliation shows an S-C' texture (Passchier and Trouw, 2005) (Figure 10c, d). The sandstone bears some irregular and widely spaced Fe-rich dissolution seams, which crosscut the calcite veins (dashed lines in Figure 10a). FE-SEM observations show that fibrous, micrometric illite-smectite lamellae have grown in strain shadows around clasts and within intragranular microcracks (Figure 10d). In the apical part of the veins (Figure 10a, e; 11a), intruded by randomly arranged clays and clasts from the shale layer, the pore spaces are filled by calcite (Figure 10e). The calcite and anhydrite crystals sealing the veins are mostly euhedral, forming a blocky texture (Passchier and Trouw, 2005) (Figure 11b), and include domains of elongated crystals (Figure 12a; 13c, d). Calcite shows thin and straight twins, a texture typical of deformation at temperatures below 200°C (Ferrill et al., 2004) (Figure 12c). Under the cathodoluminescence microscope, calcite has either dark or light orange luminescence. In the thick vein in Figure 10a, the calcite crystals close to the vein borders have a dark nucleus and a lighter rim and have a blocky texture (Figure 13a). Under the SEM, blocky calcite has inclusion rich nuclei, while along the crystal boundaries, calcite is inclusion free (Figure 13b). The calcite crystals towards the vein centre have light rims alternating with dark rims and crystals are elongated with the long axis perpendicular to the vein walls (stretched-fibrous texture) (Figure 12a). In the latter texture, the associated anhydrite crystals show similar stretched-fibrous crystals, with stylolites associated with microcracks oriented parallel to the long axis of the light and dark luminescence rims in calcite (Figure 13d). EBSD analysis on calcite has been performed along the vein borders (blocky calcite, Figure 12b), and towards the vein centre (elongated calcite, Figure 12c). The pole figures in blocky and elongated calcite show preferential distribution maximum density of the 'c' axes lower than 2.5 times the mean unit density (MUD), indicating a weak crystallographic preferred orientation (CPO). The blocky calcite is characterized by a weak maximum of the 'c' axes in a direction perpendicular to the vein borders. In elongated calcite, the distribution of 'c' axes shows a minimum parallel to the vein borders, with the 'c' axes plotting within a broad girdle roughly perpendicular to the vein borders.

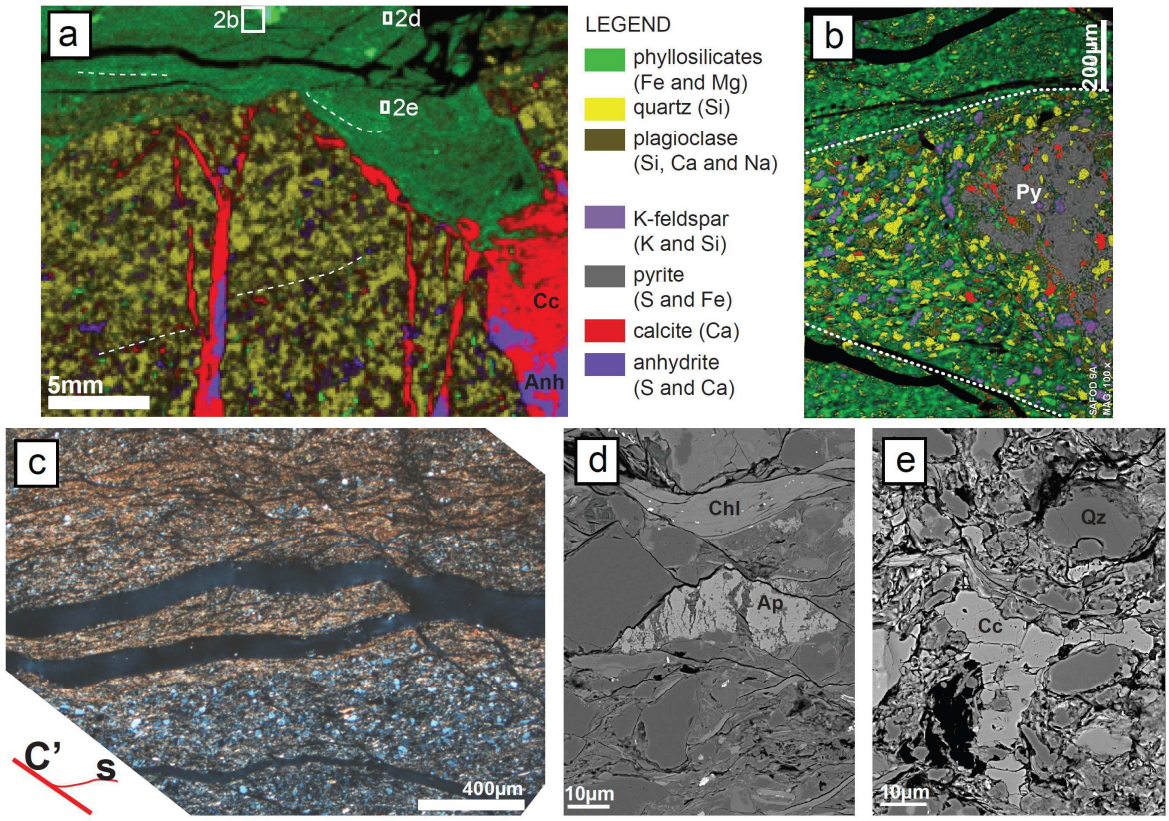


FIGURE 10. Geochemistry and microstructures. (a) Elemental chemical composition by superimposition of XRF chemical maps. Dashed lines: phyllosilicate-rich dissolution seams. (b) Detail of the elemental composition of a strain shadow around a pyrite clast (Py) within the sheared shale. Outside the strain shadow (dashed white line), there is sharp grainsize reduction, leaching of Ca and Si, and passive concentration of Fe and Mg-bearing phyllosilicates (superimposition of SEM-EDS chemical maps). (c) Foliated clay-rich shale with S-C' foliation (optical micrograph, crossed Nicols). (d) Fractures within an apatite (Ap) clast filled by fibrous Illite-Smectite (I-S) lamellae. The S foliation is defined by a chlorite crystal (FE-SEM BSE image). (e) Blocky calcite filling the pore spaces within the shale particles from the apical part of the vein intruding the sandstone (FE-SEM BSE image).

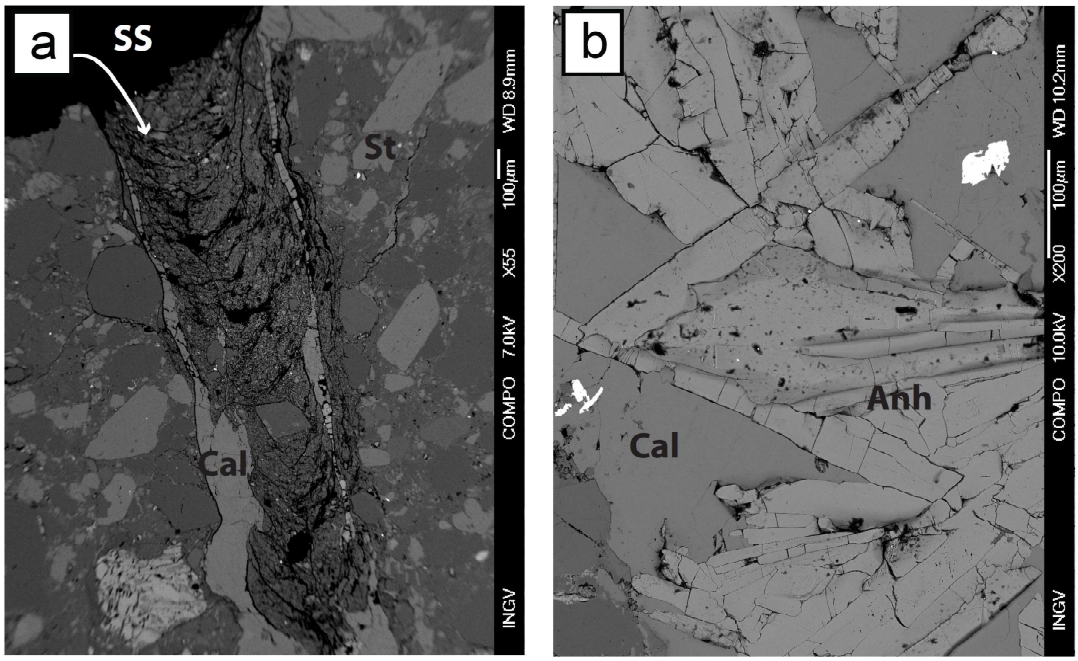


FIGURE 11. Details of the intruded veins. (a) SEM-BSE image of the apical part of a vein, intruded by shale (SS). (b) Blocky calcite and euhedral anhydrite sealing the vein.

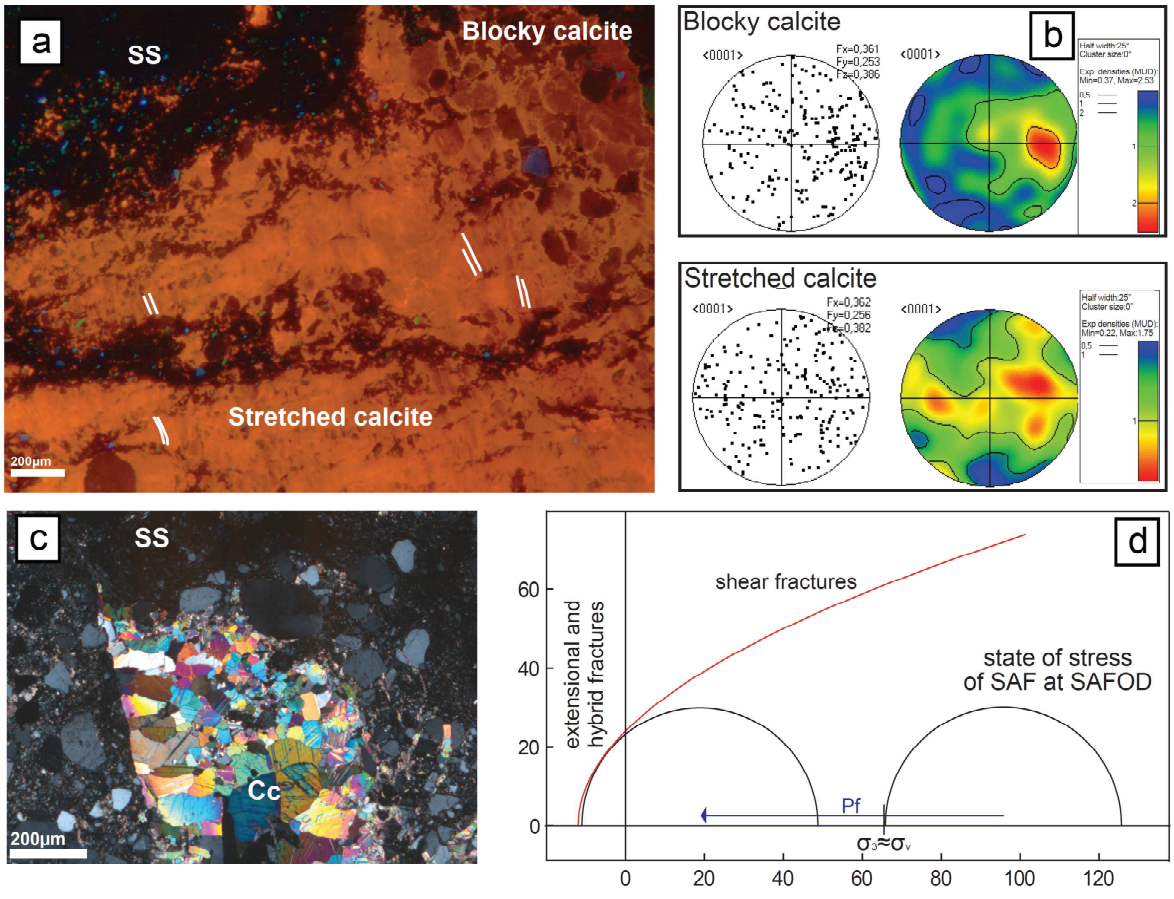

FIGURE 12. Microstructure of the calcite veins. (a) In blocky crystals close to the vein border, calcite is uniformly dark with a thin light rim; in the stretched calcite toward the vein centre, a fine scale banding of light and dark calcite is visible (CL micrograph). (b, c) EBSD data. C-axes orientation plotted in a lower hemisphere stereogram, as scattered data and contour plots; contours are expressed as multiples of mean unit density (MUD); the horizontal line in the pole figures coincides with the long axis of the CL micrograph. (d) Blocky calcite in the apical part of one of the veins, showing pervasive low temperature twinning. (e) Sketch of the Murrell-Griffith criterion of failure and the state of stress in the vicinity of the SAF (from Hickman and Zoback, 2004). The conditions for extensional or hybrid fracturing are met when the least principal stress $\sigma_3$ is negative, after a negative shift due to pore pressure higher than the lithostatic value.

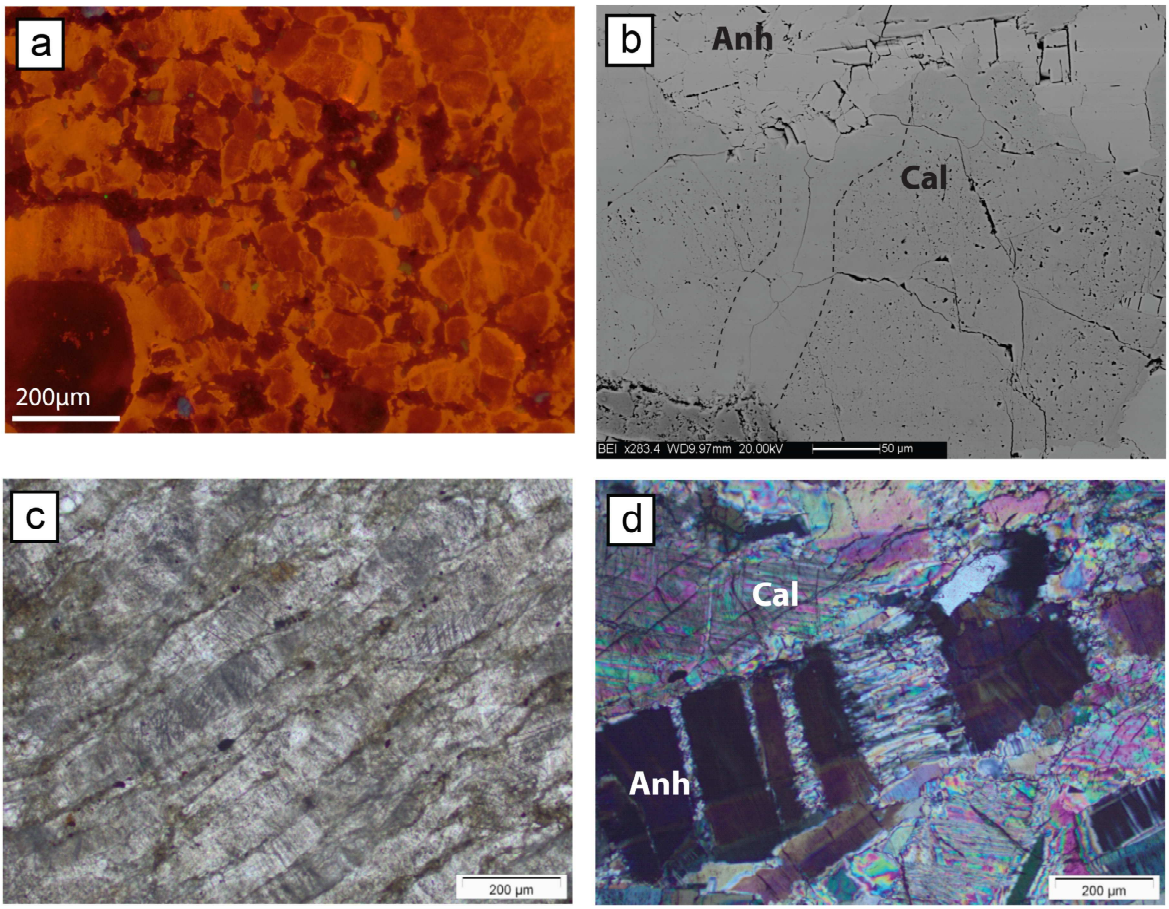


FIGURE 13. Details of the microstructures of calcite and anhydrite in the veins. (a) Cathodoluminescence image of blocky calcite, showing dark nuclei and light rims. (b) SEM BSE image of blocky calcite, with inclusion-rich nuclei and inclusion free boundaries, following the zoning found in cathodoluminescence image. (c) Stretched calcite, with crack and seal texture. Plane polarized micrograph. (d) Detail of an elongated anhydrite crystal, showing boudinage and growth of calcite in the fractures. Cross polarized light micrograph.

## 2.5 Discussion and conclusions

As revealed by downhole logging (Zoback et al., 2010), the present day creep deformation at SAFOD is localized within the two creeping zones SDZ and CDZ, composed mainly of saponite clays, having very low coefficient of friction (Lockner et al., 2011; Carpenter et al, 2011). The very low coefficient of friction of the saponite can explain the weak behavior of the SAF without invoking any super hydrostatic fluid pressure. Nevertheless, the SAF damaged zone rocks bear evidences of diffuse and localized deformation. The location of the sources of microearthquakes associated to the SAF is still poorly constrained, since they register static stress drops (up to 120 MPa) compatible with fracturing in relatively strong rocks (Imanishi and Ellsworth, 2006). We suggest that the microearthquakes might be localized within the damaged zone, or at the boundaries between creeping zones and damage zone. Here we discuss how the deformation processes active within the siliciclastic sediments in the damage zone can cause local fluid overpressure and brittle failure along a misoriented fault plane as the SAF.

The development of a foliation in the sheared shale is associated with dissolution of quartz and feldspar clasts and growth of clay lamellae in microcracks. These processes are typical of stress driven pressure solution (Gratier et al., 2009), and might cause permeability reduction due to passive concentration of clay minerals such as illite and illite-smectite, clast size reduction and pore space closure at the micrometric scale. The loss of Ca and Na and the passive enrichment in Fe and Mg along dissolution surfaces due to fault-perpendicular compression is a phenomenon documented at all scales in the SAF damage zone (Schleicher et al., 2009; Gratier et al., 2011; Holdsworth et al., 2011). Since dissolution surfaces are roughly perpendicular to the main compressive stress, they contribute to the development of fault-parallel permeability barriers that may separate compartments with distinct fluid composition, as revealed by abrupt changes in real time mud gas analysis observed during drilling into the SAF (Wiersberg and Erzinger, 2008).

Veining and dilational jogs (consistent with dextral sense of shear of the SAF) in other core sections are sealed by calcite and anhydrite, suggesting that mineral precipitation was related to the SAF activity (SAFOD 2010 core Atlas). The blocky texture of calcite and the intimate intergrowth of calcite and anhydrite in the veins indicate that vein opening was faster than calcite and anhydrite growth (e.g. Passchier and Trouw, 2005), and mineral precipitation occurred into a free fluid in an open vein. This is supported by the weak CPO of blocky calcite with the ‘c’ axis perpendicular to the vein margins: after nucleation along the vein margins, calcite crystals, which are trigonal and thus anisotropic, grow faster in direction of the ‘c’ axis. This process would result in a weak CPO due to

growth competition (Nollet et al., 2005). The intrusion of sheared shale into the veins is another indication that vein opening was sudden; disruption of foliation and calcite pore fillings within the intrusions suggest that the shale particles were mixed with fluids. The vein texture and their medium to high angle orientation to the foliation in the shale indicate that veins formed either as mode I fractures due to intrusion of pressurized shale material, or as hybrid shear – extensional (Ramsey and Chester, 2004) fractures. Following the Murrell-Griffith criterion of failure (Fig. 12de), to form either extensional (mode I) or hybrid shear – extensional (mode I/mode II) fractures, it is necessary that the effective least principal stress is tensional:

$$\sigma'_3 = (\sigma_3 - P_f) < 0 \qquad (1)$$

At about 2.7 km of depth, in the stress regime of the SAF, which is transitional between strike slip and reverse with $\sigma_h \approx \sigma_v$ as in the SAF, these conditions are satisfied when the fluid pressure is higher than lithostatic (Figure 11d).

After sealing, the veins underwent further deformation, as suggested by twinning and stretching in calcite crystals. In elongated calcite, (1) the fine-scale alternation of light and dark luminescence rims and, (2) the 'c' axis preferentially oriented perpendicular to the vein margin (similar orientation as in the blocky grains), suggest incremental grain growth ("crack-seal", Ramsay, 1980), inheriting the orientation of the former blocky crystals (Figure 12a, b, c). The change in calcite luminescence, which is influenced by traces of Fe and Mn, indicates a modification of fluid composition after the main fracturing episode.

Following these observations, we propose that one of the possible mechanisms of rupture initiation in relatively "strong" rocks embedded within the damage zone of the SAF could be a transient increase of fluid pressure in isolated compartments where the circulation of fluids is limited by fault-parallel horizons consisting of insoluble minerals. Anomalies in the focal mechanisms of two M4 earthquakes in Parkfield area support a non double couple component, suggesting that some seismic ruptures might be initiated in presence of high fluid pressure and then propagate with a dominant shear component (Johnson and McEvilly, 1995). Some of the "asperities" responsible for microearthquakes in the Parkfield segment of the SAF might thus be represented by compartments where the fluids might accumulate due to permeability reduction during compaction and pressure solution processes in clay-rich sedimentary inclusions or fault gouges (e.g., Sleep and Blanpied, 1992).

# Chapter 3. The fabric evolution with slip in natural cataclasites from seismogenic depths


## Abstract

*The complexity of the seismic cycle results from the interaction and evolution of stress (tectonic, gravitational, pore pressure, etc.) and fault zone cohesive and frictional strength with time. At seismogenic nucleation depths (7-15 km in the continental crust), fault strength and frictional behavior (velocity weakening vs. velocity strengthening) are determined by the fault zone fabric (clast shape and distribution, permeability, etc.), fault mineralogy (weak vs. strong minerals), and the kinetics of fluid rock interactions (weakening vs. healing).*

*In this study, we investigate the evolution of the fabric and mineralogy of cataclasites with finite strain from 0 to about 100. The samples were stem from the Gole Larghe Fault Zone (Southern Alps, Italy), a fault zone in tonalite which was active 30 Ma at depths of earthquake nucleation (9-11 km, 250-280$^{o}$C) and is now exposed in glacier-polished outcrops. The fault zone is composed of about two hundred sub-parallel main cataclastic horizons connected by a network of minor faults and fractures. Ancient seismicity of the fault zone is witnessed by the occurrence of pseudotachylytes associated with the cataclasites. Eleven samples were stem from faults/fractures with increasing slip (from 0 to 4.7 m), measured on displaced dykes. Samples were studied by means of microstructural (field emission scanning electron microscope, optical cathodoluminescence), mineralogical (X-Ray powder diffraction), geochemical (Energy Dispersive X-Ray Spectroscopy) and image analysis (clast size distribution and shape parameters) investigations to quantify the evolution of fabric with slip and discriminate the different physico-chemical processes active during the seismic cycle.*

*With increasing finite strain, the average grain size decrease, the fractal dimension increases (from 1.6 to 2.8 in two dimensions) and the faults develop multiple domains of foliated cataclasites and ultracataclasites. If ultracataclasite is present, thinning of the fault zone suggest strain localization and possible slip instabilities (strain weakening behavior). Fluid-rock interactions are*

*widespread in the faults and damaged tonalite, enhancing pressure-solution processes overprinting the cataclastic texture. Fluid rock interactions allow part of the deformation to be accommodated by a frictional-viscous mechanism (creep), at least for slow sliding rates.*

***This work was prepared in collaboration with G. Di Toro, J.P. Gratier, S. Aretusini.***

## 3.1 Introduction

Brittle fault zones are decorated by a layer of granular material formed by wearing of the fault walls during sliding. In the case of typical crustal geothermal gradients, the granular material is incohesive (fault gouge) at shallow depths (down to 3-7 km), cohesive due to induration by hydrothermal minerals (cataclasites) at larger depths (up to 10-15 km) (Sibson, 1977; Scholz, 2002). The fragmentation during shear of the granular material determines the size distribution (Sammis et al., 1987; Blenkinsop, 1991; Storti et al., 2003; Billi, 2005) and shapes of the grains (Storti et al., 2007; Heilbronner and Keulen, 2006). With increasing shear strain, the particle size distribution evolves to (i) fractal dimensions *D* larger than 3 (in three dimensions) (Billi, 2005), (ii) smaller grain sizes (Blenkinsop, 1991), and (iii) more rounded shapes (Storti et al., 2007; Heilbronner and Keulen, 2006). The macroscopic frictional behavior of granular materials is controlled by the interactions between particles (e.g., Biegel et al., 1989; Hazzard and Mair, 2003), and is thus strongly dependent on the mechanical properties (e.g., indentation hardness), size and shape of the particles. Friction experiments on simulated gouge (Mair et al., 2002) and 3D modeling (Abe and Mair, 2009) demonstrated that a gouge composed of angular fragments has an higher friction than one composed of spherical fragments. Experimental studies on simulated fault gouge showed that there is an evolution in the macroscopic frictional behavior with increasing displacement, as a consequence of the evolution of particle size distribution (e.g., Biegel et al., 1989) and the onset of localization of the deformation (Beeler et al., 1996; Logan et al., 1992). This behavior is of crucial importance in fault mechanics, since the evolution of fault material with increasing strain can be a factor controlling slip instability in natural fault zones. In natural faults, the fabric of granular material controls also the porosity and permeability of the fault zone, influencing its hydraulic transport properties (Faulkner and Rutter, 2001). On the other hand, the interactions with percolating fluids is a major factor in controlling the fabric of natural crustal faults and fault healing (Blenkinsop, 1991; Blenkinsop and Sibson, 1992; Gratier et al., 2002).

Here, we evaluated the effects of increasing shear strain on the fabric of small displacement faults in an ancient seismogenic fault hosted in tonalite and active at 9-11 km depth, typical earthquake nucleation depth in the continental crust. The samples were collected in the Gole Larghe fault and analyzed by means of quantitative microstructural measurements, Scanning Electron Microscope (SEM) Back Scatter Electron imaging and SEM Energy Dispersive X-Ray Spectroscopy (EDS) equipped SEM for chemical mapping. An increase in the slope of the clast size distribution with slip (from 1.2 to 2.8 in two dimensions) is measured. Possible strain localization (and weakening) is found in extremely comminuted cataclasites. Pressure-solution processes, activated by fluid infiltration upon faulting, overprint the cataclastic texture, allowing further strain to be accommodated by aseismic creep.

## 3.2 Geological setting

The Gole Larghe Fault is a dextral transpressive fault zone which cuts across the northern Adamello batholith, in the Southern Italian Alps (Figure 1a). The fault zone structure was extensively described in Di Toro and Pennacchioni (2004; 2005) and Pennacchioni et al. (2006). From regional (pseudotachylyte Ar-Ar dating, host rock dating and fission track studies, mineral assemblages in the Adamello metamorphic aureola), microstructural (evidence of incipient crystal plasticity in quartz in cataclasites) and mineralogical (mineral assemblages in cataclasites) constraints it is inferred that the fault was active at 9-11 km depth, after cooling of the host Avio tonalite, at an ambient temperature of 250-280°C (Di Toro and Pennacchioni, 2004; Pennacchioni et al., 2006). The Gole Larghe Fault is composed of hundreds of cataclasite- and pseudotachylyte-bearing fault strands which exploit pre-existing joints. The Gole Larghe Fault dips on average 65° towards N195° and the lineation has pitch of 35° to the west. Joints are pervasive within the Avio tonalite outside the fault zone, and organized in two main sub-vertical sets striking about E-W and N-S. In both sets, joints are spaced apart of 0.5-3 m (Di Toro and Pennacchioni, 2005). North-south (less commonly the E-W set) striking joints are locally activated as amphibolitic facies mylonites (Pennacchioni, 2005). Instead, in the fault zone, the East-West striking joints are usually exploited as sub-greenschist facies cataclasites and pseudotachylytes (Di Toro and Pennacchioni, 2005) and zeolite facies faults (Pennacchioni et al., 2006; Dempsey et al., 2011). From previous microstructural and field investigations (Di Toro and Pennacchioni, 2004; 2005), it is known that pseudotachylytes, which are quenched frictional melts associated with seismic sliding (Sibson, 1975), are mostly associated with

green cataclasites. The 'reactivation' of joints and the formation of a network of cataclasite-bearing faults in between the major sub-parallel joints usually predates pseudotachylyte formation (Di Toro and Pennacchioni, 2005) (Figure 1b), though there is evidence of fault segments hosting pseudotachylyte without the presence of cataclasites (Pittarello et al, 2008).

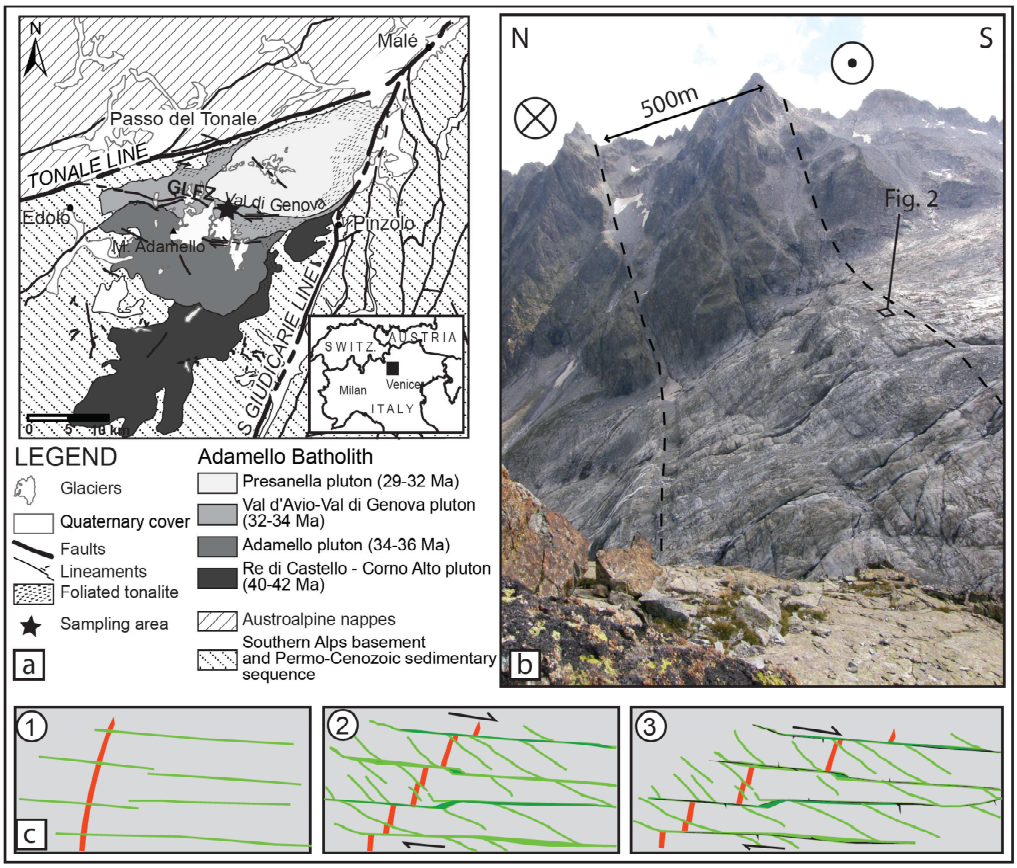


FIGURE 1. Geological setting of the Gole Larghe Fault Zone. (a) Simplified geological map of the Adamello area with location of the sampled outcrop (shown in detail in Fig. 2). (b) View of the fault zone from the west; the fault is composed of a set of about two hundred sub-parallel main faults, which exploits pre-existing joints. Joints cutting the tonalite are clearly visible outside the fault zone boundaries (to the left and to the right of the dashed lines). (c) Sketch of the possible evolution from joints (1) to pseudotachylyte-bearing faults (3), through the formation of green cataclasites (2). Pseudotachylytes, associated to seismic ruptures, record usually the last deformation event recorded by most of the individual Gole Larghe main faults.

## 3.3 Methods

### *3.3.1 Field survey and sampling*

A flat glacier-polished outcrop in the southern side of the fault zone (Figure 1b) was chosen for detailed field mapping and sample collection. The outcrop was mapped over an area of 20 $m^2$ by a mosaic of photographs taken in a rigid 60x40 cm rectangular frame, which was successively used as a reference for rectifying the pictures. The fault structures were digitized in an ArcMap project.

Eleven samples were extracted from the outcrop using a driller with diamond drill bits (20 or 40 mm in diameter). Drilling locations were chosen in order to have a complete set of displacements from zero (at the outcrop scale) to 4.3m, and fault strikes spanning over 55°. The samples were stem preferentially where the separation of the markers (aplitic dykes) was measured. The slip vector (lineation of the cataclasite fault surfaces) was not parallel to the outcrop surface, so it was necessary to convert by trivial trigonometry (i.e., relationships between the attitude of the outcrop surface, attitude of the structural marker, attitude of the fault surface and of the slickenlines, see Di Toro PhD 2003 thesis), the separations measured on the outcrop to displacements (Table 1). It was not possible to measure the attitude of the lineation on all faults, since most of the fault surfaces were not exposed. The lineation measured over the whole fault zone, including major and minor faults, is rather constant (35$^{o}$ to the west), so a mean lineation with pitch 35° to the west was used for calculations (Di Toro and Pennacchioni, 2005).

### *3.3.2 Thin section study*

Polished thin sections were cut perpendicular to the fault surface and parallel to the average lineation, after sample consolidation with epoxy. The thin sections were examined under the optical microscope for textural description. Scans of the thin sections acquired under the optical microscope (plane polarized and crossed polarized light) were used to manually map the orientation of microcracks and dissolution seams. Microcracks and dissolution seams were digitized on thin section scans (both plane and cross polarized) using a GIS (Geografic Information System) program, then the orientation of the traced segments were plotted in a rose diagram. The microfractures related to the fault activity were distinguished from those induced by sample preparation based on their fillings: only fractures bearing either fluid inclusion trails or a mineral assemblages (K-feldspar, chlorite, epidote) compatible with that cementing the cataclasites at 9-11 km depth were traced.

Cathodoluminescence images were obtained using an optical microscope equipped with an OPEA Cathodyne system (spectral range 170 to 2000nm) installed at the ISTerre, University of Grenoble. Cathodoluminescence microscopy allows to identify subsequent phases of growth in minerals, due to the possible occurrence of chemical impurities which influence the electron luminescence of the minerals (Marshall, 1988).

Microstructural study on polished, carbon coated thin sections was performed in two SEM apparatuses: a CamScan MX2500 SEM equipped with a tungsten filament or a $LaB_6$ source (Dipartimento di Geoscienze, University of Padova) and a field emission scanning electron microscope (FE-SEM) JSM6500F upgraded to version 7000 (INGV, Rome). Both devices are equipped with an energy dispersive X-ray spectroscopy (EDS) analyzer; spot analyses were collected for mineral phase determination and chemical maps were collected on selected areas (see § 6).

### *3.3.3 Image analysis*

The scanning Electron Microscope-BSE images are suitable for image analysis studies, because, once the mineralogy is known, it is possible to associate a gray intensity to a mineral phase and map its distribution over the image. The cataclasite rocks studied here have quite constant mineral composition, so this method can be easily applied. We used image analysis techniques for measuring the clast size distribution (CSD) of the clasts of plagioclase and quartz, to analyze the shapes of clasts and to measure the modal composition of the fault rock assemblage.

*Clast size analysis*

The SEM-BSE images were acquired at magnifications of 100x, 300x and 400x. Scanning Electron Microscope images were segmented to gray levels corresponding to the values of quartz and plagioclase using the threshold function of the Image analysis toolbox of MatLab® and of the software ImageJ (downloaded for free from http://rsbweb.nih.gov/ij/). The binary images were stacked over the original SEM images and manually corrected for defects such as holes due to the sample preparation, changes in brightness due to electronic gun “instabilities” and charging effects along grain boundaries. The areas of the particles with area greater than 25 pixel were then computed using the built-in function in ImageJ, excluding the particles along the edges of the image. The threshold of 25 pixel was chosen because smaller particles cannot be resolved on the SEM images, so it was not possible to check if the particle was truly a clast or, for instance, a hole or dust on the polished surface.

The area *A* of the particles was scaled to the pixel size in microns and the equivalent circular diameter $d_{eq}$ was calculated as:

$$d_{eq} = 2\sqrt{A/\pi} \qquad (1).$$

The cumulative distribution curve of the equivalent diameters was then calculated and plotted in a log-log graph. To combine data for the same sample but collected at different magnifications, the cumulative number was normalized with the area of the analyzed image, corrected for the boundary particles (i.e., the particles truncated by the edge of the image were not considered). Images at 100x were chosen for computing the slope of the cumulative curve in the log-log plot because they cover a range of grain sizes which overlaps between fine grained built and coarse grained built fault rocks. The slope of the curve was calculated in a clast size range chosen to avoid particle sub-sampling at the boundaries of the size range, either due to sub-sampling of small particles due towards the lower resolution of the image, or due to sub-sampling of the large particles towards the size of the area investigated.

*Particle shape analysis*

The binary images prepared for measuring the CSD were used also for the analysis of the particle shapes. For particle shapes, a lower threshold of 200 pixel was chosen, because, for smaller particles the effects of the shape of the pixels is not resolvable from the effects of the overall shape of the particle (e.g., Bjork et al., 2009).

The binary images were analyzed using the program ImageJ (Fiji version) and the plug-in Particle8 (http://www.dentistry.bham.ac.uk/landinig/software/software.html). The advantage of this program is that it computes both the area and the convex hull of a particle using the same method (Freeman's algorithm), so that they are directly comparable. Many of the shape parameters used to describe the roughness of the particle outlines are based on the comparison between the actual perimeter (or area) of a particle and the length (or area) of its convex hull. If the perimeter of a particle is computed for instance by pixel counting and the perimeter of the convex hull is computed as a vector polygon connecting the particle edges, in some cases the length of the convex hull might be smaller than the perimeter length. This leads to convexities, or the ratio between the perimeter and convex hull, in excess of 1, which are not realistic.

After testing the effectiveness of the shape parameters calculated by the software, we choose three parameters (the aspect ratio, orientation of the long axis (L) and solidity of the clast) which were the more robust and better described the cataclasite fabric (see section 3.8.3 and Figure 17 for definition of the shape parameters).

*Modal mineralogical composition by point counting*

In most samples, given the limited thickness (often < 2 mm) of the cataclasites and the presence of several microstructural domains (foliated cataclasites, ultracataclasites, etc.), it was not possible to obtain enough powder to determine the modal content of individual domains by means of X-ray powder diffraction (Rietveld method). At the same time, given the very similar tone of gray of epidote and chlorite, the esteem of mineral modal composition by phase mapping of SEM BSE images was not possible. For this reason, we estimated the modal composition by point counting in the images at magnitude 400x used for measuring the particle sizes. At 400x, it was possible to distinguish chlorite and epidote by eye, due to the different mineral habitus. At least 600 random points were counted for each image, and the counting was stopped when there were no more fluctuations in the distribution plot of the mineral phases.

## 3.4 The mapped outcrop

The mapped outcrop is located close to the southern boundary of the Gole Larghe Fault zone (Figure 1b). In this area, the fault zone is composed of two sub-parallel main faults, spaced 2m apart and a network of minor fractures/faults in between. The main faults dip on average 65° to N190°, roughly parallel to the E-W striking main joint set measured in the area outside the fault zone ( Di Toro and Pennacchioni, 2005) (Figures 1b and 2b). The outcrop was chosen because (i) it is flat, so its straightforward to map the surface, (ii) there are several dikes, almost perpendicular to the faults and cut by the main and minor faults. As a whole, the mapped outcrop has a finite strain $\gamma = 5.48$ (cumulative displacement $\delta$= 15224mm, outcrop thickness, 2w = 2777.3 mm), distributed over two main faults, which accumulate most of the deformation (4796mm + 1759mm = 6555mm or 43% of the cumulative displacement in the selected area) and at least 85 minor fractures which cut across the dyke marker. All the faults in the map bear cataclasites, whereas pseudotachylytes, at the outcrop scale, are found continuously on the main faults and discontinuously in some segments of the minor faults.

FIGURE 2 (next page). Surface map and structural data of the selected glacier-polished outcrop (for location, see Figure 1b). (a) Surface maps covering 20 $m^2$ and made by photomosaic of 82 orthorectified photos using a 40x60 cm frame as reference (see methods section). Main faults, having displacement > 1m and bearing pseudotachylytes, are indicated. (b) The orientation of representative structural elements measured over the selected outcrop. Lower hemisphere, equal area stereoplot.

## 3.5 Fault rocks

We focused on the (i) main faults and (ii) on the minor faults and fractures within the two main faults. The dense network of minor faults and fractures (Figure 2) is absent outside the fault zone, suggesting that it results from brittle faulting and that most minor faults are Mode II and III cracks (i.e., these minor faults and fractures are not due to cooling or other late-magmatic processes, see Di Toro and Pennacchioni, 2005). The first macroscopic effect of the increasing deformation on cataclasites is the increase in thickness and the development of multiple microstructural domains. The cataclasites evolve from very thin (less than 1mm to few millimeters thick), chlorite- and epidote-bearing fractures cutting across a weakly deformed and poorly altered tonalite, to multi-domains cataclasites bearing one or, sometimes, two or three pseudotachylyte-bearing layers surrounded by a damaged and often intensely altered tonalite.

The surface map and thin section scans were used to estimate the local thickness of the faults, estimated as area of the cataclasites divided by the length of the fault segment. The finite strain $\gamma$ accumulated by the cataclasite horizon was estimated as

$$\gamma = \delta/2w \qquad (2)$$

where $\gamma$ is the finite shear strain, $\delta$ is the displacement and $w$ is the half width of the shear zone. The displacements, thickness and shear strains of the studied samples are listed in Table 1. Fault rocks are mostly cataclasites, i.e., fragmented host rock cemented by hydrothermal minerals including chlorite and epidote, which give a macroscopic green color to the rock (for definition of the fault rocks we refer to Sibson, 1977). Layers of finer grained material, macroscopically white in color, are identified as ultracataclasites. Pseudotachylytes are macroscopically dark brown – black in color and overprint the cataclasites (Di Toro and Pennacchioni, 2004; 2005).

The thickness of the minor faults with $\delta$ < 500mm are plotted against the displacement in Figure 3. Ultracataclasite-bearing faults plot in the lower part of the diagram, suggesting that, if ultracataclasites are present, more deformation is accommodated without an increase in fault thickness.

FIGURE 3 (next page). Thickness vs displacement of the sampled faults with displacement lower than 500mm. Cataclasites bearing an ultracataclasite layer are, for a given displacement, relatively thinner than cataclasites without an ultracataclastic layer. This evidence suggests strain localization in ultracataclastic layers.

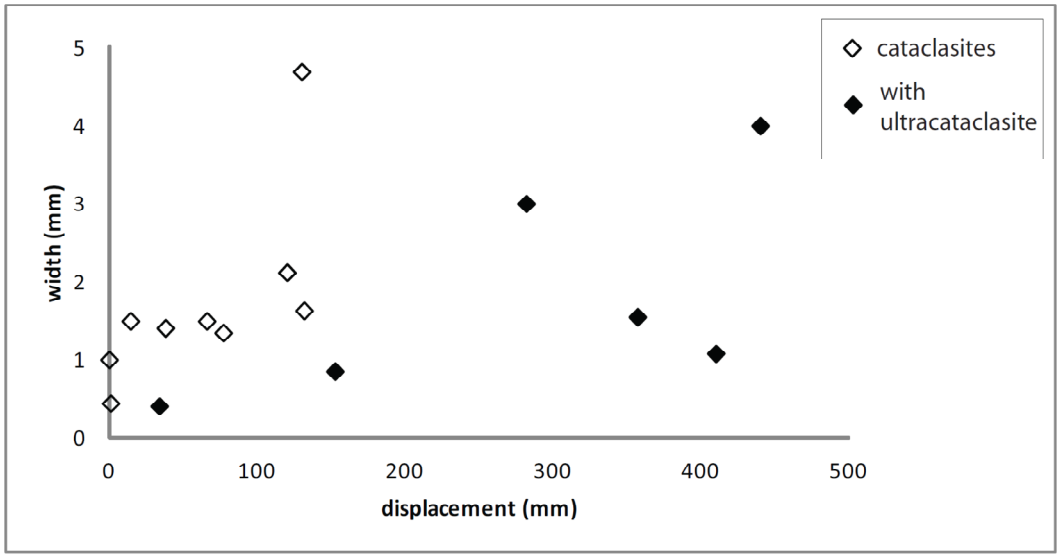


| Sample | Fault rocks | Dip (°) | Dip direction (°) | Separation (mm) | Displacement (mm) | Thickness (mm) | Shear strain (γ) |
|---|---|---|---|---|---|---|---|
| M37 | extensional joint | 88 | 205 | 0 | 0 | 1.0 | 0.0 |
| 61-2008 | cataclasite | 60 | 211 | 1 | 1 | 0.4 | 2.2 |
| 19-2008 | cataclasite ultracataclasite | 87 | 27 | 22 | 34 | 0.4 | 82.3 |
| 4-2008 | cataclasite | 85 | 26 | 24 | 38 | 1.4 | 26.9 |
| 12-2008 | cataclasite | 70 | 170 | 47 | 77 | 1.4 | 57.1 |
| 53a-2008 | cataclasite | 58 | 195 | 98 | 120 | 2.1 | 56.6 |
| S1a | cataclasite | 75 | 220 | 99 | 130 | 4.7 | 27.7 |
| | cataclasite | 80 | 190 | 91 | 132 | 1.6 | 80.8 |
| 13-2008 | cataclasite | 58 | 177 | 115 | 153 | 0.9 | 178.6 |
| S8b | cataclasite ultracataclasite | 65 | 191 | 315 | 357 | 1.6 | 230.2 |
| SM9-2008 | cataclasite ultracataclasite | 70 | 176 | 320 | 410 | 1.1 | 379.9 |
| SM-03-10 | cataclasite | 85 | 192 | 1310 | 2563 | 13.0 | 197.1 |
| 75-2008 | cataclasite pseudotachylyte | 60 | 193 | 4300 | 4796 | 68.1 | 70.4 |

TABLE 1. List of the samples used in this study.

## 3.6 Microstructures

### *3.6.1 Cataclasite-bearing minor faults*

Cataclasites are composed of clasts of plagioclase, quartz and K-feldspar, in a matrix of K-feldspar, epidote and chlorite in variable proportion (see section 3.7). The microstructure of the cataclasites changes significantly with shear strain and includes foliated and non foliated cataclasites and ultracataclasites. Here we describe the textures of three representative samples which experienced increasing shear strain (Figure 4).

In cataclasites which experienced low finite strain ($\gamma$= 1, sample 61-2008 in Figure 4a), the clasts are mostly angular and elongated, with cuspate-lobed margins, due to grain dissolution and growth of the matrix minerals along their borders (see section 7). The tonalite bounding the minor faults is cut by fractures departing from the fault. Apparently, the shape of the clasts in the cataclasite layer (Fig. 5a) is controlled by the geometry of the microfractures in the tonalite walls, which limit lozenge or rectangular shaped, cuspate-lobed, elongated clasts (Figure 5a).

With increasing shear strain cataclasites become thicker and multiple domains are developed. In sample 53a-2008 with $\gamma$ = 57 (Figure 4b), along the fault walls, a cataclastic texture similar to that found in sample 61-2008 ($\gamma$ = 1) is preserved. But towards the fault core, a fine grained (grain size < *10$\mu m$*) layer of foliated S-C' cataclasite is found. The S foliation is defined by elongated ribbons of plagioclase and quartz clasts, with wavy and jagged margins in the direction perpendicular to the S surfaces, alternated with 10-20 *$\mu m$* thick layers of matrix minerals (epidote, chlorite and K-feldspar, for details see § 7). The S foliation is deflected towards a surface of localized strain in the middle of the cataclasite layer, where the foliation is almost parallel to the localization plane (where the sample is split). The C' shears are discontinuous and strike at low angle to the fault walls, and include dragged micron-sized fragments of cataclasite minerals, mostly chlorite (Figure 5b). The sample 19-2008 (Figure 4c), which experienced higher shear strain ($\gamma$ = 82), bears a 0.4 mm thick cataclasite - ultracataclasite layer. The ultracataclasite is foliated and non-foliated. The foliated ultracataclasite is present along most of the fault core and is similar to the S-C' foliated cataclasite found in sample 53a-2008 with $\gamma$ = 57 (Figure 4b). The non-foliated ultracataclasite is made of sub-rounded grains, with average size of 5µm and occurs in discontinuous domains along the fault and continuously in fractures departing at high angle from the fault (Fig 4c; 5c). We interpret the non-foliated microstructures as probably pristine cataclastic features preserved from alteration and

chemical reactions under a gradient of stress. instead, alteration and intense fluid-rock interaction occurred in the foliated ultracataclasite (see section 3.7).

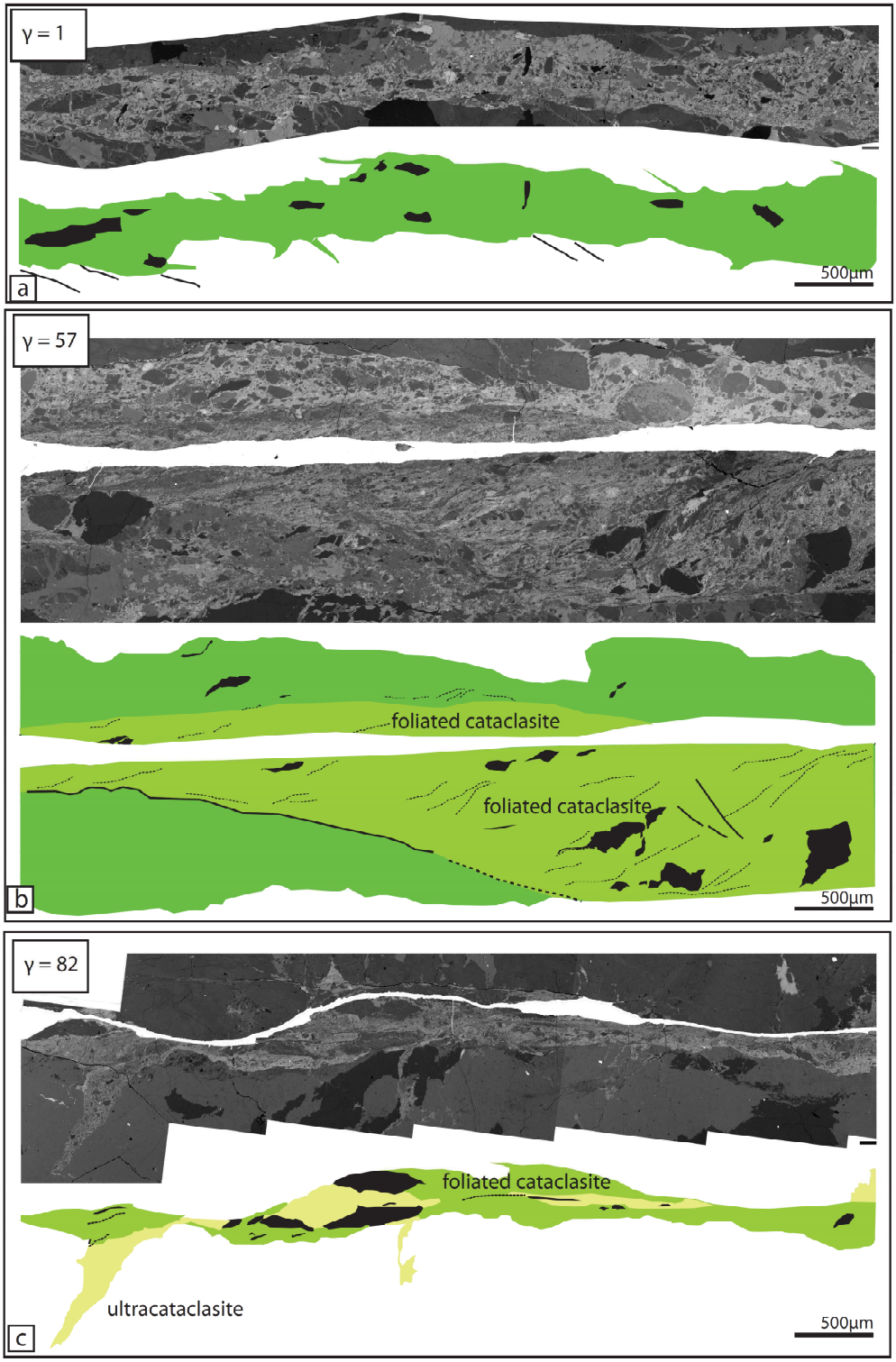

FIGURE 4 (previous page). Microstructures of cataclasites with increasing finite strain. (a) SEM-BSE image of a fault with 0.4mm of displacement and γ = 1 (sample 61-2008). It is composed of lozenge shaped clasts, preferentially aligned with the long axis parallel to the fault margins, in a matrix of epidote, chlorite, K-feldspar. Similar lozenge shaped grains are found in the wall rocks bounding the faults (Fig. 5a). (b) SEM-BSE image of a fault with 120 mm of displacement, with γ= 57 (sample 53a-2008). Compared with (a), the fault is much thicker and foliated. The foliation is defined by iso-oriented and boudinaged clasts of plagioclase and quartz and by banded matrix minerals (epidote, chlorite, K-feldspar). The grain size decreases from the fault margins towards the center (where the sample was split). (c) SEM-BSE image of a fault with 34mm of displacement with γ = 82 (sample 19-2008). Ultracataclasite is dicontinuosly present along the fault wall and fills cracks in the wall rocks. Elsewhere, the fault rock is a foliated, fine grained cataclasite.

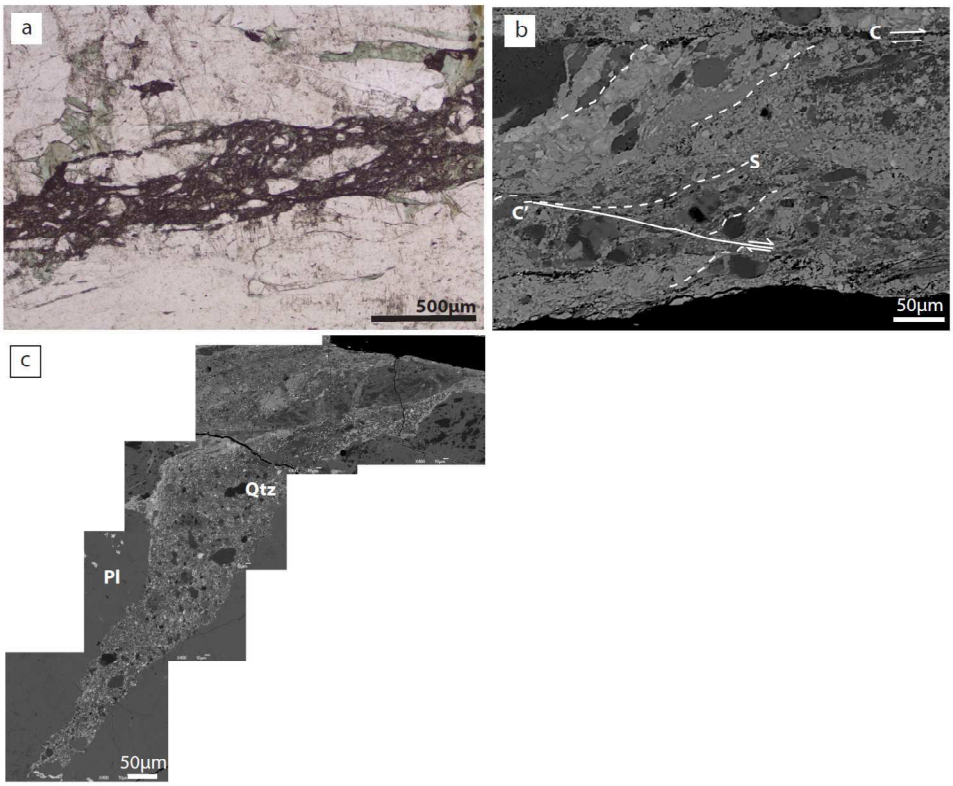


FIGURE 5. Details of the samples shown in Figure 4 (all SEM-BSE images). (a) Sample 61-2008, with γ = 1, detail of tensional fractures in host tonalite with formation of elongated clasts due to the growth of chlorite and K-feldspar in the fractures. With deformation and fluid-rock interaction these clasts are progressively included in the fault. (b) Sample 53a-2008, with γ= 57, detail of the foliation, with dragged micron sized clast fragments in C and C' type shears. (c) Sample 19-2008, with γ = 82. Ultracataclasite filling a fracture departing at high angle from the fault.

The tonalite around minor faults is characterized by pervasive microfracturing. Microfractures are either sealed by chlorite and K-feldspar (see section 3.7), or, inside quartz grains, healed by fluid inclusion trails. The microfractures are mostly clustered in two sets, one striking at low angle to the fault surface and one at 30 – 70° to the fault (Figure 6). The low angle fracture set is better represented on the southern side of the faults, the one at high angle on the northern side. Around minor faults which accommodated larger displacement, most microfractures tend to be oriented at about 30° clockwise from the fault, consistently with the likely orientation of the far field principal horizontal stress responsible for the dextral sense of shear of these minor faults.

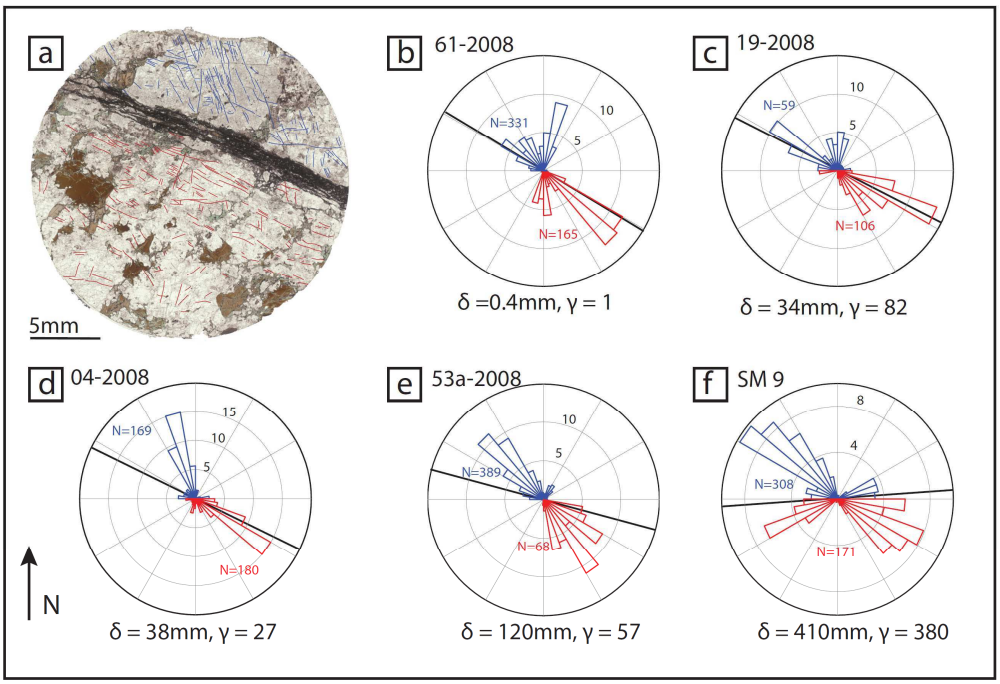


FIGURE 6. Microfractures filled by chlorite+K-feldspar or healed by fluid inclusion trails bounding the minor faults. (a) Thin section scan of a fault (sample 04-2008) with displacement of 38mm, with microfractures traced in red (southern side) and blue (northern side). The strike of the microfractures for this particular fault is represented in the rose diagram in d. The diameter of the thin section is 2.4 cm. (b) to (f), rose diagrams for microfracture orientation in tonalites bordering minor faults with increasing slip. The fracture frequency is normalized on the total number of fractures on each side and the number of measured fractures is reported in the rose diagrams (since the areas covered by the thin sections are different, the fracture intensity is not represented in these diagrams).

### *3.6.3 Cataclasite-bearing main faults*

The main faults, which accommodated more than 1000mm of displacement, are much thicker (several centimeters thick) than minor faults/fractures and are composed of several foliated and non foliated protocataclasite, cataclasite, ultracataclasite and pseudotachylyte layers (Figure 7). In sample 75-2008, which accommodated 4796 mm of displacement, we recognize two layers of ultracataclasite (uc, one light brown and the second black in color under the optical microscope) and a pseudotachylyte layer (pt, brown in color), crosscutting a cataclasite layer (cc) (Figure 7a, b). The thick layer of cataclasite borders the fault walls (cc) (Figure 7a, b). The pseudotachylyte veins are the last deformation event, because they overprint the ultracataclasite and include elongated clasts of ultracataclasite and K-feldspar + chlorite veins (in pink in Figure 7b). Based on these crosscutting relationships, the succession of deformation events is: cataclasite, ultracataclasite, veining and pseudotachylyte.

Cataclasites are composed of clasts of plagioclase, quartz and reworked cataclasite/ultracataclasite clasts in a matrix of epidote, chlorite and K-feldspar (Figure 7d). Clasts are sub-angular, and sometimes show a pervasive internal fracturing as it is highlighted by cathodolumunescence imaging (Figure 8). The clast outlines are cuspate-lobed, mainly quartz clasts where they are rimmed by chlorite. No penetrative foliation is developed in the cataclasite.

In ultracataclasites, quartz and plagioclase clasts have more regular boundaries and are overall rounded in shape. There are two domains of ultracataclasite: (i) cemented by chlorite, K-feldspar and epidote (Figure 7c, light green in the sketch in Figure 7b) or (ii) cemented by dominant K-feldspar (Figure 7e, light yellow in Figure 7b). At the optical microscope, the ultracataclasite cemented by K-feldspar appears similar to the pseudotachylyte, due to the occurrence of rounded, sparse survivor clasts in a very fine matrix. Under the SEM, it was not possible to identify any evidence of rapid quenching from a melt phase, such as microlites and spherulites. The amount of clasts is higher than in most of the pseudotachylytes, as highlighted by cathodoluminescence images (Figure 8c, d).

In pseudotachylytes, clasts are well rounded, few large clasts of quartz and plagioclase are preserved, while the average size is much smaller than the one found in the cataclasite and ultracataclasite layers (Figure 8c, d). The matrix is composed of acicular biotite in a not resolvable matrix, probably of plagioclase and K-feldspar plagues (not visible in Figure 7f; for details, see Di Toro and Pennacchioni 2004).

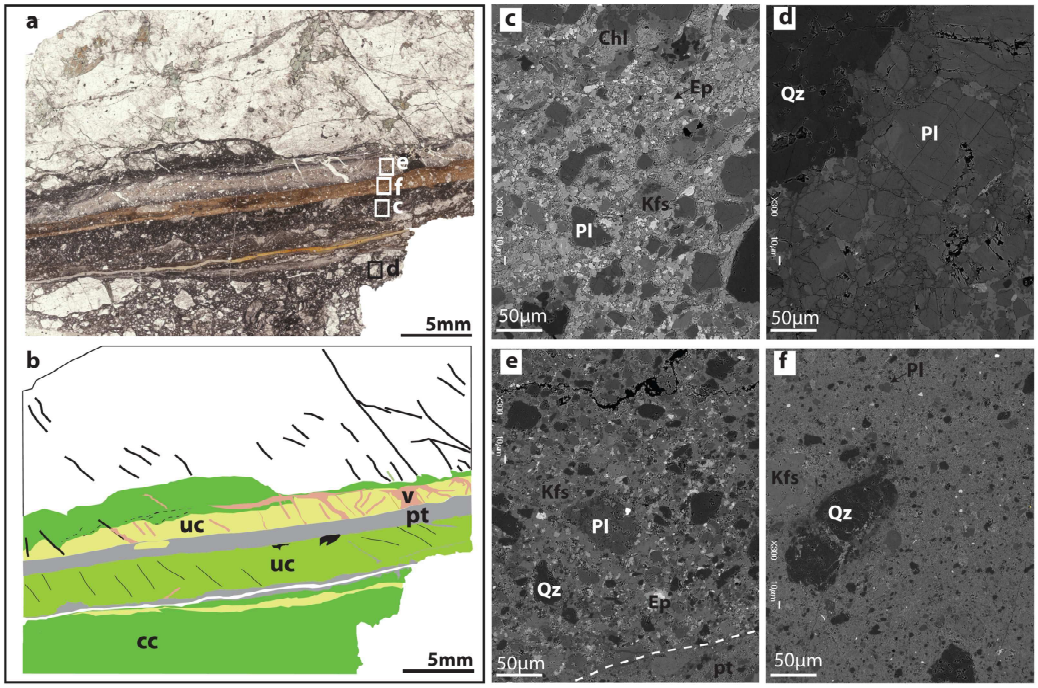


FIGURE 7. The main faults, which accommodated displacements of several meters, have multiple microstructural domains. (a) Thin section scan and (b) sketch highlighting the structure of a fault (sample 75-2008) with 4796mm of displacement (cc: cataclasite, uc: ultracataclasite, v: veins of K-feldspar and chlorite, pt: pseudotachylyte). (c) Ultracataclasite, composed of large, pervasively fractured, clasts of the host tonalite (SEM BSE image). (d) Cataclasite, composed of clasts of plagioclase and quartz (plagioclase>quartz) in a matrix of epidote, chlorite and K-feldspar (SEM BSE image). (e) Ultracataclasite composed of angular clasts of plagioclase and quartz in a matrix of dominant K-feldspar (SEM BSE image). (f) Pseudotachylyte, with rounded quartz and plagioclase clasts (quartz>plagioclase) in a cryptocrystalline matrix (SEM BSE image).

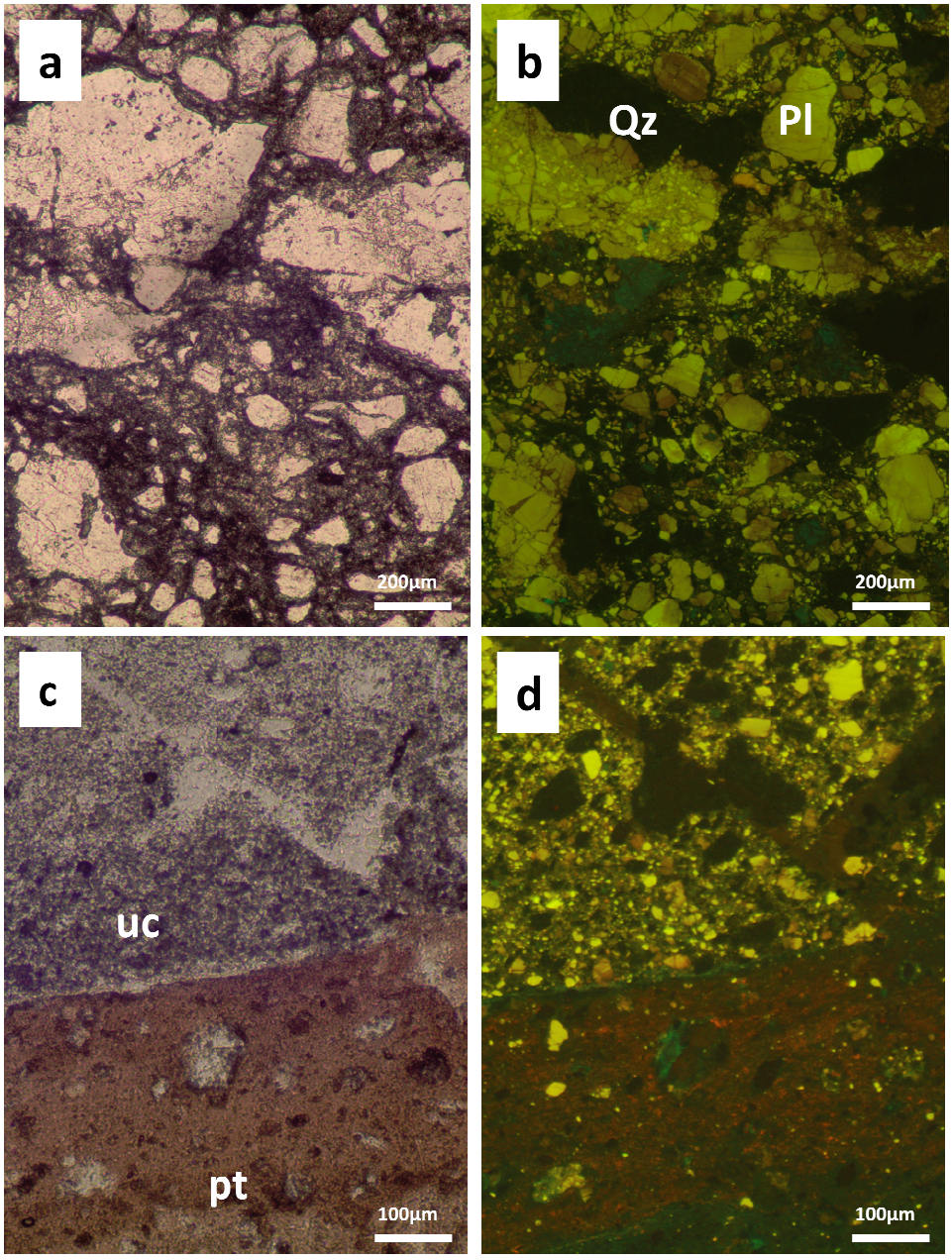


FIGURE 8. Cathodoluminescence images. (a) and (b) Strongly fractured clasts in the cataclasites close to the wall rocks of sample 75, with displacement = 4796 mm. Yellow, plagioclase, blue K-feldspar. The damaged plagioclase has a reddish luminescence. (c) and (d) The contact between the ultracataclasite (uc) cemented by K-feldspar and the pseudotachylyte (pt). Notice the large density of small plagioclase clasts (yellow). Optical and cathodoluminescence micrographs.

Protocataclasites enclosed between two fault strands or in restraining bends, own a S-C' foliation (Figure 9a). The S foliated material is composed of pervasively fractured plagioclase and

quartz, alternated with deformed biotite grains (Figure 9b-c), which are dragged in C' shears (Passchier and Trouw, 2005). At higher magnification, plagioclase and quartz in S domains appear to be fragmented down to sub-micron grain size (Figure 9d, e). Micrometric quartz aggregates have polygonal, inequigranular (with sizes spanning from 1µm to 20µm) grains; fluid inclusions are trapped in grain boundaries (Figure 9d). Plagioclase aggregates are instead composed of inequigranular fragments, with stylolitic grain boundaries (Figure 9e).

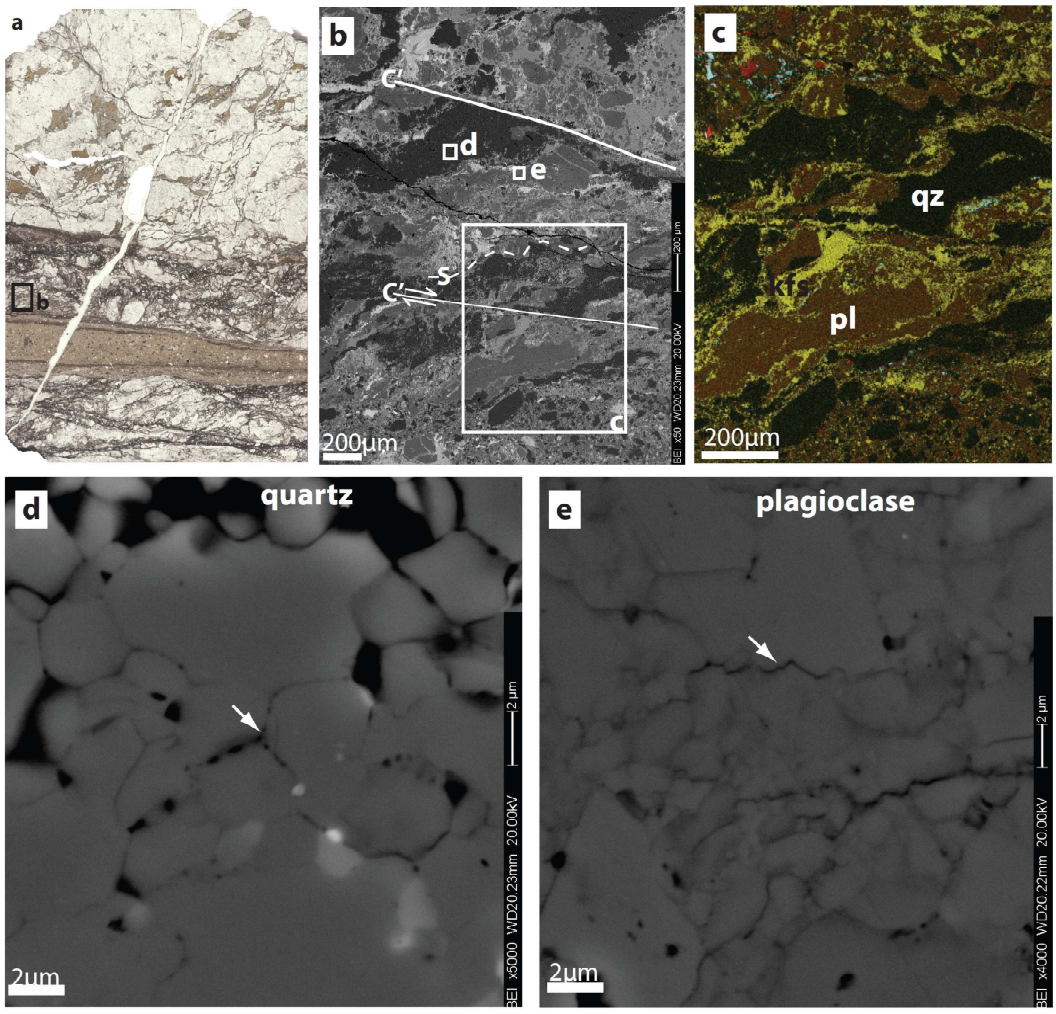


FIGURE 9. Foliated protocataclasite in a main fault (sample S4A-2010) with a cumulative displacement of 1759mm, from a contractional jog. (a) Thin section scan showing the structure of the fault zone, composed of a thick pseudotachylyte layer cutting across a foliated protocataclasite. (b) SEM-EBS image of a S-C' foliated domain, with the location of the images (d) and (e). (c) Combination of SEM EDS maps of Ca (red), K (yellow ) and Ti (light blue), so that plagioclase is orange, quartz black, K-feldspar yellow, epidote red and titanite light blue. Quartz, K-feldspar and plagioclase particles are dragged in the C' shear band. (d) Detail of a quartz

plague, which is composed of micrometric fragments. Straight grain boundaries and traces of fluid inclusions along the grain boundaries (arrow) suggest quartz recrystallization in presence of fluids. (e) Detail of a plagioclase plague, composed of micrometric fragments. Indentation of grains suggests that pressure solution processes were active after fragmentation.

## 3.7 Geochemistry and mineralogy

The Avio tonalite at the Lobbia Glacier is 1-5mm in grain size, composed of 48% $An_{45}$ plagioclase, 29% quartz, 17% biotite and 6% K-feldspar, with accessory titanite, apatite and allanite (Di Toro and Pennacchioni, 2004). The cataclasites reported here are instead composed of K-feldspar (18.1 – 42.41%), epidote (3.41 - 43.3%), chlorite (5.65 – 27%), plagioclase (3.42 – 30.18%), quartz (0.9 – 21.75%) and titanite (0 – 2.26) (modal compositions estimated by point counting, see section 3.3.3). The relative abundances of the minerals change significantly among the different samples and even among different microstructural domains (cataclasites vs. non-foliated ultracataclasites) within the same sample (Figure 10a).

The modal content of the cement minerals (K-feldspar and chlorite) was compared with the ratio of plagioclase and quartz contents. If the cataclasites underwent only mechanical fragmentation, the ratio should be the same in tonalite and cataclasite. The starting tonalite has a ratio plagioclase/quartz of 1.6, while cataclasites have al large span of plagioclase/quartz values suggesting that a loss of either mineral occurred (Figure 10b). Apparently, the plagioclase/quartz ratio increases with increasing chlorite content and decreases with increasing K-feldspar content. This suggests that precipitation of chlorite in the matrix of cataclasites occurred from silica-poor fluids which resulted in preferential dissolution of quartz. When instead K-feldspar is dominant in the matrix, plagioclase is preferentially dissolved.

The elemental bulk compositions (from X-ray fluorescence) of four cataclasites from large displacement faults was compared to the composition of the host tonalite in an isocon diagram (Grant, 1986, 2005) (Figure 11, modified from Pennacchioni et al., 2006). Using the composition of the undeformed tonalite as a reference (straight line in Figure 11), the cataclasites show (i) a strong enrichment in $K_2O$, loss on ignition and $Fe_2O_3$, (ii) a slight (within the standard deviation) enrichment in $TiO_2$, MgO and MnO, (iii) a loss of $Na_2O$, CaO, $SiO_2$ (iv) same concentration of $Al_2O_3$, $P_2O_5$, FeO.

These changes in elemental contents are well justified by the growth of K-feldspar and epidote at the expenses of plagioclase and quartz, as shown by modal mineral compositions.

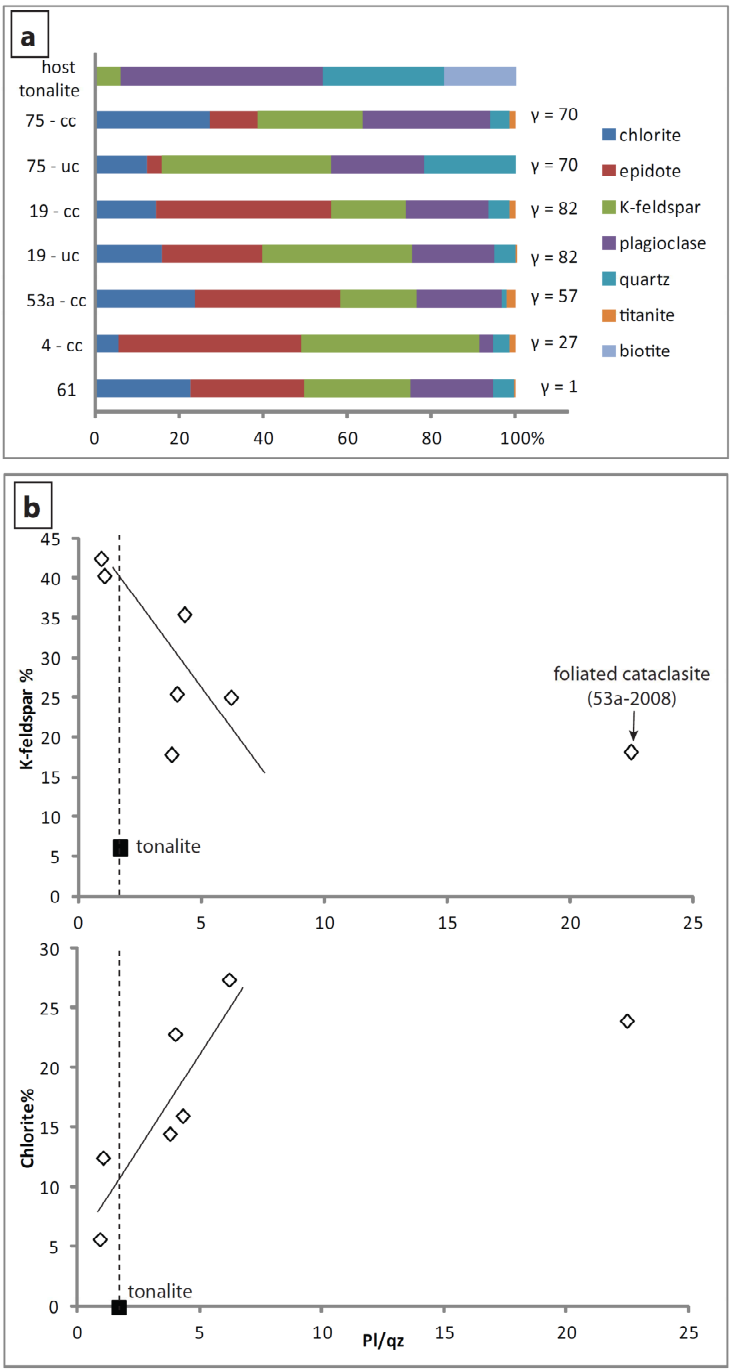


FIGURE 10. Mineral modal content of cataclasites from point counting (see section 3.3 for description of the method) and host tonalite (Di Toro and Pennacchioni, 2004). (a) Bulk modal mineral composition of

cataclasites and tonalite. Finite strain in cataclasites increases from bottom to top. (b) Content of K-feldspar and chlorite plotted against the ratio plagioclase/quartz, for cataclasites (open diamonds) and tonalite (black squares). Lines are drawn by hand (not regression lines).

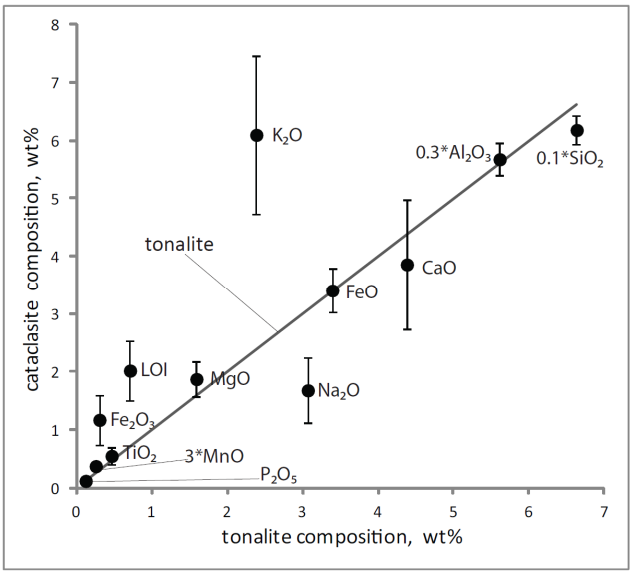


FIGURE 11. Plot of the major elements composition of cataclasite (averaged over four samples, error bars are standard deviations) compared with the composition of tonalite (straight line). Data from X-Ray fluorescence analyses (Di Toro and Pennacchioni, 2005 and Pennacchioni et al., 2006).

FIGURE 12 (next page). Fluid rock interactions in cataclasites. (a) SEM-BSE image of cataclasite with γ= 1. (b) Same area imaged in (a): combination of SEM – EDS chemical maps (K: yellow, Mg: red, Ca: blue), showing the randomly arranged matrix of epidote, chlorite and K-feldspar cementing the cataclasite. The fractures in the damaged tonalite are sealed by chlorite and K-feldspar. (c) SEM-BSE image of foliated cataclasite. (d) Sketch of image (c) showing the preferential growth of chlorite in pressure shadows (tensile cracks) between plagioclase and K-feldspar boudins. Epidote and titanite crystals are preferentially aligned along the foliation (s). In this SEM-BSE image the contrast is high, so the plagioclase appears black in color. (e) SEM-BSE image of a ultracataclasite cemented by K-feldspar. The foliation is very weak and plagioclase breakdown is suggested by the darker (Na-rich) haloes at the border of the grains. (f) Sketch of image (e) highlighting the occurrence of Na-rich rims in plagioclase.

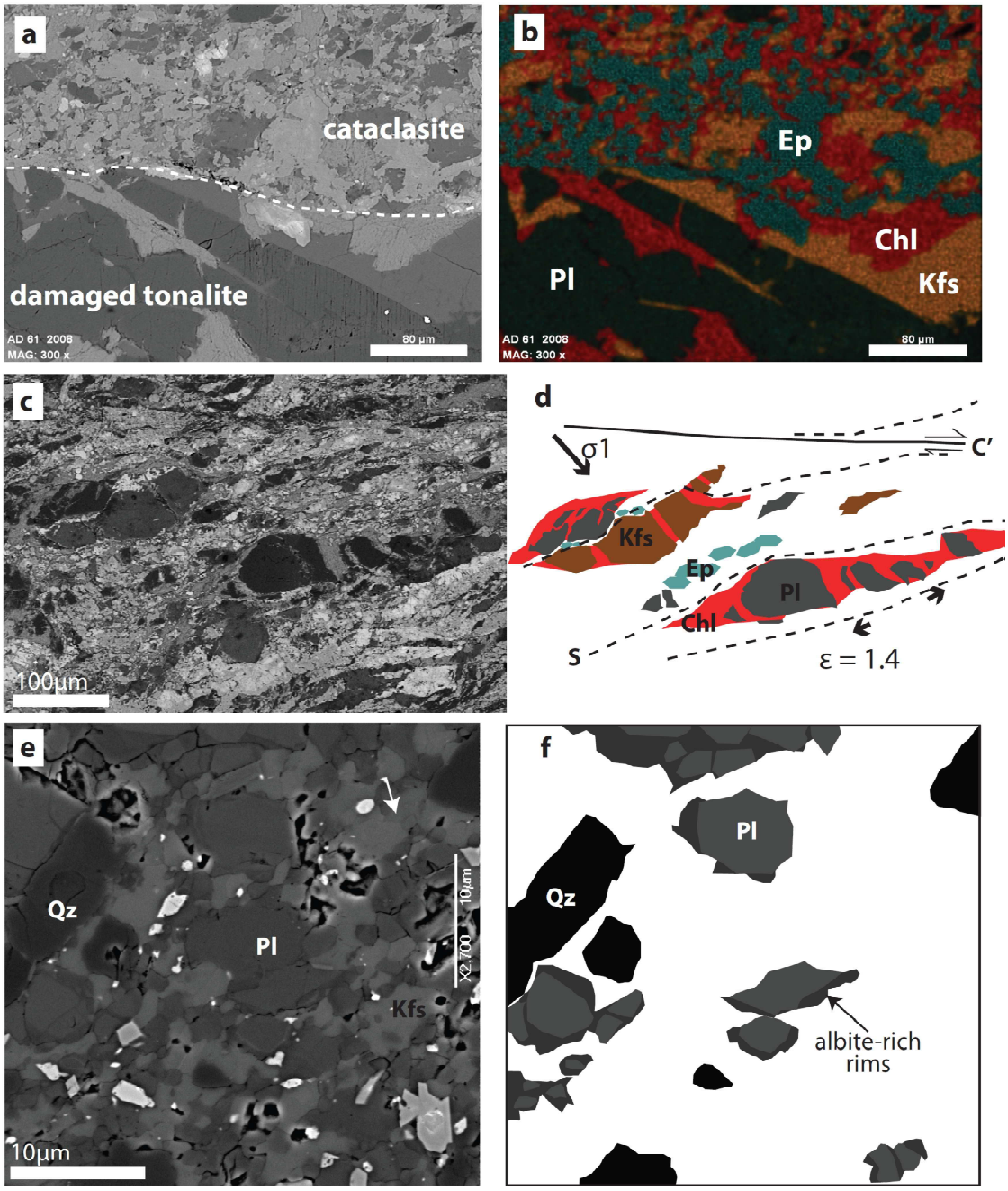


In faults with low shear strain, the cement minerals are randomly arranged. Epidote is idiomorphic or poikiloblastic (including other mineral grains), often zoned with Fe-rich cores (lighter in SEM BSE images) (Figure 12a, b); chlorite lamellae are randomly distributed and K-feldspar is in plagues. Microfractures in tonalite are sealed by chlorite and K-feldspar (Figure 12a-b).

The foliation in cataclasites with higher finite strain (e.g., γ = 57), is defined by aligned, elongated quartz and plagioclase clasts, K-feldspar plagues and epidote seams. The clasts of plagioclase are fractured in direction perpendicular to the S surfaces, and chlorite and, on less extent, K-feldspar fill the fractures (micro-boudinage, the strain along the plagioclase grain in Figure 9d is ε = 1.4), as well as in strain shadows at the tips of plagioclase clasts (Figure 12c-d). These observations suggest that chlorite and K-feldspar grow preferentially in zones of stress shadowing, such as fractures perpendicular to the foliation and around "hard" objects. The undulate boundaries of plagioclase, K-feldspar and quartz clasts along the foliation suggest instead that there is a preferential dissolution of these minerals under the driving stress (the orientation of the foliation and of the tensile cracks is consistent with the dextral sense of shear of these faults, Figure 12c-d).

In ultracataclasite domains accommodating higher finite strain, the foliation is very weak and the main cement mineral is K-feldspar with blocky texture (Figure 12e, arrow). The plagioclase clasts have albite rich rims (Figure 12f).

In the damaged tonalite close to faults, biotite is partially (retrograde) metamorphosed to an assemblage of chlorite + K-feldspar + titanite (Figure 13). Titanite grains are aligned along biotite kink bands and grain boundaries (Figure 13a), defining anastomosed surfaces. Titanite seams in biotite adjacent to faults were traced over the whole sample set, and have a quite constant orientation (Figure 13b), perpendicular to the shortening direction inferred for the outcrop (Boullier et al., 2004). The microcracks departing from the altered biotite are sealed by chlorite and K-feldspar, which grow preferentially in 'protected' sites.

Summarizing, the modes of fluid rock interactions in cataclasites which have been recognized in the analyzed samples are: (i) bulk change of chemical and mineralogical composition, with dissolution of either quartz or plagioclase depending on the mineralogy of the matrix; (ii) stress driven dissolution of quartz and plagioclase along the foliation surfaces; (iii) precipitation of chlorite and K-feldspar in protected domains (strain shadows and tensile fractures perpendicular to the foliation surfaces); (iv) retrograde metamorphism of biotite, with distribution of the reaction products controlled by stress concentration and stress shadowing.

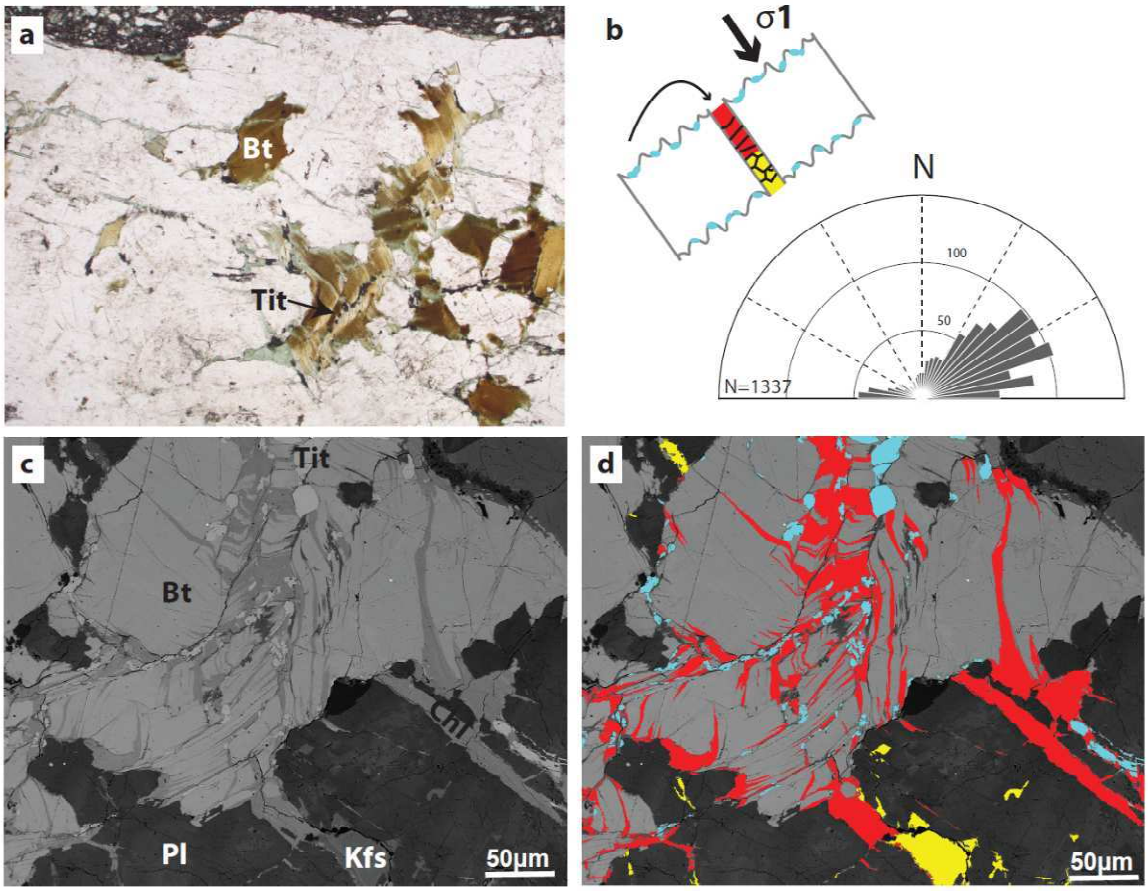


FIGURE 13. Evidence of fluid-rock interactions in damaged tonalite. (a) Biotite grains in the host tonalite break down to chlorite + titanite + K-feldspar. Titanite grains inside biotite are aligned. Their alignment forms an angle of about 30° anti-clockwise with respect to the fault. (b) Titanite seams in biotite measured over nine samples collected in the outcrop have a quite constant orientation (with a peak at 30° anti-clockwise with respect to the fault). Tensile cracks filled by chlorite and departing from the biotite grains are oriented at about 90° from the titanite seams. The orientation of the tensile cracks and of the titanite seams is consistent with the inferred far field main principal stress of the area for dextral shearing of the studied main and minor faults. (c) and (d) SEM-BSE images of a biotite grain partially altered. In the sketch, red is chlorite, yellow K-feldspar and light blue titanite.

## 3.8 Image analysis results

### *3.8.1 Clast size distribution*

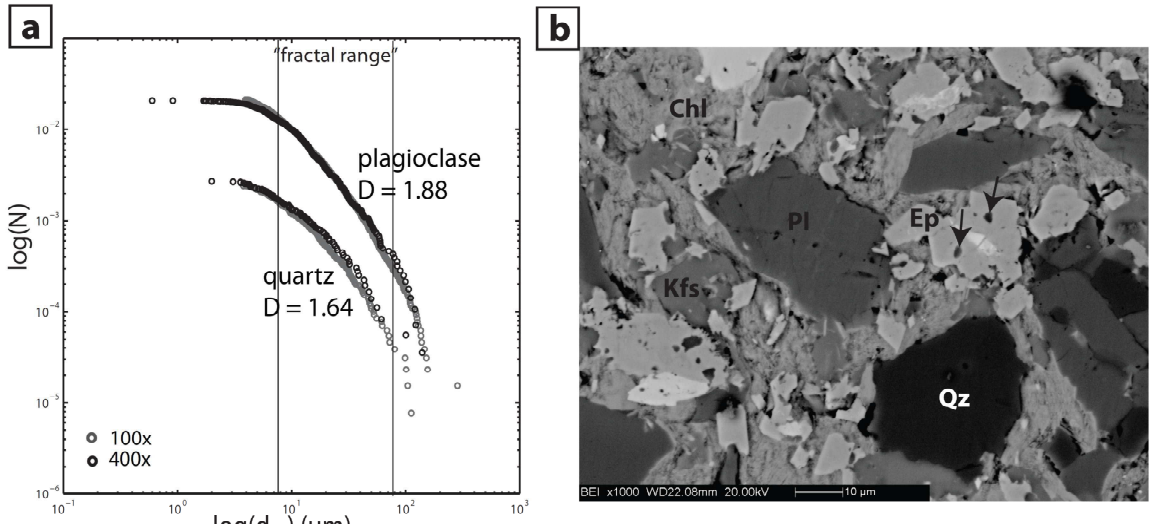


FIGURE 14. Clast size distribution and microstructure of sample 61-2008 from a low strain fault (γ=1). (a) 2-dimensional CSD from a combination of image analysis collected at 100x and 400x. The cumulative number of clasts is normalized by the area of the image. Data of quartz at 400x are quite scattered due to the very low number of clasts present in the analyzed image. (b) Scanning Electron Microscope BSE image of the at 100x magnification.

The CSD measured in images at 400x magnification shows that in low strain cataclasites, the clast fraction with equivalent circular diameter $d_{eq}$ < 6µm is under-represented (Figure 14a), i.e., in the log-log plot, the cumulative distribution curve flattens for small $d_{eq}$. Scanning Electron Microscope images collected at greater magnifications (1000x, resolution 0.1 µm) confirm that micron-size particles are few compared to larger grains (Figure 14b). A lower limit of 6 µm is thus imposed for calculating the slope *D* in the log-log diagrams, in order to have a comparable set of data among samples with different grain sizes. This restriction was chosen for the purpose of internal comparisons of the dataset collected in this study or in other studies performed on similar grain size ranges (see discussion in Di Toro and Pennacchioni, 2005). In fact, a rigorous application of power law distributions should cover several orders of magnitude in grain size (Turcotte, 1997). The exponent *D* (called 'fractal dimension' if the distribution covers several orders of magnitude in size, e.g., Turcotte 1997) was calculated as the slope of best fit of the cumulative distributions in

*log(number) – log($d_{eq}$)* space. The upper limit of the distribution was chosen to cover the linear part of the distribution curve in a log-log plot, i.e., when the linear fit was attained with $R^2 > 0.9900$ (Figure 14a). Also the under-represented coarse grain fraction is excluded in the determination of *D*. The values of *D* and the relative "fractal" range are listed in Table 2. The slope *D* was calculated for quartz and plagioclase, where the number of clasts was sufficient to have a good linear fit (N>100). Mosaics of SEM BSE images were used to measure the entire cataclasite layer and the different microstructural domains described in section 6.

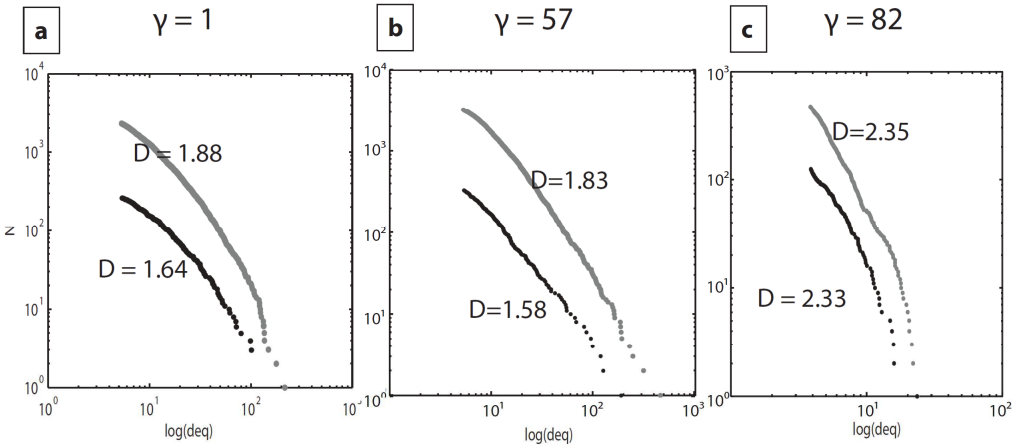


FIGURE 15. Clast size distributions of cataclasites for increasing finite strains from analysis of images collected at 100x. (a) CSD of sample 61-2008 (γ=1). (b) CSD of sample 53a-2008 (γ=57). (c) CSD of sample 19-2008 (γ=82). Black dots = quartz; gray dots = plagioclase.

In most samples, the *D* of plagioclase is higher than the *D* of quartz (Figure 15). The slope D of both plagioclase and quartz increases with increasing finite strain (Figure 15a, b, c). When measured over the whole fault layers (including different domains), the slope of the CSD of quartz increases from $D_{qz}$ = 1.41 to $D_{qz}$ = 2.05 with increasing finite strain, while plagioclase has an almost constant slope, ranging between $D_{pl}$ = 1.75 and $D_{pl}$ = 1.82 (*D* in this study is from 2-dimensional distributions) (Figure 16a). If the distributions of the cataclasite domains and ultracataclasite domains are plotted separately versus finite strain, higher *D* are measured in ultracataclastic domains ($D_{qz}$ = 2.17 and $D_{pl}$ = 2.78). Cataclasite domains have instead $0.87 < D_{qz} < 1.15$ and $1.45 < D_{pl} < 1.53$ (Figure 16b).

TABLE 2. Results of grain-size analysis.

| Sample | γ | Magnification | Mineral | Domain | Number | Mean | Mode | D | $R^2$ | range | Mean (range) | Mode (range) |
|---|---|---|---|---|---|---|---|---|---|---|---|---|
| 61-2008 | 1 | 100x | plagioclase | whole | 2757 | 10.81 | 3.64 | 1.75 | 0.9903 | 6 - 58.96 | 13.18 | 6.67 |
| | 1 | 100x | quartz | whole | 311 | 11.75 | 3.71 | 1.41 | 0.9901 | 6 - 33.64 | 12.52 | 7.32 |
| | 1 | 400x | plagioclase | whole | 591 | 15.00 | 2.19 | 1.44 | 0.9931 | 7.84-35.87 | 15.62 | 7.85 |
| | 1 | 400x | quartz | whole | 96 | 21.06 | 10.82 | 0.97 | 0.9916 | 7.09 -33.57 | 15.52 | 10.82 |
| 4 _ 2008 | 27 | 100x | plagioclase | whole | 241 | 46.07 | 13.00 | 1.20 | 0.9915 | 17.99 - 66.02 | 10.22 | 17.99 |
| | 27 | 100x | quartz | whole | 351 | 9.11 | 3.64 | 1.54 | 0.9916 | 6 - 23.71 | 10.63 | 6.26 |
| | 27 | 100x | quartz | whole | 689 | 8.80 | 3.64 | 1.24 | 0.9936 | 6 - 44.25 | 13.12 | 6.18 |
| S1A | 28 | 100x | plagioclase | whole | 593 | 12.39 | 3.78 | 1.35 | 0.9905 | 6 - 22.15 | 11.17 | 6.91 |
| | 28 | 100x | quartz | whole | 428 | 17.71 | 3.92 | 0.93 | 0.9916 | 6 - 23.24 | 11.74 | 6.18 |
| 53a-2008 | 57 | 100x | plagioclase | cataclasite | 770 | 11.59 | 4.31 | 1.45 | 0.999 | 6 - 45.84 | 12.70 | 7.24 |
| | 57 | 100x | quartz | cataclasite | 149 | 12.12 | 5.78 | 1.09 | 0.9935 | 6 - 18.44 | 10.36 | 6.79 |
| | 57 | 100x | plagioclase | cataclasite | 1650 | 10.74 | 3.78 | 1.52 | 0.9984 | 6 - 38.89 | 12.17 | 6.05 |
| | 57 | 100x | quartz | cataclasite | 360 | 13.46 | 3.64 | 1.15 | 0.9902 | 6 - 26.99 | 11.84 | 6.05 |
| | 57 | 100x | plagioclase | whole | 3783 | 10.31 | 4.24 | 1.81 | 0.9965 | 6 - 69.04 | 12.66 | 6.18 |
| | 57 | 100x | quartz | whole | 370 | 9.95 | 4.12 | 1.60 | 0.9978 | 6 - 28.61 | 10.45 | 6.09 |
| | 57 | 400x | plagioclase | whole | 657 | 7.84 | 3.09 | 1.53 | 0.9957 | 6 - 31.48 | 11.80 | 17.28 |
| 19 | 82 | 100x | plagioclase | whole 1 | 265 | 7.04 | 3.71 | 1.67 | 0.9959 | 6 - 10.79 | 7.77 | 6.71 |
| | 82 | 100x | plagioclase | whole 2 | 645 | 13.07 | 5.97 | 1.82 | 0.9983 | 6 - 17.63 | 13.62 | 6.28 |
| | 82 | 100x | plagioclase | whole 3 | 793 | 8.65 | 3.92 | 1.55 | 0.9991 | 6 - 27.06 | 10.39 | 6.18 |
| | 82 | 100x | quartz | whole 123 | 217 | 6.80 | 3.78 | 1.49 | 0.9894 | 6 - 11.21 | 7.93 | 6.30 |
| | 82 | 400x | plagioclase | ultracataclasite | 1347 | 2.80 | 1.57 | 1.98 | 0.9953 | 2.12 - 8. | 11.08 | 8.20 |
| | 82 | 400x | quartz | ultracataclasite | 165 | 4.73 | 1.35 | 2.55 | 0.9933 | 6 - 9.49 | 7.48 | 6.01 |
| 75-2008 | 70 | 100x | plagioclase | ultracataclasite | 1260 | 6.58 | 3.85 | 2.78 | 0.9981 | 6 - 19.95 | 8.79 | 6.47 |
| | 70 | 100x | quartz | ultracataclasite | 853 | 8.81 | 3.78 | 1.79 | 0.9954 | 6 - 31.52 | 11.00 | 6.83 |
| | 70 | 300x | plagioclase | ultracataclasite | 2650 | 3.99 | 1.88 | 2.10 | 0.9952 | 6 - 10.91 | 7.91 | 7.28 |
| | 70 | 300x | quartz | ultracataclasite | 898 | 5.95 | 1.81 | 2.03 | 0.99 | 6 - 27.66 | 10.39 | 7.32 |
| | 70 | 300x | plagioclase | cataclasite | 1755 | 5.68 | 1.88 | 1.53 | 0.9937 | 6 --31 | 11.18 | 6.86 |
| | 70 | 300x | quartz | cataclasite | 123 | 8.70 | 1.78 | 0.87 | 0.9949 | 2.69 - 9.29 | 5.01 | 4.91 |
| | 70 | 300x | plagioclase | pseudotchylyte | 1106 | 3.20 | 1.81 | 2.20 | 0.9978 | 1.84 - 6.75 | 2.84 | 1.91 |
| | 70 | 300x | quartz | pseudotachylite | 977 | 4.10 | 2.07 | 2.17 | 0.9945 | 6 - 13.16 | 8.33 | 7.32 |
| | 70 | 300x | plagioclase | ultracataclasite | 1083 | 3.67 | 1.81 | 2.59 | 0.9924 | 6 - 9.87 | 7.53 | 6.03 |
| | 70 | 300x | quartz | ultracataclasite | 1118 | 4.56 | 1.88 | 1.82 | 0.9947 | 3.29 - 10.38 | 5.32 | 3.45 |

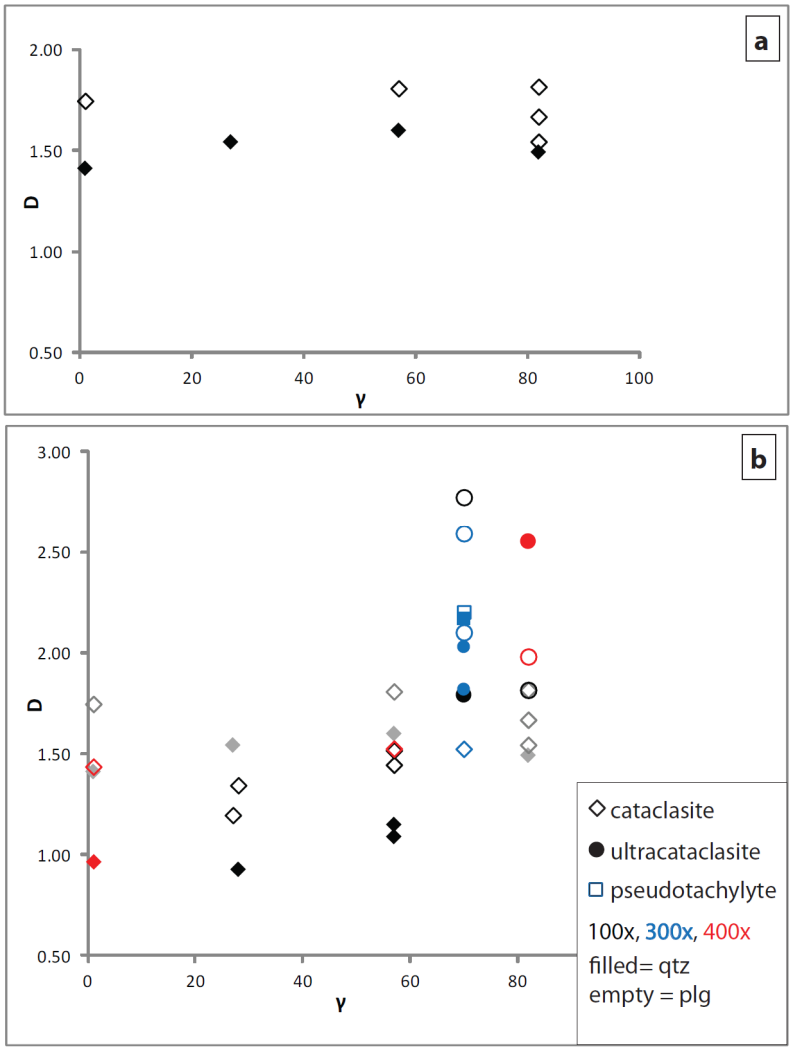


FIGURE 16. The evolution of *D* with finite strain. (a) The evolution of *D* for data collected over the entire fault thickness (including different domains). Data collected on images at 100x. (b) The evolution of *D* for different domains. Data have been collected in images at different magnifications, shown in different colors. The data plotted in (b) are reported in light gray for reference.

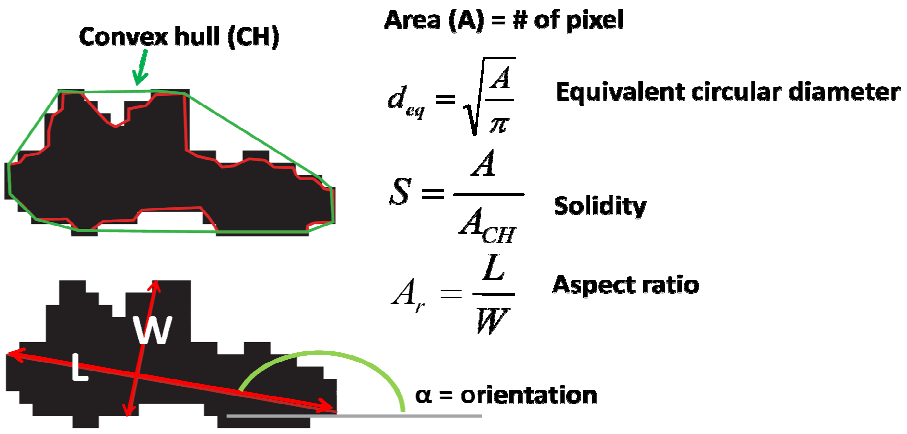


FIGURE 17. Sketch of the parameters measured by image analysis: particle area, equivalent circular diameter, solidity, aspect ratio and orientation are defined in the figure.

### *3.8.2 Clast shape analysis*

The parameters used for describing the shape evolution of plagioclase and quartz grains are defined in Figure 17. The shape parameters (aspect ratio, solidity, etc,) reported in Figure 18 were chosen among the several determined because they were the more useful in highlighting differences in the cataclasite fabric and more sensitive to the change in finite strain.

The plagioclase and quartz clasts in cataclasites have the long axis (L in Figure 17) orientated preferentially at 15 – 35° and 160° to the fault walls (Figure 18a-b), whereas in the ultracataclasites clasts are more randomly oriented (Figure 18c). The preferred orientation measured in the cataclasites (i) corresponds to clast alignment parallel to the S foliation and (ii) is more intense for clasts having larger diameter and aspect ratio, independently of their composition (Figure 18 d-i).

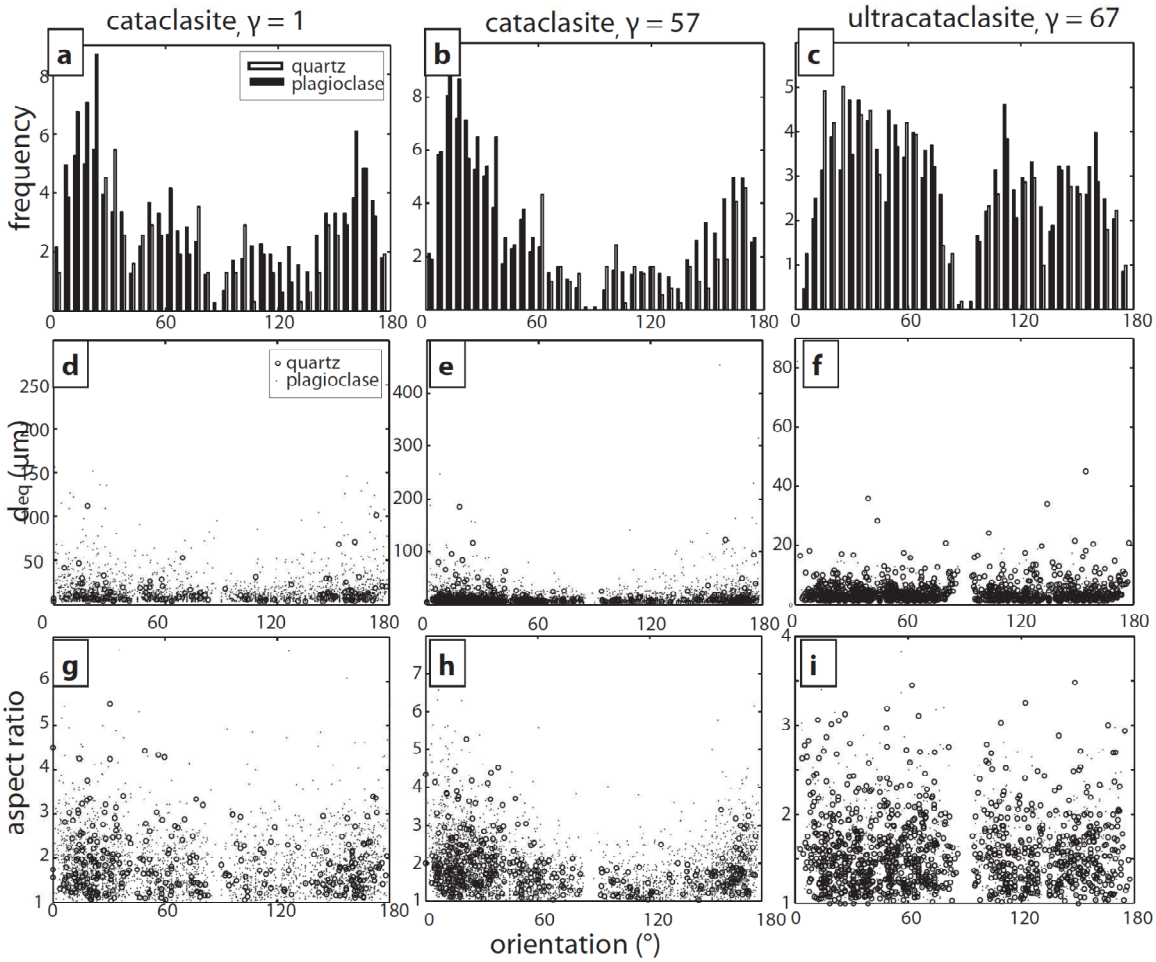


FIGURE 18. Orientation data of quartz and feldspar clasts in samples 61-2008 (γ = 1), 53a-2008 (γ = 57) and 19-2008 (γ = 82). (a - c) Frequency histograms of the orientation of quartz and plagioclase grains. Number of data are: (a) quartz 311, plagioclase 2757; (b) quartz 370, plagioclase 3783 (c) quartz 1118, plagioclase 1083. (d - f) Equivalent circular diameter versus orientation of the clast long axis (L). (g -i) Clast aspect ratio vs. orientation of the clast length (L). The shortening of data at 90$^{o}$ results from a bias due to the method for determining the long axis.

The aspect ratio of particles is computed as the ratio between the long axis (L) and the width (W, the longest chord perpendicular to L) of the particle. The aspect ratios of clasts in cataclasites are distributed over larger values (up to 5.8, Figure 19a, b) than in the ultracataclasite domain (up to 3.5, Figure 19c).

The solidity is a measure of the smoothness of the particle outlines. A fully convex object has solidity = 1, lower values indicate the occurrence of embayments or irregular shapes. The histograms of solidity of three representative samples are represented in Figure 19d - f, for quartz

and plagioclase. In sample 61-2008, with γ = 1 (Figure 19d), the maximum solidity of plagioclase and quartz are coincident, in the sample 53a-2008 with γ = 57 (Figure 19e) the peak of plagioclase clasts is centered on values higher than for quartz. In the ultracataclasite sample 19-2008 with the higher shear strain (γ = 82) (Figure 19f), the quartz has a peak on higher values of solidity. These observations are in agreement with microstructural observations and the modal content of plagioclase and quartz in these fault rocks, and possibly related to the preferential chemical alteration (dissolution) of quartz in foliated cataclasite (cemented preferentially by chlorite, see section 3.7), and of plagioclase in ultracataclasites (cementad preferentially by K-feldspar, see section 3.7).

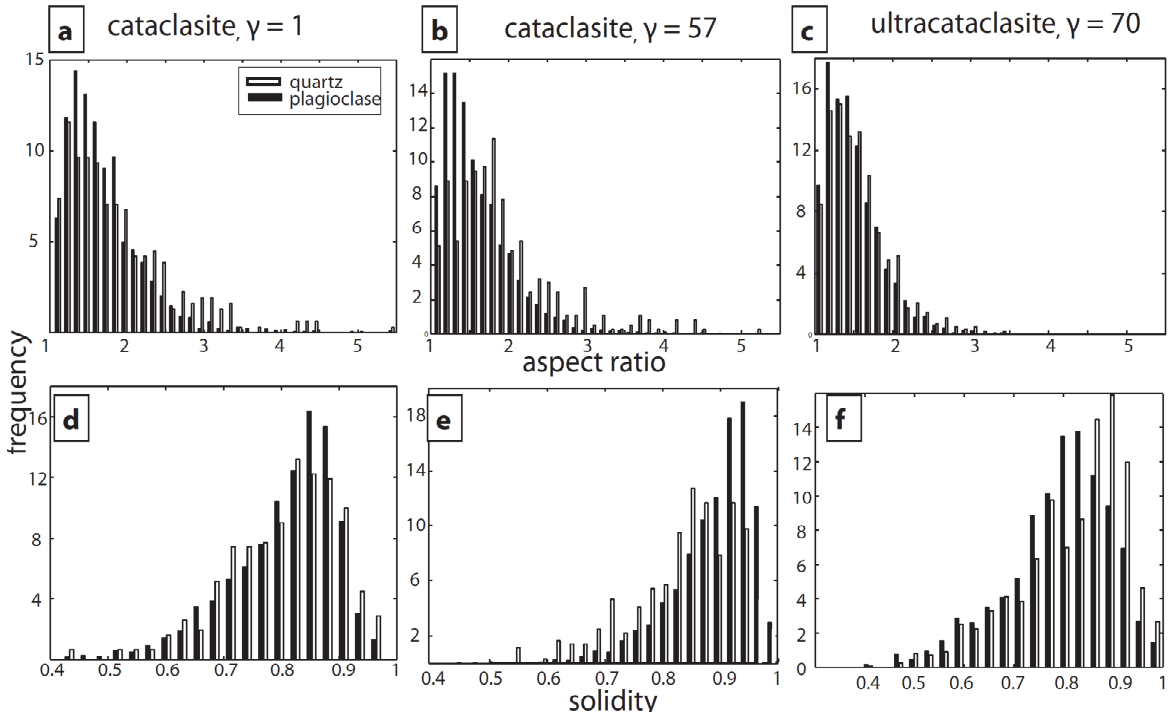


FIGURE 19. Histograms reporting the aspect ratio (a, b, c) and solidity (d, e , f) of quartz and plagioclase clasts measured in samples 61-2008, 53a-2008 and 19-2008 (same samples as in figure 18). Number of data are: (a - d) quartz 311, plagioclase 2757; (b - e) quartz 370, plagioclase 3783 (c - f) quartz 1118, plagioclase 1083.

## 3.9 Discussion

### *3.9.1 Physico-chemical processes*

The samples of minor fault for microstructural analysis were mostly stem along Riedel-type shear fractures cutting tonalite lithons between two main faults. The minor faults are linked to the

sliding along the main faults, and accommodate the deformation inside the lithons between two adjacent main faults (Di Toro and Pennacchioni, 2005; Bistacchi et al., 2011). Riedel fractures are oriented in a way such that they cannot easily accommodate a large displacement (e.g., Mandl, 1988), which is instead accumulated on the main bounding faults.

The minor faults cutting blocks of tonalite between the main faults preserve the early stages of formation and deformation of the fault material upon fracture propagation. The microfractures in tonalite adjacent to the minor faults (Figure 6), are organized in two sets: (i) at low (0 to 20°) angle to the fault surface, preferentially developed on the southern side, and (ii) at high (30° - 90°) angle to the fault, preferentially developed on the northern side of the shear fracture. One sample (53a-2008), shows just one set of microfractures at 30° to the fault surface on both sides, parallel to the inferred orientation of the main horizontal stress, as reproduced in shear fractures produced in laboratory triaxial texts (e.g., Amitrano and Schmittbuhl, 2002). The more asymmetric pattern in the other samples might arise from local stress rotations due to the propagation of mode II fractures (Vermilye and Scholz, 1998; 1999) or due local waviness of the fault surface, as measured and modeled by Griffith et al. (2010). The microfractures in tonalite are sealed by hydrothermal minerals similar to those cementing cataclasites, and biotite is partially altered to chlorite + K-feldspar + titanite (Figure 13). The biotite dissolution seams lined by titanite are preferentially perpendicular to the inferred main far field principal stress acting on the fault zone (i.e., the Gole Larghe Fault Zone is dextral., Di Toro and Pennacchioni, 2005). This pattern is consistent by pressure driven chemical reactions, favored by fluid infiltration in the host rock through pervasive microfracturing. The sealing of microcracks was thus associated with pressure solution processes and the development of a broad foliation in the damaged tonalite close to faults.

The shear fracture which did not experience a macroscopic shear strain (sample 61-2008) preserves the early microstructure of the fault filling. Many clasts have the long axis preferentially oriented sub-parallel to the fault boundaries (Figure 18a) and most tensile fractures in the host tonalite are oriented at 0-20° clockwise to the fault boundaries (Figure 6b). As observed in triaxial experiments conducted at confining stress up to 80 MPa on similar rocks (granite, Amitrano and Schmittbuhl, 2002), the tensile microcracks produced during fracture propagation release material from the intact wall rocks (like what is observed in Figure 5a), which is incorporated in the fault with increasing slip. This process is likely to produce preferentially lozenge shaped fragments with high aspect ratio, as observed in sample 61-2008 (Figure 5a, Figure 19), and the growth of hydrothermal minerals in the fractures might further enhance the process.

The power law exponent of the CSD, *D*, is an expression of the proportion of small particles over large particles, within a given grain size range. Large *D* correspond to a high proportion of small particles. In sample 61-2008, with only 0.4 mm of displacement and γ = 1, the power exponent *D* is 1.75 for plagioclase and 1.42 for quartz. Despite the small displacement, small particles of plagioclase were produced. These values are quite high for extensional fractures, which usually have $D \approx 1$ (e.g., Blenkinsop, 1991).

The accommodation of further strain on minor faults results in (i) thickening of the fault zone due to the production of new material from wearing of the fault walls (e.g., Scholz, 2002), (ii) an evolution in clast size distribution and (ii) the development of multiple textural domains. An overall increase in thickness with displacement is measured for minor faults with displacement < 500mm. The fault thickness was measured in thin section and was averaged over less than 20mm of fault length along strike, so it cannot account for variations in thickness on a larger scale. In the studied area, fault thickness is indeed expected to vary along the fault length due to variations in fault roughness (Bistacchi et al., 2011). The effects of finite shear strain on the *D* of the whole cataclasite (including all the domains and both quartz and plagioclase clasts) results in an increase of the 2-dimensional *D* from values below 1.8 in low strain faults, to values higher than 2. This evolution is associated with the development of multiple domains in cataclasites, including ultracataclasite domains which have $D>2.5$, while the cataclasite along the fault boundaries maintains a low *D* ($D<1.5$). In several samples, the slope of plagioclase distribution in the log-log *N* vs. $d_{eq}$ plots (Figure 14, 15) is steeper than that of quartz, suggesting that there are proportionally more small particles of plagioclase than of quartz. This can be interpreted as (i) due to the total dissolution of small particles of quartz in many of the examined cataclasites (see next point of the discussion), or (ii) due to the lower resistance to fracturing of plagioclase than quartz. Plagioclase has a pervasive cleavage, and such weak planes might facilitate fragmentation.

An increase of the *D* of fault gouge with increasing displacement has been found in other natural fault gouges formed at shallower crustal levels (e.g., Sammis et al., 1987; Blenkinsop, 1991; An and Sammis, 1994; Storti et al., 2003; Billi, 2005; Keulen et al., 2007 ) and reproduced in shear experiments on simulated gouge (Marone and Scholz, 1989; Biegel et al., 1989). Values of $D > 2$ (in two dimensions) has been found in other high strain fault cores (e.g., Balsamo and Storti, 2011; Billi, 2005), and cannot be explained with a self-similar type mechanism of grain size reduction, such as the constrained comminution (Sammis et al., 1987; Sammis and King, 2007). It seems that in highly strained granular fault rocks, grain abrasion becomes an important mechanism controlling the clast

size distribution (e.g., Mair and Abe, 2011). The samples of cataclasites which show a strongly comminuted layer of ultracataclasite are usually thinner then cataclasites which do not bear ultracataclasites (Figure 3); this observation suggests that strain localization is very efficient in ultracataclasite material (having $D$ >2.5). It is noteworthy that ultracataclasite fills fractures oriented at high angle with respect to the faults (Figure 5c). These intrusive features could be interpreted as injection of fluidized material into the wall rocks (e.g., Lin 1996). The intrusive habit of the fractures bordering the minor faults and the extreme localization measured in minor faults hosting ultracataclasites suggest that these fault rocks might be associated to slip instabilities and coseismic slip. The ultracataclasites do not bear evidences of having passed through a melt phase, such as chilled margins, growth of high temperature microlites, spherulites; these features are instead well developed in the associated pseudotachylytes (Di Toro and Pennacchioni, 2004; Chapter 4 of this thesis). The similarity of the CSD of ultracataclasites and pseudotachylytes (Table 2), and their similar structures (injection veins and extreme localization) suggests that the ultracataclasite could be altered pseudotachylytes (so that underwent comminution, melting, solidification and alteration) or coseismic ultracataclasites (that underwent comminution, fluidization and, possibly, alteration, but not melting).

Chlorite- and epidote-rich domains in cataclasites are strongly foliated (Figure 4b, Figure 10) and are less abundant in quartz with respect to plagioclase, at least if compared to the parent tonalite (Figure 10b). The S-C' foliation is defined by the microboudinage of plagioclase clasts; chlorite and K-feldspar fill fractures perpendicular to the foliation and strain shadows. The long axis of plagioclase and quartz clasts is aligned to the S foliation planes (Figure 18), at 20 – 30° to the fault walls. Dissolution of plagioclase and quartz along the foliation planes and precipitation of chlorite and K-feldspar in fractures are controlled by the driving stress, and contributed to accommodate part of the shear strain. In K-feldspar-rich cataclasites, the plagioclase is lost preferentially. The effect of the matrix composition, which we assume reflects a different composition of the fluid (more under-saturated in $SiO_2$ in the case of chlorite-rich matrix) is recorded by the clast outline geometry: in samples with high chlorite content, the peak solidity of quartz is lower than that of plagioclase, where instead the K-feldspar dominate, the plagioclase has a lower peak solidity. The foliation seems to overprint the ultracataclasite domains in minor faults (Figure 4c).

The main faults, accommodating displacements of more than 1m, have a complex internal structure, with coarse grained cataclasites close to the wall rocks, passing to ultracataclasites towards the fault cores, and bear pseudotachylytes, which mostly crosscut the cataclasites (Di Toro

and Pennacchioni, 2005). The damage in the material within the main faults is more intense than along the minor faults/fractures, as highlighted in Figure 8 and 9, and might be related to the intense stress perturbation associated with the propagation of seismic ruptures along the main faults (e.g., Reches and Dewers, 2005; Pittarello et al., 2008). The wall rock grains are crushed down to sub-micron size fragments and, in the case of quartz, they preserve a foam-like recrystallized microstructure possibly due to the heat pulse typical of seismic slip (Bestmann et al., 2012; Figure 9d). The sutures inside the highly comminuted plagioclase along main faults (Figure 9e) suggest pressure-solution driven clast indentation, probably enhanced by the extremely fine grain size. An S-C' foliation is developed in this domain (Figure 9b, c).

Cataclasites in the main faults registered multiple events, as suggested by the occurrence of reworked cataclasite and ultracataclasite clasts, and of multiple pseudotachylyte layers. As seen in Figure 8a and b, cataclasites in the main faults do not show a penetrative foliation, unlike minor faults.

### *3.9.3 Implications for the seismic cycle*

Experimental work demonstrated that the fabric *latu sensu* of gouge determines its strength, sliding stability and friction coefficient (e.g., Beeler et al., 1996; Biegel et al., 1989; Mair et al., 2002). As observed in natural and experimental gouges, both grain shapes (Storti et al., 2003; Heilbronner and Keulen, 2006; Stunitz et al., 2010) and CSD (e.g., Sammis et al., 1987; Blenkinsop, 1991; An and Sammis, 1994; Storti et al., 2003; Billi, 2005; Keulen et al., 2007) of gouge evolves with displacement, to values of $D>2$ (in two dimensions) and more rounded particles (e.g., Storti et al., 2003). Understanding the evolution of gouge fabric (including its mineralogy) with displacement is thus of great importance for understanding the behavior of faults, i.e., if they will slide aseismically or if they will undergo slip instabilities. The most "evolved" material, i.e., having the highest $D$, found in the studied samples is localized within the ultracataclasite layers, which are associated with a possible strain weakening behavior (they accommodated more displacement without a large increase in thickness) (Beeler et al., 1996). The cataclasite samples which instead are thicker are composed of coarser, less evolved and foliated fault material, suggesting a strain strengthening behavior.

However, the application of models of grain size evolution developed for granular material (e.g., Sammis et al., 1987; Sammis and King, 2007; Mair and Abe, 2011) on faults which were active at seismogenic depth is not straightforward, because of the intense fluid-rock interactions occurring in

natural faults. We measured a trend in grain size evolution with slip and finite strain which is coherent with that measured in other natural faults and in shear experiments, but we documented also the onset of chemical reactions which is coeval to cataclasite formation.

Rock fragmentation and the percolation of reactive fluids cause some of the cataclasites to develop a foliated texture, similar to that found in mylonites, which is more intense where the matrix mineral assemblage is dominated by chlorite. The onset of pressure-solution driven creep at the brittle ductile transition is considered a relevant weakening process, especially in presence of phyllosilicates (e.g., Renard et al., 1997; Renard et al., 2001). From experiments on rock analogs (halite – kaolinite, halite – muscovite mixtures), it resulted that such conditions can be modeled as a frictional – viscous flow (i.e., dependent on both sliding rate and normal stress) (Bos and Spiers, 2002; Niemeijer and Spiers, 2005), where the limiting process for the flow law changes depending on the sliding velocity: (i) at low velocity, pressure solution is so efficient that the strength is determined by the sliding friction along the foliation; (ii) at intermediate velocity, the strength of the gouge is determined by the kinetics of the pressure-solution processes; (iii) at high velocities, pressure solution is too slow for accommodating the deformation, so that dilatational cataclastic flow occurs. In the rocks of the Gole Larghe Fault, interconnected layers of chlorite are developed only locally. The kinetics of the pressure driven mass transfer processes is much more complex than the conditions reproduced in laboratory, where pressure-solution involves dissolution and precipitation of the same mineral. Nevertheless, the microstructures produced in experiments on rock analogs are somewhat similar to those found in nature. At low (0.1 – 0.3 μm $s^{-1}$) sliding rate, a foliation is developed, similar to that found in low displacement natural faults (Figure 4 b, c), or in strongly damaged protocataclastic domains along main faults (Figure 9b). At high (5 – 13 μm $s^{-1}$) sliding velocities, a cataclastic texture is developed, which disrupts former foliation. The main faults are often decorated by non-foliated cataclasites (Figure 8a, b), suggesting that they experienced multiple stages of sliding at high rates, as witnessed by reworked cataclasite clasts and multiple pseudotachylyte events.

Thus, summarizing the implications of the observations here discussed:

(i) Minor faults are likely shear fractures formed in intact tonalite (they do not exploit preexisting joints). The initial clasts are coarse, angular and elongated. Depending on the finite strain, the material evolves to finer grained material, up to form ultracataclasites in zones of strain localization.

(ii) Fracturing allows the ingression of fluids, which enhance pressure solution processes in the slipping zone and in the damage zone. Depending on the local composition of the fluids and the minerals precipitated, pressure-solution processes accommodate further deformation, and at the same time, cause healing of microfractures and cementation of the minor faults, which are mostly abandoned.

(iii) Major faults experienced multiple cycles of fracturing – frictional melting – pressure-solution – healing. Most cataclasites along the main fault surfaces are not foliated, suggesting that the foliation might have been developed and then reworked in a successive event. A penetrative foliation is instead preserved in protocataclastic domains (Figure 9a).

**3.10 Conclusions**

One of the aims of this study was the quantitative comparison of the microstructures found in natural faults with increasing displacement with those produced under controlled conditions in the laboratory and described in the literature. In fact, extrapolation to natural conditions of experimental observations (i.e., mechanical data) fails if the artificial fault rock products are dissimilar to natural ones: microstructural differences might result from other physico-chemical processes operating in nature with respect to those triggered in the laboratory. The evolution of the fabric of natural fault rocks with increasing deformation was investigated by means of microstructural and geochemical studies on a set of samples from the seismogenic Gole Larghe fault. The samples experienced displacements from $\delta$ = 1 - 4797mm; faults with $\delta$<500mm have been more thoroughly examined and compared with large displacement faults.

The clast size distribution of quartz and plagioclase clasts, in the limited range of grainsizes here measured, evolves with increasing shear strain from $D < 1.5$ to $D > 2$, in agreement with previous studies on natural and experimental fault gouges. The aspect ratio of the clasts is higher for low strain faults and decreases with increased shearing. If highly sheared material (ultracataclasite) is present in the slipping zone, the deformation is accommodated more efficiently without an increase in thickness (which would correspond to a strain weakening behavior).

Besides mechanical fracturing and comminution processes, the interaction with fluids strongly influences the fabric of natural cataclasites. The most relevant effect is the formation of a foliation and the transfer of dissolved chemical mass in solution, which is an efficient mechanism for accommodating bulk deformation at low sliding velocities. Chemical aggression on the plagioclase and quartz clasts is evidenced by the low values of some shape descriptors such as solidity and

convexity, indicating lobed clast outlines. According to the natural example investigated here, multiple processes are activated in a seismogenic fault at earthquake nucleation depths in the continental crust, depending on the different sliding rates occurring in the seismic cycle.

a

main fault 1

main fault 2

N

60 cm

74-2008

75-2008

S1a

61-2008

53-2008

S2a

S3a

S4a

S5a

S6a

S7a

S8a

S8b

19-2008

13-2008

12-2008

4-2008

**Legend**

- Joints
- Cataclasites
- Secondary cataclasite faults
- Pseudotachylytes
- Mylonites
- Mafic enclaves
- Aplitic dykes
- Debris
- Samples

b

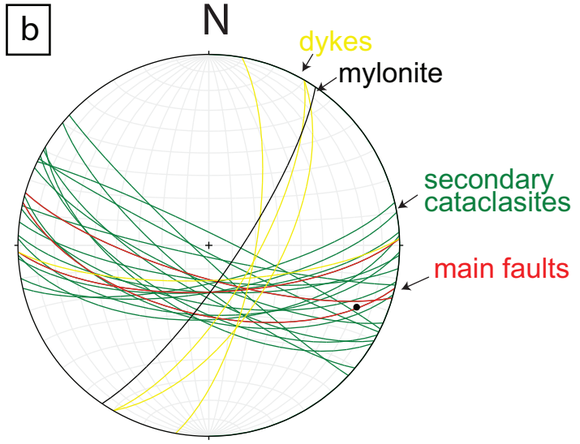

# Chapter 4. Origin of hydrous fluids in faults at seismogenic depth: constraints from the hydrogen isotope geochemistry

**Abstract**

*Fluids in fault zones have both mechanical and chemical effects on the seismic cycle and earthquake nucleation. The presence of a free fluid phase at hypocentral depth has been detected by geophysical methods in many seismically active areas. By contrast, geological evidence of high fluid pressure, such as abundant veining, is not commonly associated with pseudotachylyte bearing fault systems.*

*In this study, we performed microstructural, mineralogical and geochemical characterization, and hydrogen isotope analysis, on fault rocks from the Gole Larghe Fault Zone (Southern Italian Alps), an exhumed seismogenic fault zone in tonalite, which was active at 9 – 11 km depth. Fault products span from early stage, high temperature (T = 550°C) mylonites, to cataclasites and pseudotachylytes (formed at T = 250 – 280°C ambient temperature). In nature, pseudotachylytes were formed by frictional melting of host tonalite and cataclasite. Here, these fault rocks are compared with pseudotachylytes produced in room humidity, high velocity (up to 1.2 $ms^{-1}$) friction experiments simulating seismic slip on samples of tonalite and cataclasite collected in the same fault zone.*

*In nature, the bulk tonalite bears 0.96% , the mylonites 1.4 – 1.7 % ,the cataclasites 1.3 – 3.2 % and the pseudotachylytes 2.3 – 4.4% of $H_2O$. The increased water content in cataclasites is explained by growth of hydrothermal minerals, while the strong enrichment in water in pseudotachylytes is due to (i) growth of biotite during cooling of the frictional melts and (ii) the occurrence of weakly bonded water in de-vitrified domains. The tonalite has hydrogen isotope composition δD = -74 ± 1‰, close to the δD value in mylonites, δD = -78 ± 1‰. Instead, cataclasites have δD = -65 ± 4‰ and pseudotachylytes have δD of -93 ± 9‰. Experimental pseudotachylytes have δD = -75 ± 2‰ when produced from frictional melting of tonalite, and δD = -83 ± 1‰ when produced from frictional melting of cataclasite.*

*At the scale of the fault zone evolution, the formation of cataclasite-bearing faults allowed the ingression of fluids with higher δD value than that in equilibrium with the host tonalite. Natural pseudotachylytes have lower δD values than that cataclasites, possibly due to the absorption of present day high altitude rain water, having δD ≈ -90‰. This hypothesis is supported by step heating FTIR spectroscopy data: in natural pseudotachylytes, part of the water is released at 50° C. If the contribution from the present day rain water is subtracted from the bulk δD value, the δD of the pseudotachylyte is in the range -75 to –80‰. This δD value is compatible to the one obtained in room-humidity rock friction experiments, or due to crystallization of biotite during pseudotachylyte cooling. We conclude that, in the case of this seismogenic fault zone, there is no isotopic signature which supports an external origin of the fluids associated to seismic faulting.*

***(this study was done in collaboration with Luigi Dallai, Giulio Di Toro, Giorgio Pennacchioni)***

## 4.1 Introduction

Fluids are thought to be crucial in controlling the physics of earthquakes and faulting (e.g., Miller et al., 2004; Chiarabba et al., 2009), but fluid origin and circulation paths at the base of the seismogenic crust are poorly known (for reviews, Scholz, 2002; Abercrombie et al., 2006; Handy et al., 2007). Exhumed seismogenic faults offer the opportunity to investigate the mechanical and chemico-physical processes during the nucleation and propagation of seismic ruptures at the base of the seismogenic crust (7-15 km, Scholz, 2002), and the role of fluids in the seismic cycle. In silicate-bearing rocks, fast (about 1 $ms^{-1}$) sliding during earthquake propagation may result in melting of the fault rocks due to frictional heating (Jeffreys, 1942; McKenzie and Brune, 1972; Sibson, 1975). The friction melts quench in seconds to minutes (depending on melt thickness and temperature of melt and host rock) forming a dark-colored, glassy rock called pseudotachylyte (after Shand, 1916). Pseudotachylytes often preserve flow structures (e.g., Lin, 1994), microlites and spherulites, vesicles, amygdale (Magloughlin, 1992) and rare glass (for a review, Di Toro et al., 2009; Lin, 2007). Pseudotachylytes are considered evidence of past seismic activity in an exhumed fault (Sibson, 1975; Cowan, 1999) and, if not altered, they potentially retain information on fluid-rock interaction during an earthquake (O'Hara and Sharp, 2001; Moecher and Sharp, 2004). Frictional melting is a process which is commonly assumed to occur under "dry" conditions (Sibson and Toy, 2006, for a review). In fact, (i) coseismic frictional heating would result in thermal expansion of pore fluids which would

pressurize the fault impeding the achievement of melting temperatures (Sibson, 1973; Rice, 2006) and (ii) water vaporization adsorbs heat and buffers the increase in temperature in the slipping zone. On the other hand, the presence of water might lower the melting point of slipping zone minerals and should promote melting (Allen, 1979). Field evidence exist that pseudotachylytes are spatially and kinematically associated with cataclastic zones and breccias cemented by hydrothermal minerals (e.g., Magloughlin, 1992; Fabbri et al., 2000; Di Toro and Pennacchioni, 2005; Griffith et al., 2008). In particular, some pseudotachylytes hosted in the Sierra Nevada granodiorites (California) were probably produced in the same rupture event that produced the hydrothermal-mineral rich cataclasites (Kirkpatrick and Shipton, 2009; Griffith et al., 2010). The presence of vesicles and amygdales in some pseudotachylytes requires that a fluid phase was generated during melting and pseudotachylyte formation (Maddock, 1987; Boullier et al., 2001).

Oxygen and hydrogen isotope compositions of silicatic minerals are useful tracers for water-rock interactions in geological processes (Taylor, 1977). The oxygen isotopic ratio in pseudotachylytes is buffered by the oxygen of the silicate minerals undergoing melting and is sensitive to the ingression of an external fluid for high fluid/rock ratios (O'Hara and Sharp, 2001). In contrast, the hydrogen isotopic ratio is more sensitive to the exchange of small amounts of water (Moecher and Sharp, 2004). The occurrence of meteoric water within a fault zones should be readily detected on the basis of the isotope composition of hydrogen. The only available hydrogen isotope data on pseudotachylytes and host gneiss are from the Homestake shear zone (Moecher and Sharp, 2004). The Homestake Shear Zone pseudotachylytes likely formed at 5-7 km depth as constrained by the thickness of overlying sedimentary sequences and are not associated with cataclasites (Allen, 2005). Pseudotachylytes contain white mica as product of devitrification of former glass and their hydrogen isotope compositions indicate that the main source of hydrogen in the melt was the dehydration of hydrous mineral in the host rock, with minor effects of hydrogen fractionation due to crystallization of white mica.

In this work we investigated the origin of hydrous fluids in mylonites, cataclasites and pseudotachylytes from two outcrops of a seismogenic fault zones cutting the northern Adamello massif (Southern Italian Alps), the Gole Larghe Fault Zone (Di Toro and Pennacchioni, 2004; 2005). After characterizing the mineralogy and the speciation of water in the fault rocks and the tonalitic host rock, hydrogen isotope measurements were performed on bulk rocks and mineral separates. For constraining the mechanisms of isotope fractionation during seismic slip, the products of

frictional melting reproduced in high velocity friction experiments starting from rock sampled in the same outcrops were analyzed as well.

## 4.2 Geological setting

The E-W-trending Gole Larghe fault zone cuts across the northern Adamello batholith in the Southern Italian Alps (Figure 1). The host rock is tonalite of the Val d'Avio pluton, whose crystallization and cooling ages range from 32 to 34 Ma (Del Moro et al., 1983), while new measurements report cooling ages higher than 33 Ma (Skopelitis et al., 2011). Successive deformation phases are recorded along the GLFZ, localized along pre-existing joints (Pennacchioni et al., 2006): amphibolitic facies mylonites (T = 550°C), low greenschist facies cataclasites associated with pseudotachylytes (T = 250 – 280°C) and late zeolite bearing faults (T < 200°C). Mylonitic and brittle faulting occurred at 9-11 km depth, before the exhumation of the Adamello batholith (Di Toro and Pennacchioni, 2004). This is constrained by stepwise heating $^{39}Ar$ - $^{40}Ar$ dating on pseudotachylytes matrix at an average age of about 30 Ma (Pennacchioni et al., 2006). The GLFZ was sampled in two locations, at the base of the Lobbia glacier to the East (= Lobbia location) and in the Avio valley to the West (= Avio location) (Figure 1).

FIGURE 1 (next page). Geological setting. Sketch of the Adamello batholith and the Gole Larghe Fault Zone; the sampling localities (Avio and Lobbia) are indicated by black stars.

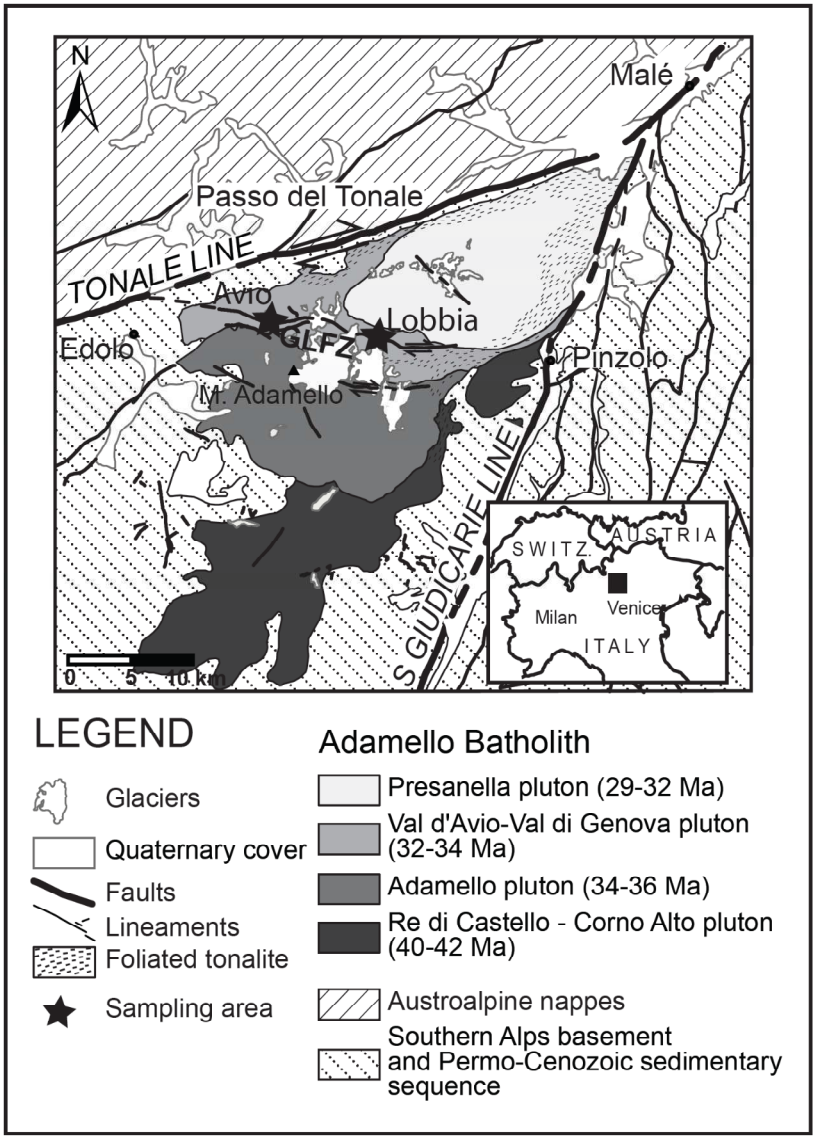


## 4.3 Methods

The type of analyses performed are summarized in Table 1. Composite samples including different lithologies (tonalite, mylonite, cataclasite and pseudotachylyte) were cut to produce subsamples of the individual rock types. Polished thin sections obtained from the samples were analyzed with a scanning electron microscope (SEM, Camscan-Mx2500, resolution in back scattering of 100 nm, Dipartimento di Geoscienze, University of Padova, Italy) and with a Field Emission SEM (FE-SEM, JEOL 7000, resolution in back scattering of 4 nm, Istituto Nazionale di Geofisica e Vulcanologia, Rome, Italy). Both electron microscopes were equipped for energy dispersive

spectrometric (EDS) X-ray microanalysis microanalysis. The EDS activation volume was 1 - 2 μm in radius for the SEM and 400 nm in radius for the FE-SEM (Del Gaudio et al., 2009).

X-Ray diffraction (XRD) was performed on representative host and fault rock powdered samples. Powder XRD data were obtained by step scanning using an automated diffractometer system (Philips X'Change) with incident- and diffracted-beam Soller slit (0,04 rad.). Diffraction profiles were obtained using a step interval of 0.02° 2θ with a counting time of 15 s. Scanning was performed over the range 3-70° 2θ. All the samples were ground to a particle size of <10 micron to minimize the possible microabsorption effect and to improve accuracy in measuring the intensities. Powders were loaded in Al sample holders with an area of 2×1.15 $cm^2$. The program High Score Plus (Panalytical) was used for the phase identification and the Rietveld refinement.

Infrared spectra were acquired on doubly polished rock thin sections 50-60 μm thick using Fourier Transform Infrared (FTIR) spectrometer (Bruker Vertex) with an optical/IR microscope (Bruker HYPERION 3000). Conditions for spectra acquisition include a resolution of 4 $cm^{-1}$ and 32 scans per acquisition. A detector MCT (Mercury Cadmium Telluride) was used for the acquisition of spectra with a spot size of 50 $\mu m^2$. FTIR spectra were acquired at room conditions (25°C) and using an heating stage under vacuum ($10^{-7}$ mbar), for the following heating steps: 50°C, 100°C, 150°C, 200°C, 300°C. Background correction for the air and the windows of the heating chamber were calibrated before each acquisition.

Electron Microprobe data were obtained with the Cameca SX50 apparatus of the Geosciences Department of Padova University.

| *Bulk sample* | *Rock type* | *Outcrop* | *Analyses on the bulk samples* | *Sub-samples* | *Type of sample* | *Analyses on the sub-samples* |
|---|---|---|---|---|---|---|
| ***Natural samples*** | | | | | | |
| 20b-00 | pt in tonalite and cataclasite | Lobbia | XRF | 20b-00-md | | XRF |
| | | | | 20b-00-sd | | XRF |
| 07 162 | mylonite | Lobbia | | 07-162-umyl | bulk myl | |
| 99-D7 | mylonite | Lobbia | | 99-D7-umyl | bulk myl | |
| 50-00 | cataclasite | Lobbia | XRF | | | |
| 23-00 | cataclasite | Lobbia | XRF | | | |
| 2-99 | pt in tonalite and cataclasite | Lobbia | | 2-99-bt | biotite separate | TC/EA, CHN |
| | | | | 2-99-pt | pt separate | TC/EA, CHN |
| 21-00 | tonalite | Lobbia | | | biotite separate | TC/EA |
| 3-02 | pt in tonalite | Lobbia | | 3-02-bt | biotite in tonalite | TC/EA |
| | | | | 3-02-pt | bulk pt | TC/EA, CHN |
| | | | | 3-02-pt-c | bulk pt | TC/EA |
| 10-04 | pt in tonalite | Lobbia | XRPD, FE-SEM | 10-04-pt | bulk pt | TC/EA, CHN |
| 46-99 | pt in tonalite and cataclasite | Lobbia | XRF, XRPD, FE-SEM | 46-99-cc | bulk cc | TC/EA, CHN |
| | | | | 46-99-ptm-a | bulk pt | TC/EA, CHN |
| | | | | 46-99-pt-a | bulk pt | TC/EA |
| | | | | 46-99-pt-b | bulk pt | TC/EA |
| | | | | 46-99-pt-c | bulk pt | TC/EA |
| | | | | 46-99-pt-d | bulk pt | TC/EA |
| 24-00 | pt in tonalite and cataclasite | Lobbia | XRF, FE-SEM | 24-00-cc | bulk cc | TC/EA, CHN |
| | | | | 24-00-pt | bulk pt | TC/EA, CHN |
| 32-00 | pt in tonalite and cataclasite | Lobbia | XRF, XRPD, FE-SEM | 32-00-cc | bulk cc | TC/EA, CHN |
| | | | | 32-00-pt | bulk pt | TC/EA |
| | | | | 32-00-pts | bulk pt | TC/EA, CHN |
| 11-01 | pt in tonalite and cataclasite | Lobbia | | 11-01-cc | bulk cc | TC/EA, CHN |
| | | | | 11-01-pts | bulk pt | TC/EA, CHN |
| 19-01 | pt in tonalite and cataclasite | Lobbia | | 19-01-pt-c | bulk pt | TC/EA |
| | | | | 19-01-pt-f | bulk pt | TC/EA, CHN |
| 17-01 | pt in tonalite and cataclasite | Lobbia | | 17-01-pt | bulk pt | TC/EA, CHN |
| 13-01 | pt in tonalite and cataclasite | Lobbia | XRPD, FE-SEM | 13-01-pt-a | bulk pt | TC/EA |
| | | | | 13-01-pt-b | bulk pt | TC/EA, CHN |

| | | | | | | |
|---|---|---|---|---|---|---|
| 2-01 | pt in tonalite and cataclasite | Lobbia | | 2-01-pt | bulk pt | TC/EA, CHN |
| 21-01 | pt in tonalite and cataclasite | Lobbia | | 21-01-pt-a | bulk pt | TC/EA, CHN |
| | | | | 21-01-pt-b | bulk pt | TC/EA |
| G 5 | tonalite | Avio | | G5-bt | biotite separate | TC/EA, CHN |
| L 65 | pt in tonalite e cataclasite | Avio | | L-65-pt | bulk pt | TC/EA, CHN |
| | | | | L-65-cc | bulk cc | TC/EA, CHN |
| ***HVFRE samples*** | | | | | | |
| 370-06 | artificial pt in tonalite | | SEM | 370-06-pt | bulk pt | TC/EA, CHN |
| 372-06 | artificial pt in tonalite | | SEM | 372-06-pt | bulk pt | TC/EA, CHN |
| 376-06 | artificial pt in tonalite | | SEM, EMPA | 376-06-pt | bulk pt | TC/EA, CHN |
| 371-06 | artificial pt in cataclasite | | SEM | 371-06-pt | bulk pt | TC/EA, CHN |
| | | | | 371-06-cc | bulk cc | TC/EA, CHN |
| 378-06 | artificial pt in cataclasite | | SEM | 378-06-pt | bulk pt | TC/EA, CHN |
| | | | | 378-06-cc | bulk cc | TC/EA, CHN |
| 379-06 | artificial pt in cataclasite and tonalite | | SEM | 379-06-pt | bulk pt | TC/EA, CHN |
| | | | | 379-06-cc | bulk cc | TC/EA, CHN |

TABLE 1. List of the studied samples and subsamples. pt: pseudotachylyte, cc: cataclasite, bt: biotite, md: microlitic domain, sd: spherulitic domain, XRF: X-ray fluorescence, XRPD: X-ray powder diffraction, SEM: Scanning Electron Microscope, FE-SEM: Field Emission SEM, EMPA: Electron Micro-Probe Analysis, TC/EA: High Temperature Conversion Elemental Analyzer, CHN: Carbon, Hydrogen Nitrogen analyzer.

Hydrogen isotope ratios were measured on: (i) biotite mineral separates from the host tonalite, (ii) bulk mylonites, (iii) bulk cataclasite, (iv) bulk natural and (v) bulk artificial pseudotachylyte powders. The samples were analyzed using a High Temperature Conversion Elemental Analyzer (TC/EA) in line with a Thermo-Finnigan Delta XP IRMS, at the IGG-CNR in Pisa, following the method described in Sharp et al. (2001). Each sample was analyzed twice, and if the two *δD* values had differed by more than 10‰, the analysis was repeated until a reproducibility of ±5‰ was achieved. Results of the analyses are presented in the standard *delta* notation

$$\delta = \left( \frac{R_x - R_{std}}{R_{std}} \right) \times 1000 \qquad (1),$$

where *R* is the ratio of the abundance of the heavy to the light isotope, *x* denotes the sample and *std* the reference standard SMOW (Standard Mean Ocean Water). A sample of NBS30 biotite was analyzed every 10 analyses, to correct the apparatus drift; the measured values were corrected for an NBS30 biotite value of $\delta$D = -67.5 (USGS, http://www.rcamnl.wr.usgs.gov/isoig/res/guide.html). The samples analyzed for hydrogen isotope were also measured for their Carbon Hydrogen Nitrogen (CHN) contents by means of a Fisons CE-EA 1108. A series of blank samples and standard urea standards were analyzed each 10 samples to correct the contamination of the sample by atmospheric N and the instrumental drift. No N was detected, and the content of C was too low to be correctly calibrated with the standard urea series.

## 4.4 Petrography and microstructure

### *4.4.1 Host tonalite*

In the Gole Larghe Fault, the host rock is the Val d'Avio tonalite. It is a medium grained rock composed of 48 wt.% plagioclase, 29% quartz, 17% biotite and 6% K-feldspar, with accessory titanite, allanite and apatite (Di Toro and Pennacchioni, 2004) (Figure 2a). Plagioclase is idiomorphic and shows oscillatory and normal zoning, with anorthite-rich cores. Biotite is idiomorphic and locally defines a foliation, probably magmatic in origin. Quartz and K-feldspar occur as interstitial phases. Close to faults, tonalite is commonly altered with growth of chlorite at the expense of biotite and saussuritization of plagioclase (Figure 2). In both outcrops, the analyzed tonalite samples were collected in unaltered rock volumes between fault horizons.

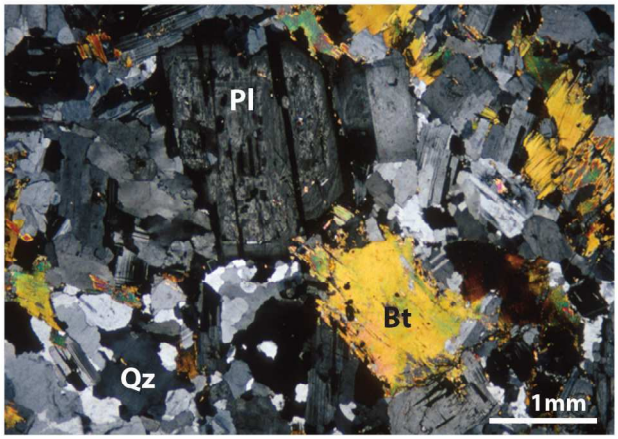


FIGURE 2. Microstructure of the Avio tonalite, showing an incipient saussuritization within plagioclase nuclei.

### *4.4.2 Mylonites, cataclasites and pseudotachylytes of the GLFZ*

The mylonitic deformation in the Avio pluton is localized along pre-existing joints (Pennacchioni, 2005; Pennacchioni et al., 2006). Various grades of deformation affect the tonalite within the shear zones, from a S-C' fabric to foliated ultramylonite. The two samples analyzed in this study were extracted from strongly foliated ultramylonites, where quartz is dynamically recrystallized, plagioclase forms rounded porphyroclasts, K-feldspar is preserved in pressure shadows and biotite is present as mica fish (relict grains from the tonalite) or as recrystallized aggregates (Figure 3).

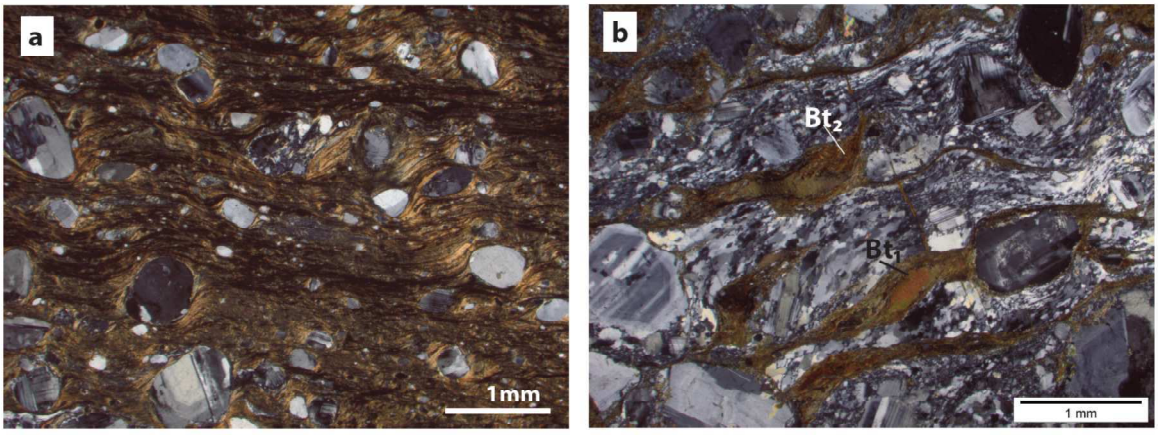


FIGURE 3. (a) Ultramylonite composed of a matrix of recrystallized biotite and rounded plagioclase porphyroclasts. (b) Mylonite, showing relicts of deformed magmatic biotite ($Bt_1$) rimmed by seams of recrystallized biotite ($Bt_2$), dynamically recrystallized quartz and rounded porphyroclasts of plagioclase.

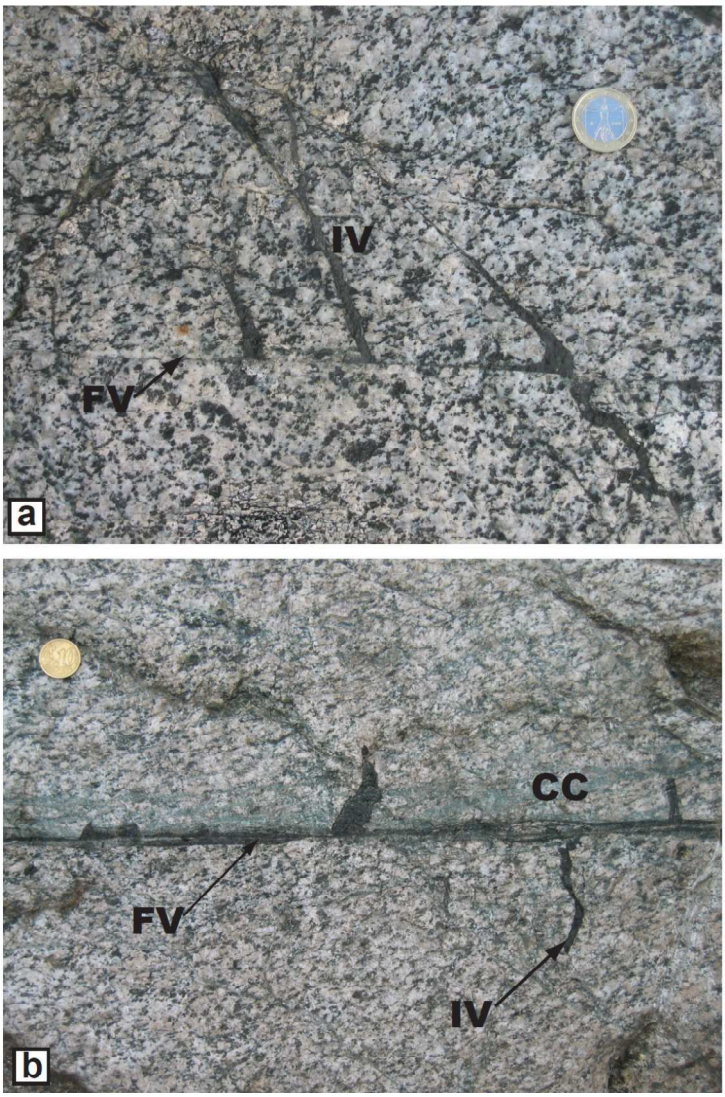


FIGURE 4. Field photographs of fault rocks of the GLFZ. (a) A pseudotachylyte-bearing fault in tonalite, composed of a fault vein (FV) and injection veins (IV); most of the pseudotachylyte volume (black in color) is concentrated in the injection veins. (b) A pseudotachylyte hosted in cataclasite (CC, green in color); pseudotachylyte fault and injection veins clearly intrude and postdate the cataclasite.

Cataclasites and pseudotachylytes of the GLFZ were described by Di Toro and Pennacchioni (2004; 2005) and Pennacchioni et al. (2006). The cataclasites are green in color and contain clasts of (often altered) tonalite and reworked cataclasite, cemented by micrometric epidote+K-feldspar+chlorite (Figure 4b, 5a).

The pseudotachylytes are sharply-bounded veins, occurring both as fault veins and injection veins (Figure 4), whose thickness varies from about 0.5 mm up to 10-20 cm in pull-apart structures.

Most of the pseudotachylyte volume is found filling the injection veins (after Sibson, 1975) branching at high angle from the slipping zone of the main faults (Figure 4). Pseudotachylytes are mostly associated with precursor cataclasites, except in some fault branches where they occur within intact tonalite (Figure 4a) (Pittarello et al., 2008). Pseudotachylytes are composed of angular clasts embedded in a microcrystalline to cryptocrystalline matrix. The clasts consist of quartz, plagioclase and K-feldspar and, locally, cataclasite and altered pseudotachylyte. In thin (<4 mm) pseudotachylyte veins, the matrix is composed of an intergrowth of lath shaped plagioclase and acicular biotite microlites (Figure 5b, d). Thick veins show a symmetrical zoning with "chilled" microlitic margins, bordering a central domain composed of spherulitic aggregates floating in a cryptocrystalline matrix (Di Toro and Pennacchioni, 2004) (Figure 4c). The spherulites are formed of plagioclase microlites radially arranged around plagioclase clast cores, or of silica-rich and K-feldspar-rich concentric rims surrounding quartz clasts (Figure 5e). The cryptocrystalline matrix in the spherulitic domains is formed of an aggregate of sub-micrometric biotite and of analytically not resolvable (under the EDS-equipped SEM with a a spot size having diameter of about 0.4 μm, Del Gaudio et al., 2009) phases (probably plagioclase and K-feldspar) (Figure 5e). Epidote plagues sometimes overprint the high temperature mineral assemblage of pseudotachylytes, confirming that pseudotachylytes are coeval with cataclasites. The amount of epidote and/or chlorite in the pseudotachylytes is very low (less than 5 % in volume, as it will be discussed in section 4.5), except in sample 13-01, where epidote and chlorite overprint the microlitic aggregate (Figure 5f).

FIGURE 5 (next page). Microstructures of cataclasites and pseudotachylytes of the Gole Larghe Fault Zone. (a) SEM-BSE image of the cataclasite matrix. Clasts of quartz (Qz) are embedded in a matrix of randomly oriented epidote (Ep) and chlorite (Chl). (b) SEM-BSE image of a thin (4 mm thick) pseudotachylyte fault vein composed of angular clasts of quartz (Qz) and plagioclase (Pl) embedded in a microcrystalline to cryptocrystalline matrix. (c) Thin section scan, plane polarized light of a zoned pseudotachylyte fault vein, cutting cataclasite (CC); the microlitic domains (MD) are brownish in color and have very sharp contacts with the inner, pale green in color, spherulitic domain (SD). (d) SEM-BSE image of a microlitic domain, composed of an intergrowth randomly oriented plagioclase microlites (dark grey) surrounding quartz (Qz) clasts; bright acicular biotite (Bt) microlites are enclosed between and inside in the plagioclase microlites. (e) FE-SEM BSE image of spherulites developed around quartz clasts. The cryptocrystalline matrix is formed of a coalescence of sub-micrometric biotite and other phases. (f) FE-SEM BSE image of a detail of the microstructure of sample 13-01, where the original plagioclase (Pl) and biotite microlites are overprinted by hydrothermal epidote (Ep) and chlorite (Chl).

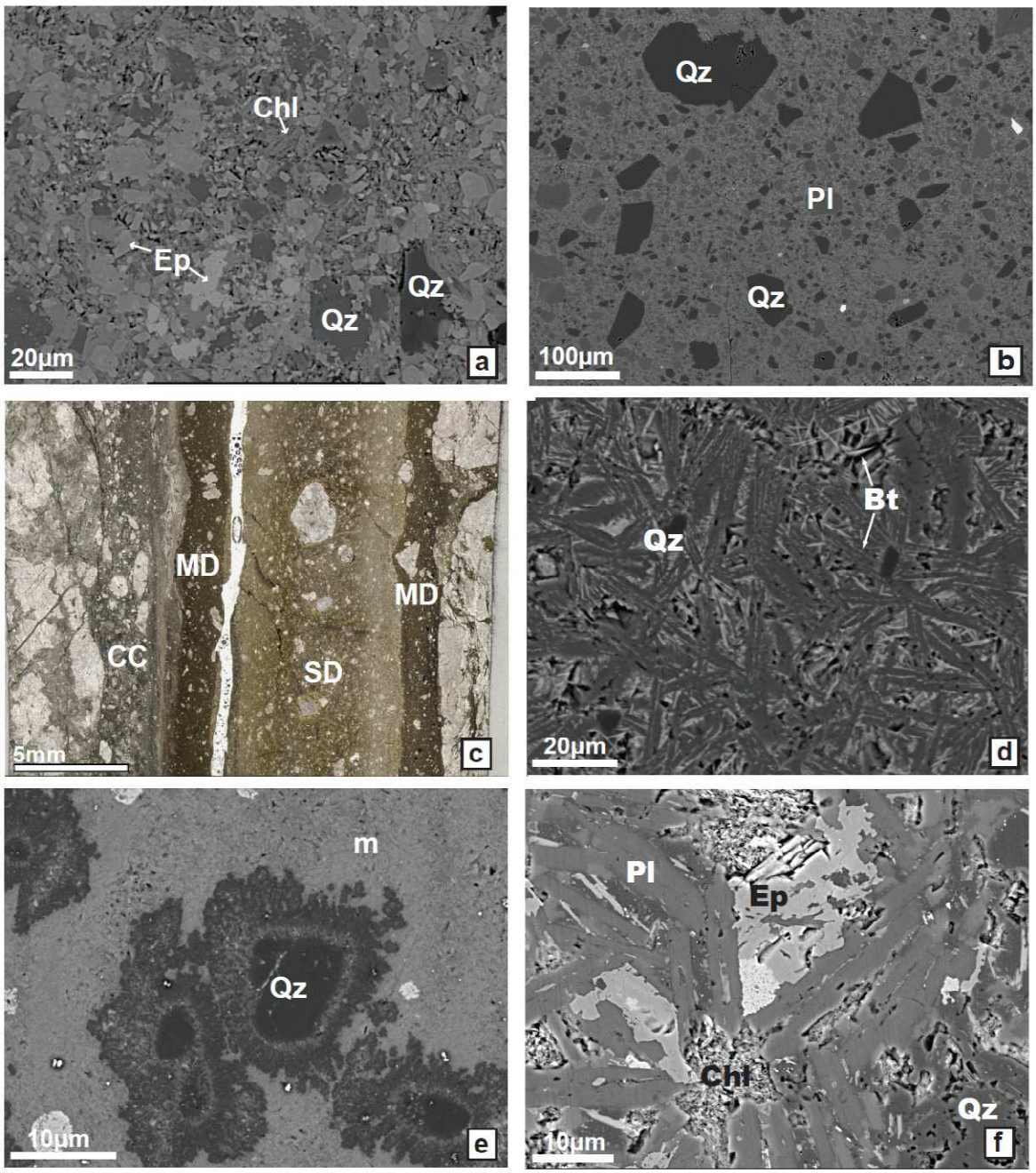


### *4.4.3 Artificial pseudotachylytes*

Artificial pseudotachylytes were produced in high velocity friction experiments performed on tonalites and cataclasites sampled within the GLFZ with the HV-1 rotary shear apparatus installed at Kyoto University (now installed at Kochi, Japan: for a description of the apparatus, see Shimamoto and Tsutsumi, 1994; Hirose and Shimamoto, 2005). A pair of rock cylinders (22.3-22.5 mm in diameter) was used for each experiment. To impose normal stresses up to 20 MPa, the samples

were jacketed in aluminium rings, but without confining the slipping zone (i.e., powders and melt could extrude from the slipping zone). During the experiments, the sliding velocity was 1.75 $ms^{-1}$ at the outer boundary of the specimen, which corresponded to an effective (a sort of average slip rate along the radius of the sample, see Shimamoto and Tsutsumi, 1994; Hirose and Shimamoto, 2005) slip rate of about 1.2 $ms^{-1}$, and under an imposed normal stress of 5, 10, 12.5, 15 and 20 MPa. The effective slip in these experiments was limited to about 4 m at most (Di Toro et al., 2006a; 2006b). All the experiments were conducted at room temperature and room humidity conditions (for a description of the experimental methods and results, see Di Toro *et al.*, 2006a; 2006b). During the experiments, after the initial expulsion of powders of crushed material, the slip surfaces melted (see video in Supplementary material of Di Toro et al., 2006a). Since the slipping zone was not confined, most of the melt was extruded and a thin (<0.5 mm) melt layer solidified on the artificial fault at the end of the experiment, welding the samples (Figure 6a, d, g). Polished rock thick sections were cut parallel to the cylinder axis perpendicular to the slipping zone and examined under the SEM.

FIGURE 6 (next page). Microstructures of the artificial pseudotachylytes and host rocks. (a) Polished sample of two tonalite cylinders welded, after the experiment, by a thin layer of artificial pseudotachylyte (black in color). (b) SEM-BSE image of the artificial pseudotachylyte (PT) in tonalite; the PT-tonalite boundary has deep embayments due to preferential melting of biotite (Bt) grains. (c) SEM-BSE image, a detail of the PT in tonalite. Angular quartz (Qz) and plagioclase (Pl) fragments are floating in the glass. The rounded features (indicated by the white arrows) are vesicles in the glass. (d) Polished sample of two cataclasite (green in color) cylinders welded, after the experiment, by a thin layer of artificial pseudotachylyte (black in color). (e) SEM-BSE image of the artificial pseudotachylyte (PT) in cataclasite; the cataclasite adjacent to the pseudotachylyte (PT) shows a pervasive porosity, and the PT-cataclasite boundaries are rough at the scale of the cataclasite grains. The rectangle shows the area enlarged in Figure 4f. (f) Detail of the contact between pseudotachylyte and cataclasite; note the evanescent and irregular boundary between melt and cataclasite (dotted lines), due to incipient melting of the low-melting point minerals (chlorite and epidote), while plagioclase grains (Pl) are not affected by melting. (g) Polished section of a cylinder of tonalite and one of cataclasite welded together by a thin layer of artificial pseudotachylyte (black in color).(h) SEM-BSE image of the artificial pseudotachylyte (PT) between cataclasite and tonalite; the cataclasite shows a pervasive porosity, while, on the opposite side, the boundary with tonalite is straight. (i) Further away from the pseudotachylyte-cataclasite boundary, where heating was less intense, chlorite grains (Chl) shows incipient melting, while epidote (Ep) is unaffected by melting.

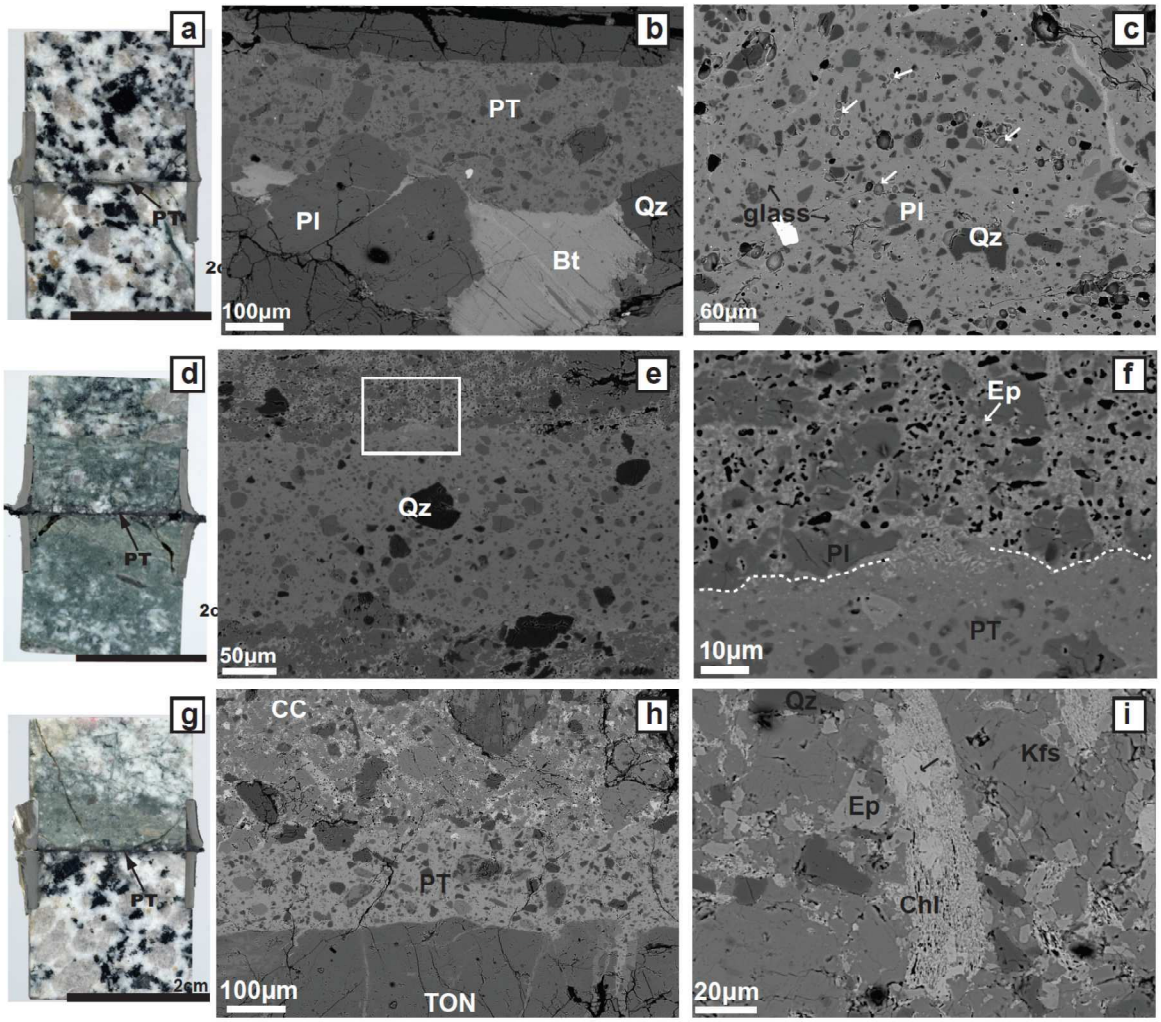


The artificial pseudotachylyte had a microstructure very similar to the natural one (compare Figure 6e with Figure 5b). Artificial pseudotachylytes are formed by clasts of quartz, plagioclase and K-feldspar suspended in a matrix of glass (Figure 6b, c, e). In some of the samples, the glass includes round-shaped vesicles (Figure 6c).

The boundaries between the pseudotachylyte and the wall rocks have different roughness depending on the grain size and the mineral and modal composition of the host rock. In tonalite, the boundary has embayments (due to preferential wear and melting) in the presence of biotite (Figure 6b), and it is straight in the presence of quartz and plagioclase. In cataclasite, the boundary profile is rough at the micrometer scale due to preferential wear and melting of micrometric grains of chlorite and epidote (Figure 6e, f). Inside the wall rocks cataclasite is vesiculated up to distance of 150-200 µm from the wall rock-pseudotachylyte boundary, due to the breakdown and selective melting of

epidote and chlorite grains. At further distance from the pseudotachylyte-cataclasite boundary, vesiculation and break down structures are found only in chlorite (Figure 6i), while nearby epidote grains are unaffected.

## 4.5 Mineralogical and chemical composition

Four samples of natural pseudotachylytes (including the matrix and suspended clasts) were analyzed by means of XRD: three pseudotachylyte samples within cataclasite (46-99-pt, 32-00-pt, 13-01-pt) and one pseudotachylyte sample within tonalite (10-04-pt). The pseudotachylytes are composed of quartz, plagioclase, dmisteinbergite, biotite, indialite (46-99-pt and 32-00-pt) and scapolite (46-99-pt and 32-00-pt). The biotite peak at 10Å is anomalously broad. To test if the broadness of the peak is due to the occurrence of smectite as sub-micrometric interlayers in biotite, the sample was treated with ethylene glycol and heated up to 800°C (Moore and Reynolds, 1997). The treated sample does not show any change in the spectrum profile, which suggests that the broad peak in untreated samples is actually due to the nanometric size of the crystallites of biotite in the spherulitic domains (e.g., Langford and Wilson, 1978). The sample 13-01-pt is mainly composed of quartz, plagioclase, biotite, and significant (> 5%) amounts of epidote and chlorite; no anomalies in the biotite spectrum are present.

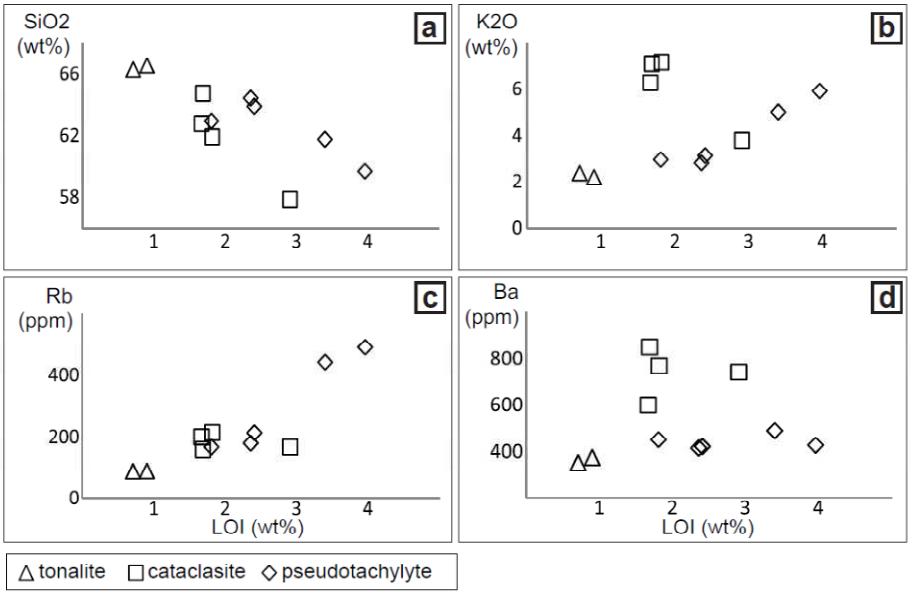


FIGURE 7. Major (in oxides) and trace elements (in ppm) plotted vs. the volatile content (LOI), data from Table 2. See text for discussion.

TABLE 2. XRF bulk rocks composition of fault and host rocks of the Gole Larghe Fault and average of point EMPA analysis of the glass produced in experiments. ton: tonalite, av: average. XRF (c) are pseudotachylyte bulk chemical compositions recalculated subtracting the clast content (Di Toro and Pennacchioni, 2004).

| | av. ton | st dev | av. Cc | st dev | 46-99-pt | 46-99-pt | 24-00-pt | 24-00-pt | 32-00-pt | 20b-00-m-pt | 20b-00-m-pt | 20b-00-s-pt | 20b-00-s-pt | av. glass exp. pt | st dev |
|---|---|---|---|---|---|---|---|---|---|---|---|---|---|---|---|
| | XRF (5 data) | | XRF (4 data) | | XRF | XRF (c) | XRF | XRF (c) | XRF | XRF | XRF (c) | XRF | XRF (c) | EMPA (6 data) | |
| $SiO_2$ | 66.56 | 0.94 | 61.86 | 2.35 | 59.69 | 55.05 | 63.89 | 60.08 | 61.78 | 62.95 | 58.99 | 64.42 | 61.08 | 52.21 | 0.33 |
| $TiO_2$ | 0.46 | 0.05 | 0.57 | 0.05 | 0.55 | 0.65 | 0.53 | 0.66 | 0.55 | 0.54 | 0.63 | 0.53 | 0.59 | 1.16 | 0.07 |
| $Al_2O_3$ | 16.53 | 0.37 | 17.71 | 1.06 | 17.13 | 19.03 | 16.57 | 17.76 | 17.06 | 17.00 | 18.93 | 16.68 | 18.24 | 22.11 | 0.28 |
| FeO | 3.41 | 0.29 | 3.71 | 0.48 | 3.09 | 3.65 | 3.19 | 3.99 | 3.50 | 3.74 | 4.34 | 3.19 | 3.59 | 7.71 | 0.25 |
| $Fe_2O_3$ | 0.33 | 0.08 | 0.96 | 0.08 | 2.00 | 2.36 | 1.22 | 1.51 | 0.83 | 0.87 | 1.00 | 0.92 | 1.03 | | |
| MnO | 0.10 | 0.01 | 0.12 | 0.03 | 0.11 | 0.12 | 0.12 | 0.13 | 0.13 | 0.14 | 0.16 | 0.10 | 0.11 | 0.26 | 0.03 |
| MgO | 1.57 | 0.18 | 1.94 | 0.21 | 1.95 | 2.31 | 1.77 | 2.22 | 1.84 | 1.91 | 2.22 | 1.71 | 1.92 | 3.92 | 0.19 |
| CaO | 4.44 | 0.15 | 4.16 | 0.24 | 3.55 | 3.77 | 3.58 | 3.44 | 3.62 | 4.09 | 4.47 | 3.89 | 4.19 | 4.84 | 0.18 |
| $Na_2O$ | 2.95 | 0.05 | 3.25 | 0.23 | 1.26 | 1.21 | 3.03 | 3.12 | 1.59 | 3.22 | 3.56 | 2.99 | 3.25 | 2.88 | 0.16 |
| $K_2O$ | 2.20 | 0.11 | 3.11 | 0.26 | 5.92 | 6.99 | 3.15 | 3.90 | 5.02 | 2.98 | 3.44 | 2.83 | 3.18 | 4.18 | 0.13 |
| $P_2O_5$ | 0.11 | 0.01 | 0.15 | 0.01 | 0.13 | 0.16 | 0.13 | 0.16 | 0.14 | 0.14 | 0.16 | 0.14 | 0.15 | | |
| *L.O.I.* | 0.91 | 0.07 | 2.23 | 0.36 | 3.96 | 4.69 | 2.41 | 3.03 | 3.40 | 1.81 | 2.10 | 2.36 | 2.66 | | |
| Tot | 99.56 | 0.14 | 99.78 | 0.29 | 99.34 | 100 | 99.58 | 100 | 99.45 | 99.39 | 100 | 99.74 | 100 | 99.27 | 0.46 |
| V | 57.9 | 6.5 | 70.80 | 1.70 | 67.5 | | 67.5 | | 66.8 | 69.6 | | 72.0 | | | |
| Rb | 90.4 | 12.6 | 173.85 | 8.70 | 492.4 | | 213.7 | | 443.0 | 167.7 | | 180.0 | | | |
| Sr | 225.2 | 9.7 | 238.75 | 12.23 | 196.7 | | 235.8 | | 221.8 | 247.4 | | 230.1 | | | |
| Y | 26.4 | 5.6 | 31.70 | 0.42 | 30.4 | | 32.2 | | 28.9 | 32.0 | | 31.4 | | | |
| Zr | 117.0 | 9.7 | 135.50 | 0.42 | 136.4 | | 134.9 | | 139.9 | 135.2 | | 135.8 | | | |
| Nb | 10.2 | 1.0 | 12.05 | 0.64 | 12.3 | | 10.8 | | 12.5 | 12.5 | | 11.6 | | | |
| Ba | 374.8 | 25.3 | 433.40 | 25.46 | 427.2 | | 422.1 | | 489.7 | 451.4 | | 415.4 | | | |
| La | 30.3 | 4.5 | 46.60 | 4.95 | 34.9 | | 40.5 | | 29.8 | 50.1 | | 43.1 | | | |
| Ce | 52.8 | 15.2 | 76.20 | 8.20 | 55.5 | | 64.7 | | 69.8 | 82.0 | | 70.4 | | | |
| Nd | 23.2 | 7.3 | 21.85 | 7.00 | 29.3 | | 31.8 | | 10.1 | 26.8 | | 16.9 | | | |
| U | 3.2 | 0.5 | 6.25 | 0.35 | 17.6 | | 7.7 | | 16.2 | 6.0 | | 6.5 | | | |

The bulk elemental composition from XRF analyses of some representative samples of the main rock types of the Gole Larghe Fault Zone was published in previous studies (Di Toro and Pennacchioni, 2004; 2005; Pennacchioni et al., 2006); the data are reported in Table 2. The cataclasites are strongly enriched in $Fe_2O_3$, $K_2O$, LOI (Loss On Ignition), Rb, Ba and U; the pseudotachylytes have a similar chemical composition, suggesting that they formed by melting of the cataclasites which already interacted with fluids enriched in LOI (Di Toro and Pennacchioni, 2005; Pennacchioni et al., 2006). The content in volatiles (LOI) in pseudotachylytes is very high (>3%) in some of the samples. To test if there is a correlation between chemical (and mineralogical) composition with the LOI content, we plotted the contents in $SiO_2$, $K_2O$, barium and rubidium versus the LOI content (Figure 7). Cataclasites and pseudotachylytes are depleted in $SiO_2$ and enriched in $K_2O$ if compared with tonalite. The $K_2O$ in pseudotachylytes is positively correlated with the LOI content, while the $K_2O$ in cataclasites is independent on the LOI value. We used the Rb and Ba contents for discriminating the contribution in K from K-feldspar (bearing Ba) and that from biotite (bearing Rb). In pseudotachylytes, rubidium has a similar positive correlation with LOI (as $K_2O$), while no correlation exists in cataclasites. Cataclasites are instead enriched in barium, suggesting that they are enriched in K-feldspar. Apparently, the pseudotachylytes having an high content of LOI have also an high content in biotite.

The composition of the glassy matrix of artificial pseudotachylytes was analyzed by means of microprobe spot analyses. Compared with the starting tonalite, the glass composition (average of six microprobe point analyses performed in areas without evidence of the presence of clasts) shows (Table 2): (i) a lower content of $SiO_2$ (52.2wt % vs. 66.5 wt %), (ii) an higher content of $Al_2O_3$ (22.1wt% vs. 16.5 wt %), FeO (7.7% vs. 3.4 wt %), MgO (3.9% vs. 1.6 wt %), $K_2O$ (4.18% vs. 2.2 wt %) and $TiO_2$ (1.1% vs. 0.5 wt %), and (iii) a similar content of CaO (4.8% vs. 4.4 wt %), and $Na_2O$ (2.88% vs. 2.9 wt %).

## 4.6 The content of water

The water content in bulk tonalite is 0.96% from CHN analyses (Table 3). The LOI value in tonalite ranges between 0.71 and 0.91 wt.% (Table 2), suggesting that water is the main volatile species. Considering a modal content of biotite of 17% (Di Toro and Pennacchioni, 2004), the volatiles are most likely derived from OH in biotite. The water content of biotites in the tonalite from CHN analysis is of 3.49 - 4.24%. The high content in water of some of the biotites might be

interpreted as due to the occurrence of chlorite interlayers inside the biotite lattice (see the large biotite grain in Figure 5b ), not seen under the binocular microscope used for separating the biotite grains.

The water content in mylonites is of 1.4 – 1.7%, higher than in the bulk tonalite. The modal content of biotite in ultramylonites is likely to be higher than in the host tonalite (Figure 3a).

The bulk natural pseudotachylyte samples have a water content ranging between 2.33 and 4.41%. The water content (2.33 - 4.41%) is higher than expected for a modal content of biotite of 17% as estimated by Rietveld refinement in one of the pseudotachylyte samples (Nestola et al., 2010): if water was only hosted in biotite, the sample should have the 0.7% in water, instead of the measured 2.8%.

Although the experiments were performed without confining the slipping zone (i.e., frictional melts could potentially degas) the artificial pseudotachylytes produced from tonalites and cataclasites have a water content of 0.85% – 2.44%, similar to the values of their respective protoliths.

## 4.7 FTIR spectra in natural pseudotachylytes

As mentioned above, the content of water in pseudotachylytes is higher than expected for the measured modal content of biotite (for instance, a rock with bulk water content of 4.24% would be composed only of biotite). The presence of clay minerals has been excluded by XRD analyses at temperature up to 800°C. Glass is not seen in XRD analyses, and was not found in TEM investigations on some of the samples analyzed (Di Toro and Pennacchioni, 2004). The structural position of water was thus investigated by infrared (FTIR) spectroscopy.

The absorbance infrared spectra were acquired in the range of wavenumbers 1400 – 4000 $cm^{-1}$, in order to identify the main peaks of vibration of water: the OH stretch region (2700 $cm^{-1}$ – 3650 $cm^{-1}$), which is produced in both molecular water and hydroxyl ions, and the peak of the H-O-H bending (1630 $cm^{-1}$), indicative of the presence of molecular water.

FIGURE 8 (next page). Fourier Transform Infrared absorbance pectra of natural pseudotachylytes. (a) Microlitic domain. (b) Matrix of spherulitic domain. The spectra were collected at ambient temperature (25°C, blue curve) and at T>50°C (red curve). Between 50 and 300°C the shape of both spectra did not change significantly.

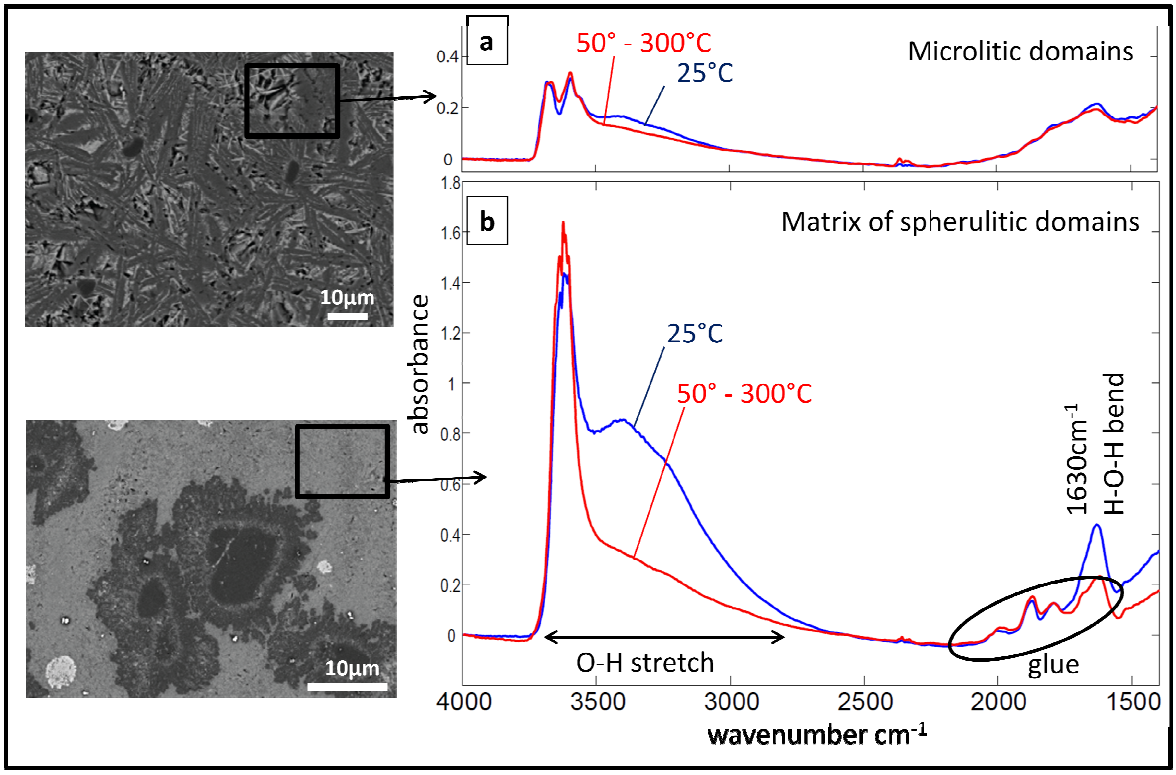


In microlitic domains, two peaks in the region of the OH stretching are measured and the shape of the spectrum doesn't change by step heating up to 300°C (Figure 8a). In the cryptocrystalline matrix of the spherulitic domains, an intense peak is found in the OH stretch region (3600 $cm^{-1}$), with a broad shoulder towards lower wavenumbers. A peak in the HOH bending region is present as well (although in the region 1500 – 2000 $cm^{-1}$ there are some peaks due to the presence of glue). Upon heating over 50°C under vacuum ($10^{-7}$ mbar), the shoulder in the OH region and the peak at 1603 $cm^{-1}$ (HOH bending) disappear (Figure 8b). Upon heating at 50°C, the release of water produced a loss of vacuum. This is indicative of loosely bonded molecular water, which might explain the anomalously high water content of the natural pseudotachylytes (Table 2).

## 4.8. Hydrogen isotope composition

The hydrogen isotope compositions of the analyzed samples are listed in Table 3 together with the volatile composition from CHN analyses, and both data are plotted in Figure 9. The hydrogen isotope composition of the bulk tonalite is most likely represented by the H-isotope composition of biotite, for which a $\delta$D value of -74 ± 1 ‰ was measured. The hydrogen isotope composition of bulk mylonites is -77 and -79 ‰, slightly lower than the host tonalite.

Hydrogen isotope compositions of cataclasites are clustered in the interval -65 ± 4 ‰. The large span in $H_2O$ contents and $\delta$D depends on the variable modal abundance of epidote and chlorite, the hydrogen bearing minerals in cataclasite.

The hydrogen isotope composition of the bulk natural pseudotachylytes is in the range -92 ± 13 ‰. Disregarding subsamples 13-01-pta and 13-01-ptb, where there is evidence of overgrowth of epidote and chlorite (Figure 4f), the range of hydrogen isotope composition decreases to -93 ± 9 ‰, with all but one sample exhibiting a range of -103 to -85‰. The microlitic and spherulitic domains (Figure 4c) of the pseudotachylyte veins have been analyzed separately and have similar isotope composition in the limits of the instrumental resolution.

The $\delta$D value of artificial pseudotachylytes obtained from tonalite is $\delta$D= -75±2‰, and that of pseudotachylytes produced using at least one cylinder of cataclasite is $\delta$D = -83±1‰. Thus, the artificial pseudotachylytes produced from frictional melting of tonalites have $\delta$D indistinguishable from that of the source tonalite. In contrast, the artificial pseudotachylytes produced from cataclasites have $\delta$D lower by ~20‰ than that of the source cataclasite.

| | wall rocks | δD‰ | N | st. dev. | $H_2O$ wt% |
|---|---|---|---|---|---|
| ***Biotite separates in Avio tonalite*** | | | | | |
| 2-99-bt | To | -75 | 2 | 0.4 | 4.24 |
| 21-00-bt | To | -73 | 2 | 1.9 | 3.49 |
| 3-02-bt | To | -74 | 2 | 3.0 | |
| G 5-bt | To | -74 | 2 | 2.2 | 4.10 |
| ***Bulk tonalite*** | | | | | |
| 19-00 | To | | | | 0.97 |
| ***Mylonites*** | | | | | |
| 07 162 | To | -78 | 2 | 2.4 | 1.40 |
| 99 D7 umyl | To | -80 | 3 | 3.7 | 1.70 |
| ***Cataclasites (natural faults)*** | | | | | |
| 46-99-cc | To | -62 | 2 | 2.8 | 2.15 |
| 24-00-cc | To | -65 | 2 | 0.5 | 2.01 |
| 32-00-cc | To | -67 | 2 | 4.7 | 2.27 |
| 11-01-cc | To | -65 | 2 | 2.8 | 3.15 |
| L65-cc | To | -69 | 2 | 0.9 | 2.90 |
| ***Cataclasites (after HVFRE)*** | | | | | |
| 371-06-cc | To | -60 | 2 | 4.5 | 1.99 |
| 378-06-cc | To | -69 | 2 | 0.2 | 1.66 |
| 379-06-cc | To | -65 | 2 | 4.2 | 1.30 |
| ***Natural pseudotachylytes*** | | | | | |
| 3-02-pt | To | -96 | 2 | 2.7 | 3.03 |

| | | | | | |
|---|---|---|---|---|---|
| 3-02-pt-c | To | -95 | 2 | 4.0 | |
| 10-04-pt | To | -95 | 3 | 5.1 | 2.8 |
| 2-99-pt | Cc/To | -90 | 2 | 2.5 | 3.09 |
| 46-99-ptm-a | Cc/To | -94 | 2 | 3.6 | 3.95 |
| 46-99-pt-a | Cc/To | -86 | 2 | 0.9 | |
| 46-99-pt-b | Cc/To | -86 | 2 | 3.7 | |
| 46-99-pt-c | Cc/To | -87 | 2 | 1.9 | |
| 46-99-pt-d | Cc/To | -85 | 3 | 2.5 | |
| 24-00-pt | Cc/To | -97 | 3 | 4.7 | 4.24 |
| 32-00-pts | Cc/To | -101 | 2 | 1.1 | |
| 32-00-pt | Cc/To | -104 | 2 | 3.3 | 4.41 |
| 19-01-pt-c | Cc/To | -97 | 2 | 0.5 | |
| 19-01-pt-f | Cc/To | -91 | 2 | 4.3 | 2.44 |
| 11-01-pts | Cc/To | -92 | 2 | 0.1 | 2.81 |
| 17-01-pt | Cc/To | -94 | 4 | 4.9 | 3.80 |
| 13-01-pt-a | Cc/To | -83 | 3 | 1.7 | |
| 13-01-pt-b | Cc/To | -77 | 2 | 0.5 | 2.33 |
| 2-01-pt | Cc/To | -96 | 2 | 1.3 | 3.06 |
| 21-01-pt-a | Cc/To | -89 | 3 | 4.0 | 3.55 |
| 21-01-pt-b | Cc/To | -96 | 3 | 4.8 | |
| L65-pt | Cc/To | -88 | 3 | 1.9 | 2.6 |
| ***Artificial pseudotachylytes*** | | | | | |
| 370-06-pt | To/To | -74 | 4 | 2.5 | 1.85 |
| 372-06-pt | To/To | -74 | 4 | 1.0 | 1.37 |
| 376-06-pt | To/To | -76 | 4 | 4.7 | 0.85 |
| 371-06-pt | Cc/Cc | -85 | 4 | 2.2 | 1.77 |
| 378-06-pt | Cc/Cc | -82 | 4 | 2.8 | 2.44 |
| 379-06-pt | Cc/To | -84 | 4 | 2.0 | 1.47 |

Table 3. Summary of the results of TC/EA analyses ($\delta$D‰) and CHN analyses ($H_2O$ contents in wt%). N is the number of analysis used for calculating the average $\delta$D.

FIGURE 9 (next page). Plot of the $\delta$D vs. the water content (CHN analyses) of host rocks and artificial and natural pseudotachylytes from the GLFZ (data in Table 3). (a) Data of artificial pseudotachylytes and their source rocks. (b) Data of natural fault and host rocks from the Lobbia and Avio outcrops.

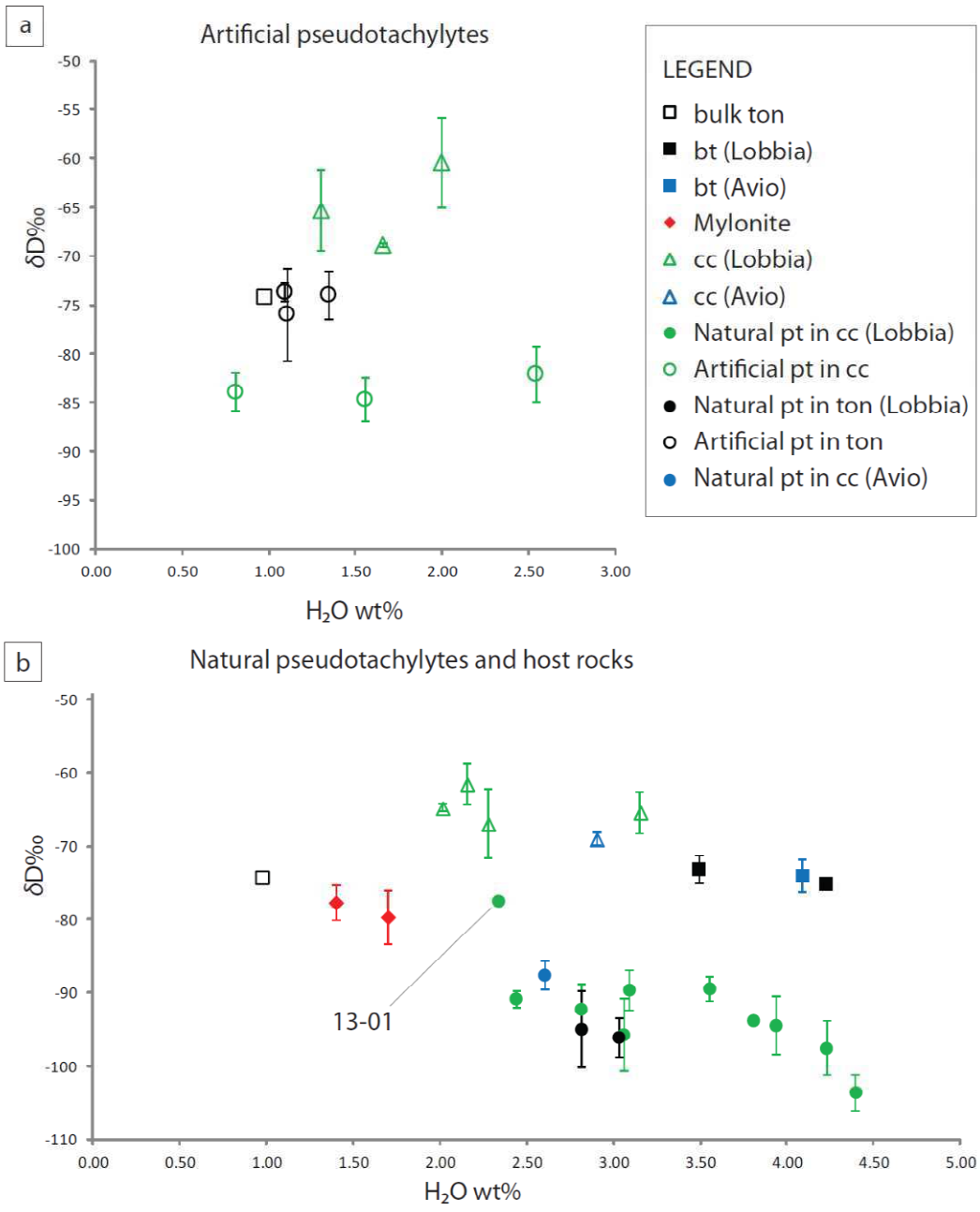


## 4.9 Discussion

### *4.9.1 Hydrogen isotope fractionation in the artificial pseudotachylytes*

In artificial pseudotachylytes, the source of hydrogen which can potentially be dissolved in the frictional melt is the dehydration of the hydrous minerals of the starting rocks, i.e. biotite in tonalite and chlorite + epidote in cataclasite. Ingress of water from room humidity in the slipping zone during

the experiments is impeded by (i) the large applied normal stress (5 to 20 MPa), (ii) the extrusion of melt and (iii) the centrifugal forces due to the high revolution rates of the sample (1500 rpm). The specimen surfaces are ground and the powders are expelled before the onset of melting, so the possible layer of humidity adsorbed on the specimen surfaces probably do not enter in the melt. The pseudotachylytes ($\delta$D= -75±2‰) produced in tonalite (Figure 9a) retain indeed a $\delta$D indistinguishable from that of biotite ($\delta$D = -74 ± 1 ‰) in tonalite, while pseudotachylytes ($\delta$D = -83±1‰) produced in cataclasite ($\delta$D = -65 ± 4 ‰, Figure 9a)have $\delta$D lower by ~20‰ than the source cataclasite. Based on microstructural observations, the processes that might have caused isotopic fractionation during melting are: (i) degassing of the melt, as suggested by the occurrence of vesicles and bubbles within the glass of some artificial pseudotachylytes (Figure 6c); (ii) selective melting and breakdown of chlorite and epidote in the cataclasite next to the slipping surfaces, as suggested by vesiculation in cataclasite close to artificial pseudotachylytes (Figure 6e, f, h, i). Hydrogen fractionation due to degassing is accompanied by a loss of water from the melt, as measured in volcanic glasses (Taylor et al., 1983; Rust et al., 2004; De Hoog et al., 2009). In our samples, the water content of artificial pseudotachylytes is higher or equal to the water content of the source rock. For causing the -20‰ isotopic shift of artificial pseudotachylytes from the source cataclasites, a loss of water would have been required. Degassing should have affected both melts produced in tonalite and cataclasite, while the negative shift in hydrogen isotope composition is observed only in samples obtained in cataclasite.

The wall rocks adjacent to the melt layer heat up during the experiments. When, under these experimental conditions (1.3 m/s and 10 to MPa normal stress) a continuous layer of melt forms in the slipping zone (after about 1-2 s of slip) steady state conditions are achieved: the melt strength is constant and low (fault lubrication), and the shortening rate of the sample, about 0.5 mm $s^{-1}$, is constant (Figure 2 in Di Toro et al., 2006a). Sample shortening results from a balance between the solid rock entering in the slipping zone and the melt extruded from the slipping zone (Nielsen et al., 2008). The temperature in the wall rocks increases because the rock migrates towards the slipping zone pushed by the applied normal stress and because of the heat diffusion from the slipping zone towards the wall rocks. The effects of the thermal perturbation in the wall rocks bounding the slipping zone are evident in cataclasite (Figure 6e, f, h, i): chlorite (melting T = 650$^{o}$C) and epidote grains undergo selective melting, break down and vesiculation, which are more intense close to the cataclasite–melt interface. In the experiments in tonalites, biotite grains, which have melting temperature of about 650°C (Spray, 1992), lower than that of feldspar (about 1200°C for andesine)

and quartz (about 1700°C) are preferentially melted (and vesiculated) forming embayments along the rock-melt interface (Figure 6b). In Figure 10, the temperature in the wall rocks calculated for the steady state conditions and melt thickness of 0.2 mm (Nielsen et al., 2008) are reported for cataclasite and tonalite. Due to their fine grained texture (<50µm), cataclasites furnish a continuous layer of OH bearing minerals along the melt interface (T=1200°C). Chlorite and epidote grains melt along the interface (black color), and at the same time, chlorite and epidote in the walls are heated and release part of their hydroxyl ions, likely the lighter (thus, having low $\delta$D). A similar trend has been measured in dehydrated biotites in volcanic ambient (Feeley and Sharp, 1996) (Figure 10a). The tonalite has sparse, coarse biotite grains (>500 µm), which melt completely in contact with the melt layer, with minor vesiculation. The $\delta$D of the frictional melt results thus from two components: (i) the hydroxyl ions of the minerals which melt completely, having a value identical to that of the starting material (ii) the hydroxyl ions released by the OH-bearing minerals which are dehydrated, but do not melt completely, having lower $\delta$D. In melts from tonalite, the component of low $\delta$D released by partially melted biotite is smaller than that due to complete melting of biotite (compare black and dotted areas in biotite grains, Figure 10b), and, accordingly, the $\delta$D of artificial pseudotachylytes in tonalite have $\delta$D indistinguishable from that of the biotite. In cataclasites, the proportion of low $\delta$D entering in the melt is higher (compare the black and dotted areas in Figure 10a), thus causing a lowering of the bulk $\delta$D of the artificial pseudotachylytes if compared with the $\delta$D of the source cataclasite.

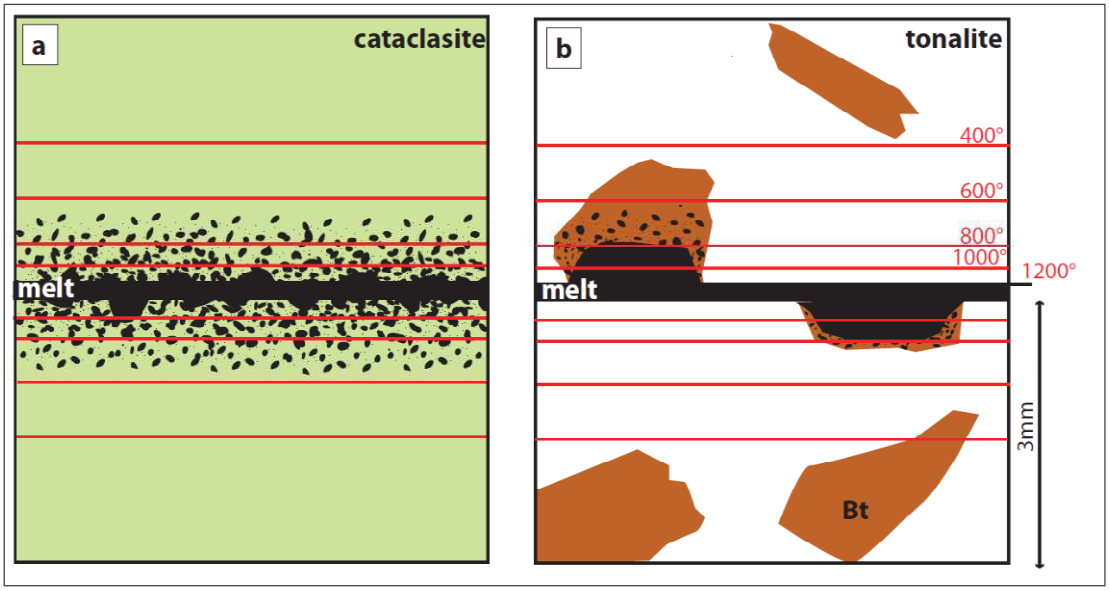


FIGURE 10. Sketch of the distribution of temperatures within cataclasite (a) and tonalite (b) samples within the first 3mm around the slipping surface, when an interconnected layer of 0.2mm of melt is present (steady

state). Isotherms are reported from the model of Nielsen et al. (2008). Dotted texture represent the zone of partially melted minerals, as observed in Figure 6 e, f, h, i.

### *4.9.2 Hydrogen isotope compositions of the GLFZ*

The biotite in the Val d'Avio tonalite has $\delta$D of -74 ± 1 ‰, a value consistent with the hydrogen composition of biotite in plutonic rocks measured worldwide (Taylor, 1978). The two samples of mylonite analyzed have hydrogen isotope composition very similar to the biotite in tonalite ($\delta$D = -75 ‰ and -79 ‰), implying no ingression of an external fluid. The -4 ‰ shift of $\delta$D measured in one sample can be due to the recrystallization of biotite ($Bt_2$, Figure 3b; Pennacchioni, 2005) at T=550°C estimated for the mylonitic deformation. A Rayleigh fractionation between water with $\delta$D = -74 ± 1 ‰ and biotite at such temperature would produce a -4 ‰ isotopic shift with a loss of water of 1% (using the fractionation coefficient of Suzuoki and Epstein, 1976). Cataclasites have higher $\delta$D values ($\delta$D =-65 ± 4 ‰) which are rather constant over samples collected in the Lobbia and in the Avio outcrops (Figure 9b). The hydrogen bearing minerals in cataclasites are chlorite and epidote, which have micrometric grain size and cement the cataclasite matrix (Figure 5a). The hydrogen isotope composition of bulk cataclasites can be evaluated as

$$\delta D_{ccbulk} = \chi_{ep}\delta D_{ep} + \chi_{chl}\delta D_{chl} = \chi_{ep}(\delta D_w + 1000\ln\alpha_{ep-w}) + \chi_{chl}(\delta D_w + 1000\ln\alpha_{chl-w}) \quad (2),$$

where $\chi$ is the molar fraction, *ccbulk* states for bulk cataclasite, *ep* for epidote, *chl* for chlorite. $1000\ln\alpha_{ep\text{-}w}$ is an expression of the fractionation between epidote and water in equilibrium conditions. The fractionation coefficient $\alpha$ between the species A and B is defined as

$$\alpha_{A-B} = \frac{R_A}{R_B} \quad (3),$$

where *R* is the ratio of the abundance of the heavy to the light isotope. $\alpha$ has typically values close to unit, on the order of 1.00*X*. Since 1000ln1.00X ≈ X, the notation 1000lnα is very useful expression of the fractionation in per mil. The value $1000\ln\alpha$ can be approximated as the difference in the isotope composition of the two species *A* and *B* ($\Delta_{A\text{-}B}$) (within the analytical error of ±5‰ in our data):

$$\Delta_{A-B} = \delta_A - \delta_B \approx 10^3 \ln\alpha_{A-B} \quad (4),$$

From equation (2), we calculated the hydrogen isotope composition of water ($\delta D_w$) in equilibrium with both epidote and chlorite using the experimentally determined fractionation coefficients epidote-water (Graham et al., 1987) and chlorite-water (Graham et al., 1980) at 250°C. Assuming a mean mineral modal content of chlorite and epidote of 6.2% and 11.8% respectively, as obtained

averaging eleven semi-quantitative modal compositions from XRPD analysis (Di Toro and Pennacchioni, 2005), the isotopic composition of water in cataclasites is $\delta$D = -41 ± 4 ‰ (Graham et al., 1980; 1987). These values of $\delta$D are in the highest range of the field of magmatic water measured worldwide (-80 < $\delta$D < - 40‰, Taylor, 1974). A late magmatic origin of the fluids cementing cataclasites was suggested by Di Toro and Pennacchioni (2005) based on the enrichment in Large Ions Lithophile Elements (Rb, Ba, U, Th, etc.) in cataclasite. The seismic activity of the GLFZ was contemporary to the cooling of the Presanella pluton (Del Moro et al., 1983; Skopelitis et al., 2011), located few km north from the studied outcrops (Figure 1a), so a late-magmatic origin of the fluids involved in the fault zone is likely.

The pseudotachylyte sample (13-01), where epidote and chlorite (Figure 5f) overgrow on the microlitic texture, has the highest $\delta$D values among the natural pseudotachylytes ( -83 < $\delta$D < -77‰) (Figure 9b). The other natural pseudotachylyte samples have $\delta$D values in the range -93 ± 9 ‰, about 20 - 40‰ lower than in the cataclasites ($\delta$D = -65 ± 4 ‰), confirming that most pseudotachylytes do not bear a significant amount of epidote and chlorite, as observed under the SEM and in XRPD analysis. Apparently, the more water is present in pseudotachylytes, the lower is their $\delta$D value (Figure 9b). This trend could be associated with hydration of pseudotachylytes by absorption of water having lower $\delta$D value. In fact, infrared spectroscopy demonstrated the occurrence of loosely bonded molecular water (i.e., released at T > 50 $^{o}$C, Fig. 8b) in the cryptocrystalline matrix of spherulitic domains of natural pseudotachylytes. According to the infrared spectroscopy, the water in pseudotachylytes is present as: (i) hydroxyl ions in biotite (in both microlitic and spherulitic domains) and, (ii) adsorbed molecular water. By knowing the hydrogen isotope composition of bulk pseudotachylyte (in sample 10-04pt, $\delta D_{PTbulk}$ = -95 ‰), the bulk water content (2.8%), the amount of biotite (17% in weight) and thus the molar fraction of hydrogen hosted in biotite, and assuming that biotite has the same $\delta$D value as the biotite in the host tonalite (-75‰), we can calculate the isotopic composition of the adsorbed water ($\delta D_x$ ):

$$\delta D_{PTbulk} = \chi_{Bt}\delta D_{Bt} + \chi_x \delta D_x \qquad (5)$$

$$\delta D_x \approx -104\,‰ \qquad (6).$$

The present day hydrogen isotope composition of the sampling area can be estimated by knowing the isotope compositions in nearby pluviometric stations and correcting the measured values for the effect of the higher elevation. Starting from the values in two nearby pluviometric stations listed in Longinelli and Selmo (2003) (Campo Carlo Magno, 1685 m a.s.l. and Rifugio Graffer, 2263 m a.s.l.),

assuming a mean vertical isotope gradient of 0.2$\delta^{18}$O/100m and using the equation of the global meteoric water line

$$\delta D = 8\delta^{18}O + 10 \qquad (7)$$

the $\delta$D values of precipitation in the area where pseudotachylytes were collected (2800 m a.s.l.) are in the range -93‰ to -91‰ (-90‰ to -87‰ according to the equation 5 calculated for the specific case of northern Italy in Longinelli and Selmo, 2003). The measured $\delta$D values in natural pseudotachylytes are thus likely to be lowered (more negative) by the adsorbtion of low $\delta$D water from local rainfall and glacier ablation. The amount of LOI (which, from CHN analyses, are composed mostly of water) in pseudotachylytes seems to be correlated with the amount of (nanometric, as suggested by XRPD analyses) biotite present in the pseudotachylyte matrix, as suggested by the high content in $K_2O$ and Rb in the most water-rich pseudotachylytes (Figure 7b, c). This could be an indication that, the more amount of cryptocrystalline biotite is present, the more water is absorbed. We will test this hypothesis by measuring the hydrogen isotope composition of pseudotachylyte samples dehydrated in oven at T>50°C.

Following the calculation for sample 10-04 (equation 5), the hydrogen isotope composition of the bulk pseudotachylytes before the ingression of weakly bounded water should have $\delta$D values (-75 < $\delta$D < -85‰) higher by 10-20‰ than the measured ones ($\delta$D = -93.2 ± 9.2 ‰). Noteworthy, these $\delta$D values (-75 < $\delta$D < -85‰) are lower than those from cataclasites ($\delta$D = -65 ± 4 ‰). Since the source rock of most of the pseudotachylytes is the cataclasite, this implies a negative shift of the hydrogen isotope composition from the $\delta$D values of cataclasites (-65 ± 4 ‰) to $\delta$D of -75 to -85‰. This shift is in the same range to the one measured in the artificial pseudotachylytes produced from frictional melting of cataclasites, suggesting that a similar hydrogen fractionation mechanism could operate in nature and in the laboratory. On the other hand, natural pseudotachylytes do not bear glass (Di Toro and Pennacchioni, 2004), thus the melt underwent crystallization and/or devitrification. Here we discuss the two possible mechanisms affecting the isotope composition of natural pseudotachylyte: (i) the coseismic dehydration of the wall rocks, as reproduced in experimental dry conditions, and (ii) the growth of biotite in the devitrified pseudotachylyte matrix.

(i) Pseudotachylytes overprint and intrude the cataclasites. Artificial pseudotachylytes produced in experiments performed on cohesive cataclasites are thus somewhat reproducing the conditions of formation of natural pseudotachylytes. In artificial pseudotachylytes produced from cataclasites, a negative shift in hydrogen isotope ratio of the frictional melts with respect to the cataclasite protholith, is produced without the ingression of any external fluid, nor devitrification processes. In

artificial pseudotachylytes produced from tonalite, the hydrogen isotope ratio of the frictional melts is identical to the tonalite protholith: so the isotopic signature of artificial pseudotachylyte produced from tonalites and cataclasites is different. Instead, natural pseudotachylytes have a similar isotopic signature independently of the host rock This might be due to the complex architecture of the GLFZ, which is formed of a network of faults: the pseudotachylyte veins apparently hosted in tonalite could have intersect cataclasites in not outcropping sections of the fault. Natural pseudotachylytes often show flow structures, which are independent of the sense of shear of the fault, indicating that melt migration in slipping zones (= fault veins) is driven by the large pressure gradients related to opening of fractures (injection veins) and fault waviness (presence of compressive and extensional domains, Griffith et al., 2010). We propose that selective melting of low melting temperature minerals and dehydration of hydrous minerals in the cataclasite along the sliding surfaces caused the enrichment in water and lowering in $\delta$D measured in the natural pseudotachylytes.

(ii) A negative shift of 20‰ in hydrogen isotope composition of pseudotachylytes of the Homestake Shear Zone if compared with source rock was measured by Moecher and Sharp (2004). The authors suggest that the lowering in $\delta$D was due to crystallization of white mica during devitrification processes, accompanied by a loss of water. In the GLFZ pseudotachylytes, the same $\delta$D difference from the source rock was measured. However, differently from the Homestake pseudotachylytes, neither white mica, nor clay minerals have been detected, and the only OH-bearing phase is biotite. Hydrogen dissolves in silicatic melts either as $OH^-$ or $H_2O$ (Stolper, 1989) and during cooling and devitrification of the pseudotachylyte veins, hydrogen is incorporated in the hydroxyl ions of hydrated minerals. Crystallization of phyllosilicates causes a negative fractionation of hydrogen, the new minerals having lower $\delta$D value if compared with the residual water (Suzuoki and Epstein, 1976). If the residual water is free to leave the system, the process results in lowering the isotopic composition of the bulk pseudotachylyte. If the water remains in the system, the bulk pseudotachylyte retains the isotopic composition of the melt. Assuming that the initial isotope composition of the melt was the same as the one of biotite in tonalite ($\delta$D≈-75‰) (this is a lower bound, because the starting cataclasites have still higher $\delta$D), we estimate the loss of water due to crystallization of biotite with a Rayleigh distillation process

$$(\delta D_f - \delta D_i) = 1000[F^{(\alpha-1)} - 1] \qquad (8),$$

where $f$ and $i$ stand for final and initial, $F$ is the fraction of hydrogen remaining in the system and α the temperature-dependent isotopic fractionation factor between biotite and water. In microlitic domains, biotite crystallized together with plagioclase, since acicular biotite grains are embedded in

plagioclase microlites (Figure 5d). At high cooling rates, a reliable crystallization window for plagioclase is between 1000 and 800°C (Lesher et al., 1999). At T = 800 °C, H-isotope fractionation between biotite and water is low ($1000\ln\alpha_{Bt\text{-}w}$ = -21.29‰; Suzuoki and Epstein, 1976) and F=0.39 is necessary to lower the bulk $\delta$D by 20‰. Instead, the matrix of the spherulitic domains crystallized during the late stage of cooling of the vein, and has possibly crossed the glass transition and undergone devitrification (Di Toro and Pennacchioni, 2004). At low temperature, the hydrogen fractionation between water and biotite is larger (e.g., at 600 °C, $1000\ln\alpha_{Bt\text{-}w}$ = -30.74 ‰, at 400°C $1000\ln\alpha_{Bt\text{-}w}$ = -49.80 ‰) (Suzuoki and Epstein, 1976), and F= 0.52 and F=0.66 are required at 600 and 400°C respectively. In both spherulitic and microlitic domains crystallization of biotite should be accompanied by an important loss of water to be effective in lowering the bulk $\delta$D of the pseudotachylytes.

### *4.9.3 Implications for the fluid circulation in seismic fault zones*

The hydrogen isotope composition of mylonites suggests that no ingression of fluids with a different isotopic composition from that of the magmatic biotite was associated with the ductile phase of deformation. As suggested by studies in other fault zones (e.g., Kerrich et al., 1984), in the Gole Larghe Fault Zone the ingression of external fluids could be associated with the development of a brittle fault system, in this case a network of interconnected cataclasites. However, the involvement of hydrous fluids having different in composition from those typical of late-magmatic systems during seismic faulting and frictional melting is difficult to assess, because of the complex mineral composition of the pseudotachylyte matrix, which apparently has an hygroscopic behavior. If the contribution of the adsorbed water is subtracted from the measured bulk hydrogen isotope compositions of pseudotachylytes, the $\delta$D value of pseudotachylytes can be the result of (i) coseismic heating and decomposition of the hydrogen-bearing minerals in the wall rocks close to the slipping zone, as reproduced in experiments or (ii) the growth of sub-micrometric biotite in the pseudotachylyte matrix. Both mechanisms are likely to be effective in lowering the hydrogen isotope composition of the natural pseudotachylytes without implying an ingression of an external fluid.

## 4.10 Conclusions

At the scale of the fault zone, the formation of a brittle fault network in the GLFZ was associated with the ingression of an external fluid, which has similar hydrogen isotope composition over distances of 10 km along the fault. In contrast, the hydrous fluids involved in mylonitic deformation were derived exclusively from the biotite in tonalite.

Microstructural, geochemical and hydrogen isotope analysis were conducted on artificial friction melts produced in high velocity rock sliding experiments performed on tonalite and cataclasites of the GLFZ. These data suggest that, in presence of a continuous reservoir of hydrous minerals bordering the sliding surfaces in cataclasites, the process of friction melting itself produces a relative enrichment of H (i.e., a more negative $\delta$D) in the melt if compared with the source cataclasite.

The hydrothermal cementation by epidote and chlorite within the cataclasites of the GLFZ might have had the effect to facilitate friction melting and to furnish a reservoir of water for successive frictional melting. However, the hydrogen isotope composition of natural pseudotachylytes is the result of the combination of different processes affecting the frictional melts during and after their formation: (i) primary fractionation during melting due to partial melting/degassing of cataclasite in the wall rocks, as measured in the artificial pseudotachylytes; (ii) the effect of crystallization of biotite during melt cooling and devitrification (lasting minutes to days after melt formation); (iii) the effect of adsorbed, loosely bonded molecular water, likely associated with present day hydration by rainfall or glacial water. All these processes have the effect of lowering the $\delta$D value of pseudotachylytes, thus it was not possible to identify an influx of an external fluid during the pseudotachylyte formation.

# Bibliography


Abercrombie, R., McGarr, A., Kanamori, H., Di Toro, G., 2006. Earthquakes: Radiated Energy and the Physics of Faulting. American Geophysical Union, Washington, D.C. Geophysical Monograph Series, 170 pp.

Abe, S., Mair, K., 2009. Effects of gouge fragment shape on fault friction: New 3D modelling results. Geophysical Research Letters 36, L23302, doi:10.1029/2009GL040684, 2009

Allen, A. R., 1979. Mechanism of frictional fusion in fault zones. Journal of Structural Geology 1, 231-243.

Allen, J.,L., 2005. A multi-kilometer pseudotachylyte system as an exhumed record of earthquake rupture geometry at hypocentral depths (Colorado, USA). Tectonophysics 402, 37 – 54.

Amitrano, D., Schmittbuhl, J., 2002. Fracture roughness and gouge distribution of a granite shear band. Journal of Geophysical Research 107(B12), 2375-2391, doi:10.1029/2002JB001761.

An, L-J., Sammis, C.G., 1994. Particle size distribution of cataclastic fault materials from southern California. Pure and Applied Geophysics 143, 203-227.

Bakun, W. H., Aagard, B., Dost, B., Ellsworth, W. L., Hardebeck, J. L., Harris, R. A., Ji, C., Johnston, M. J. S., Langbein, J., Lienkaemper, J. J., Michael, A. J., Murray, J. R., Nadeau, R. M., Reasenberg, P. A., Reichle, M. S., Roeloffs, E. A., Shakal, A., Simpson, R. W., Waldhauser, F., 2005. Implications for prediction and hazard assessment from the 2004 Parkfield earthquake. Nature 437, 969-974, doi:10.1038/nature04067.

Balsamo, F., Storti, F., 2011. Size-dependent comminution, tectonic mixing, and sealing behavior of a “structurally oversimplified” fault zone in poorly lithified sands: Evidence for a coseismic rupture? Geological Society of America Bulletin 123, 601-619.

Beeler, N. M., Tullis, T. E., Blanpied, M. L., Weeks, J. D., 1996. Frictional behavior of large displacement experimental faults. Journal of Geophysical Research 101(B4), 8697-8715.

Bestmann, M., Pennacchioni, G., Nielsen, S., Göken, M., de Wall, H., 2012. Deformation and ultrafine dynamic recrystallization of quartz in pseudotachylyte-bearing brittle faults: A matter of a few seconds. Journal of Structural Geology, in press.

Biegel, R.L., Sammis, C.G., Dieterich, J.H., 1989. The frictional properties of a simulated gouge having a fractal particle distribution, Journal of Structural Geology, 11, 827-846, 1989.

Billi, A., 2005. Grain size distribution and thickness of breccia and gouge zones from thin (<1 m) strike-slip fault cores in limestone. Journal of Structural Geology 27, 1823–1837

Bistacchi, A., Griffith, W. A., Smith, S. A. F., Di Toro, G., Jones, R., Nielsen, S., 2011. Fault Roughness at Seismogenic Depths from LIDAR and Photogrammetric Analysis. Pure and Applied Geophysics 168, 2345-2363, doi: 10.1007/s00024-011-0301-7.

Blanpied, M. L., Lockner, D. A., Byerlee, J. D., 1992a. An earthquake mechanism based on rapid sealing of faults. Nature 358, 574-576.

Blanpied, M. L., Lockner, D. A., Byerlee, J. D., 1992b. Fault stability inferred from granite sliding experiments at hydrothermal conditions. Geophysical Research Letters 18, 609-612.

Blenkinsop, T. G., 1991. Cataclasis and processes of particle size reduction. Pure and Applied Geophysics 136(1), 59-86.

Blenkinsop, T. G., Sibson, R. H., 1992. Aseismic Fracturing and Cataclasis Involving Reaction Softening Within Core Material From the Cajon Pass Drill Hole. Journal of Geophysical Research 97(B4), 5135-5144, doi:10.1029/90JB02285.

Boness, N., Zoback, M. D., 2006. A multi-scale study of the mechanisms controlling shear velocity anisotropy in the San Andreas Fault Observatory at Depth, Geophysics, 71(5), F131-F146, doi:10.1190/1.2231107.

Bos, B., Spiers, C. J., 2002. Frictional-viscous flow of phyllosilicate-bearing fault rock: microphysical model and implications for crustal srength profiles. Journal of Geophysical Research 107, 1 – 13.

Boullier, A. M., 2011. Fault zone geology: lessons from drilling through the Nojima and Chelungpu faults. Geological Society, London, Special Publications 2011 359, 17-37.

Boullier, A. M., Fujimoto, K., Ito, H., Ohtani, T., Keulen, N., Fabbri, O., Amitrano, D., Dubois, M., Pezard, P., 2004. Structural evolution of the Nojima fault (Awaji Island, Japan) revisited from the GSJ drill hole at Hirabayashi. Earth Planets Space 56, 1233-1240.

Boullier, A. M., Ohtani, K., Fujimoto, K., Ito, H., Dubois, M., 2001. Fluid inclusions in pseudotachylytes from the Nojima Fault. Journal of Geophysical Research 106(B10), 21965-21977, doi:10.1029/2000JB000043.

Bradbury, K. K., Barton, D.C., Solum, J.G., Draper, S.D., Evans J.P., 2007. Mineralogic and textural analyses of drill cuttings from the San Andreas Fault Observatory at Depth (SAFOD) boreholes: Initial interpretations of fault zone composition and constraints on geologic models. Geosphere, 3, 299–318, doi:10.1130/GES00076.1.

Bradbury, K. K., Evans, J. P., Chester, J. S., Chester, F. M., Kirschner, D. L., 2011. Lithology and internal structure of the San Andreas fault at depth based on characterization of Phase 3 whole-rock core in the San Andreas Fault Observatory at Depth (SAFOD) borehole. Earth and Planetary Science Letters 310, 131 – 144.

Brantut, N., Schubnel, A., Rouzaud, J. N., Brunet, F., Shimamoto, T., 2008. High-velocity frictional properties of a clay-bearing fault gouge and implications for earthquake mechanics. Journal of Geophysical Research 113(B10), B10401.

Brenguier, F., Campillo, M., Hadziioannou, C., Shapiro, N. M., Nadeau, R. M., Larose, E., 2008. Postseismic Relaxation Along the San Andreas Fault at Parkfield from Continuous Seismological Observations. Science 321, 1478-1481.

Brune, J. N., Henyey, T. L., Roy, R. F., 1969. Heat flow, stress, and rate of slip along the San Andreas Fault, California. Journal of Geophysical Research 74, 3821-3827.

Byerlee, J. D., 1993. Model for episodic flow of high pressure water in fault zones before earthquakes: Geology 21, 303-306.

Byerlee, J.D., 1990. Friction, overpressure and fault normal compression. Geophysical Research Letters 17, 2109- 2112.

Carpenter, B. M., Marone, C., Saffer, D. M., 2011. Weakness of the San Andreas Fault revealed by samples from the active fault zone. Nature Geosciences 4, 251-254

Chéry, J., Zoback, M. D., Hickman, S., 2004. A mechanical model of the San Andreas fault and SAFOD Pilot Hole stress measurements. Geophysical Research Letters 31, L15S31, doi:10.1029/2004GL019521.

Chiarabba, C., De Gori, P., Boschi, E., 2009. Pore-pressure migration along a normal-fault system resolved by time-repeated seismic tomography. Geology 38, 1015-1018.

Collettini, C., Viti, C., Smith, S. A. F., Holdsworth, R. E., 2009a. The development of interconnected talc networks and weakening of continental low-angle normal faults. Geology 37(6), 567-570.

Collettini, C., Niemeijer, A., Viti, C., Marone, C., 2009b. Fault zone fabric and fault weakness. Nature 462, 907-910.

Cowan, D. S., 1999. Do faults preserve a record of seismic slip? A field geologist's opinion. Journal of Structural Geology 21, 995-1001.

De Hoog, J. C. M., Taylor, B. E., Van Bergen, M. J., 2009. Hydrogen-isotope systematics in degassing basaltic magma and application to Indonesian arc basalts. Chemical Geology 266, 256-266.

Del Gaudio, P., Di Toro, G., Han, R., Hirose, T., Nielsen, S., Shimamoto, T., Cavallo, A., 2009. Frictional melting of peridotite and seismic slip. Journal of Geophysical Research 114(B6), B06306, doi:1029/2008JB005990.

Del Moro, A., Pardini, G., Quercioli, C., Villa, I. M., Callegari, E., 1983. Rb/Sr and K/Ar chronology of Adamello granitoids, southern Alps. Memorie della Società Geologica Italiana 26, 285-299.

Dempsey, E. D., Holdsworth, B. E., Di Toro, G., 2011. The role of reactivation and fluid pressure cycling in the development of late zeolite-bearing faults and fractures from the Adamello batholith, Italy. Eos, Transactions American Geophysical Union T31C-2361.

Di Toro, G., Han, R., Hirose, T., De Paola, N., Nielsen, S., Mizoguchi, K., Ferri, F., Cocco, M., Shimamoto, T., 2011. Fault lubrication during earthquakes. Nature 471, 494-498.

Di Toro, G., Hirose, T., Nielsen, S., Pennacchioni, G., Shimamoto, T., 2006a. Natural and experimental evidence of melt lubrication of faults during earthquakes. Science 311, 647-649.

Di Toro, G., Hirose, T., Nielsen, S., Shimamoto, T., 2006b. Relating high-velocity rock-friction experiments to coseismic slip in the presence of melts, in: Abercrombie R., McGarr, A., Kanamori, H., Di Toro, G., Editors, Earthquakes. Radiated Energy and the Physics of Faulting. American Geophysical Union, Washington, D.C., 121-134.

Di Toro, G., Pennacchioni, G., 2004. Superheated friction-induced melts in zoned pseudotachylytes within the Adamello tonalites (Italian Southern Alps). Journal of Structural Geology 26, 1783-1801.

Di Toro, G., Pennacchioni, G., 2005. Fault plane processes and mesoscopic structure of a strong-type seismogenic fault in tonalites (Adamello batholith, Southern Alps). Tectonophysics 402, 55-80.

Di Toro, G., Pennacchioni, G., Nielsen, S., 2009. Pseudotachylytes and earthquake source mechanics, in: Fukuyama, Eiichi, Editors, Fault-Zone Properties and Earthquake Rupture Dynamics. International Geophysics Series, Elsevier.

Dreger, D., Nadeau, R. M., Chung, A., 2007. Repeating earthquake finite source models: Strong asperities revealed on the San Andreas Fault. Geophysical Research Letters 34, L23302, doi:10.1029/2007GL031353.

Etheridge, M. A., Wall, V. J., Cox, S. F., Vernon, R. H., 1984. High fluid pressure during regional metamorphism and deformation: inplications for mass transport and deformation mechanisms. Journal of Geophysical Research 89, 4344-4358.

Evans, J. P., 1988. Deformation mechanisms in granitic rocks at shallow crustal levels. Journal of Structural Geology 10, 437-443.

Fabbri, O., Lin, A. M., Tokushigé, H., 2000. Coeval formation of cataclasite and pseudotachylyte in a Miocene forearc granodiorite, southern Kyushu, Japan. Journal of Structural Geology 22, 1015-1025.

Fagereng , A, Sibson, R. H., 2010. Mélange rheology and seismic style. Geology 38, 751 – 754.

Fagereng, A., Remitti, F., Sibson, R. H., 2010. Shear veins observed within anisotropic fabric at high angles to the maximum compressive stress. Nature Geoscience 3, 482-485.

Faulkner, D. R., Rutter, E. H., 2001. Can the maintenance of overpressured fluids in large strike-slip fault zones explain their apparent weakness? Geology 29, 503-506.

Feeley, T.C., Sharp, Z.D., 1996. Geochemical and hydrogen isotopic evidence for in situ dehydrogenation of biotite in silicic magma chambers. Geology 24,1021-1024.

Ferrill, D. A., Morris, A. P., Evans, M. A., Burkhard, M., Groshong, R. H., Onasch, C. M., 2004. Calcite twin morphology: a low temperature deformation geothermometer. Journal of Structural Geology 26, 1521-1529.

Gilbert, G. K., 1909. Earthquake forecast. Science XXIX, 121-138.

Gomberg, J., Reasenberg, P. A., Bodin, P., Harris, R. A., 2001. Earthquake triggering by seismic waves following the Landers and Hector Mine earthquakes. Nature 411, 462–-466.

Graham, C. M., Sheppard, S. M. F., Heaton, T. H. E., 1980. Experimental hydrogen isotope studies - I. Systematics of hydrogen isotope fractionation in the systems epidote-H2O, zoisite-H2O and AlO(OH)-H2O. Geochimica et Cosmochimica Acta 44, 353-364.

Graham, C. M., Viglino G. A., Harmon, R. S., 1987. Experimental study of hydrogen isotope exchange between aluminous chlorite and water and of diffusion in chlorite. American Mineralogist 72, 566-579.

Grant, J. A., 1986. The isocon diagram-a simple solution to Gresens' equation for metasomatic alteration. Economic Geology 81, 1976-1982.

Grant, J. A., 2005. Isocon analysis: A brief review of the method and applications. Physics and Chemistry of the Earth, Parts A/B/C 30, 997-1004, doi:10.1016/j.pce.2004.11.003.

Gratier, J-P., Guiguet R., Renard F., Jenatton L., Bernard D. 2009. A pressure solution creep law for quartz from indentation experiments. Journal of Geophysical Research, 114, B03403, doi:10.1029/2008JB005652.

Gratier, J. P., Favreau, P., Renard, F., 2003. Modeling frluid transfer along California Faults when integrating pressure solution crack sealing and compaction processes. Journal of Geophysical Research 108(B2), 2104.

Gratier, J. P., Favreau, P., Renard, F., Pili, E., 2002. Fluid pressure evolution during the earthquake cycle controlled by fluid flow and pressure solution crack sealing. Earth Planets and Space 54, 1139-1146.

Gratier, J. P., Richard, J., Renard, F., Mittempergher, S., Doan, M. L., Di Toro, G., Hadizadeh, J., Boullier, A. M., 2011. Pressure solution creep as a mechanism of aseismic sliding in active faults: evidence from the San Andreas Fault Observatory at Depth (SAFOD). Geology 39, 1131-1134.

Griffith, A., Nielsen, S., Di Toro, G., Smith, F. A. S., 2010. Rough Faults, Distributed Weakening, and Off-Fault Deformation. Journal of Geophysical Research 115(B08409), 1-22, doi:10.1029/2009JB006925.

Griffith, W. A., Di Toro, G., Pennacchioni, G., Pollard, D. D., 2008. Thin pseudotachylytes in Faults of the Mt. Abbot Quadrangle, Sierra Nevada: physical constraints for small seismic slip events. Journal of Structural Geology 30, 1086-1094, doi:10.1016/jsg.2008.05.003.

Handy, M. R., Hirth, G., Hovious, N., Editors, 2007. Tectonic faults: Agents of change in a dynamic Earth, Report of the 95th Dahlem Workshop on the Dynamics of Fault Zones, Berlin, January 16-21, 2005, MIT Press.

Hazzard, J. F., Mair, K., 2003. The importance of the third dimension in granular shear, Geophyical Research Letters, 30(13), 1708, doi:10.1029/2003GL017534.

Heilbronner, R., Keulen, N., 2006. Grain size and grain shape analysis of fault rocks. Journal of Structural Geology 427, 199-216.

Hickman, S. H., Zoback M. D., 2004. Stress orientation and magnitudes in the SAFOD Pilot hole, Geophysical Research Letters 31(L15S12), doi:10.1029/2004GL020043.

Hickman, S., Sibson, R., Bruhn, R., 1995. Introduction to special section: meachanical involvement of fluids in faulting. Journal of Geophysical Reseach 100(B7), 12831-12840.

Hickman, S., Zoback, M., Ellsworth, W., 2004. Introduction to special section: Preparing for the San Andreas Fault Observatory at depth. Geophysical ResearchLetters 31, L12S01.

Hirose, T., Shimamoto, T., 2005. Growth of molten zone as a mechanism of slip weakening of simulated faults in gabbro during frictional melting. Joural Geophysical Research 110(B05202), doi:10.1029/2004JB003207.

Holdsworth, R. E., van Diggelen, E. W. E., Spiers, C. J., de Bresser, J. H. P., Walker, R. J., Bowen, L., 2011. Fault rocks from the SAFOD core samples: Implications for weakening at shallow depths along the San Andreas Fault, California. Journal of Structural Geology 33(2), 132-144.

Hubbert, M. K., Rubey, W. W., 1959. Role of fluid pressure in mechanics of overthrusting faulting. Geological Society of America Bulletin 70, 115-205.

Imanishi, K., Ellsworth, W. L., 2006. Source scaling relationships of microearthquakes at Parkfield, CA, determined using the SAFOD pilot hole seismic array, in Eartyhquakes: Radiated energy and the physics of earthquake faulting. Geophysical Monograph Series 170, edited by R. Abercrombie et al., 81-90, AGU, Washington, D.C.

Janecke, S.U., Evans J.P., 1988. Feldspar-influenced rock rheologies. Geology 16, 1064-1067, doi:10.1130/0091-7613(1988)016\1064:FIRR[2.3.CO;2

Janssen, C., Wirth, R., Reinickke, A., Rybacki, E., Naumann, R., Wenk, H. R., Dresen, G., 2011. Nanoscale porosity in SAFOD core samples (San Andreas Fault). Earth and Planetary Science Letters 301, 179 – 189.

Janssen, C., Wirth, R., Rybacki, E., Naumann, R., Kemmnitz, H., Wenk, H.-R., Dresen, G., 2010. Amorphous material in SAFOD core samples (San Andreas Fault): evidence for crush-origin pseudotachylytes? Geophysical Research Letters 37. doi:10.2029/GL040993.

Jefferies, S. P., Holdsworth, R. E., Shimamoto, T., Takagi, H., Lloyd, G. E., Spiers, C. J., 2006. Origin and mechanical significance of foliated cataclastic rocks in the cores of crustal-scale faults: Examples from the Median Tectonic Line, Japan. Journal of Geophysical Research: Solid Earth 111(B12303).

Jeffreys, H., 1942. On the mechanics of faulting. Geological Magazine 79, 291-295.

Jeppson, T.N., Bradbury, K.K., Evans, J.P., 2010. Geophysical properties within the San Andreas Fault Zone at the San Andreas Fault Observatory at Depth and their relationships to rock properties and fault zone structure. Journal of Geophysical Research 115, B12423.

Johanson, I.A., Fielding, E.J., Rolandone, F., Burgmann, R., 2006. Coseismic and Postseismic Slip of the 2004 Parkfield Earthquake from Space-Geodetic Data. Bulletin of the Seismological Society of America 96, S269–S282.

Johnson, P. A., Mc Evilly, T. V., 1995. Parkfield seismicity: fluid driven?. Journal of Geophysical Research 100(B7), 12937-12950.

Johnson, P. A., Xiaoping, J., 2005. Nonlinear dynamics, granular media and dynamic earthquake triggering. Nature 437, 871-874.

Jordan, T.H., Chen, Y-T., Gasparini, P., Madariaga, R., Main, I., Marzocchi, W., Papadopoulos, G., Sobolev, G., Yamaoka, K., Zschau, J., 2011. Operational earthquake forecasting. Annals of Geophysics 54, 315-391.

Kanamori, H., Brodsky, E. E., 2004. The physics of earthquakes. Reports on Progress in Physics 67(8), 1429-1496.

Kennedy, B. M., Kharaka, Y. K., Evans, W. C., Ellwood, A., DePaolo, D. J., Thordsen, J., Ambats, G., Mariner, R. H., 1997. Mantle fluids in the San Andreas fault system, California. Science 278, 1278-1281.

Kerrich, R., La Tour, T. E., Willmore, L., 1984. Fluid participation in deep fault zones: Evidence from geological, geochemical and 18O/16O relations. Journal of Geophysical Research 89, 4331-4343.

Keulen, N., Heilbronner, R., Stünitz, H., Boullier, A. M., Ito, H., 2007. Grain size distributions of fault rocks: A comparison between experimentally and naturally deformed granitoids. Journal of Structural Geology 29, 1282-1300.

Kirkpatrick, J. D., Shipton, Z. K., 2009. Geologic evidence for multiple slip weakening mechanisms during seismic slip in crystalline rock. Journal of Geophysical Research 114(B12401), doi:10.1029/2008JB006037.

Lachenbruch A. H., Sass, J., 1980. Heat flow and energetics of the San Andreas fault zone. Journal of Geophysical Research 85, 6185-6222.

Lachenbruch, A. H., 1980. Frictional heating, fluid pressure, and the resistance to fault motion. Journal of Geophysical Research 85, 6097-6112.

Langford, J. I., Wilson, A. J. C., 1978. Scherrer after Sixty Years: A Survey and Some New Results in the Determination of Crystallite Size, Journal of Applied Crystallography 11, 102-113.

Lesher, C. E., Cashman, K. V., Mayfield, J. D., 1999. Kinetic controls on crystallization of Tertiary North Atlantic basalt and implications for the emplacement and cooling history of lava at Site 989, Southeast Greenland rifted margin. In: Larsen, H. C., Duncan, R. A., Allan, J. F., Brooks, K., Editors. Proceeding of the ODP. Scientific Results 163, College Station, Texas (Ocean Drilling Program), 3-16.

Lin, A., 1994. Glassy pseudotachylytes from the Fuyun Fault Zone, Northwest China. Journal of Structural Geology 16, 71-83.

Lin, A., 2007. Fossil earthquakes: The formation and preservation of pseudotachylytes, Lecture Notes in Earth Sciences 111, Springer.

Lockner, D. S., Morrow, C., Moore, D. E., Hickman, S., 2011. Low strength of deep San Andreas fault gouge from SAFOD core. Nature 472, 82-85.

Logan, J. M., Dengo, C. A., Higgs, N.G., Wang, Z. Z., 1992. Fabrics of experimental fault zones: their development and relationship to mechanical behavior, in: Evans, B., Wong, T. F., Editors. Fault mechanics and transport properties of rocks, Academic Press.

Longinelli, A., Selmo, E., 2003. Isotopic composition of precipitation in Italy: a first overall map. Journal of Hydrology 270, 75–88.

Maddock, R. H., Grocott, J., Van Nes, M., 1987. Vesicles, amygdales and similar structures in fault-generated pseudotachylytes. Lithos 20, 419-432.

Magloughlin, J. F., 1992. Microstructural and chemical changes associated with cataclasis and frictional melting at shallow crustal levels: the cataclasite-pseudotachylyte connection. Tectonophysics 204, 243-260.

Magloughlin, J. F., 1998. Amygdales within pseudotachylyte. In: Snoke, A. W., Tullis, J., Todd, V. R., Editors. Fault Related Rocks-A Photographic Atlas. Princeton, New Jersey, 88-89.

Mair, K., Abe, S., 2011. Breaking up: Comminution mechanisms in sheared simulated fault gouge. Pure and Applied Geophysics 168(12), 2277- 2288 . doi: 10.1007/s00024-011-0266-6

Mair, K., Frye, K., Marone, C., 2002. Influence of grain characteristics on the friction of granular shear zones. Journal of Geophysical Research 107(B10).

Mandl, G., 1988. Mechanics of tectonic faulting. Models and basic concepts. Developments in Structural Geology. Zwart, H.J., Editor, Elsevier.

Marone, C., Scholz, C. H., 1989. Particle size distribution and microstructures within simulated fault gouge. Journal of Structural Geology 11, 799-814.

Marshall, D. J., 1988. Cathodoluminescence in geological materials. Unwin Hyman, Boston.

McKenzie, D., Brune, J. N., 1972. Melting on Fault Planes During Large Earthquakes. Geophysical Journal of the Royal Astronomical Society 29, 65-78.

Meneghini, F., Marroni, M., Moore, J.C., Pandolfi , L., and Rowe, C.D., 2009, The processes of underthrusting and underplating in the geologic record: Structural diversity between the Franciscan Complex (California), the Kodiak Complex (Alaska) and the Internal Ligurian Units (Italy): Geological Journal, v. 44, p. 126–152, doi: 10.1002/gj.1144.

Miller, S. A., Collettini, C., Chiaraluce, L., Cocco, M., Barchi, M.R., Kaus, B., 2004. Aftershocks driven by a high pressure CO2 source at depth. Nature 427, 724-727.

Miller, S. A., Nur, A., Olgaard, D., 1996. Earthquake as a coupled shear stress-high pore pressure dynamical system. Geophysical Research Letters 23, 197-200.

Mitchell, T. M., Faulkner, D. R., 2009. The nature and origin of off-fault damage surrounding strike-slip fault zones with a wide range of displacements: A field study from the Atacama fault system, northern Chile. Journal of Structural Geology 31, 802-816.

Mittempergher S., Di Toro G., Gratier J.P., Hadizadeh J., Smith S., Spiess R.,2011. Evidence of transient increases of fluid pressure in SAFOD phase III cores. Geophysical Research Letters, vol. 38, L03301, doi:10.1029/2010GL046129

Moecher, D. P., Sharp Z. D., 2004. Stable isotope and chemical systematics of pseudotachylyte and wall rock, Homestake shear zone, Colorado, USA: Meteoric fluid or rock-buffered conditions during coseismic fusion?. Journal of Geophysica Research 109(B12206), doi:10.1029/2004JB003045.

Moore, D. E., Rymer, M. J., 2012. Correlation of clayey gouge in a surface exposure of serpentinite in the San Andreas Fault with gouge from the San Andreas Fault Observatory at Depth (SAFOD). Journal of Structural Geology, in press.

Moore, D., E., Rymer, M. J., 2007. Talc-bearing serpentinite and the creeping section of the San Andreas fault. Nature 448, 795-797, doi:10.1038/nature06064.

Moore, D., Reynolds, R.C., 1997. X-Ray Diffraction and the Identification and Analysis of Clay Minerals. Oxford University Press, New York, 378 pp.

Nadeau, R. M., Johnson, L. R., 1998. Seismological studies at Parkfield VI: Moment release rates and estimates of source parameters for small repeating earthquakes. Bulletin of the Seismological Society of America 88, 790-814.

Nadeau, R. M., Michelini, A., Uhrhammer, R. A., Dolenc, D., McEvilly, T. V., 2004. Detailed kinematics, structure and recurrence of micro-seismicity in the SAFOD target region. Geophysical Research Letters 31(L12S08), doi:10.1029/2003GL019409.

Nestola, F., Mittempergher, S., Di Toro, G., Zorzi, F., Pedron, D., 2010. Evidence of hexagonal anorthite in pseudotachylyte: a tool to constrain the thermal history during a seismic event. American Mineralogist 95, 405-409, doi:10.2138/am.2010.3393.

Nielsen, S., Di Toro, G., Hirose, T., Shimamoto, T., 2008. Frictional melt and seismic slip. Journal of Geophysical Research 113(B01308), doi:10.1029/2007JB005122.

Niemeijer, A. R., Spiers, C. J., 2005. Influence of phyllosilicates on fault strength in the brittle-ductile transition: insights from rock analogue experiments. In Bruhn, D., Burlini, L. (Eds.), High strain zones: Structure and physical properties. Geological Society of London, Special Publications 245, 303 – 327.

Nollet, S., Urai, J. L., Bons, P. D., Hilgers, C., 2005. Numerical simulations of polycrystal growth in veins. Journal of Structural Geology 27, 217-230, doi:10.1016/j.jsg.2004.10.003.

O'Hara, K. D., Sharp, Z. D., 2001. Chemical and oxygen isotope composition of natural and artificial pseudotachylyte: Role of water during frictional fusion. Earth and Planetart Science Letters 184, 393-406.

Passchier, C. W., Trouw, R. A. J., 2005. Microtectonics, Springer, Berlin, 366 pp.

Pennacchioni, G., 2005. Control of the geometry of precursor brittle structures on the type of ++ductile shear zone in the Adamello tonalites, Southern Alps (Italy). Journal of Structural Geology 27, 627-644.

Pennacchioni, G., Di Toro, G., Brack, P., Menegon, L., Villa, I. M., 2006. Brittle-ductile-brittle deformation during cooling of tonalite (Adamello, Southern Italian Alps). Tectonophysics 427, 171-197.

Pili, E., Kennedy, B. M., Conrad, M. E., Gratier, J. P., 2011. Isotopic evidence for the infiltration of mantle and metamorphic fluids from below in faulted rocks from the San Andreas Fault System. Chemical Geology 281(3-4), 242-252.

Pili, E., Poitrasson, F., Gratier, J. P., 2002. Carbon-oxygen isotope and trace element constraints on how fluids percolate faulted limestones from the San Andreas Fault system: partitioning of fluid sources and pathways. Chemical Geology 190(1-4), 231-250.

Pittarello, L., Di Toro, G., Bizzarri, A., Pennacchioni, G., Hadizadeh, J., Cocco, M., 2008. Energy partitioning during seismic slip in pseudotachylyte-bearing faults (Gole Larghe Fault, Adamello, Italy). Earth and Planetary Science Letters 269, 131-139, doi:10.1016/j.epsl.2008.01.052.

Prior, D. J., Trimby, P.W., Weber, U. D., Dingley, D. J., 1996. Orientation contrast imaging of microstructures in rocks using forescatter detectors in the scanning electron microscope. Mineralogical Magazine 60, 859-869.

Ramsay, J.G., 1980. The crack-seal mechanism of rock deformation. Nature 284, 135-139.

Ramsey, J. M., Chester, F. M., 2004. Hybrid fracture and the transition from extension fracture to shear fracture. Nature 428, 63-66, doi://10.1038/nature02333.

Reches, Z., Dewers, T. A., 2005. Gouge formation by dynamic pulverization during earthquake rupture. Earth and Planetary Science Letters 235, 361-374.

Reid, H. F., 1910. The Mechanics of the Earthquake, The California Earthquake of April 18, 1906. Report of the State Investigation Commission Vol. 2. Carnegie Institution of Washington, Washington, D.C.

Renard F., Ortoleva P., Gratier J.-P., 1997. Pressure solution in sandstones: Influence of clays and dependence on temperature and stress. Tectonophysics, 280, 257-266.

Renard, F., Dysthe, D., Feder, J., Bjorlikke, K., Jamtveit, B., 2001. Enhanced pressure solution creep rates induced by clay particles: Experimental evidence in salt aggregates. Geophysical Research Letters 28, 1295 – 1298.

Rice, J. R., 1992. Fault stress states, pore pressure distribution, and the weakness of the San Andreas Fault, in: Fault mechanics and transport properties of rocks, edited by Evans, B., Wong, T. F., 475-503, Academic Press, San Diego, California, USA.

Rice, J. R., 2006. Heating and weakening of faults during earthquake slip. Journal of Geophysical Research 111(B05311), doi:10.1029/2005JB004006.

Rietveld, H. M., 1967. Line profiles of neutron powder-diffraction peaks for structure refinement. Acta Crystallographica 22, 151-152.

Robert, F., Boullier, A. M., Firdaos, K., 1995. Gold-quartz veins in metamorphic terranes and the role of fluids in faulting. Journal of Geophysical Research 100, 12861-12879.

Rust, A. C., Cashman, K. V., Wallace, P. J., 2004. Magma degassing buffered by vapour flow through brecciated conduit margins. Geology 32, 349-352.

SAFOD (2010). The core Atlas (version 4), http://www.earthscope.org/es_doc/data/safod/Core%20Photo%20Atlas%20v4.pdf .

Sammis, C. G., King, G. C. P., 2007. Mechanical origin of power law scaling in fault zone rocks. Geophysical Research Letters 34, L04312.

Sammis, C. G., King, G. C. P., Biegel, R., 1987. The kinematics of gouge deformation. Pure and Applied Geophysics 125, 777-812.

Schleicher, A. M., Tourscher, S. N., Van der Pluijm, B. A., Warr, L. N., 2009. Constraints on mineralization, fluid-rock interaction, and mass transfer during faulting at 2-3 km depth from the SAFOD drill hole, Journal of Geophysical Research 114(B04202), doi:10.1029/2008JB006092.

Scholz, C. H., 2002. The mechanics of earthquakes and faulting. Cambridge Univerity Press, 471 pp.

Shand, S. J., 1916. The pseudotachylyte of Parijs (Orange Free State) and its relation to “trap-shotten gneiss” and “flinty crush rock”. Quarterly Journal of the Geological Society, London 72, 198-221.

Sharp, Z. D., Atudorei, V., Durakiewicz, T., 2001. A rapid method for determination of hydrogen and oxygen isotope ratios from water and hydrous minerals. Chemical Geology 178, 197-210, doi:10.1016/S009-2541(01)00262-5.

Shimamoto, T., Tsutsumi, A., 1994. A new rotary-shear high-speed frictional testing machine: its basic design and scope of research (in Japanese with English abstract). Journal of Tectonic Research Group of Japan 39, 65-78.

Sibson, R. H., 1973. Interactions between temperature and pore fluid pressure during earthquake faulting - a mechanism for partial or total stress relief. Nature 243, 66-68.

Sibson, R. H., 1975. Generation of pseudotachylyte by ancient seismic faulting. Geophysical Journal of the Royal Astronomical Society 43, 775-794.

Sibson, R. H., 1977. Fault rocks and fault mechanisms. Journal of the Geological Society of London 133, 191-213.

Sibson, R. H., 1990. Rupture nucleation on unfavorably oriented faults, Bulletin of the Seismological Society of America 80, 1580-1604.

Sibson, R. H., Toy, V. G., 2006. The habitat of fault generated pseudotachylyte: presence vs. absence of frictional melt, in: Abercrombie, R., McGarr, A., Kanamori, H., Di Toro, G., Editors, Earthquakes: Radiated Energy and the Physics of Faulting. Geophysical Monograph Series 170, AGU, 153-166.

Sibson, R.H., 1985. Stopping of earthquake ruptures at dilational fault jogs. Nature 316, 248 - 251, doi:10.1038/316248a0.

Sibson, R.H., 1987. Earthquake faulting as a mineralizing agent in hydrothermal systems. Geology 15, 701 – 704.

Simpson, D. W., Leith, W. S., Scholz, C. H., 1988. Two types of reservoir induced seismicity. Bulletin of the seismological Society of America 78, 2025-2040.

Skopelitis, A., Bindeman, I. N., Ulianov, A., Brack, P., Schaltegger, U., 2011. Tracing episodic magma accretion by stable and radiogenic isotopes and U-Pb dating in the Adamello batholith, Italy. Abstract V21D-2526 presented at 2011 Fall Meeting, AGU, San Francisco, Calif., 5-9 Dec.

Sleep, N. H., Blanpied, M. L., 1992. Creep, compaction and the weak rheology of major faults. Nature 359, 687-692.

Smith, S. A. F., Collettini, C., Holdsworth, R. E., 2008. Recognising the seismic cycle along ancient faults: CO2-induced fluidization of breccias in the footwall of sealing low-angle normal fault. Journal of Structural Geology 30, 1034-1046.

Solum, J. G., Hickman, S. H., Lockner., D. A., Moore, D. E., Van der Pluijm, B. A., Schleicher, A., Evans, J. P., 2006. Mineralogical characterization of protolith and fault rocks from the SAFOD main hole. Geophysical Research Letters 33(L21314), doi:10.1029/2006GL027285.

Sone, H., Shimamoto, T., 2009. Frictional resistance of faults during accelerating and decelerating earthquake slip. Nature Geoscience, doi:10.1038/NGEO637

Sone, H., Shimamoto, T., Diane, E. Moore Frictional properties of saponite-rich gouge from a serpentinite-bearing fault along the Gokasho-Arashima Tectonic Line, central Japan. Journal of Structural Geology, in press.

Spray, J. G., 1992. A physical basis for the frictional melting of some rock-forming minerals. Tectonophysics 204, 205-21.

Springer, S. D., Evans, J. P., Garver, J. , Kirschner, D., Janecke, S. U., 2009. Arkosic rocks from the San Andreas Observatory at Depth (SAFOD) borehole, central California: Implications for structure and tectonics of the San Andreas Fault zone. Lithosphere 1, 206 – 226

Stein, R., 1999. The role of stress transfer in earthquake occurrence. Nature 402, 605-609.

Stolper, E. M., 1989. Temperature dependence of the speciation of water in rhyolitic melt and glasses. American Mineralogist 74, 1247-1257.

Storti, F., Balsamo, F., Salvini, F., 2007. Particle shape evolution in natural carbonate granular wear material. Terra Nova 19, 344-352.

Storti, F., Billi, A., Salvini, F., 2003. Particle size distribution in natural carbonate fault rocks: Insighets for non-self-similar cataclasis. Earth and Planetary Science Letters 206, 173-186.

Suzuoki, T., Epstein, S, 1976. Hydrogen isotope fractionation between OH-bearing minerals and Water. Geochimica et Cosmochimica Acta 40, 1229-1240.

Taylor, B. E., Eichelberger, J. C., Westrich, H. R., 1983. Hydrogen isotopic evidence of rhyolitic magma degassing during shallow intrusion and eruption. Nature 306, 541-545.

Taylor, H. P. Jr., 1974. The application of oxygen and hydrogen studies to problems of hydrothermal alteration and ore deposition. Economic Geology 69, 843-883.

Taylor, H. P. Jr., 1977. Water/rock interactions and the origin of fluids in granitic batholiths. Journal of the Geological Society, London 133, 509-558.

Taylor, H. P. Jr., 1978. Oxygen and hydrogen isotope studies of plutonic granitic rocks. Earth and Planetary Science Letters 38, 177-210.

Terzaghi, K., 1943. Theoretical Soil Mechanics. John Wiley and Sons, New York.

Thurber, C., Roecker, S., Zhang, H., Baher, S., Ellsworth, W., 2004. Fine-scale structure of the San Andreas fault zone and location of the SAFOD target earthquakes. Geophysical Research Letters 31, L12S02.

Titus, S. J., DeMets, C., Tikoff, B., 2006. Thirty-five-year creep rates for the creeping segment of the San Andreas Fault and the effects of the 2004 Parkfield earthquake: constraints from alignment arrays, continuous global positioning system, and creepmeters, Bulletin of the Seismological Society of America 96(4B), S250-S268, doi:10.1075/0120050811.

Turcotte, D. L., 1997. Fractals and chaos in geology and geophysics. Cambridge University Press, 398 pp.

Vannucchi, P., 2001. Monitoring paleo-fluid pressure through vein microstructures. Journal of Geodynamics 32, 567-581.

Vermilye, J. M., Scholz, C. H., 1998. The process zone: A microstructural view of fault growth. Journal of Geophysical Research - Solid Earth 103, 12223-12227.

Vermilye, J. M., Scholz, C. H., 1999. Fault propagation and segmentation: insight from the microstructural examination of a small fault. Journal of Structural Geology 21, 1623-1636.

Wiersberg, T., Erzinger, J., 2008. Origin and spatial distribution of gas at seismogenic depths of the San Andreas Fault from drill-mud gas analysis. Applied Geochemistry 23, 1675-1690, doi:10.1016/j.apgeochem.2008.01.012.

Zoback, M. D., Harjes H. P., 1997. Injection-induced earthquakes and crustal stress at 9 km depth at the KTB deep drilling site, Germany. Journal of Geophysical Research 02(B8), 18477-18491.

Zoback, M. D., Hickman, S., Ellsworth, W., 2010. Scientific Drilling Into the San Andreas Fault Zone. Eos, Transactions American Geophysical Union 91(22), doi:10.1029/2010EO220001.

# Appendix 1. Curriculum vitae

**PERSONAL DATA**


| | |
|---|---|
| Name | Silvia Mittempergher |
| Date of birth | May 5., 1982 |
| Address | via della Polla 41,<br>38052 Caldonazzo (TN) - Italy. |
| Work address | Dipartimento di Geoscienze – Università degli Studi di Padova<br>Via G. Gradenigo 6<br>35131 Padova – Italy |
| E-mail | silvia.mittempergher@unipd.it, silviamitti@yahoo.it |


**PREVIOUS WORK EXPERIENCES**

February – July 2007
Geological mapping for the Museo Tridentino di Scienze Naturali (Natural Sciences Museum of Trento) and the Geological Survey of Trento.

August 2007 – July 2008
Research scholarship ("*Study of fossil earthquakes in the Adamello Massif*"), scientific directors Prof. Giorgio Pennacchioni and Prof. Giulio Di Toro, Dipartimento di Geoscienze, Università degli Studi di Padova.

June 2008
Graduate assistant, field course in Geological mapping (Bachelor Degree in Geological Sciences, Padova University).

August – December 2008
Research scholarship within the project *"Revealing the secrets of an earthquake: physico-chemical constraints from a multidisciplinary study of exhumed faults"*, supervisor Prof. Giorgio Pennacchioni.

January 2009 – December 2011
PhD student at the Doctorate school in Earth Sciences of the University of Padova and at the Ecole Doctorale Terre Univers Environnement of the University of Grenoble, within a co-tutelle agreement. Thesis *"Physico-chemical processes in seismogenic faults: active and exhumed examples"*, supervisors: Prof. G. Di Toro (University of Padova) and Prof. Jean-Pierre Gratier (Université J. Fourier, Grenoble).

June 2009

Graduate assistant, field course in Geological mapping (Bachelor Degree in Geological Sciences, Padova University).

March – June 2011
Graduate assistant, course "Elementi di geologia" (interpretation of geological maps, Bachelor Degree in Geological Sciences, Padova University)

**EDUCATION**

M.S. Geology, *Università degli Studi di Padova*, received on December 15, 2006
Research Dissertation *"Effects of fluids on the seismicity of a fault. Study of exhumed structures in the Northern Adamello (Southern Alps, Italy)"*, (in English) with points 110/110 cum laude; supervisor Prof. Giorgio Pennacchioni; co-examiner Dr. Giulio Di Toro.
Exchange student (Erasmus program) at the University of Tromsø (Tromsø, Norway) from January 9 to June 10, 2006.
B.S. Geological sciences, *Università degli Studi di Padova,* received on December 15, 2004
Field mapping dissertation "*Geologia della Riserva Corna Piana-Corne di Bes, Trentino*" (in italian), with points 110/110 cum laude.
High school certificate *Liceo Classico "Giovanni Prati"*, Trento, received on July 2001 with points of 100/100 (characterizing subjects: Italian literature, Latin and ancient Greek languages and literatures).

**LANGUAGES**

Italian (mother tongue), English, French, German (elementary).

**ACTIVITIES DURING THE PhD**

**Courses**
"Introduction to MatLab", G. Teza, Geosciences Department, University of Padova
"The role of mineral physics (parts I and II)"; "Elasticity"; "Structural evolution in High Pressure", R.J. Angel (Virginia Tech), held at the Geosciences Department, University of Padova
"Scientific comunication", A. Fioretti, G. Di Toro, G. Artioli, Geosciences Department, University of Padova
"Statistical methods applied to the scientific experimentation", L. Salmaso, Centro Studi per l'Ambiente Alpino - S. Vito di Cadore
"Diffusion in Minerals and Melts", short course of the Mineralogical Society of America, Napa, California.
J. Weiss, "Complexity of geophysical objects". IsTerre, Université J. Fourier, Grenoble
F. Remondino: "Introduction to photogrammetry and laser scanning". Geosciences Department, University of Padova

**Stages in other universities:**
April 2009
Collaboration with Prof. F. Renard, Prof. A.M. Boullier, Pro M:L: Doan, Laboratoire de Géophysique Interne et Tectonophysique, Université J. Fourier, Grenoble, France.
May-June 2009

Collaboration with Prof. J. Hadizadeh, Department of Geography and Prof. Jacek Jasinski, Institute for Advanced Materials and Renewable Energy, University of Louisville, Louisville, KY.
February – August 2010
Research activity at the laboratory Is-Terre, Grenoble, under the supervision of Prof. Jean Pierre Gratier.
March – April 2011
Research activity at the laboratory Is-Terre, Grenoble, under the supervision of Prof. Jean Pierre Gratier.
October 2011.
Research activity at the laboratory Is-Terre, analyses with a FTIR microscope (Fourier Transform Infrared) in collaboration with Prof. Francois Renard and E. Quirico.

**Field work**
1-8 August 2009
Field work in the Adamello area, front of the Lobbia glacier, collection of structural geology data, sampling and differential GPS survey (Collaboration with the USEMS team, INGV, Rome).
25 August – 3 September 2010
Field work in the Adamello area, front of the Lobbia glacier, collection of structural geology data, sampling and differential GPS survey (Collaboration with the USEMS team, INGV, Rome).
16 – 24 August 2011
Field work in the Adamello area, front of the Lobbia glacier (in collaboration with the USEMS research group, INGV, Rome).

**Other activities**
Co – organizer (with F. Ferri, G. Di Toro, G. Pennacchioni) of the workshop "Physico-chemical processes in seismic faults", 18-20 November 2010, Geosciences Department, University of Padova.

Guest editor of Journal of Structural Geology, for the Special Volume "Chemico-physical processes in seismogenic faults", in honor of Prof. T. Shimamoto (two manuscripts edited).

**GRANTS**

August 2007 – July 2008 : Fondazione Cassa di Risparmio di Trento e Rovereto (CARITRO) – Borsa di studio per giovani ricercatori, anno 2007 (Private research scholarship) *Studio di terremoti fossili nel Massiccio dell'Adamello* (Study of fossil earthquakes in the Adamello Massif).
August 2008 – December 2008 : Fondazione Cassa di Risparmio di Padova e Rovigo (CARIPARO) – Research scholarship within the project *"Revealing the secrets of an earthquake: physico-chemical constraints from a multidisciplinary study of exhumed faults"*, supervisor Prof. Giorgio Pennacchioni.
12 – 15 May 2009 : Earthscope National Meeting 2009, travel and expenses support ($850).
8-13 August 2010 : Gordon Research Conference on Rock Deformation, , Tilton, NH, USA, student grant ($540).
February 2010 – August 2010 : Fondazione Ing. Aldo Gini grant 2009 – "Physico-chemical processes in seismogenic faults: active and exhumed examples" (€ 3800).
2010 – 2012 : Vinci grant of the "Università Italo-Francese – Université Franco-Italienne" - *Chapter 2: Travel grant for students in cotutelle between Italian and French universities* (€ 4500).

**TALKS**

Mittempergher S., Di Toro G., Pennacchioni G. - *Effects of fluids on the seismicity of a fault. Study of exhumed structures in the northern Adamello (Southern Alps, Italy).* GIGS, Urbino, 2007.
Mittempergher, S., Dallai L., Di Toro G., Pennacchioni G. - *Origin of fluids in seismic faults from stable isotopes study of pseudotachylytes*. GIGS, Udine, 2009.
Mittempergher, S., Di Toro, G., Gratier, J.P., Hadizadeh, J., Smith, S.A., Desbois, G., Spiess, R. 2009. *Evidences of transient increase of fluid pressure in isolated patches of the active San Andreas Fault in SAFOD phase III cores.* AGU Fall Meeting 2009, San Francisco, USA

**ABSTRACTS AND CONGRESS PRESENTATIONS**

Mittempergher S., Di Toro G., Pennacchioni G. (2007) - *Effects of fault orientation on fault rock assemblages of exhumed seismogenic sources (NW Adamello, Italy).* DRT 2007, Milan.
Mittempergher S., Di Toro G., Pennacchioni G. (2008) - *Effects of fault orientation on the fault rock assemblage of exhumed seismogenic sources (Adamello, Italy).* Fault Zones: Structure, Geomechanics and Fluid Flow, London, Geological Society. (Poster)
Mittempergher S., Dallai L., Di Toro G., Pennacchioni G. (2008) - *Hydrogen isotopes in natural and experimental pseudotachylyte-bearing faults: the origin of fluids at seismogenic depth.* Fault Zones: Structure, Geomechanics and Fluid Flow, London, Geological Society. (Poster)
Mittempergher S., Pennacchioni G., Di Toro G. (2008) - *Effects of fault orientation on fault rock assemblages of exhumed seismogenic sources (NW Adamello, Italy).* EGU Annual Assembly 2008, Vienna.
Mittempergher S., Dallai L., Di Toro G., Pennacchioni G. (2008) - *Hydrogen isotopes in pseudotachylyte-bearing faults of the Adamello batholith, Italy: the origin of fluids at seismogenic depth.* EGU Annual Assembly 2008, Vienna.
Mittempergher S., Pennacchioni G., Di Toro G. (2008) - *Effects of fault orientation on fault rock assemblages of exhumed seismogenic sources (NW Adamello, Italy).* AGU Fall Meeting 2008, San Francisco.
Mittempergher S., Dallai L., Di Toro G., Pennacchioni G. (2008) - *Involvement of pore fluids during frictional melting from hydrogen isotopic investigation of pseudotachylytes.* AGU Fall Meeting 2008, San Francisco.
Mittempergher S., Dallai L., Di Toro G., Pennacchioni G. (2009) - *Origin of fluids in seismic faults from stable isotopes study of pseudotachylytes.* EGU Annual Assembly 2009, Vienna.
Mittempergher S., Di Toro G., Spiess, R. (2009) - *Evidences for multiple episodes of fluid flow in veins of the SAFOD phase 3 cores.* Earthscope National Meeting, Boise 2009, Idaho, USA.
Mittempergher S., Di Toro G., Zorzi F.. (2009) - *Fracturing and sealing in the SAF damage zone: insights from microstructural investigations of a SAFOD phase 3 core sample.* Earthscope National Meeting 2009, Boise, Idaho, USA.
Bistacchi, A., Griffith, W.A., Smith, S., Mittempergher, S, Niemeijer, A., Di Toro, G. 2009. *Roughness of paleoseismic fault surfaces exhumed from seismogenic depth (Gole Larghe Fault, Italian Alps).* AGU Fall Meeting 2009, San Francisco, USA.
Di Toro, G., Griffith, W.A., Nielsen, S., Smith S.A., Niemeijer, A., Bistacchi, A., Mittempergher, S. 2009. *Inferring earthquake mechanics from exhumed faults.* AGU Fall Meeting 2009, San Francisco, USA.
Gratier, J.P., Richard, J., Mittempergher, S., Renard, F., Doan, M., Di Toro, G., Hadizadeh, J, Boullier, A.M. 2009. *Pressure solution as a mechanism of creep and sealing in active faults: evidence from the SAFOD samples.* AGU Fall Meeting 2009, San Francisco, USA.

Hadizadeh, J., Gratier, J.P., Richard, J., Renard, F., Doan, M., Mittempergher, S., Di Toro, G. 2009. *Role of coupled cataclasis-pressure solution deformation in generating microearthquakes in the creeping segment of the SAF: Inferences from studies of the SAFOD core samples*. AGU Fall Meeting 2009, San Francisco, USA.

Nestola F., Mittempergher S., Di Toro G., Zorzi F., Pedron D. 2009. *Evidence of hexagonal anorthite in pseudotachylyte: a tool to constrain the thermal history during a seismic event.* AGU Fall Meeting 2009, San Francisco, USA.

Smith, S., Jones, R., Di Toro, G., Mariano, S., Niemeijer, A., Griffith, W.A., Bistacchi, A., Mittempergher, S., Nielsen, S. 2009. *Quantifying the structure of an exhumed seismogenic fault zone using terrestrial laser-scanning and differential GPS.* AGU Fall Meeting 2009, San Francisco, USA.

Mittempergher S., Di Toro G., Gratier J.P., Hadizadeh J., Smith S., Spiess R., *Evidence of transient increases of fluid pressure in SAFOD phase III cores*. Gordon Research Conference on Rock Deformation 2010, Tilton, NH, USA.

Mittempergher S., Di Toro G., Gratier J.P., Hadizadeh J., Smith S., Spiess R., *Evidence of transient increases of fluid pressure in SAFOD phase III cores.* AGU Fall Meeting 2010, San Francisco, USA.

Hadizadeh J., Gratier J.-P., Mittempergher S., Renard F., Richard J., Di Toro G., Babaie H.A., *Implications of Microstructural Studies of the SAFOD Gouge for the Strength and Deformation Mechanisms in the Creeping Segment of the San Andreas Fault.* AGU Fall Meeting 2010, San Francisco, USA.

Gratier J.P., Richard J., Renard F., Mittempergher S., Doan M.-L-, Di Toro G., Hadizadeh J., Boullier A.-M., *Pressure solution creep as a mechanism of aseismic sliding in active faults: evidence from the San Andreas Fault Observatory at Depth (SAFOD).* AGU Fall Meeting 2010, San Francisco, USA.

Mittempergher S., Di Toro G., Gratier J.P., Hadizadeh J., Smith S., Spiess R., *Evidence of transient increases of fluid pressure in SAFOD phase III cores.* Earthscope National Meeting 2011, Austin, Texas, USA..

Mittempergher S., Di Toro G., Gratier J.P., Boullier, A.M., Aretusini S., *The evolution of fabric with displacement in natural brittle faults.* AGU Fall Meeting 2011, San Francisco, USA.

**PUBLICATIONS**


Eccheli, M., Gennaro, M, Mittempergher, S. (2006) – *Geologia della Riserva Naturale di Corna Piana, Brentonico (Trento)*. Studi Trentini di Scienze Naturali, Acta Geologica, 81(2004), 29-39.

Mittempergher S., Pennacchioni G., Di Toro G. (2009) – *The effects of fault orientation and fluid infiltration on fault rock assemblages at seismogenic depths.* Journal of structural Geology, vol. 31, 1511-1524.

Nestola F., Mittempergher S., Di Toro G., Zorzi F., Pedron D. (2010) - *Evidence of hexagonal anorthite in pseudotachylyte: a tool to constrain the thermal history during a seismic event*. American Mineralogist, 95, 405–409.

Mittempergher S., Di Toro G., Gratier J.P., Hadizadeh J., Smith S., Spiess R. (2011) - *Evidence of transient increases of fluid pressure in SAFOD phase III cores*. Geophysical Research Letters, vol. 38, L03301, doi:10.1029/2010GL046129

Gratier J.P., Richard J., Renard F., Mittempergher S., Doan M.-L-, Di Toro G., Hadizadeh J., Boullier A.-M. (2011) - *Pressure solution creep as a mechanism of aseismic sliding in active faults: evidence from the San Andreas Fault Observatory at Depth (SAFOD).* Geology 39, 1135-1138, DOI: 10.1130/G32073.1.

Di Toro, G., Mittempergher, S., Ferri, F., Mitchell, T., Pennacchioni, G.. *The contribution of structural geology, experimental rock 1 deformation and numerical modelling to an improved understanding of the seismic cycle. Preface to the Special Volume "Physico-chemical processes in seismic faults".* Journal of Structural Geology 38, 3-10.

Hadizadeh, J., Mittempergher, S., Gratier, J.P., Renard, F., Di Toro, G., Richard, J., Babaie, H.A. *A microstructural study of fault rocks from the SAFOD; Implications for the deformation mechanisms and strength of the creeping segment of the San Andreas Fault*. Journal of Structural Geology, accepted.

# Appendix 2. Published papers

In this section, the papers published in peer reviewed journals during the PhD course are reproduced. Here, the contribution of SM to each publication is explained.

***1.*** **Mittempergher, S.**, Pennacchioni G., Di Toro, G., 2009. The effects of fault orientation and fluid infiltration on fault rock assemblages at seismogenic depths. Journal of Structural Geology 31, 1511 – 1524. *This paper is based on the data collected during the master thesis in Geology (2006) by SM. SM did the field and analytical work, participated to the conceptual development of the paper and wrote the text.*

***2.*** Nestola, F., **Mittempergher, S.**, Di Toro, G., Zorzi, F., Pedron, D., 2010. Evidence of hexagonal anorthite in pseudotachylyte: a tool to constrain the thermal history during a seismic event. American Mineralogist 95, 405-409, doi:10.2138/am.2010.3393. *SM contributed to the analytical work (XRD, Raman), to the writing and the general idea development.*

***3.*** **Mittempergher, S.**, Di Toro, G., Gratier, J.P., Hadizadeh, J., Smith, S.A.F., Spiess, R., 2011. Evidence of transient increases of fluid pressure in SAFOD phase III cores. Geophysical Research Letters 38, L03301. *This work was part of this PhD thesis. SM performed the analytical work, wrote the text and participated to the development of the idea.*

**4.** Gratier, J. P., Richard, J., Renard, F., **Mittempergher, S.**, Doan, M. L., Di Toro, G., Hadizadeh, J., Boullier, A. M., 2011. Pressure solution creep as a mechanism of aseismic sliding in active faults: evidence from the San Andreas Fault Observatory at Depth (SAFOD). Geology 39, 1131-1134. *SM participated to the microstructural analysis of the samples and contributed to write the text.*

Journal of Structural Geology 31 (2009) 1511–1524

Contents lists available at ScienceDirect

Journal of Structural Geology

journal homepage: www.elsevier.com/locate/jsg

# The effects of fault orientation and fluid infiltration on fault rock assemblages at seismogenic depths

Silvia Mittempergher [a,*], Giorgio Pennacchioni [a], Giulio Di Toro [a,b]

[a] Dipartimento di Geoscienze, Università di Padova, Via Giotto 1, 35137 Padua, Italy
[b] Istituto Nazionale di Geofisica e Vulcanologia, Via di Vigna Murata 605, 00143 Rome, Italy

ARTICLE INFO

*Article history:*
Received 25 March 2009
Received in revised form
31 August 2009
Accepted 4 September 2009
Available online 12 September 2009

*Keywords:*
Fault mechanics
Pseudotachylyte
Cataclasite
Fault rocks
Fluids
Veining
Earthquakes
Adamello

ABSTRACT

The factors controlling the development of different types of fault rock assemblages and, more specifically, the formation of friction melts are still not fully understood. In this study we compared two exhumed strike–slip faults in the Adamello batholith (Southern Alps): the Gole Larghe and the Passo Cercen fault zones, active at 9–11 km depth and temperatures of 250–300 °C. Each fault zone consists of hundreds of sub-parallel strands exploiting pre-existing joints. The Gole Larghe fault strikes N105 ± 5° and is dextral; the fault rocks are cataclasites and widespread, centimetre-thick pseudotachylytes. The Passo Cercen fault strikes on average N130° and is formed by multiple fault horizons: fault segments striking N105°–N130° are mainly dextral, whereas faults striking N135°–N140° are mainly sinistral. Microstructural, mineralogical and geochemical investigations show that the fault rocks are cataclasites associated with thick epidote + K-feldspar + quartz veins and rare, millimetre-thick pseudotachylytes. Field evidence suggests that in both fault zones, the direction of the maximum horizontal stress $\sigma_1$ was N135°. The Gole Larghe fault strikes at about 30° to $\sigma_1$ and is favourably oriented for reactivation. By contrast, the Passo Cercen fault strikes at low angles to $\sigma_1$ and is unfavourably oriented for reactivation, therefore requiring the development of high pore pressures, as suggested by the occurrence of extensive epidote veining and hydraulic breccias. It is proposed that frictional melting in the Passo Cercen fault zone was inhibited by the development of high pore pressures and low effective normal stresses.



## 1. Introduction

The study of exhumed faults in the field provides complementary information to seismological, geophysical and experimental data for understanding fault plane processes and mechanics during earthquakes (Sibson, 1977; Scholz, 1988; Imber et al., 2001; Abercrombie et al., 2006; Di Toro et al., 2009 for a review). However, few exhumed faults can be proved to have been seismic. At present, only tectonic pseudotachylytes (fault rocks formed by solidified friction-induced melts produced during seismic slip in silicate rocks: Sibson, 1975; Spray, 1995) are unambiguously recognized as the signature of ancient earthquakes in exhumed faults (e.g. Cowan, 1999). Nevertheless, pseudotachylyte occurrences are not as widespread as seismic activity in the Earth crust (Sibson and Toy, 2006; Kirkpatrick et al., 2009). If pseudotachylytes in exhumed seismogenic faults are uncommon, this could be related to the occurrence of thermal pressurization of pore fluids (or other coseismic fault weakening mechanisms such as flash heating, e.g. Rice, 2006) along the fault surfaces which may impede frictional melting (Sibson, 1973; Lachenbruch, 1980; Andrews, 2002; Rice, 2006; Bizzarri and Cocco, 2006).

In this field-based study, the influence of fault orientation and pore fluids on the development of pseudotachylytes is investigated by comparing faults that were active close to the base of the seismogenic crust within the Adamello batholith in the Southern Alps, Italy. In the northern Adamello batholith, pseudotachylyte-bearing faults have already been described in detail along the Gole Larghe fault zone (Di Toro and Pennacchioni, 2004, 2005; Pennacchioni et al., 2006). In the present contribution, the Gole Larghe fault zone is compared with the Passo Cercen fault zone, located few kilometres to the north, where pseudotachylytes are rare and there is evidence of widespread fluid infiltration. We conclude that, in the case of the Passo Cercen fault zone, fault orientation was favourable for fluid infiltration which, in turn: (1) allowed hydraulically induced failure under low normal effective stresses; and (2) impeded the production of abundant pseudotachylytes.

## 2. Geological setting

The Adamello batholith is located within the central Southern Alps (Italy) close to the intersection of two major segments of the

* Corresponding author. Tel.: +39 49 827 1912; fax: +39 49 827 1868.
*E-mail address:* silvia.mittempergher@unipd.it (S. Mittempergher).

0191-8141/$ – see front matter © 2009 Elsevier Ltd. All rights reserved.
doi:10.1016/j.jsg.2009.09.003

Periadriatic Line: the Tonale Line to the north, and the Southern Giudicarie Line to the east (Fig. 1a). The Periadriatic Line separates the south-verging thrusts and folds of the Southern Alps, not affected by Alpine metamorphism, from the north-verging stack of Alpine metamorphic units (e.g. Schmid et al., 1989). The Adamello batholith is the largest Tertiary magmatic body intruded adjacent to the Periadriatic lineament ("Periadratic plutonism", Salomon, 1897). It is a composite pluton consisting of four main intrusions of dominantly tonalitic–granodioritic composition (Bianchi et al., 1970) (Fig. 1a), whose ages progressively young from south-west (Re di Castello: 42–38 Ma) to north-east (Presanella: 32–30 Ma) (Del Moro et al., 1983; Hansmann and Oberli, 1991; Viola, 2000; Viola et al., 2001; Mayer et al., 2003; Stipp et al., 2004). Within each intrusion, the overlap between U–Pb zircon ages and different mineral ages suggests a rapid cooling to the zircon fission track closure temperature (250 ± 50 °C) after emplacement (Pennacchioni et al., 2006). Ambient temperature before emplacement of the Adamello batholith is estimated to be about 250 °C, based on muscovite and biotite Rb/Sr dating of the pre-Permian basement rocks hosting the Adamello pluton, which indicates no or little post-Triassic reheating above 300–350 °C (De Capitani et al., 1994; Martin et al., 1996), on zircon fission track studies, which indicate cooling below 250 ± 50 °C during the Late Cretaceous (Viola et al., 2001) and on the illite crystallinity of Permian sandstones outcropping close to the Adamello pluton, which underwent, at most,

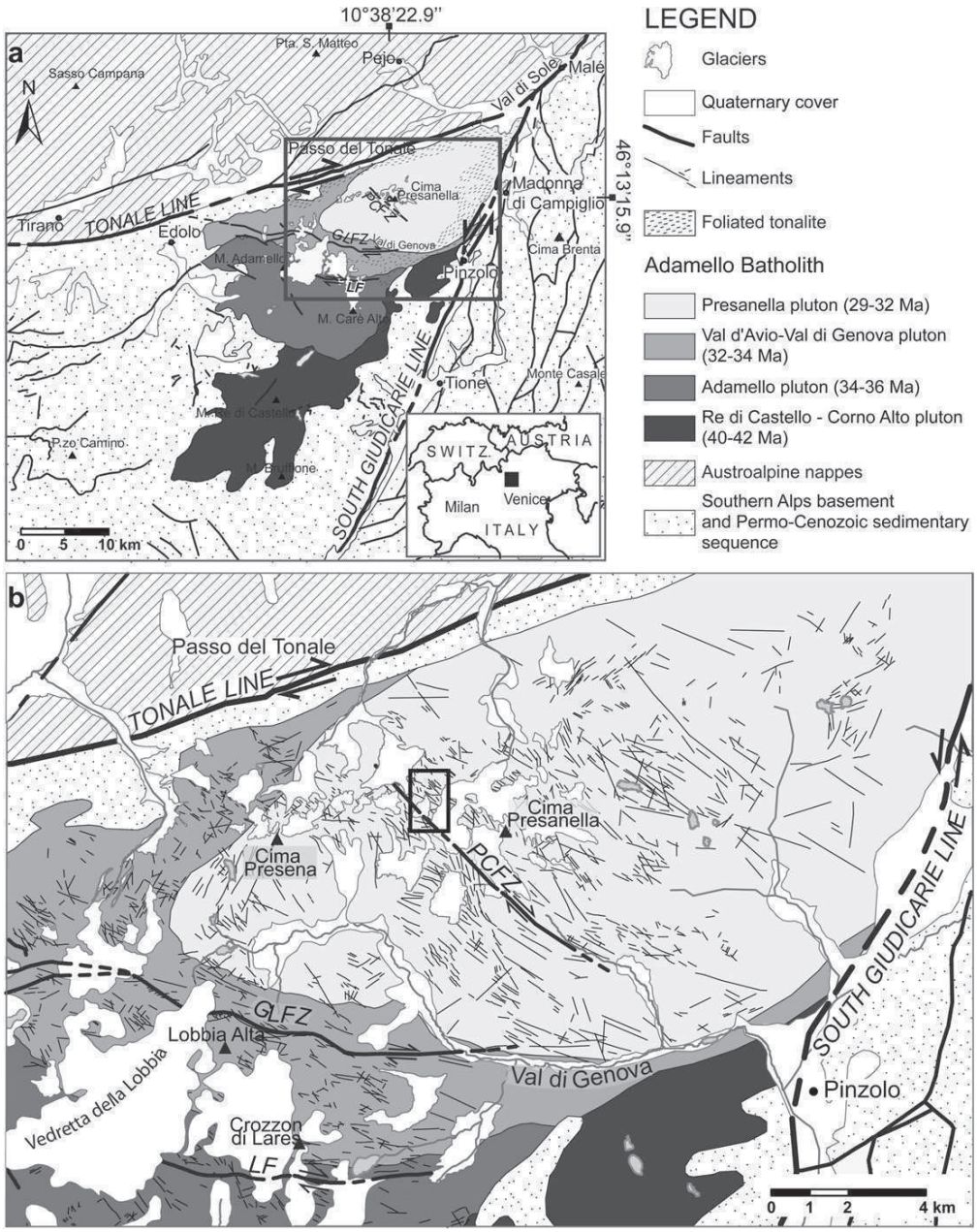


**Fig. 1.** Geological setting. (a) Simplified map of the central Alps and the Adamello batholith; GLFZ: Gole Large fault zone, PCFZ: Passo Cercen fault zone, LF: Lares fault. The rectangle is the area enlarged in Fig. 1b. (b) Schematic structural map, showing the main faults and the lineaments traced from aerial photographs. The wavy geometry of the GLFZ is due to the intersection with the irregular topography of the steeply (70°) dipping towards SSW fault plane. The rectangle is the area enlarged in Fig. 3a.

anchizonal metamorphic conditions (Riklin, 1985; see Pennacchioni et al., 2006 for discussion). Contact metamorphic mineral assemblages suggest pressures of >0.2 GPa in the northern aureole (Werling, 1992; Stipp et al., 2002), and as high as 0.35 GPa in the southern sector (John and Blundy, 1993).

### 2.1. Post-magmatic deformation of the Adamello pluton

Cooling of the Presanella and Avio plutons is believed to have been contemporary with dextral strike–slip motion along the Tonale Line (Stipp et al., 2004); the plutons show widespread solid state post-magmatic ductile and brittle deformation structures. A kilometer-thick belt of early post-magmatic foliated tonalites is developed along the north-eastern rim of the Presanella and Avio plutons and along the contact between the plutons in Val di Genova (Trener, 1906; Bianchi et al., 1970) (Fig. 1a). In the Avio pluton, the tonalite is cut by different sets of joints, intruded by aplitic dykes and decorated by biotite and An-rich plagioclase, suggesting temperatures of formation above or around 600 °C (Pennacchioni et al., 2006). Joints and aplitic dykes were first exploited by ductile amphibolite facies shear zones at $T > 500$ °C, as indicated by the stability of relatively An-rich plagioclase and biotite, the formation of strain-induced myrmekites and the crystallographic preferred orientation of the syn-kinematically recrystallized quartz aggregates (Pennacchioni, 2005). Joints were then exploited by pseudotachylyte- and cataclasite-bearing faults active at temperatures ranging between 250 and 300 °C, as indicated by the presence of chlorite and epidote assemblages (Di Toro and Pennacchioni, 2004). Lastly, zeolite-bearing faults ($T < 200$ °C) cut the previously described deformation structures (Pennacchioni et al., 2006).

The cataclasite–pseudotachylyte horizons are clustered defining some major fault zones, such as the Lares fault zone (LF), the Gole Larghe fault zone (GLFZ) and the Passo Cercen fault zone (PCFZ) (Fig. 1). The GLFZ is an E–W-trending, steeply dipping towards the SSW, dextral strike–slip fault extending from the Tonale Line into the Adamello pluton for about 20 km. In the Lobbia area (upper Val Genova), the GLFZ is about 500 m thick, with a total offset of 1 km distributed over a few hundred, sub-parallel main cataclastic horizons (Di Toro and Pennacchioni, 2005). The average fault dip is 60° towards N195° identical to the orientation of the main joint set outside the fault zone. The cataclasites are green and are enriched in epidote + K-feldspar + chlorite compared to the host tonalite. The same minerals fill millimetre-thick veins, which both pre-date and post-date cataclasites (Di Toro and Pennacchioni, 2004). Abundant pseudotachylytes occur as fault veins parallel to the cataclasite layers and injection veins intruding both the host tonalites and the cataclasites (Di Toro and Pennacchioni, 2004).

The pseudotachylytes of the GLFZ were dated using the stepwise heating $^{39}Ar$–$^{40}Ar$ method (Villa et al., 2000) on bulk pseudotachylytes, obtaining an average age of ca. 30 Ma (Pennacchioni et al., 2006). Fission track data on zircons indicate that exhumation of the Adamello batholith occurred after 22 Ma (Stipp et al., 2004; Viola, 2000). Therefore, seismic faulting occurred before substantial uplift of the pluton, at a depth of 9–11 km, estimated from the metamorphic assemblages preserved in the contact aureole and assuming an average rock density of 2650 kg m$^{-3}$ (Di Toro et al., 2005).

## 3. The Passo Cercen fault zone

### 3.1. Structure of the fault zone

The PCFZ crops out on glacier-polished surfaces exposed NW of the Cima Presanella (3558 m) in the upper Val di Sole (Fig. 1a). The host rock is the Presanella tonalite (Bianchi et al., 1970), characterized by coarse (up to 2 cm long) prismatic hornblende set in a sub-centimetric matrix of plagioclase, quartz, biotite and K-feldspar. The tonalite is cut by pervasive joints with a main joint system (J1) consisting of two sets dipping either 66° to N040° (dominant set) or 56° to N218° (subordinate set) (stereoplot in Fig. 2a). Joints are spaced 0.1–15 m apart and are composed of segments 20–30 m long forming *en echelon* arrays (Fig. 2b). Joints are locally filled with quartz, epidote, K-feldspar and chlorite. A set of closely spaced joints (J2) striking NNE–SSW and steeply dipping towards ESE is discontinuously present within the area.

Cataclasite–pseudotachylyte-bearing faults, which are visible as lineaments striking from NW to WNW in aerial photographs (Fig. 3a), are clustered in the 1 km thick PCFZ. The faults have two main orientations, identical to those of the J1 joints: dipping 69° to N046° or 62° to N223°. The fault zone is formed by surfaces dipping preferentially towards SW, whereas joints outside the fault zone show the opposite, with a preponderance of joints dipping towards NE (Figs. 2a and 3b). In map view, NW-striking faults are formed of interconnected decametric segments, while WNW faults are more continuous (Fig. 3a). Lineations on NW and WNW fault planes plunge gently (about 30°) towards the SE or NW (Fig. 3c). The separation of offset markers such as mafic enclaves and magmatic bands along faults ranges from few centimetres up to 15 m and indicate both dextral and sinistral senses of offset; the switch in the sense of shear of the faults occurs around a strike of N135° (Fig. 3d); the overlapping of the dextral and sinistral faults suggests that the faults were oriented very close to the direction of $\sigma_1$.

Within the PCFZ, individual faults typically consist of a cataclasite layer ranging in thickness from millimetres to several

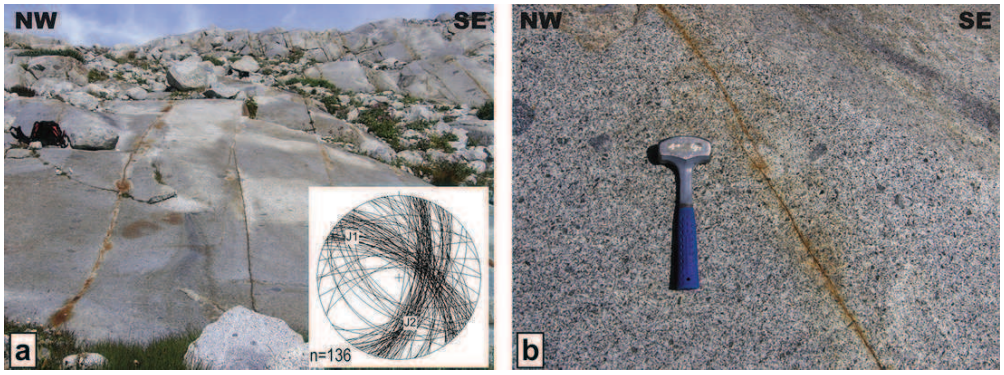


**Fig. 2.** Joints in the Passo Cercen fault zone area. (a) Joints of the main system (J1 in the inserted stereoplot) are formed by continuous and widely spaced segments; lower hemisphere, equal area projection stereoplot. (b) Details of the linkage between two parallel joint strands (J1) organized in an *en echelon* fashion.

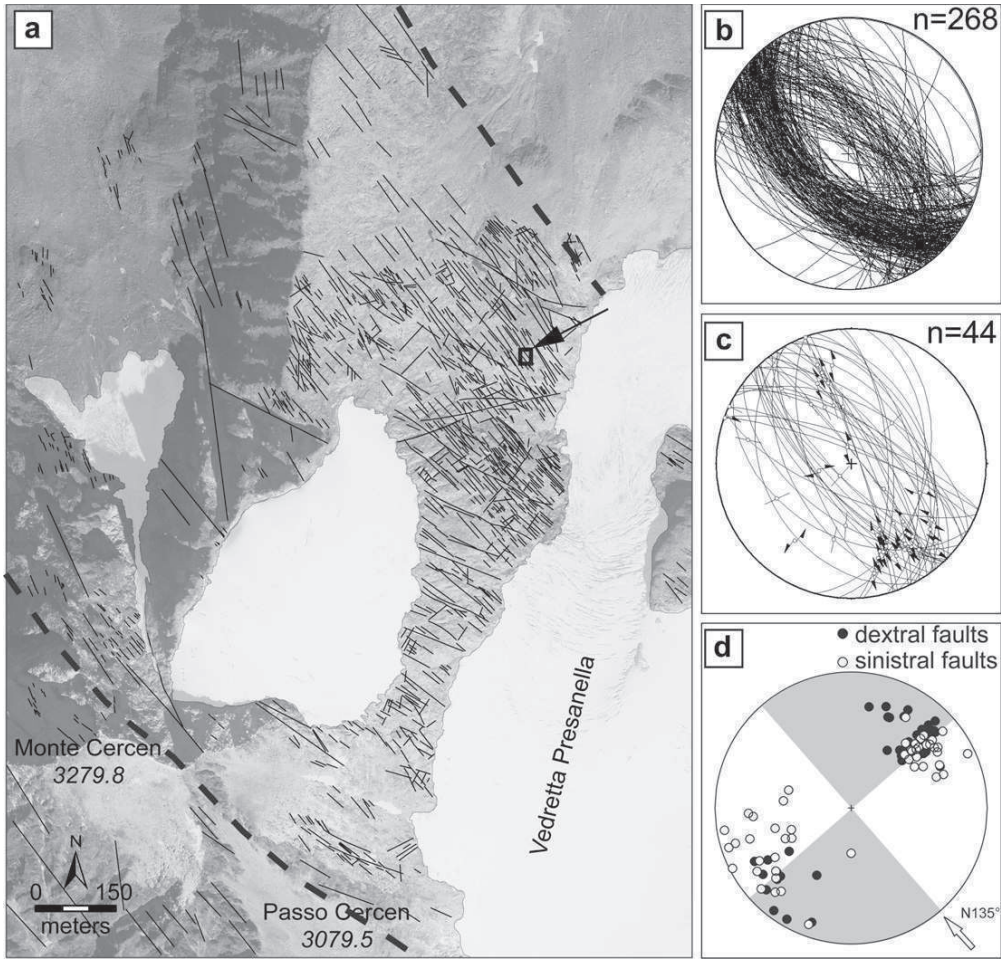


**Fig. 3.** Structural data from the PCFZ. (a) The internal architecture of the PCFZ, reconstructed from high resolution aerial photographs. Dashed lines are the limits of the fault zone. Some WNW-striking faults are outlined by narrow (2–3 m wide) troughs resulting from the intense fracturing and alteration of the fault rock assemblage, formed by the coalescence of multiple fault planes overprinted by late-stage zeolites. The small rectangle indicated by an arrow outlines the area of Fig. 5. (b) Stereoplot of cataclasite–pseudotachylyte-bearing faults (all data). (c) Stereoplot of cataclasite–pseudotachylyte-bearing faults (lineated faults); slickenlines are gently dipping towards SE or SW, with some dip slip planes. (d) Equal area, lower hemisphere cumulative plot of poles to fault planes separated by shear sense; the shaded and white quadrants represent the orientation ranges of faults with respectively sinistral and dextral shear sense. The overall switch in shear sense occurs around N135°.

decimetres. Faults are continuous for a few tens of meters and are spaced less than 1 m to 10–15 m apart (Fig. 4a). Many faults with a spacing of less than few meters are linked by a network of secondary shear and tensional fractures, whereas faults spaced several meters apart consist of sharp isolated structures (Fig. 4b).

A selected outcrop of the fault zone has been mapped at a scale of 1:10 (Fig. 5). In this outcrop, the sense of shear along the faults can be locally determined by the offset of basic enclaves and by the geometry of the secondary fracture network. Sinistral faults mostly strike NW whilst dextral faults strike WNW. In the southern part of the map, a dextral and sinistral fault set intersect each other at an angle of about 30° (Fig. 5a) and thin, discontinuous tensional fractures bisect the dihedral angle between the two faults. Along strike, faults show variations in thickness, due to the linkage between adjacent *en echelon* joint strands (Fig. 5b, see Fig. 2).

### 3.2. Field description of the fault rocks

The fault rocks are predominantly cataclasites, ranging in colour from dark (Fig. 6a) to light-yellowish green (Fig. 6b and c) and rare black pseudotachylytes (Fig. 6b).

Dark green cataclasites are thin (up to a few centimetres), continuous layers of ultracataclasite–cataclasite–protocataclasite (Fig. 6a). Boundaries with the host rock are either sharp, or transitional through a volume of fractured and altered tonalite.

Pseudotachylytes are distinguishable in the field from ultracataclasites on the basis of their black colour and presence of injection veins, even though only microstructural features are indicative of their melt origin. Pseudotachylytes occur as thin (up to 1 cm thick), discontinuous fault veins developed within cataclasite or at the cataclasite–tonalite boundary (Fig. 6b); injection veins are rare and up to a few centimetres long. Pseudotachylytes are mostly spatially associated with dark green cataclasites, but some very thin (<4 mm) pseudotachylyte fault veins have been found in association with light green cataclasites.

Light green cataclasites are more common in the southern part of the studied fault zone section showed in Fig. 3. They are up to 80 cm thick and are associated with pervasive alteration of the adjacent tonalite, as evidenced by its greenish colour (see Section 3.3.2) (Fig. 6c and d). Cataclasites are either homogeneous, fine grained ultracataclasites, or are formed by a breccia of angular tonalite clasts. In this sector, cataclasites are often associated with

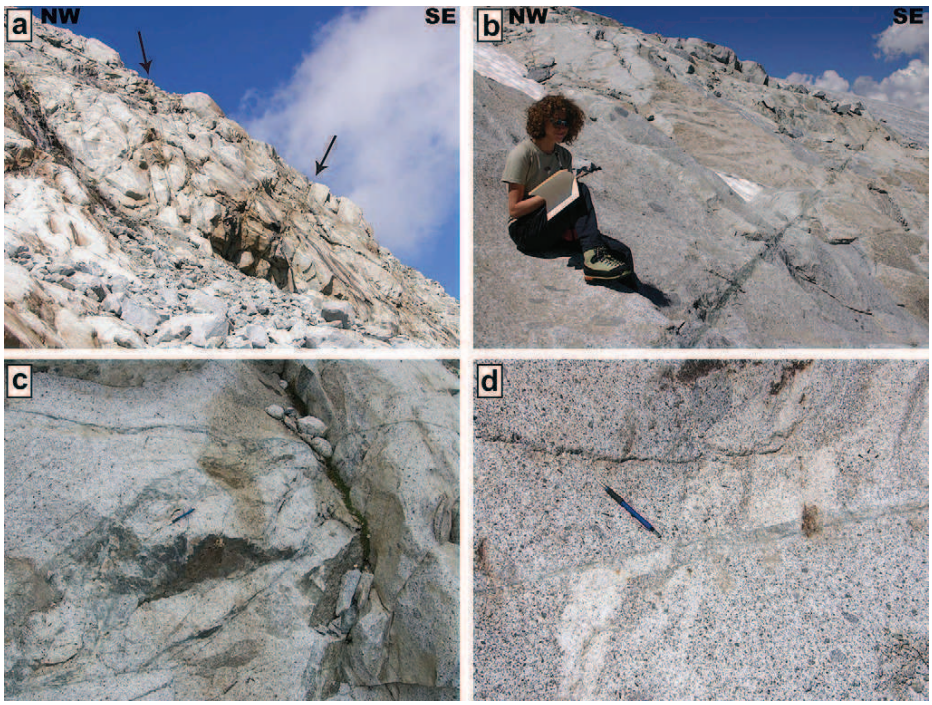


**Fig. 4.** Exposures of the PCFZ. (a) Faults exploit both joints dipping towards NE and SW (arrows). Note the variable spacing between adjacent fault zones. (b) Widely spaced faults are very sharp and continuous along strike. (c) Linkage between parallel fault strands, spaced about 1 m apart, occurs by intense fracturing of the "sandwiched" intervening panel of tonalite. (d) Dextral offset of a leucocratic magmatic band.

green, epidote-bearing veins branching at low angles from the fault planes (Fig. 6d).

### 3.3. Microstructure of the fault zone rocks

#### 3.3.1. Damaged host tonalite

The Presanella tonalite consists of $An_{52-59}$ plagioclase (45.8% in volume), quartz (23.4%), biotite (16%), hornblende (9.1%), K-feldspar (2.1%) and accessory apatite, allanite and titanite (Bianchi et al., 1970). Outside the damage zone, the texture is characterized by centimetre long, prismatic poikilitic hornblende, zoned euhedral plagioclase with Ca-rich nuclei and interstitial quartz and K-feldspar; the contacts between K-feldspars and quartz grains sometimes display myrmekite lobes. The tonalite close to cataclasites is altered and bleached for a few centimetres in thickness. In the altered tonalite: (1) plagioclase is partially replaced by an aggregate of epidote and fine white mica (saussuritization); (2) quartz is fractured and shows local patchy/undulose extinction, deformation lamellae (mostly related to fluid inclusion trails) and very incipient development of fine grained (20–50 μm) new grains; (3) magmatic biotite is kinked and broken down to chlorite and titanite (Fig. 7a), and (4) hornblende is fractured and substituted by actinolite, in particular along fractures and cleavage planes. The tonalite close to faults is commonly foliated due to the development of wavy pressure solution seams, sealed by chlorite, titanite and Ti–Fe oxides, branching at low angles to the fault planes and localized in Riedel fractures. The microstructures and the mineral assemblages described here suggest greenschist facies conditions, which are likely representative of those found close to the brittle–ductile transition.

#### 3.3.2. Cataclastic rocks

Individual faults are associated with the development of protocataclasites, cataclasites and ultracataclasites. Protocataclasites are formed by large polymineralic fragments, slightly rotated and separated by thin cataclasite layers. Cataclasites are matrix-supported rocks, with angular clasts of quartz, plagioclase, K-feldspar and reworked precursor cataclasite (Fig. 7c). In some cases, the cataclasites have a wriggled foliation oriented at a low angle to the fault boundary. Ultracataclasites are thin (up to few millimetres) layers of highly comminuted material with a few rounded clasts. Under the Scanning Electron Microscope (SEM), the outlines of quartz clasts are commonly cuspate–lobate and corroded. The matrix is composed of chlorite, epidote, actinolite, Ti-poor biotite, K-feldspar and albite with textural evidence for static growth (e.g. presence of randomly oriented poikilitic epidote and acicular actinolite, Fig. 7d). In the matrix of some fault horizons, the growth of hydrothermal minerals (usually epidote, in grains of $<100$ micron in size) overprints the cataclasite texture. In such cases, we distinguished cataclasites from veins based on: (i) field evidence (e.g. cataclasite-bearing fractures offset structural markers, see above); and (ii) microstructural evidence (e.g. presence of relict cataclastic texture, such as comminuted grains).

#### 3.3.3. Veins and implosion hydraulic breccias

The veins are filled with epidote, quartz, K-feldspar, albite and chlorite. Crystals in veins are blocky, suggesting that vein opening was faster than mineral growth (Passchier and Trouw, 2005). Quartz, albite and K-feldspar have mostly equidimensional habits, sometimes elongated; epidote crystals are acicular, and are either randomly oriented (Fig. 7e), or arranged perpendicular to the vein margins. Some veins have jigsaw puzzle textures formed by angular clasts of tonalite and cataclasite with little or no internal clast deformation and well-sorted clast size distributions (Fig. 7f). The fragmented clasts are suspended in an exotic hydrothermal cement of epidote, chlorite, K-feldspar, albite and quartz (Fig. 7f). The above microstructures are typical features of implosion hydraulic breccias

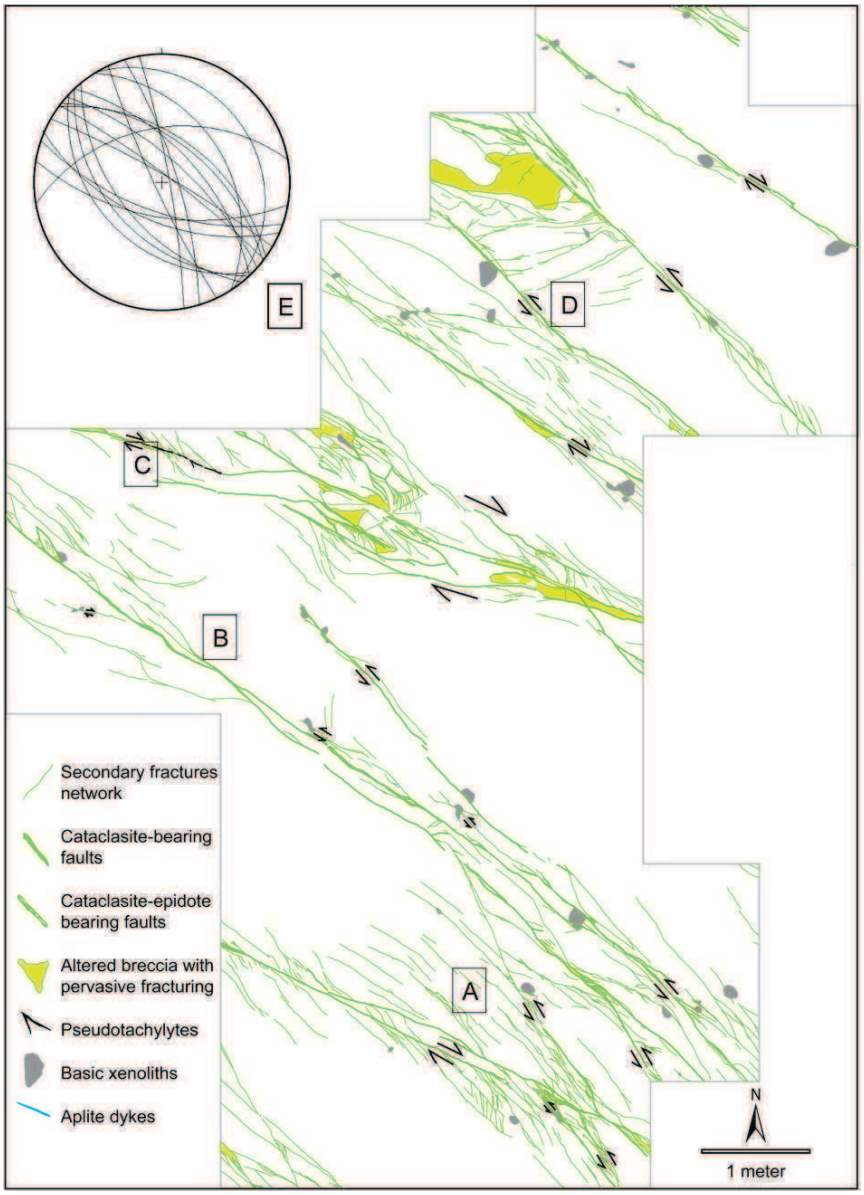


**Fig. 5.** High resolution surface map of the PCFZ (the map was drawn at 1:10 scale using a rigid frame of 1 $m^2$). (A) Intersection between two conjugate fault strands, with opposite sense of shear. (B) Variations in thickness along strike, due to linkage of adjacent *en echelon* segments. (C) Fault segment carrying pseudotachylyte, with a centimetre-long injection vein. (D) Faults spaced about 1 m apart linked by high angle fractures and domains of fragmented and altered tonalite. (E) Stereoplot of the fault planes represented in the surface map. Equal area, lower hemisphere plot.

according to the genetic classification of Sibson (1986) and could be classified as cement-supported chaotic breccias, following Woodcock and Mort (2008).

### 3.3.4. Pseudotachylytes

Pseudotachylytes of the PCFZ show microstructures typical of rapid cooling of a melt (e.g. Magloughlin and Spray, 1992; Di Toro and Pennacchioni, 2004; Di Toro et al., 2004), such as the development of flow structures, spherulites, plagioclase and biotite microlites, and a cryptocrystalline matrix (Fig. 7g and h). Clasts are rounded to angular and consist of quartz, plagioclase and K-feldspar. Under the Field Emission SEM the cryptocrystalline matrix is seen to comprise an aggregate of biotite, titanite and K-feldspar. Spherulitic aggregates form around quartz, plagioclase and K-feldspar clasts, as rims of radially arranged aggregates of plagioclase microlites and quartz. Spherical amygdale-like features filled by quartz and K-feldspar are often found dispersed in the pseudotachylyte matrix (Fig. 7h).

## 3.4. Geochemistry and mineralogy

X-ray fluorescence (XRF) and X-ray powder diffraction (XRPD) analyses were conducted on the cataclasites and host tonalite. Elemental XRF analyses show that light green cataclasites are highly enriched in $Fe^{3+}$, Ca, K and LILE (Rb, Sr, Ba) compared to the host rock (Table 1). Dark green cataclasites have less scattered elemental compositions and are enriched in Na with respect to unaltered tonalite. The relative change in major element

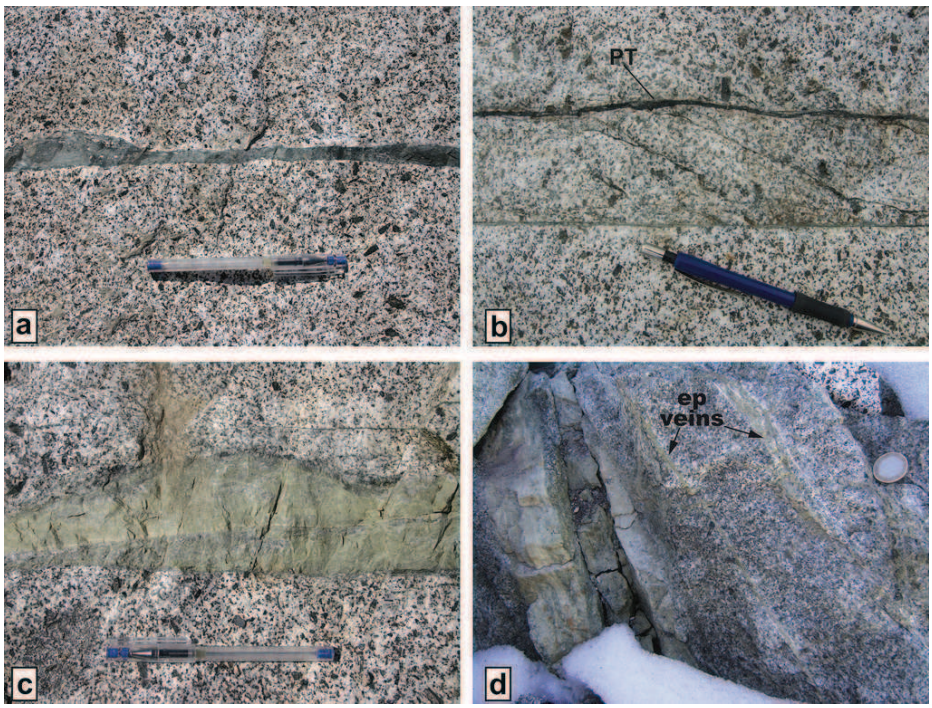


**Fig. 6.** Fault rocks from the PCFZ. (a) Dark green cataclasite; the edges with the host tonalite are sharp. (b) Paired faults, linked by oblique fractures, decorated by pseudotachylyte (PT) and dark green cataclasite. The secondary Riedel shear type fractures are decorated by cataclasite. The tonalite adjacent to the faults is bleached. (c) Thick light green cataclasite, composed of multiple layers. (d) Light green cataclasite, associated with epidote veins, oriented at low angle to the cataclasite. The tonalite adjacent to the fault and veins is strongly altered and has greenish colour. (For interpretation of references to colour in this figure legend the reader is referred to web version of the article).

composition is reflected in the abundances of minerals cementing the cataclasite matrix, determined from XRPD analysis (Fig. 8).

## 4. Passo Cercen fault zone vs. Gole Larghe fault zone

The scarcity of pseudotachylytes in the PCFZ and their abundance in the GLFZ (Fig. 9a and b) is a major difference between the fault zone rocks; the possible reasons for this difference in the two fault zones will be discussed in this section.

The GLFZ and PCFZ developed under similar ambient conditions at the base of the seismogenic crust during the final stages of cooling of the Avio and Presanella plutons and before their exhumation (Pennacchioni et al., 2006). The occurrence of sub-horizontal roof pendants in the inner parts of the Southern Adamello batholith (Brack, 1983), suggests that no tilting occurred during exhumation of the plutons from seismogenic depths. The depth of faulting is estimated at 9–11 km (Di Toro et al., 2005) and the ambient temperature was about 250 °C, as suggested by the presence of local incipient bulging recrystallization in quartz associated with cataclastic deformation, by the greenschist facies mineral assemblage (epidote, chlorite, K-feldspar, actinolite, albite) cementing the cataclasites (Fig. 9c and d) and the onset of stress induced solution-precipitation processes (i.e. presence of pressure solution seams) in both fault zones (Di Toro and Pennacchioni, 2005). The texture of the cataclasite matrix suggests precipitation under static conditions. The occurrence of reworked clasts of cemented cataclasite indicates that cementation was syn- to post-deformational. The host rock of both fault zones is tonalite (Table 1), though the Presanella tonalite (PCFZ) contains hornblende, which is absent in the Avio tonalite (GLFZ). Cataclasitic deformation was assisted by extensive percolation of fluids and pervasive precipitation of epidote + K-feldspar + chlorite ± actinolite and the occurrence of pressure-solution related microstructures in both faults (Fig. 9c and d). The extensive fluid-assisted alteration of cataclasites is attested by their enrichment in LILE and loss of Na and $Fe^{3+}$ (Di Toro and Pennacchioni, 2005) compared to the host tonalites in both fault zones. The isocon diagrams (Grant, 2005) of Fig. 9e and f highlight the changes in major and trace elements of the fault rocks relative to the host tonalite due to interaction with fluids. The comparison between the cataclasite compositions of the PCFZ and GLFZ shows a larger data scattering in the former case, which is consistent with a stronger fluid-induced alteration in the fault rocks of the PCFZ compared to those of the GLFZ. This interpretation is based on the evidence that fluid flow was localized along fault horizons and that the fluid transfer between host and fault rocks could not equilibrate the compositional differences, as has been seen in other fault zones (e.g. Jefferies et al., 2006).

Both faults exploited pre-existing joints (Di Toro and Pennacchioni, 2005); the GLFZ exploits joints striking on average N105° whereas the PCFZ exploits joints striking on average N130°. The plane bisecting the average orientation of dextral and sinistral fault segments in the PCFZ strikes approximately at N135°. Since these are all strike slip faults, this orientation should correspond to the direction of the maximum horizontal stress $\sigma_1$ during faulting. A similar orientation of the regional $\sigma_1$ is inferred for the GLFZ (Di Toro and Pennacchioni, 2005). An identical shortening direction could also be inferred from the orientation of the flattening zones (Pennacchioni and Mancktelow, 2007) formed at the intersection between conjugate ductile shear zones exploiting the different sets of joints during the high temperature stages of pluton cooling preceding the cataclastic faulting (Pennacchioni, 2005) (Fig. 10). The orientation of $\sigma_1$ about N135° corresponds to the main regional compressive stress active in this area during the collisional stage of the Alpine orogeny (Castellarin et al., 2006; Castellarin and Cantelli, 2000). The different orientation of the fault

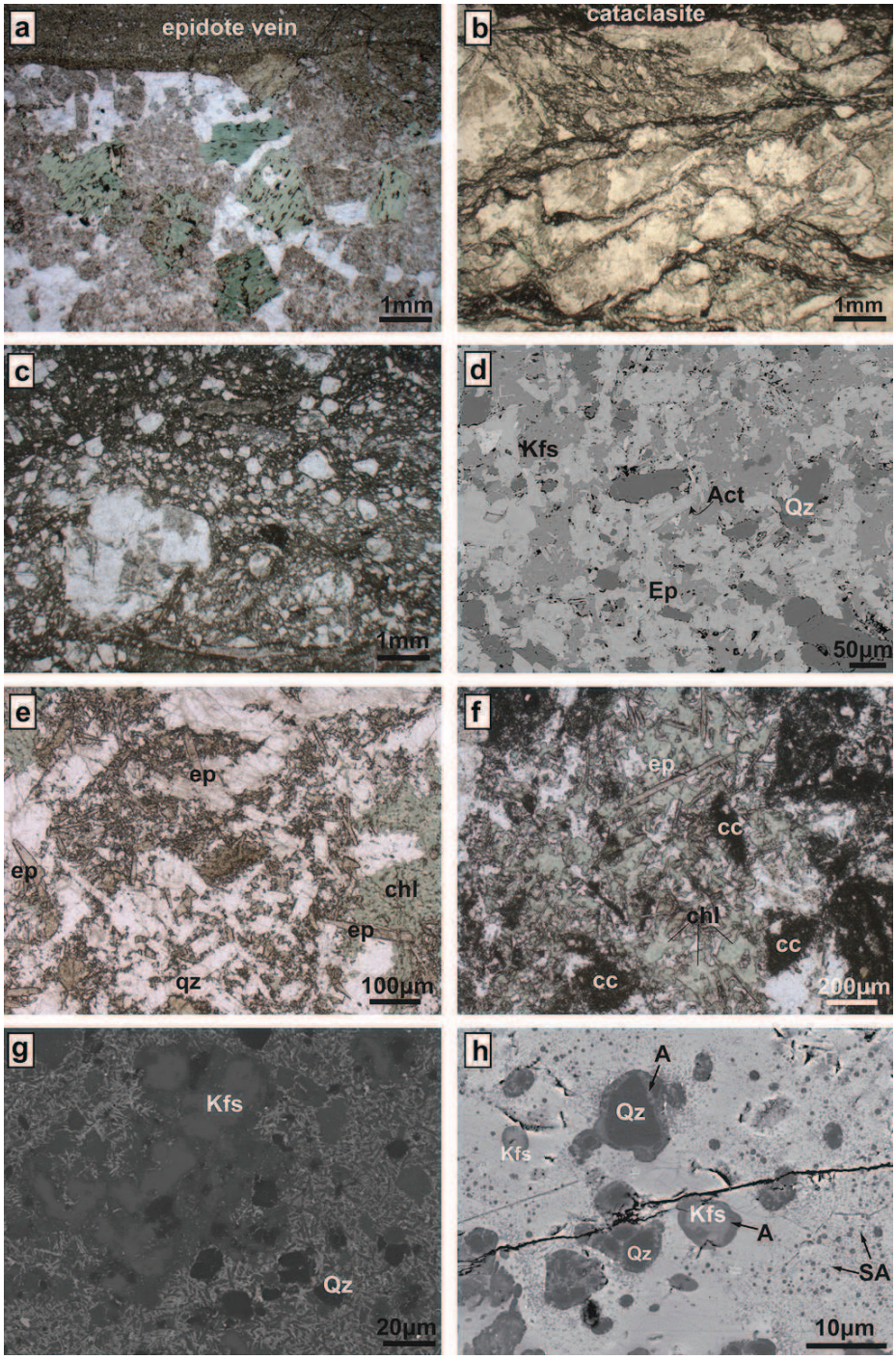


**Fig. 7.** Microstructures in the Passo Cercen fault rocks. (a) Altered tonalite adjacent to an epidote-bearing vein. Biotite is broken down to chlorite (green) and titanite aggregates, plagioclase is saussuritized (optical microscope, plane polarized light). (b) Close to cataclasites, tonalite is fractured and foliated due to the formation of wriggled surfaces cemented by chlorite, titanite, actinolite and remnants of biotite (optical microscope, plane polarized light). (c) Cataclasite is formed by angular clasts in a microcrystalline matrix (optical microscope, plane polarized light). (d) Cataclasite matrix, characterized by grain size on the order of the tens of micron and evidence of static growth and interactions with percolating fluids: quartz clasts have lobate edges, epidote has poikilitic texture, actinolite is acicular and is randomly oriented (Back Scatter Electron-SEM image). (e) Epidote (ep), chlorite (chl) and quartz (Qz)-bearing vein cutting altered tonalite; minerals sealing the vein are randomly oriented (optical microscope, plane polarized light). (f) The texture of a vein in cataclasite; randomly oriented, prismatic epidote crystals are floating in an aggregate of chlorite, plagioclase and quartz with blocky texture. Clasts of cataclasite (cc) are suspended in the vein (optical microscope, plane polarized light). (g) Microstructure of pseudotachylyte: partially melted K-feldspar clasts and rounded quartz clasts are immersed in a matrix composed by the fine intergrowth of biotite and plagioclase microlites (Back Scatter Electron-SEM image). (h) Detail of a pseudotachylyte characterized by a crypto-crystalline, bright matrix composed mainly of biotite, with dispersed small, spherical (amygdale-like) aggregates of plagioclase and silica (SA); quartz (Qz) and K-feldspar (Kfs) rounded clasts are rimmed by an aggregate of plagioclase and silica (A) (Field Emission Back Scatter Electron-SEM image). (For interpretation of references to colour in this figure legend the reader is referred to web version of the article).

**Table 1**
X-ray fluorescence analyses of fault and host rocks of the PCFZ and the GLFZ; PT, pseudotachylytes, CC, cataclasites. The data for the GLFZ are from Pennacchioni et al. (2006).

| Rock type area | Avio tonalite | | PT Avio | | CC Avio | | Presanella tonalite | | Dark g. CC | Light g. CC | |
|---|---|---|---|---|---|---|---|---|---|---|---|
| | GLFZ | | GLFZ | | GLFZ | | PCFZ | | PCFZ | PCFZ | |
| | $n=5$ | $n=5$ | $n=5$ | $n=5$ | $n=4$ | $n=4$ | $n=3$ | $n=3$ | $n=1$ | $n=3$ | $n=3$ |
| Wt% | Mean | *S.d.* | Mean | *S.d.* | Mean | *S.d.* | Mean | *S.d.* | | Mean | *S.d.* |
| $SiO_2$ | 66.56 | *0.84* | 62.52 | *1.54* | 61.83 | *2.51* | 61.83 | *0.23* | 60.75 | 60.61 | *10.10* |
| $TiO_2$ | 0.46 | *0.04* | 0.56 | *0.05* | 0.56 | *0.14* | 0.74 | *0.02* | 0.70 | 0.34 | *0.16* |
| $Al_2O_3$ | 16.53 | *0.33* | 16.83 | *0.24* | 17.03 | *0.84* | 16.41 | *0.02* | 16.63 | 15.94 | *3.58* |
| FeO | 3.41 | *0.26* | 3.50 | *0.41* | 3.41 | *0.38* | 5.06 | *0.14* | 3.93 | 1.45 | *1.04* |
| $Fe_2O_3$ | 0.33 | *0.07* | 1.10 | *0.43* | 1.18 | *0.42* | 0.40 | *0.13* | 0.67 | 4.05 | *2.20* |
| MnO | 0.10 | *0.01* | 0.12 | *0.01* | 0.13 | *0.01* | 0.11 | *0.00* | 0.17 | 0.10 | *0.04* |
| MgO | 1.57 | *0.16* | 1.89 | *0.14* | 1.88 | *0.30* | 2.35 | *0.05* | 2.64 | 0.82 | *0.68* |
| CaO | 4.44 | *0.13* | 3.85 | *0.30* | 3.86 | *1.12* | 5.67 | *0.15* | 6.13 | 8.77 | *4.15* |
| $Na_2O$ | 2.95 | *0.05* | 2.47 | *0.76* | 1.69 | *0.56* | 2.62 | *0.06* | 6.36 | 0.85 | *0.16* |
| $K_2O$ | 2.20 | *0.10* | 3.73 | *1.27* | 6.10 | *1.37* | 2.26 | *0.16* | 0.42 | 5.17 | *1.14* |
| $P_2O_5$ | 0.11 | *0.01* | 0.13 | *0.01* | 0.13 | *0.01* | 0.13 | *0.01* | 0.10 | 0.07 | *0.02* |
| *L.O.I.* | *0.91* | *0.06* | *2.77* | *0.71* | *2.02* | *0.52* | *1.47* | *0.11* | *0.95* | *1.44* | *0.43* |
| Tot | 99.56 | *0.12* | 99.46 | *0.16* | 99.80 | *0.35* | 99.05 | *0.03* | 99.45 | 99.60 | *0.15* |
| ppm | | | | | | | | | | | |
| Sc | 14 | *4* | 16 | *1* | 17 | *1* | 14 | *0* | 10 | 7 | *2* |
| V | 58 | *6* | 71 | *6* | 77 | *13* | 106 | *4* | 99 | 166 | *80* |
| Cr | 13 | *3* | 27 | *13* | 24 | *17* | 14 | *2* | 12 | 27 | *27* |
| Co | 8 | *1* | 7 | *3* | 7 | *2* | 195 | *15* | 124 | 147 | *62* |
| Ni | 9 | *3* | 14 | *8* | 12 | *9* | 5 | *0* | 6 | 7 | *6* |
| Cu | 6 | *2* | 12 | *11* | 8 | *5* | 53 | *20* | 32 | 18 | *23* |
| Zn | 57 | *5* | 81 | *28* | 61 | *11* | 45 | *0* | 61 | 9 | *11* |
| Ga | 22 | *2* | 22 | *4* | 22 | *5* | 5 | *0* | 5 | 11 | *7* |
| Rb | 90 | *11* | 265 | *149* | 186 | *23* | 99 | *1* | 13 | 190 | *32* |
| Sr | 225 | *9* | 226 | *16* | 229 | *25* | 208 | *6* | 279 | 294 | *128* |
| Y | 26 | *5* | 30 | *2* | 39 | *9* | 25 | *0* | 22 | 19 | *10* |
| Zr | 117 | *9* | 135 | *4* | 126 | *12* | 137 | *5* | 137 | 65 | *29* |
| Nb | 10 | *1* | 12 | *1* | 12 | *1* | 11 | *0* | 11 | 6 | *2* |
| Ba | 375 | *23* | 447 | *28* | 740 | *91* | 343 | *26* | 285 | 573 | *74* |
| La | 30 | *4* | 39 | *7* | 38 | *8* | 29 | *9* | 29 | 16 | *6* |
| Ce | 53 | *14* | 66 | *9* | 68 | *8* | 43 | *10* | 37 | 35 | *10* |
| Nd | 23 | *7* | 22 | *8* | 24 | *10* | 15 | *1* | 20 | 10 | *0* |
| Pb | 29 | *11* | 37 | *12* | 32 | *10* | 5 | *0* | 5 | 7 | *4* |
| Th | 10 | *2* | 12 | *1* | 10 | *2* | 3 | *0* | 3 | 3 | *0* |
| U | 3 | *0* | 9 | *5* | 7 | *1* | 3 | *0* | 3 | 3 | *1* |

segments with respect to the maximum horizontal stress appears to be the most striking difference between the fault zones. The possible mechanical implications of this difference and influence on the development of the fault rock assemblages are discussed in the following section.

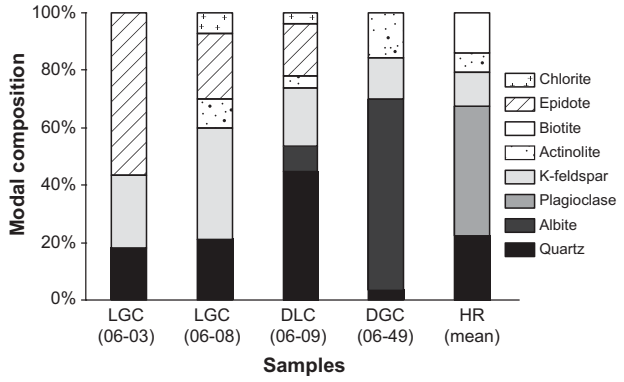


**Fig. 8.** Semi-quantitative modal composition of cataclasites and host tonalite from X-ray powder diffraction analyses (LGC: light green cataclasite, DLC: dark and light green cataclasite, DGC: dark green cataclasite, HR: host rock). The mineral composition of the cataclasites is strongly variable in the analysed samples. The reported modal compositions are based on the mathematical elaboration of the XRPD spectra. Since we did not use an internal standard, the analyses are semi-quantitative. (For interpretation of references to colour in this figure legend the reader is referred to web version of the article).

## 5. Discussion

The GLFZ and PCFZ were active in similar host rocks (tonalite), geochemical environment and P–T conditions, as discussed in the previous section. The faults have different orientations, which is determined by the attitude of pre-existing joints. We discuss below how fault orientation could affect the magnitude of the effective stresses normal to the fault surfaces and, as a consequence, the type of fault rock assemblages that may develop.

Tectonic pseudotachylytes form by the melting of fault and host rocks due to frictional heating along a fault surface during seismic slip (i.e. slip rates on average of about 1 m $s^{-1}$). The work done during faulting is (Kostrov and Das, 1988):

$$W_f = Q + U_s \quad (1)$$

where $Q$ is heat and $U_s$ is surface energy for gouge and fracture formation. Since $U_s$ is considered negligible (Lockner and Okubo, 1983), the majority (>95%) of the work is converted to heat (Scholz, 2002). In the case of the Gole Larghe fault zone, this assumption was confirmed using a microstructural study of a pseudotachylyte-bearing fault (Pittarello et al., 2008). Thus, the amount of heat generated during seismic slip for unit area of the fault is (Price and Cosgrove, 1990):

$$W_f = \mu\left(\sigma_n - p_p\right)d \approx Q \quad (2)$$

Where $\mu$ is the friction coefficient, $\sigma_n$ is the stress normal to the fault plane, $p_p$ is the pore pressure and $d$ is the coseismic slip.

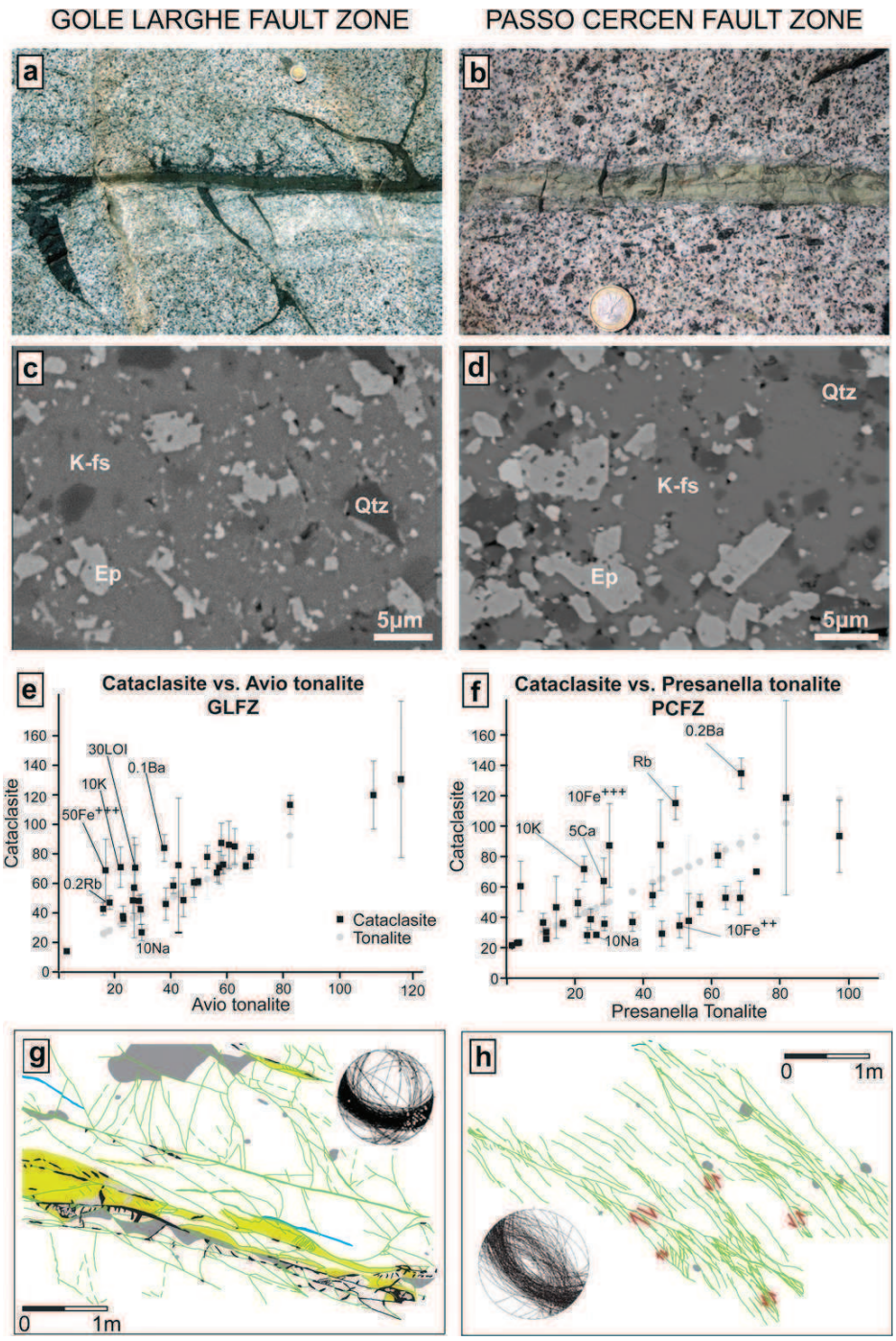


**Fig. 9.** Comparison of the main features of the GLFZ (left column) and PCFZ (right column). (a) and (b) Fault rock assemblage in the field: (a) a thin cataclasite is associated with a thick pseudotachylyte (GLFZ). (b) Thick cataclasite (PCFZ), in most cases pseudotachylytes are absent. (c) and (d) Cataclasite matrix under the SEM: mineral assemblages in the GLFZ (c) and PCFZ (d) are identical, with evidence for static growth of epidote (BSE-SEM images). (e) and (f) Elemental compositions from X-ray fluorescence analyses. The isocon diagrams (e.g. Grant, 2005) compare the elemental compositions of cataclasites (black dots) with that of the host tonalite (gray dots), normalized to the elemental composition of the host tonalite (Avio tonalite for the GLFZ, Presanella tonalite for the PCFZ); the shift of the cataclasite composition with respect to the host rock composition (host rock data form a straight line in the diagram) is proportional to the relative enrichment or loss of chemical components during hydrothermal alteration (and cementation) of cataclasites. Compared to the GLFZ, in the PCFZ the elemental composition of the cataclasites is more scattered with respect to the host tonalite. This geochemical evidence suggests a more intense chemical exchange with percolating fluids (XRF data of the GLFZ are from Di Toro and Pennacchioni, 2005). (g) and (h) Details of surface maps of the GLFZ (g) and the PCFZ (h), and cumulative stereoplots of all the fault data collected in the two fault zones; the legend is the same as in Fig. 5. Structural data for the GLFZ are from Di Toro and Pennacchioni (2005).

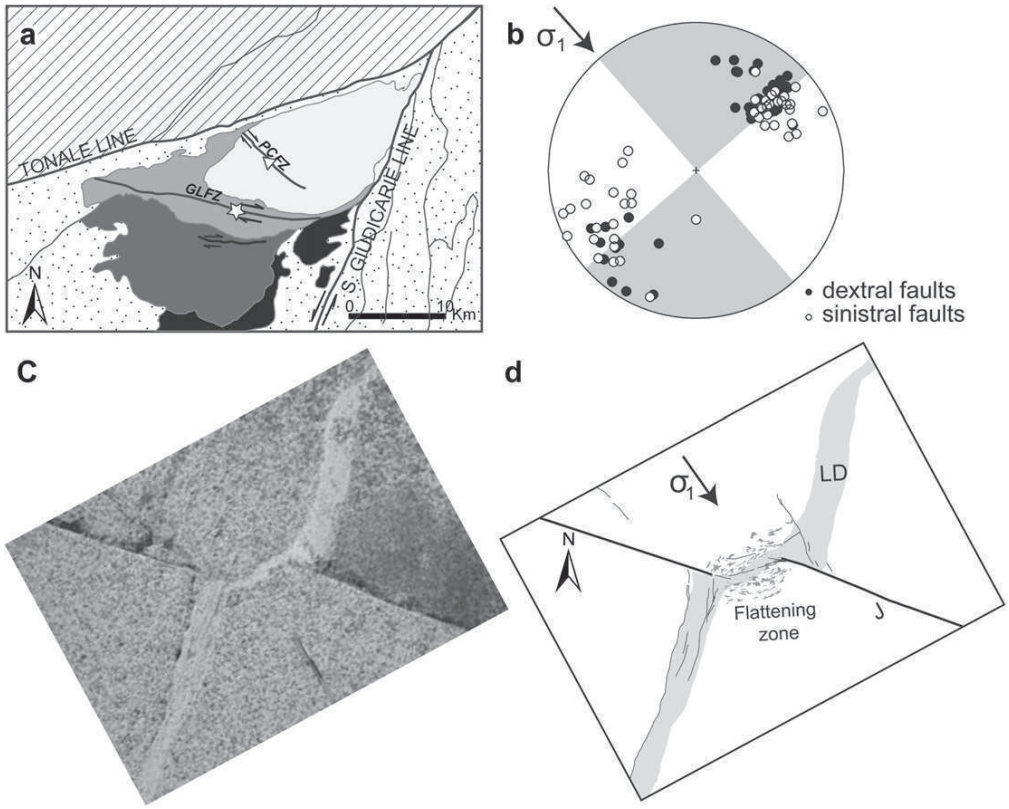


**Fig. 10.** Orientation of the regional maximum principal horizontal stress. (a) Geological sketch of the northern Adamello; the star indicates the Lobbia outcrop, where the field picture in Fig. 10c was taken, the triangle indicates the Passo Cercen area, where the structural data from the PCFZ were collected. (b) The orientation of the regional $\sigma_1$ as inferred from the switch in the shear sense of faults within the PCFZ. (c) Field photograph of a flattening zone developed at the intersection of two nearly orthogonal shear zones during amphibolite facies ($T$ about 550 °C) deformation of the Avio tonalite (Lobbia outcrop), and (d) the same structure redrawn. The shear zones are localized along a joint (J) and a leucocratic dyke (LD). The orientation of $\sigma_1$ is similar to that inferred for the PCFZ.

Following McKenzie and Brune (1972), the heat flux generated per unit area of the fault is:

$$q \approx \mu\left(\sigma_n - p_p\right)V = \mu\sigma'_n V \tag{3}$$

where $\sigma'_n$ is the effective normal stress acting on the fault plane and $V$ is slip rate. The frictional heating depends on the friction coefficient, the velocity of sliding and the effective normal stress on the fault plane. The friction coefficient for granitoid rocks and the minerals cementing cataclasites (epidote + K-feldspar) is Byerlee-type, i.e. $0.6 < \mu < 0.85$, and minerals with significantly lower friction coefficient (e.g. talc, Byerlee, 1978) are absent in the studied faults. Slip rates were seismic in both fault zones, since the presence of pseudotachylyte is documented in both GLFZ and PCFZ.

The strength of the brittle crust depends on the ratio between the normal stress and shear stress acting on the fault plane and is described by the empirical Coulomb failure criterion (Sibson, 1990):

$$\tau = C + \mu_i\sigma'_n = C + \mu_i\left(\sigma_n - p_p\right) \tag{4}$$

where $C$ is the cohesive strength, $\mu_i$ is the coefficient of internal friction, and $\tau$ is the resolved shear stress. For pre-existing cohesion-less faults, the fault strength is (Jaeger et al., 2007):

$$\tau = \mu\sigma'_n = \mu\left(\sigma_n - p_p\right) \tag{5}$$

(Amonton's law combined with Terzaghi's law), where $\mu$ is the friction coefficient. The reactivation of a cohesion-less fault whose pole lies in the $\sigma_1/\sigma_3$ plane is controlled by the ratio of effective principal stresses, which depends upon the angle $\theta_r$ within the fault plane and the direction of $\sigma_1$ (reactivation angle, Sibson, 1985):

$$R = \frac{\sigma'_1}{\sigma'_3} = \frac{\sigma_1 - p_p}{\sigma_3 - p_p} = \frac{1 + \mu\cot\theta_r}{1 - \mu\tan\theta_r} \tag{6}$$

This function has a positive minimum at

$$\theta_r{}^* = 0.5\tan^{-1}(1/\mu) = 26.5^\circ \tag{7}$$

defining the most favourable orientation for fault reactivation. If the angle $\theta_r$ departs more than 15° from $\theta_r{}^*$, the stress ratio to initiate sliding increases $b \sim 50\%$ and faults may be considered to be *unfavourably* oriented for reactivation (Sibson, 1990). Reactivation in these conditions is possible for low differential stresses and under elevated fluid pressure, with $\sigma'_3$ approaching 0; otherwise, the differential stress required for reactivation exceeds that needed to form a new fault (Sibson, 1985).

The GLFZ and the PCFZ are oriented at different angles with the inferred direction of $\sigma_1$ (Fig. 11a), the GLFZ being favorably oriented for reshear ($\theta_r \approx \theta_r{}^*$) and the PCFZ being oriented at $\theta_r << \theta_r{}^*$. The variations in effective normal stresses on the GLFZ and PCFZ have been estimated under the following assumptions and approximations:

(1) The coefficient of internal friction $\mu_i$ generally lies between 0.5 and 1.0 for rocks (Sibson, 1985), the coefficient of sliding friction is $0.6 < \mu < 0.85$ for most rocks (Byerlee, 1978); for

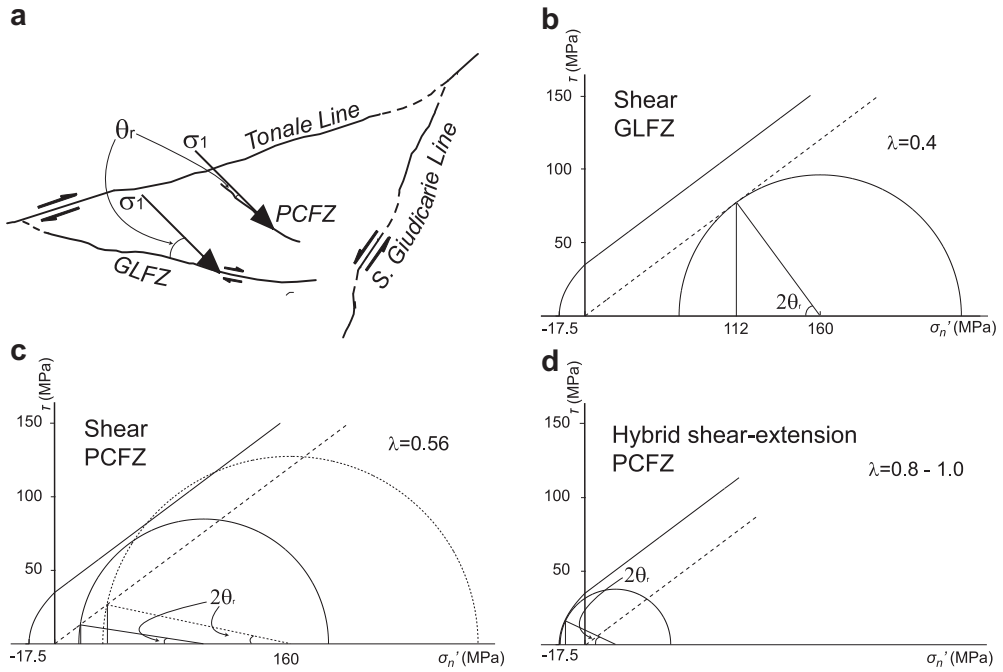


**Fig. 11.** Mechanics of the GLFZ and PCFZ. (a) The reactivation angle $\theta_r$ for the GLFZ and PCFZ. (b) Mohr analysis for the GLFZ. The failure envelopes for intact tonalite (solid line) and for reactivation of a cohesion-less fault (dashed line) have been drawn based on the parameters and boundary conditions discussed in the text. The conditions for failure are reached when the Mohr circle representing the state of stress of the fault zone strikes the failure envelope; the reactivation angle $\theta_r$ is half of the angle between the radius connecting the centre of the Mohr circle and the point of contact (labelled $2\theta_r$). For sliding along a fault oriented like the GLFZ, with a reactivation angle $\theta_r \approx 30^\circ$ and assuming hydrostatic pore pressure ($\lambda = 0.4$), the estimated effective stress normal to the fault plane is 112 MPa. (c) Plot of the state of stress for the PCFZ in Mohr space. Since the depth of faulting and thus $\sigma_2$ are the same as in the GLFZ, the Mohr circle can touch the failure envelope at an angle $\theta_r$ for $\lambda = 0.4$ and high differential stress (dotted circle) or for pore pressures higher than hydrostatic and lower differential stress (solid circle). For $\lambda = 0.56$ the estimated effective stress normal to the fault is on the order of 10–20 MPa. (d) The conditions for the formation of hybrid shear extension fractures in the PCFZ. The effective normal stress of the fault is tensile.

convenience, the failure of intact rock and the sliding failure envelopes have been drawn parallel with $\mu_i = \mu = 0.75$.

(ii) A cohesive strength $C = 35$ MPa has been chosen as representative for granitoid rocks (Amitrano and Schmittbuhl, 2002).

(iii) The faults are assumed to be vertical with pure strike–slip kinematics; averaged fault orientation is assumed to be N105° for the GLFZ and N130° ± 15° for the PCFZ.

(iv) The stress field is Andersonian (Di Toro et al., 2005), so that in a strike–slip regime, the effective vertical stress ($\sigma'_v$) corresponds to the intermediate principal stress ($\sigma'_2$), $\sigma'_v = \rho g z - p_p = \sigma'_2$ (Sibson, 1974), where $\rho$ is the rock density, $g$ is the acceleration due to gravity and $z$ is the depth.

(v) The $\sigma_1$ and $\sigma_3$ axes are assumed to be horizontal and $\sigma_1$ strikes N135°, as inferred from the field evidence in the GLFZ and PCFZ.

(vi) The value of the intermediate principal stress is assumed to be $\sigma_2 = (\sigma_1 - \sigma_3)/2$, following Sibson (1974).

In the GLFZ, despite the extensive fluid–rock interaction in the cataclasites, there is no evidence for pervasive macroscopic veining. This field observation suggests that pore pressure was hydrostatic or lower (Di Toro et al., 2005). Assuming a depth $z = 10$ km and an average rock density of 2.65 g cm$^{-3}$, the effective vertical stress (and the effective intermediate normal stress) is $\sigma'_2 = \sigma'_v = \rho g z - p_p = \rho g z - \rho_w g z \approx 160$ MPa for a hydrostatic pore-fluid factor $\lambda = p_p/\rho g z = 0.4$ (Fig. 11a). The GLFZ makes an angle $\theta_r = 30^\circ \approx \theta_r^*$ with the inferred direction of $\sigma_1$. For reactivation of pre-existing joints, the effective normal stress acting on the fault plane is $\sigma' = 112$ MPa (Di Toro et al., 2005) (Fig. 11b).

In the PCFZ, the presence of pervasive macroscopic veining in the tonalite suggests that fluid pressure was locally higher than hydrostatic. The fault surfaces and epidote-bearing veins are mostly oriented at low angles to the $\sigma_1$ direction, with $\theta_r = 5 \pm 15^\circ$. The depth of faulting and the vertical stress $\sigma_v = \sigma_2$ are assumed to be the same as the GLFZ, but to allow reactivation of faults with this orientation or vein opening, it is necessary to assume either higher differential stresses or higher fluid pressures (Fig. 11c). The $\sigma'_n$ on the PCFZ fault planes was thus significantly lower than in the GLFZ, since:

(i) For shear reactivation of joints, it is necessary to assume high differential stresses, or higher fluid pressure (Fig. 11c); in both cases, however, the $\sigma'_n$ on fault planes is on the order of 10–20 MPa, significantly lower than in the GLFZ.

(ii) Tensional veins form in planes perpendicular to the least compressive stress $\sigma_3$, for $(\sigma_3 - p_p) = -T$ and $(\sigma_1 - \sigma_3) < 4\,T$, where $T = 0.5$ °C is the tensile strength of the rock (Price and Cosgrove, 1990). However, the veins in the PCFZ, striking at low angles to the $\sigma_1$ direction, are better described as hybrid extension and shear fractures, where $0.8 < (\sigma_3 - p_p) < T$ and $4\,T < (\sigma_1 - \sigma_3) < 5.5\,T$ (Price and Cosgrove, 1990). In both extension or hybrid fracture, the effective stresses on the fault planes is tensile, implying pore pressures approaching lithostatic values ($\lambda \approx 1.0$) (Fig. 11d).

This analysis suggest that effective normal stresses acting on the fault planes of the PCFZ were significantly lower than those inferred for the GLFZ, and that episodes of pore pressure approaching lithostatic values are likely in the PCFZ based on the observed field occurrence of extensive veining parallel to faults. It is therefore proposed that the production of frictional melting in the PCFZ was in most cases inhibited by: (i) low effective normal stresses acting on

fault planes, allowing only limited frictional heating; (ii) high fluid pressures, which, besides lowering the effective normal stresses for mechanical reasons, could also trigger weakening mechanisms such as thermal pressurization of fluids during earthquakes (Sibson, 1973; Lachenbruch, 1980; Bizzarri and Cocco, 2006; Rice, 2006); (iii) the presence of fluids in the slipping zone that adsorb a relevant amount of heat during frictional heating and buffer the increase in temperature.

Summarizing, field, geochemical and microstructural evidence suggests fluid–rock interaction during brittle deformation both in the PCFZ and in the GLFZ. However, alteration and veining are more intense in the PCFZ compared to the GLFZ (see Fig. 9e and f, Table 1). This suggests that in the PCFZ faulting occurred in a more fluid-rich environment, which possibly experienced build ups of fluid pressures higher than hydrostatic. The more intense fluid circulation in the PCFZ with respect to the nearby GLFZ could be a consequence of the different orientations of the pre-existing joints which localized the subsequent brittle deformation (Fig. 1b). In the Adamello batholith, the network of joints was the preferential pathway for fluid circulation, as suggested by the intense fluid–rock alteration found along joints and faults (e.g. Fig. 2), while the host tonalite was almost unaltered. The joints in the Presanella area (PCFZ) were oriented at low angles with respect to the inferred regional $\sigma_1$, and could have acted as dilational fractures, allowing greater amounts of fluid infiltration during faulting. Fluids could have been subsequently trapped and overpressurized by the precipitation of subgreenschist facies minerals (epidote, chlorite) in the fault zones. In contrast, the joints in the Avio area (GLFZ) were oriented at higher angles with respect to the regional $\sigma_1$, in a more compressive setting which might have impeded abundant fluid infiltration (Fig. 1b).

## 6. Conclusions

Two closely located fault zones (GLFZ and PCFZ) cutting the northern Adamello massif that were active at the same time and in the same regional stress field have been compared to highlight the factors affecting the formation of pseudotachylyte during seismic sliding. The most relevant difference between the two fault zones is their orientation, which is inferred to determine the different mechanics and resulting fault rock assemblages. The GLFZ strikes at ca. 30° to the inferred regional $\sigma_1$, being active under high normal stresses (ca. 100 MPa) and low (i.e. hydrostatic) fluid pressures: the fault rock assemblage includes abundant pseudotachylytes. The PCFZ strikes almost parallel to the $\sigma_1$ direction, allowing lower (10–20 MPa) normal stresses and higher fluid infiltration (up to fluid pressure higher than hydrostatic). Frictional heating is proportional to the normal stress resolved on the fault plane. Under low normal stresses, such as those developed along the PCFZ, melting could be reached only locally. The fault rock assemblage is associated with abundant epidote-bearing veins and cataclasites, but few pseudotachylytes. Other seismically activated processes, such as thermal pressurization of pore fluids may have further inhibited the frictional heating along the PCFZ.

## Acknowledgements

Many thanks to Leonardo Tauro and Antonio Novello (thin sections preparation), Federico Zorzi (XRD), Daria Pasqual (XRF), Luca Peruzzo (SEM), Andrea Cavallo and Piergiorgio Scarlato (FE-SEM at INGV in Rome) and Stefano Castelli (image acquisition). The people of the Museo Tridentino di Scienze Naturali, especially Marco Avanzini, are thanked for the constant support and the stimulating discussions. The Servizio Meteorologico della Provincia di Trento kindly provided high resolution aerial photographs of the northern Adamello. The constructive reviews and comments of Robert Holdsworth and Zoe Shipton improved substantially the manuscript and addressed very interesting topics. Mirko and Erika Dezulian of the Francesco Denza mountain hut (Vermiglio, Trento) are also greatly acknowledged. This study was founded by the Fondazione CARITRO, by the CA.RI.PA.RO Project (progetti di Eccellenza 2006) and by the European Research Council Starting Grant project USEMS (Nr. 205175).

## References

Abercrombie, R., McGarr, A., Kanamori, H., Di Toro, G. (Eds.), 2006. Earthquakes: Radiated Energy and the Physics of Faulting. Geophysical Monograph Series, 170. AGU.

Amitrano, D., Schmittbuhl, J., 2002. Fracture roughness and gouge distribution of a granite shear band. Journal of Geophysical Research 107, B12. doi:10.1029/2002JB001761.

Andrews, D.J., 2002. A fault constitutive relation accounting for thermal pressurization of pore fluid. Journal of Geophysical Research 107 (B12), 2363. doi:10.1029/2002JB001942.

Bianchi, A., Callegari, E., Jobstraibizer, P.G., 1970. I tipi petrografici fondamentali del plutone dell'Adamello (tonaliti, quarzodioriti, granodioriti e loro varietà leucocrate). Memorie dell'Istituto di Geologia e Mineralogia dell'Università di Padova 27, 1–148.

Bizzarri, A., Cocco, M., 2006. A thermal pressurization model for the spontaneous dynamic rupture propagation on a three-dimensional fault: 1. Methodological approach. Journal of Geophysical Research 111, B05303. doi:10.1029/2005JB003862.

Brack, P., 1983. Multiple intrusions – examples from the Adamello batholith (Italy) and their significance on the mechanisms of intrusion. Memorie della Società Geologica Italiana 26, 145–157.

Byerlee, J.D., 1978. Friction of rocks. Pure and Applied Geophysics 116, 615–626.

Castellarin, A., Cantelli, L., 2000. Neo-Alpine evolution of the Southern Eastern Alps. Journal of Geodynamics 30, 251–274.

Castellarin, A., Vai, G.B., Cantelli, L., 2006. The alpine evolution of the Southern Alps around the Giudicarie faults: a Late Cretaceous to Early Eocene transfer zone. Tectonophysics 414, 203–223.

Cowan, D.S., 1999. Do faults preserve a record of seismic slip? A field geologist's opinion. Journal of Structural Geology 21, 995–1001.

De Capitani, L., Delitala, M.C., Liborio, G., Mottana, A., Rodeghiero, F., Thöni, M., 1994. The granitoid rocks of Val Navazze, Val Torgola and Val di Rango (Val Trompia, Lombardy, Italy). Memorie di Scienze Geologiche 46, 329–343.

Del Moro, A., Pardini, G., Quercioli, C., Villa, I.M., Callegari, E., 1983. Rb/Sr and K/Ar chronology of Adamello granitoids, southern Alps. Memorie della Società Geologica Italiana 26, 285–299.

Di Toro, G., Pennacchioni, G., 2004. Superheated friction-induced melts in zoned pseudotachylytes within the Adamello tonalites (Italian Southern Alps). Journal of Structural Geology 26, 1783–1801.

Di Toro, G., Pennacchioni, G., 2005. Fault plane processes and mesoscopic structure of a strong-type seismogenic fault in tonalites (Adamello batholith, Southern Alps). Tectonophysics 402, 55–80.

Di Toro, G., Pennacchioni, G., Teza, G., 2005. Can pseudotachylytes be used to infer earthquake source parameters? An example of limitations in the study of exhumed faults. Tectonophysics 402, 3–20.

Di Toro, G., Pennacchioni, G., Nielsen, S., 2009. Pseudotachylytes and earthquake source mechanics. In: Fukuyama, Eiichi (Ed.), Fault-Zone Properties and Earthquake Rupture Dynamics. International Geophysics Series. Elsevier.

Grant, J.A., 2005. Isocon analysis: a brief review of the method and applications. Physics and Chemistry of the Earth 30, 997–1004.

Hansmann, W., Oberli, F., 1991. Zircon inheritance in an igneous rock suite from the southern Adamello batholith (Italian Alps). Contributions to Mineralogy and Petrology 107, 501–518.

Imber, J., Holdsworth, R.E., Butler, C.H., Strachan, R.A., 2001. A reappraisal of the Sibson–Scholz fault zone model: the nature of the frictional to viscous ("brittle–ductile") transition along a long-lived, crustal-scale fault, Outer Hebrides, Scotland. Tectonics 20 (5), 601–624.

Jefferies, S.P., Holdsworth, R.E., Wibberley, C.A.I., Shimamoto, T., Spiers, C.J., Niemeijer, A.R., Lloyd, G.E., 2006. The nature and importance of phyllonite development in crustal-scale fault cores: an example from the Median Tectonic Line, Japan. Journal of Structural Geology 28, 220–235.

Kirkpatrick, J.D., Shipton, Z.K., Persano, C., 2009. Pseudotachylytes: rarely generated, rarely preserved or rarely reported? Bulletin of the Seismological Society of America 99, 382–388.

Kostrov, B., Das, S., 1988. Principles of Earthquake Source Mechanics. Cambridge University Press, London.

Jaeger, J.C., Cook, N.G.W., Zimmerman, R.W., 2007. Fundamentals of Rock Mechanics. Blackwell Publishing.

John, B.E., Blundy, J.D., 1993. Emplacement-relate deformation of granitoid magmas, southern Adamello Massif, Italy. Geological Society of America Bulletin 105, 1517–1541.

Lachenbruch, A.H., 1980. Frictional heating, fluid pressure and the resistance to fault motion. Journal of Geophysical Research 85, 6097–6112.

Lockner, D.A., Okubo, P.G., 1983. Measurements of frictional heating in granite. Journal of Geophysical Research 88, 4313–4320.

Magloughlin, J.F., Spray, J.G., 1992. Frictional melting processes and products in geological materials: introduction and discussion. Tectonophysics 204, 197–206.
Martin, S., Zattin, M., Del Moro, A., Macera, P., 1996. Chronologic constraints for the evolution of the Giudicarie belt (Eastern Alps, NE Italy). Annales Tectonicae 10, 60–79.
Mayer, A., Cortiana, G., Dal Piaz, G.V., Deloule, E., De Pieri, R., Jobstraibizer, P., 2003. U–Pb single zircon ages of the Adamello batholith, Southern Alps. Memorie di Scienze Geologiche 55, 151–167.
McKenzie, D., Brune, J.N., 1972. Melting on fault planes during large earthquakes. Geophysical Journal of the Royal Astronomical Society 29, 65–78.
Passchier, C.W., Trouw, R.A.J., 2005. Microtectonics, second ed. Springer, Berlin.
Pennacchioni, G., 2005. Control of the geometry of precursor brittle structures on the type of ductile shear zone in the Adamello tonalites, Southern Alps (Italy). Journal of Structural Geology 27, 627–644.
Pennacchioni, G., Di Toro, G., Brack, P., Menegon, L., Villa, I.M., 2006. Brittle–ductile–brittle deformation during cooling of tonalite (Adamello, Southern Italian Alps). Tectonophysics 427, 171–197.
Pennacchioni, G., Mancktelow, N., 2007. Nucleation and initial growth of a shear zone network within compositionally and structurally heterogeneous granitoids under amphibolite facies conditions. Journal of Structural Geology 29, 1757–1780.
Pittarello, L., Di Toro, G., Bizzarri, A., Pennacchioni, G., Hadizadeh, J., Cocco, M., 2008. Energy partitioning during seismic slip in pseudotachylyte-bearing faults (Gole Larghe Fault, Adamello, Italy). Earth and Planetary Science Letters 269, 131–139. doi:10.1016/j.epsl.2008.01.052.
Price, N.J., Cosgrove, J.W., 1990. Analyses of Geological Structures. Cambridge University Press.
Rice, J.R., 2006. Heating and weakening of faults during earthquake slip. Journal of Geophysical Research 111, B05311. doi:10.1029/2005JB004006.
Riklin, K., 1985. Contact metamorphism of Permian "red sandstones" in the Adamello area. Memorie della Società Geologica Italiana 26, 159–169 (1983).
Salomon, W., 1897. Über Alter, Lagerungsform und Entstehungsart der periadriatischen granitisch-körnigen Massen. Tschermaks mineralogische und petrographische Mitteilungen 17 (H 2/3), 109–284.
Scholz, C.H., 1988. The brittle–plastic transition and the depth of seismic faulting. Geologische Rundschau 77, 319–328.
Scholz, C.H., 2002. The Mechanics of Earthquakes and Faulting, second ed. Cambridge University Press.
Schmid, S.M., Aebli, H.R., Heller, F., Zingg, A., 1989. The role of the Periadriatic Line in the tectonic evolution of the Alps. In: Coward, M.P., Dietrich, D., Park, R.G. (Eds.), Alpine Tectonics. Geological Society Special Publication 45, pp. 153–171.
Sibson, R.H., 1973. Interactions between temperature and pore fluid pressure during earthquake faulting – a mechanism for partial or total stress relief. Nature 243, 66–68.
Sibson, R.H., 1974. Frictional constraints on thrust, wrench and normal faults. Nature 249, 542–544.
Sibson, R.H., 1975. Generation of pseudotachylyte from ancient seismic faulting. Geophysical Journal of the Royal Astronomical Society 43, 775–794.
Sibson, R.H., 1977. Fault rocks and fault mechanisms. Journal of the Geological Society 133 (3), 191–213.
Sibson, R.H., 1985. A note on fault reactivation. Journal of Structural Geology 7, 751–754.
Sibson, R.H., 1986. Brecciation processes in fault zones: inferences from earthquake rupturing. Pure and Applied Geophysics 124, 159–175.
Sibson, R.H., 1990. Rupture nucleation on unfavorably oriented faults. Bulletin of the Seismological Society of America 80, 1580–1604.
Sibson, R.H., Toy, V.G., 2006. The habitat of fault generated pseudotachylyte: presence vs. absence of frictional melt. In: Abercrombie, R., McGerr, A., Kanamori, H., Di Toro, G. (Eds.), Earthquakes: Radiated Energy and the Physics of Faulting. Geophysical Monograph Series, 170. AGU, pp. 153–166.
Spray, J.G., 1995. Pseudotachylyte controversy: fact or friction? Geology 23, 1119–1122.
Stipp, M., Stünitz, H., Heilbronner, R., Schmid, S.M., 2002. The eastern Tonale fault zone: a 'natural laboratory' for crystal plastic deformation of quartz over a temperature range from 250 °C to 700 °C. Journal of Structural Geology 24, 1861–1884.
Stipp, M., Fügenschuh, B., Gromet, L.P., Stünitz, H., Schmid, S.M., 2004. Contemporaneous plutonism and strike slip faulting: a case study from the Tonale fault zone north of the Adamello pluton (Italian Alps). Tectonics 23, TC3004. doi:10.1029/2003TC001515.
Trener, G.B., 1906. Geologische Aufnahme in nördlichen Abhang der Presanellagruppe. Jahrbuch der Kaisaerlich-königlichen geologische Reichsanstalt 56, 405–496.
Villa, I.M., Hermann, J., Müntener, O., Trommsdorff, V., 2000. 39Ar–40Ar dating of multiply zoned amphibole generations (Malenco, Italian Alps). Contributions to Mineralogy and Petrology 140, 363–381.
Viola, G., 2000. Kinematics and timing of the Periadriatic fault system in the Giudicarie region (central-eastern Alps). PhD thesis, ETH Zürich, Nr. 13590.
Viola, G., Mancktelow, N.S., Seward, D., 2001. Late Oligocene–Neogene evolution of Europe–Adria collision: new structural and geochronological evidence from the Giudicarie fault system (Italian Eastern Alps). Tectonics 20, 999–1020.
Werling, E., 1992. Tonale-, Pejo- und Judicarien-Linien: Kinematik, Mikrostrukturen und Metamorphose von Tektoniten aus räumlich interferienden aberverschiedenaltrigen Verwerfungszonen. PhD thesis, ETH, Zürich.
Woodcock, N.H., Mort, K., 2008. Classification of fault breccias and related fault rocks. Geological Magazine 145, 435–440.

*American Mineralogist, Volume 95, pages 405–409, 2010*

# Evidence of dmisteinbergite (hexagonal form of $CaAl_2Si_2O_8$) in pseudotachylyte: A tool to constrain the thermal history of a seismic event

**Fabrizio Nestola,[1,2,*] Silvia Mittempergher,[1] Giulio Di Toro,[1,3] Federico Zorzi,[1] and Danilo Pedron[4]**

[1]Dipartimento di Geoscienze, Università di Padova, Via Giotto 1, I-35137 Padova, Italy
[2]CNR-IGG, Sezione di Padova, Via Giotto 1, I-35137 Padova, Italy
[3]Istituto Nazionale di Geofisica e Vulcanologia, Via di Vigna Murata 605, 00143 Roma, Italy
[4]Dipartimento di Scienze Chimiche, Università di Padova, Via Marzolo 1, I-35137 Padova, Italy

## Abstract

The determination of the maximum temperature achieved by friction melt ($T_{melt}$) in pseudotachylyte-bearing faults is crucial to estimate earthquake source parameters (e.g., earthquake energy budgets, co-seismic fault strength) on a geological basis. Here we investigated the mineralogy of a pseudotachylyte from the Gole Larghe Fault (Italian Alps) by using X-ray powder diffraction, micro-Raman spectroscopy, and EDS-equipped field emission scanning electron microscopy. In particular, we report the presence of the hexagonal polymorph of $CaAl_2Si_2O_8$ (dmisteinbergite) in a pseudotachylyte. Published experimental work shows dmisteinbergite can crystallize at 1200–1400 °C by rapid quenching. Therefore, the presence of dmisteinbergite in pseudotachylyte could be a reliable geothermometer for friction melts for which $T_{melt}$ has only as yet been estimated.

**Keywords:** Pseudotachylyte, earthquake, dmisteinbergite, geothermometer

## Introduction

Tectonic pseudotachylyte (solidified friction melt produced during seismic slip) is the only fault rock that records unambiguously the occurrence of seismic ruptures in exhumed faults (Sibson 1975; Cowan 1999). Therefore, pseudotachylytes may potentially be used to constrain fault processes and seismic source parameters during an earthquake (Sibson 1975; Wenk et al. 2000; Hirose and Shimamoto 2005; Di Toro et al. 2005). For example, pseudotachylyte-bearing faults retain information on the earthquake energy budget (Pittarello et al. 2008) or on fault strength during seismic slip (Sibson 1975; Di Toro et al. 2005; Andersen et al. 2008) that is out of the range of seismological investigations (Kanamori and Heaton 2000). However, to determine, for instance, the amount of heat produced during seismic slip, one poorly constrained unknown parameter is the maximum temperature achieved by the friction melt ($T_{melt}$). The difficulty in estimating $T_{melt}$ arises from the fact that frictional melting is a non-equilibrium process (Bowden and Tabor 1950). Based on the melting temperatures of the single mineral phases of the host rock, it is only possible to estimate the minimum temperature of the melt (Spray 1992). Because melts may undergo further viscous shear heating during seismic slip (melt superheating, Di Toro and Pennacchioni 2005; Nielsen et al. 2008), it follows that $T_{melt}$ could be higher than temperature estimated from melting of single minerals. Pseudotachylytes consist of lithic clasts (i.e., grains that survive melting) suspended in glass-like (glass or cryptocrystalline to microcrystalline) matrix, which includes microlites nucleated during cooling of the melt (Shand 1916; see also Magloughlin and Spray 1992, Snoke et al. 1998, Lin 2008, and Di Toro et al. 2009 for reviews). Given the difficulties highlighted above, several methods have been used to estimate $T_{melt}$. These include the composition of the glass (Lin 1994a), the mineralogy of the newly grown microlites [two pyroxene geothermometer, Toyoshima (1990); omphacite-garnet geothermometer, Austrheim and Boundy (1994); plagioclase crystallization, Lin (1994b); olivine crystallization, Obata and Karato (1995); pigeonite crystallization, Camacho et al. (1995); mullite crystallization, Moecher and Brearley (2004); olivine, clino-, and ortho-pyroxene crystallization, Andersen and Austrheim (2006); the volume ratio between lithic clasts and matrix in pseudotachylytes, O'Hara (2001), the distribution of microstructures in pseudotachylyte veins, Di Toro and Pennacchioni (2004); or commonly, the mineralogy of the lithic clasts, Maddock (1983), Boullier et al. (2001)]. Using these methods, estimates of $T_{melt}$ in natural pseudotachylytes range between 750–1750 °C.

Here we have investigated pseudotachylytes from the Gole Larghe Fault (Italian Alps, Di Toro and Pennacchioni 2004) using X-ray powder diffraction (XRPD), micro-Raman spectroscopy (MRS), and EDS-equipped field emission scanning electron microscope (FESEM). Using this multidisciplinary approach, we have identified unambiguously in a pseudotachylyte the presence of the hexagonal polymorph of $CaAl_2Si_2O_8$ called dmisteinbergite (Chesnokov et al. 1990). Dmisteinbergite, although included in the feldspar group, is quite different in that it has a phyllosilicate crystal structure. Microlites of plagioclase are well known to be one of the most common constituents of the pseudotachylytes (Shand 1916; Philpotts 1964; Sibson 1975; Passchier 1982; Maddock 1983; Macaudière et al. 1985; Magloughlin 1992; Lin 1994b, 2008; Snoke et al. 1998 for several examples; Shimada et al. 2001; Plattner et al. 2003; Caggianelli et al. 2005), but until now, no dmisteinbergite has been identified, probably due to the analytical techniques applied. Dmisteinbergite was originally

* E-mail: fabrizio.nestola@unipd.it

0003-004X/10/0203–405$05.00/DOI: 10.2138/am.2010.3393 

described in pyrometamorphic rocks from naturally burned coal-bearing spoil-heaps (Chelyabinsk coal basin, Russia) (Chesnokov et al. 1990; Sokol et al. 1998 and references therein). However, unpublished data also describe large crystals of dmisteinbergite in association with a zeolite (wairakite, $CaAl_2Si_4O_{12}\cdot 2H_2O$) in a gabbro (Kurumazawa, Japan). Thus, dmisteinbergite apparently can form both from high temperature combined with rapid cooling (Sokol et al. 1998) or hydrothermally (wairakite occurs widely in low-grade metamorphic rocks, sedimentary environments, and hydrothermal areas; Ori et al. 2008 and references therein). Prior to these reports, dmisteinbergite was obtained only in the laboratory under specific conditions. For instance, Abe et al. (1991) demonstrated that dmisteinbergite crystallizes from a supercooled anorthitic melt and at temperatures between 1200–1400 °C. However, Borghum et al. (1993) showed that dmisteinbergite can also grow in hydrothermal conditions, confirming the above finding of such a phase in association with zeolites.

In this work, we report dmisteinbergite from a pseudotachylyte vein. As such a phase can crystallize only under specific conditions of temperature and cooling rate, its occurrence could be a useful temperature marker (possibly approaching $T_{melt}$) for extrapolating earthquake source parameters from exhumed faults.

## Geological setting

The pseudotachylyte was collected from the Gole Larghe Fault Zone, which cuts the tonalites of the Adamello batholith (Italian Southern Alps, for details about the fault zone, see Di Toro and Pennacchioni 2005). The fault zone consists of more than 200 sub-parallel cataclasite-pseudotachylyte-bearing faults and was active 30 Ma ago, at 9–11 km depth, 250–300 °C ambient temperature, and under low pore fluid conditions (Di Toro et al. 2005). The pseudotachylytes are associated with cataclasites (cohesive fault rocks formed by fragmented tonalite cemented by epidote, K-feldspar, and minor chlorite) within the host tonalites (plagioclase 48%, quartz 29%, biotite 17%, and K-feldspar 6%) (Di Toro and Pennacchioni 2004; the whole-rock chemical composition of the initial tonalite and of the pseudotachylyte matrix are reported in the same work). The studied sample is a 5–8 mm thick pseudotachylyte fault vein hosted in tonalite (no evidence of cataclasite precursor) and described in detail by Pittarello et al. (2008).

## Experimental methods

Microstructural investigations were performed on carbon-coated, polished thin sections with a field emission scanning electron microscope (FE-SEM) JSM6500F upgraded to version 7000 and equipped with an energy dispersive X-ray spectroscopy (EDS) analyzer with internal standards for quantitative chemical composition (Istituto Nazionale di Geofisica e Vulcanologia, Rome, INGV, Italy). Backscattered electron (BSE) images were collected at working distance of 10 mm and accelerating voltage of 10 kV; the BSE resolution in these conditions is 4 nm. The EDS electron beam spot size for analysis was 400 nm as estimated by means of Monte Carlo Method simulations.

Powder X-ray diffraction (XRPD) data were obtained by step scanning using an automated diffractometer system (Philips X'Change) with incident- and diffracted-beam soller slit (0.04 rad.). The instrument was equipped with a curved graphite diffracted-beam monochromator and a gas proportional detector. Divergence and antiscatter slits of 1/2° were used so that the irradiated area could be confined to the sample at angles >10 °2θ. A receiving slit of 0.2 mm was used. A long fine focus Cu X-ray tube was operated at 40 kV and 30 mA. Diffraction pattern was obtained using a step interval of 0.02 °2θ with a counting time of 15 s. The scan was performed over the range 3–70 °2θ. The program High Score Plus (PANalytical) was used for phase identification and Rietveld refinement (Rietveld 1967). The starting structural model of dmisteinbergite was from Takeuchi and Donnay (1959) (ICSD code 26486). A pseudo-Voigt function was employed for the profile shapes. Refined parameters were scale factors, zero-shift, background (Chebyshev function with 6 coefficients), lattice constants, and profile parameters (Gaussian and Lorentzian coefficients). The agreement indices were $R_p$ = 7.3% and $R_{wp}$ = 9.9%. For dmisteinbergite, $R_{Bragg}$ = 6.3%.

Raman spectra were collected from the same powdered material studied by XRPD with a home-built micro-Raman system, based on a single 320 mm focal length imaging spectrograph, a Triax-320 ISA instrument, equipped with a holographic 1800 g/mm grating and a liquid-nitrogen-cooled CCD detector (Spectrum One ISA Instruments). The excitation source was a Spectra Physics Ar+ laser (Stabilite 2017-06S) operating at 514.5 nm. A Kaiser Optical System holographic notch filter (514.5 nm) was used to reduce the stray-light level. An Olympus BX 40 optical microscope equipped with three objectives, 20×/0.35, 50×/0.75, and 100×/0.90, was optically coupled to the spectrograph. This made it possible to observe the sample with the microscope and then to select particular micrometric regions for Raman analysis. With the 100× objective, the lateral resolution is estimated to be 0.5 μm and the depth of focus between 1–2 μm. To avoid optical damage to the sample, the power of the exciting radiation was maintained between 10 and 50 mW. The Raman spectra were recorded between 147 and 1200 $cm^{-1}$ with an instrumental resolution of about 2 $cm^{-1}$.

## Results

Under the FE-SEM, the pseudotachylyte vein comprises clasts of quartz and plagioclase, immersed in a cryptocrystalline rock matrix composed of nanometer-sized biotite and plagioclase (as demonstrated by XRPD, see below) and micrometer-scale titanite-rich clusters (Fig. 1). The quartz clasts are rimmed by 500 nm thick, medium-gray Ca-rich layers and by micrometer-thick, dendritic, silica-rich layers (Fig. 1). EDS analysis of the medium-gray layer indicates the presence of a mineral phase with $CaAl_2Si_2O_8$ composition. Due to its identical composition to anorthite, we combined the experimental techniques of X-ray diffraction and Raman spectroscopy to determine that the $CaAl_2Si_2O_8$ phase was dmisteinbergite. Dmisteinbergite is likely also present in the cryptocrystalline pseudotachylyte. In fact, based on the quantitative analysis by the Rietveld method, the volume proportion of dmisteinbergite is too high to be accounted for solely by the thin rims surrounding the quartz grains. However, we could not identify dmisteinbergite in the matrix by Raman spectroscopy due to its small grain size, probably much smaller than the Raman probe size.

The XRPD diffractogram presented in Figure 2 unambiguously indicates the presence of dmisteinbergite with a volume proportion refined by Rietveld analysis (Rietveld 1967) of 18.2 wt%. The match between the XRPD profile of the Gole Larghe Fault dmisteinbergite and that reported in the literature (PDF2 ICDD 74-0814) is excellent (Fig. 2). The unit-cell parameters for dmisteinbergite obtained by indexing the reflections in Figure 2 are $a$ = 5.1100(2) Å, $c$ = 14.738(1) Å, and $V$ = 333.278 $Å^3$. The calculated $V$ reported here is 0.7% smaller than that given by Sokol et al. (1998), but this difference can be understood because the latter sample contained a small fraction of Na substituting for Ca. The overall quantitative analysis by the Rietveld method gives (in wt%): 40.5 quartz, 20.5 plagioclase, 18.2 dmisteinbergite, 17.5 biotite, and 3.3 titanite (Fig. 2).

Micro-Raman spectra collected on several pseudotachylyte grains in every case indicate the presence of dmisteinbergite and quartz. In Figure 3, the published spectrum of dmisteinbergite from the RRUFF Raman database (identification code R061075; Downs 2006) is compared to the spectrum collected in this work. At least five peaks match well those of the reference dmistein-

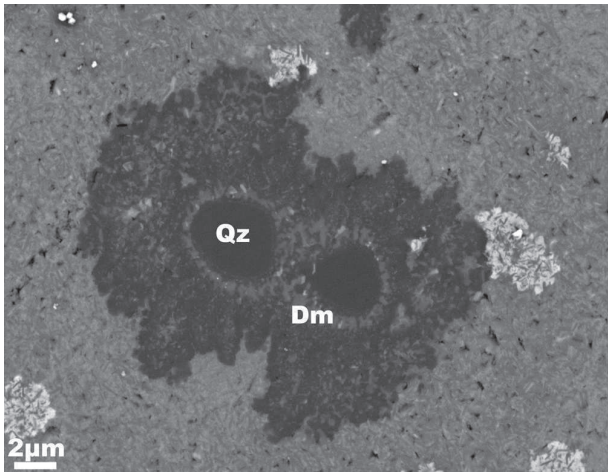


**FIGURE 1.** Pseudotachylyte from the Gole Larghe Fault. Microstructure of the pseudotachylyte vein: quartz clasts (Qz) are surrounded by a silica-rich, dendritic-like, dark colored halo; the dmisteinbergite (Dm) is the medium gray phase (grains are 200 nm in length) between the quartz clast and the dark halo. The matrix is composed of biotite, plagioclase and aggregates of titanite (bright spots) (BSE, FE-SEM image).

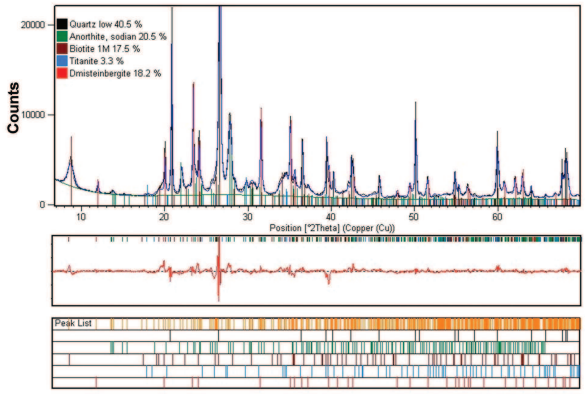


**FIGURE 2.** X-ray powder diffraction pattern of the Gole Larghe Fault pseudotachylyte. Black line = observed diffraction profile; blue line = calculated diffraction profile by Rietveld refinement; green line = background; red line = difference plot between observed and calculated diffraction profile.

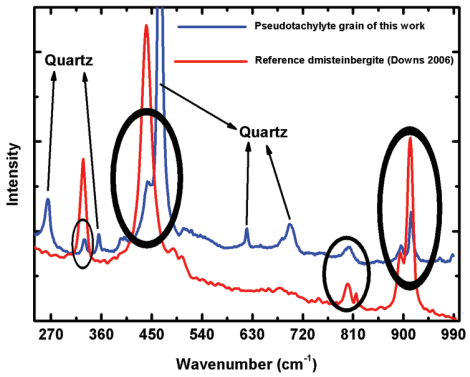


**FIGURE 3.** Raman spectrum of one grain from the same sample of pseudotachylyte studied by X-ray powder diffraction. Black line = measured spectrum; red line = Raman spectrum of dmisteinbergite (sample R040031, http://rruff.info/, Downs 2006). The ellipses highlight the match between the dmisteinbergite studied in this work and that reported in the RRUFF database.

bergite; the observed peaks 329.8, 441.8, 800.6, 895.5, and 913.6 $cm^{-1}$ exactly match the reference peaks 327.9, 439.8, 800.4, 894.4, and 912.3 $cm^{-1}$, within the 2 $cm^{-1}$ instrument resolution. The remaining peaks of our spectrum clearly belong to quartz (see reference quartz in the same Raman database, code R040031). For purpose of comparison and to show how dissimilar are the Raman spectra of the main phases found in our vein, we also give the main Raman peaks for anorthite (Raman database, code R040059, Downs 2006): 147, 196, 488, 505 (these two are the more intense for anorthite) and 559 $cm^{-1}$; and for biotite (Wang et al. 1994): 178, 549, 679, 717, 767 (these last three peaks are the more intense for biotite), and 3650 (OH group) $cm^{-1}$.

## DISCUSSION

Before it was identified in nature, dmisteinbergite was studied by several authors as a synthetic phase, and it was demonstrated that it could be obtained under high-temperature conditions and in a supercooled melt (e.g., Abe et al. 1991). Its rarity in nature is likely due to its metastability (Abe and Sunagawa 1995). Nucleation of metastable phases is known for several silicates and they are observed, for example, when a melt is cooled instantaneously or a glass is heated rapidly (Putnis and Bish 1983). Hexagonal form of $CaAl_2Si_2O_8$ was also synthesized by hydrothermal processing of monocalcium aluminate ($CaAl_2O_4$) and quartz at temperatures as low as 200 °C (Borghum et al. 1993), but such ambient conditions are ruled out for a pseudotachylyte produced by frictional melting of tonalite where the temperatures achieved are markedly higher and no monocalcium aluminate is available. Moreover, hydrothermal processing and alteration of the pseudotachylyte should have caused the breakdown of microlites of biotite into chlorite, a breakdown reaction that is not observed in the rocks studied. We consider dmisteinbergite found in this work of high-temperature origin for the following reasons: (1) presence of nano-crystals of dmisteinbergite, which is inconsistent with the hypothesis of a low-temperature and hydrothermal environment of crystallization (the only reported dmisteinbergite of low temperature in nature is present in crystals of centimeter size), and (2) absence of wairakite or other zeolite-type minerals that are found in association with dmisteinbergite in a hydrothermal environment.

Recent works focused on the high-temperature modifications of $CaAl_2Si_2O_8$ polymorphs reported by Abe et al. (1991) and Abe and Sunagawa (1995). In those works, the authors investigated a melt of pure anorthitic composition (plus a melt with composition anorthite:wollastonite = 80:20) and a melt with composition anorthite:forsterite:silica = 70:10:20, respectively. Abe et al. (1991) found that the hexagonal form of $CaAl_2Si_2O_8$ nucleates and grows prior to the appearance of stable anorthite when the melt is supercooled below 1200 °C, has a melting point of 1400 ± 15 °C, and rapidly disappears in the presence of anorthite. Abe and Sunagawa (1995), studying an impure anorthitic composition, found that by supercooling the melt (with a $\Delta T$ = 350–400 °C) down to 1100–1000 °C, dmisteinbergite nucleates dominantly instead of anorthite (similar to the $An_{100}$ and $An_{80}Wo_{20}$ melts see Abe et al. 1991). In conclusion, they found that the hexagonal form of

$CaAl_2Si_2O_8$ cannot coexist in nature with anorthite. In early work on anorthitic melt compositions (Davis and Tuttle 1951), it was found that rapid quenching of the melt to 1200 °C yields only the hexagonal polymorph. Bruno et al. (1976) also observed that for an anorthitic melt quenched from 1530 °C to room temperature in a few seconds, only anorthite is produced. Based on these experimental results, it appears that the presence of dmisteinbergite in natural pseudotachylytes could be a reliable indicator of high-temperature conditions and extremely rapid quenching.

The direct extrapolation of experimental results to natural conditions is not straightforward. First, the bulk composition of the pseudotachylyte precursor (i.e., tonalite or cataclasite in the case of the Gole Larghe Fault zone) is not pure anorthite. However, the high-temperature experiments on the hexagonal form of $CaAl_2Si_2O_8$ were also performed on impure anorthitic composition, yielding similar results (Abe and Sunagawa 1995). Therefore, the temperature of the polymorphic transformation of $CaAl_2Si_2O_8$ does not depend upon the initial bulk composition of the melt but only on the temperature and on the rate of supercooling. Second, the pseudotachylyte from the Gole Larghe Fault Zone was produced at 10 km depth (which corresponds to a confining pressure of 0.25 GPa) and probably under low pore pressures (Di Toro and Pennacchioni 2004; Di Toro et al. 2005). However, Morse (1980) showed that the confining pressure (at least up to 1 GPa) does not have any effect on the melting point for a pure anorthite and it increases the melting point by only 10–15 °C for $An_{80}Ab_{20}$ compositions. Third, dmisteinbergite has a crystal structure (i.e., sheet silicate) totally distinct from that of anorthite (Ito 1976). This implies that the transformation from dmisteinbergite to anorthite must be reconstructive (i.e., breaking and formation of new chemical bonds), a type of lattice rearrangement that requires high activation energies and transition times on the order of minutes.

The sample studied was extracted from a pseudotachylyte-bearing fault vein that was 8 mm thick. In the case of an 8 mm thick melt layer with an initial temperature of 1450 °C and hosted in a rock at 250 °C, thermal modeling suggests that cooling rates can be as large as 100–200 °C/s approaching the center of the vein (at the vein margins cooling to about half of the initial temperature of the melt is almost instantaneous: see Di Toro and Pennacchioni 2004 for thermal modeling details). It follows that the dmisteinbergite was preserved in the pseudotachylyte because the lattice rearrangement to anorthite would have required longer times to transform (Abe and Sunagawa 1995). The finding of dmisteinbergite suggests $T_{melt}$ close to 1400 °C, consistent with the previous estimate of 1450 °C based on the distribution of the microstructures in the pseudotachylyte (Di Toro and Pennacchioni 2004). However, the previous $T_{melt}$ estimate was based on many assumptions and time consuming microstructural work.

This is only the third reported occurrence of dmisteinbergite in nature; therefore, it would appear that dmisteinbergite cannot be a useful thermal marker because of its rarity. In addition, to identify this mineral several analytical techniques in combination are required. However, given the small grain size, we suggest that dmisteinbergite may not be so rare, but rather that its abundance is simply underestimated. We expect dmisteinbergite is probably more common than reported in rocks produced during large thermal pulses (e.g., seismic faulting, but also meteorite impacts).

## Acknowledgments

Anne Marie Boullier, Torgeir Andersen, John Spray, and Chris Holl are thanked for carefully reading and strongly improving the work. G.J. Redhammer and an anonymous referee together provided crucial help. We thank the HPHT INGV laboratories (P. Scarlato. J. Taddeucci, and A. Cavallo) in Rome for FESEM facilities and L. Tauro and E. Masiero for thin section preparation. S.M. was granted by CARIPARO foundation (project code: CD0504012134), G.D.T. by the European Research Council Starting Grant project no. 205175 (USEMS).

## References cited

Abe, T. and Sunagawa, I. (1995) Hexagonal $CaAl_2Si_2O_8$ in a high-temperature solution; metastable crystallization and transformation to anorthite. Mineralogical Journal, 17, 257–281.

Abe, T., Tsukamoto, K., and Sunagawa, I. (1991) Nucleation, growth and stability of $CaAl_2Si_2O_8$ polymorphs. Physics and Chemistry of Minerals, 17, 473–484.

Andersen, T.B. and Austrheim, H. (2006) Fossil earthquakes recorded by pseudotachylytes in mantle peridotite from the Alpine subduction complex of Corsica. Earth and Planetary Science Letters, 242, 58–72.

Andersen, T.B., Mair, K., Austrheim, H., Podladchikov, Y.Y., and Vrijmoed, J.C. (2008) Stress release in exhumed intermediate and deep earthquakes determined from ultramafic pseudotachylyte. Geology, 36, 995–998.

Austrheim, H. and Boundy, T.M. (1994) Pseudotachylytes generated during seismic faulting and eclogitization of the deep crust. Science, 265, 82–83.

Borghum, B.P., Bukowski, J.M., and Young, J.F. (1993) Low-temperature synthesis of hexagonal anorthite via hydrothermal processing. Journal of the American Ceramic Society, 76, 1354–1356.

Boullier, A.M., Ohtani, T., Fujimoto, K., Ito, H., and Dubois, M. (2001) Fluid inclusions in pseudotachylytes from the Nojima fault, Japan. Journal of Geophysical Research, 106, 21965–21977.

Bowden, F.P. and Tabor, D. (1950) The Friction and Lubrication of Solids, 374 p. Clarendon Press, Oxford.

Bruno, E., Chiari, G., and Facchinelli, A. (1976) Anorthite quenched from 1530 °C. Structure refinement. Acta Crystallographica, B32, 3270–3280.

Caggianelli, A., De Lorenzo, S., and Prosser, G. (2005) Modeling the heat pulses generated on a fault plane during coseismic slip: Inferences from the pseudotachylytes of the Copanello cliffs (Calabria, Italy). Tectonophysics, 405, 99–119.

Camacho, A., Vernon, R.H., and Fitz Gerald, J.D. (1995) Large volumes of anhydrous pseudotachylyte in the Woodroffe Thrust, eastern Musgrave Ranges, Australia. Journal of Structural Geology, 17, 371–383.

Chesnokov, B.V., Lotova, E.V., Nigmatulina, E.N., Pavlyuchenko, V.S., and Bushmakin, A.F. (1990) Dmisteinbergite $CaAl_2Si_2O_8$ (hexagonal)—A new mineral. Zapiski Vsesoyuz Mineralogicheskogo Obshchestva, 119, 43–45.

Cowan, D.S. (1999) Do faults preserve a record of seismic faulting? A field geologist's opinion. Journal of Structural Geology, 21, 995–1001.

Davis, G.L. and Tuttle, O.F. (1951) Two new crystalline phases of the anorthite composition, $CaO\,Al_2O_3{\cdot}SiO_2$. American Journal of Sciences, Bowen Volume, 107–114.

Di Toro, G. and Pennacchioni, G. (2004) Superheated friction-induced melts in zoned pseudotachylytes within the Adamello tonalites (Italian Southern Alps). Journal of Structural Geology, 26, 1783–1801.

——— (2005) Fault plane processes and mesoscopic structure of a strong-type seismogenic fault in tonalites (Adamello batholith, Southern Alps). Tectonophysics, 402, 54–79.

Di Toro, G., Pennacchioni, G., and Teza, G. (2005) Can pseudotachylytes be used to infer earthquake source parameters? An example of limitations in the study of exhumed faults. Tectonophysics, 402, 3–20.

Di Toro, G., Pennacchioni G., and Nielsen, S. (2009) Pseudotachylytes and earthquake source mechanics. In E. Fukuyama, Ed., Fault-zone Properties and Earthquake Rupture Dynamics, p. 87–133. International Geophysics Series, Elsevier, Amsterdam.

Downs, R.T. (2006) The RRUFF Project: An integrated study of the chemistry, crystallography, Raman and infrared spectroscopy of minerals. Program and Abstracts of the 19th General Meeting of the International Mineralogical Association in Kobe, Japan. O03-13.

Hirose, T. and Shimamoto, T. (2005) Slip-weakening distance of faults during frictional melting as inferred from experimental and natural pseudotachylytes. Bullettin of the Seismological Society of America, 95, 1666–1673.

Ito, J. (1976) High temperature solvent growth of anorthite on the join $CaAlSi_2O_8$-$SiO_2$. Contributions to Mineralogy and Petrology, 59, 187–194.

Kanamori, H. and Heaton, T.H. (2000) Microscopic and macroscopic physics of earthquakes. In J. Rundle, D.L. Turcotte, and W. Klein, Eds., Geocomplexity and the Physics of Earthquakes, 120, p. 147–163. AGU Monograph Series, Washington, D.C.

Lin, A. (1994a) Glassy pseudotachylytes from the Fuyun Fault Zone, Northwest China. Journal of Structural Geology, 16, 71–83.

——— (1994b) Microlite morphology and chemistry in pseudotachylyte, from the Fuyun Fault Zone, Northwest China. Journal of Geology, 102, 317–329.

——— (2008) Fossil Earthquakes: The Formation and Preservation of Pseudotachylytes, 348 p. Springer, Berlin.
Macaudière, J., Brown, L.W., and Ohnenstetter, D. (1985) Microcrystalline textures resulting from rapid crystallization in a pseudotachylite melt in a metaanorthosite. Contribution to Mineralogy and Petrology, 89, 39–51.
Maddock, R.H. (1983) Melt origin of fault-generated pseudotachylytes demonstrated by textures. Geology, 11, 105–108.
Magloughlin, J.F. (1992) Microstructural and chemical changes associated with cataclasis and frictional melting at shallow crustal levels: The cataclasite-pseudotachylyte connection. Tectonophysics, 204, 243–260.
Magloughlin, J.F. and Spray, J.G. (1992) Frictional melting processes and products in geological materials: introduction and discussion. Tectonophysics, 204, 197–206.
Moecher, D.P. and Brearley, A.J. (2004) Mineralogy and petrology of a mullite-bearing pseudotachylyte: Constraints on the temperature of coseismic frictional fusion. American Mineralogist, 89, 1486–1495.
Morse, S.A. (1980) Basalts and Phase Diagrams, p. 493. Springer-Verlag, New York.
Nielsen, S., Di Toro, G., Hirose, T., and Shimamoto, T. (2008) Frictional melt and seismic slip. Journal of Geophysical Research, 113, B01308, DOI: 10.1029/2007JB005122.
Passchier, C.W. (1982) Pseudotachylyte and the development of ultramylonite bands in the Saint-Barthelémy Massif, French Pyrenees. Journal of Structural Geology, 4, 69–79.
Philpotts, A.R. (1964) Origin of Pseudotachylites. American Journal of Science, 262, 1008–1035.
Plattner, U., Markl, G., and Sherlock, S. (2003) Chemical heterogeneities of Caledonian (?) pseudotachylites in the Eidsfjord Anorthosite, north Norway. Contributions to Mineralogy and Petrology, 145, 316–338.
Obata, M. and Karato, S. (1995) Ultramafic pseudotachylyte from the Balmuccia peridotite, Ivrea-Verbano zone, Northern Italy. Tectonophysics, 242, 313–328.
O'Hara, K. (2001) A pseudotachylyte geothermometer. Journal of Structural Geology, 23, 1345–1357.
Ori, S., Quartieri, S., Vezzalini, G., and Dmitriev, V. (2008) Pressure-induced structural deformation and elastic behavior of wairakite. American Mineralogist, 93, 53–62.
Pittarello, L., Di Toro, G., Bizzarri, A., Pennacchioni, G., Hadizadeh, J., and Cocco, M. (2008) Energy partitioning during seismic slip in pseudotachylyte-bearing faults (Gole Larghe Fault, Adamello, Italy). Earth and Planetary Science Letters, 269, 131–139.
Putnis, A. and Bish, D.L. (1983) The mechanism and kinetics of Al,Si ordering in Mg-cordierite. American Mineralogist, 68, 60–65.
Rietveld, H.M. (1967) Line profiles of neutron powder-diffraction peaks for structure refinement. Acta Crystallographica, 22, 151–152.
Shand, S.J. (1916) The pseudotachylyte of Parijs (Orange Free State) and its relation to "trap-shotten gneiss" and "flinty crush-rock." Quarterly Journal of the Geological Society of London, 72, 198–221.
Shimada, K., Kobari, Y., Okamoto, T., Takagi, H., and Saka, Y. (2001) Pseudotachylyte veins associated with granitic cataclasite along the Median Tectonic Line, eastern Kii Peninsula, Southwest Japan. The Journal of the Geological Society of Japan, 107, 117–128.
Sibson, R.H. (1975) Generation of pseudotachylyte by ancient seismic faulting. Geophysical Journal of the Royal Astronomical Society, 43, 775–794.
Snoke, A.W., Tullis, J., and Todd, V. (1998) Fault-related Rocks. A Photographic Atlas, p. 617. Princeton University Press, New Jersey.
Sokol, E., Volkova, N., and Lepezin, G. (1998) Mineralogy of pyrometamorphic rocks associated with naturally burned coal-bearing spoil-heaps of the Chelyabinsk coal basin, Russia. European Journal of Mineralogy, 10, 1003–1014.
Spray, J.G. (1992) A physical basis for the frictional melting of some rock-forming minerals. Tectonophysics, 204, 205–221.
Takeuchi, Y. and Donnay, G. (1959) The crystal structure of hexagonal $CaAl_2Si_2O_8$. Acta Crystallographica, 12, 465–470.
Toyoshima, T. (1990) Pseudotachylite from the Main Zone of the Hidaka metamorphic belt, Hokkaido, northern Japan. Journal of Metamorphic Geology, 8, 507–523.
Wang, A., Han, J., Guo, L., Yu, J., and Zeng, P. (1994) Database of standard Raman spectra of minerals and related inorganic crystals. Applied Spectroscopy, 48, 959–968.
Wenk, H.R., Johnson, L.R., and Ratschbacher, L. (2000) Pseudotachylites in the Eastern Peninsular Ranges of California. Tectonophysics, 321, 253–277.

Manuscript received September 3, 2009
Manuscript accepted October 20, 2009
Manuscript handled by Bryan Chakoumakos

# Evidence of transient increases of fluid pressure in SAFOD phase III cores

Silvia Mittempergher,[1,2] Giulio Di Toro,[1,3] Jean Pierre Gratier,[2] Jafar Hadizadeh,[4] Steven A. F. Smith,[3] and Richard Spiess[1]

Received 11 November 2010; revised 13 December 2010; accepted 27 December 2010; published 1 February 2011.

[1] The San Andreas Fault Observatory at Depth (SAFOD) in Parkfield, central California, has been drilled through a fault segment that is actively deforming through creep and microearthquakes. Creeping is accommodated in two fault strands, the Southwest and Central Deforming Zones, embedded within a damaged zone of deformed shale and siltstone. During drilling, no pressurized fluids have been encountered, even though the fault zone acts as a permeability barrier to fluid circulation between the North American and Pacific plates. Microstructural analysis of sheared shales associated with calcite and anhydrite-bearing veins found in SAFOD cores collected at 1.5m from the Southwest Deforming Zone, suggests that transient increases of pore fluid pressure have occurred during the fault activity, causing mode I fracturing of the rocks. Such build-ups in fluid pressure may be related to permeability reduction during fault creep and pressure-solution processes, resulting in localized failure of small fault zone patches and providing a potential mechanism for the initiation of some of the microearthquakes registered in the SAFOD site. **Citation:** Mittempergher, S., G. Di Toro, J. P. Gratier, J. Hadizadeh, S. A. F. Smith, and R. Spiess (2011), Evidence of transient increases of fluid pressure in SAFOD phase III cores, *Geophys. Res. Lett.*, *38*, L03301, doi:10.1029/2010GL046129.

## 1. Introduction

[2] The NSF EarthScope San Andreas Fault Observatory at Depth (SAFOD) in Parkfield offers the opportunity to correlate physical and chemical processes identified in core samples with high-resolution seismological and geophysical data [*Zoback et al.*, 2010]. The SAFOD is located in the transition zone between the creeping segment of the SAF (to the north), and the southern "locked" segment, which lastly ruptured in the 1857 $M_w$7.8 Fort Tejon earthquake (Figure 1a). Near Parkfield, the SAF activity includes permanent creep at about 20 mm $yr^{-1}$ [*Titus et al.*, 2006], microearthquakes [e.g., *Nadeau and Johnson*, 1998] and moderate (~M6) earthquakes-that have nucleated at fairly regular intervals between 1857 and 2004 [e.g., *Bakun et al.*, 2005]. The SAFOD main hole crosses the actively deforming SAF at about 2.7km of vertical depth, approximately 100m above the hypocentral area of a cluster of repeating M2 earthquakes, which was one of the targets for drilling [*Nadeau et al.*, 2004]. During 2007, about 40 m of core was extracted parallel to the main hole, including a section that crosses the two actively creeping strands of the fault detected by borehole casing deformation, named Southwest Deforming Zone (SDZ) and Central Deforming Zone (CDZ) [*Zoback et al.*, 2010] (Figures 1a–1c).

[3] Slip in the SAF occurs at much lower shear stress than expected based on laboratory friction of rock forming minerals [*Brune et al.*, 1969], suggesting that it behaves as a weak fault in a strong crust [*Rice*, 1992]; such a model is confirmed by down hole stress measurements and mechanical modeling [*Hickman and Zoback*, 2004; *Chéry et al.*, 2004; *Boness and Zoback*, 2006]. Pressurization of the fault core by pore fluids was one of the explanations suggested for the low strength of the SAF [*Rice*, 1992]. Since no fluid pressure higher than hydrostatic has been detected during drilling [*Zoback et al.*, 2010], the most convincing mechanisms remain the presence of intrinsically weak material within the actively creeping sections [e.g., *Moore and Rymer.*, 2007] and the effect of stress driven pressure solution creep processes [*Gratier et al.*, 2009]. The study of the source mechanisms of repeating microearthquakes in Parkfield at depth of 2–5 km reveals peak stress drops exceeding 50MPa [*Imanishi and Ellsworth*, 2006; *Dreger et al.*, 2007], suggesting that relatively strong asperities exist within an otherwise weak fault zone.

[4] We performed microstructural, mineralogical and geochemical analyses on samples collected at 1.5m from the south-eastern boundary of the SDZ. The sampled core shows contemporary occurrence of veins and sheared shales (Figure 1d). Here we provide possible evidence of fracture opening in the presence of fluids and discuss mechanisms for permeability reduction and strength recovery after failure. The analytical techniques applied, including X-Ray Powder Diffraction (XRPD), X-Ray Fluorescence (XRF) mapping, Field-Emission Scanning Electron Microscope (FE-SEM), cathodoluminescence (CL) optical microscope and Electron Back Scatter Diffraction (EBSD), are described in the auxiliary material.[1]

## 2. The Sample

[5] The damage zone of the SAF is identified in the borehole as a zone of low seismic velocities (Figure 1c), and is composed of sheared and fractured shales, siltstones and sandstones of the Great Valley Formation [*Solum et al.*, 2006] (Figure 1b). The studied core section includes sheared Fe-rich

[1]Dipartimento di Geoscienze, Università di Padova, Padua, Italy.
[2]LGIT, Université Joseph Fourier – Grenoble I, Grenoble, France.
[3]Istituto Nazionale di Geofisica e Vulcanologia, Rome, Italy.
[4]Department of Geography and Geosciences, University of Louisville, Louisville, Kentucky, USA.


0094-8276/11/2010GL046129

[1]Auxiliary materials are available in the HTML. doi:10.1029/2010GL046129.

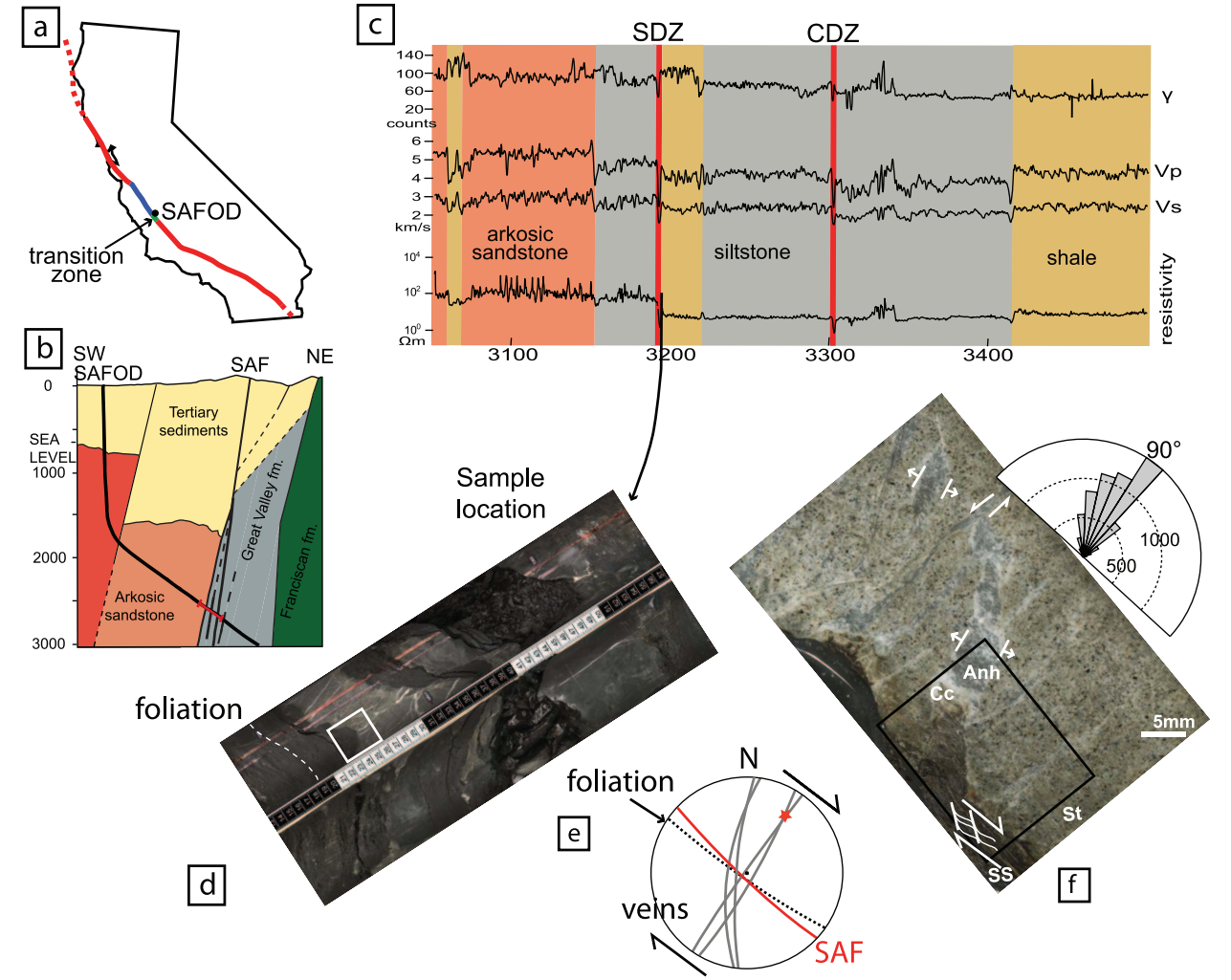


**Figure 1.** Sample location. (a) Sketch of the SAFOD location in California. The SAF is in red (locked segments), blue (creeping section) and green (transition zone). (b) Schematic geological section of the SAFOD site, parallel to the borehole trajectory (thick black line) [*Zoback et al.*, 2010]. In red, the segment enlarged in Figure 1a. (c) The downhole geophysical logs of the SAFOD main hole, with the location of the sample (black arrow). Highlighted in red, the actively deforming fault strands. (d) The studied core section (image from http://www.earthscope.org/observatories/safod/). (e) Lower hemisphere stereoplot of great circles corresponding to the attitude of the SAF in Parkfield (red, datum from *Boness and Zoback* [2006]) and the inferred attitude of the foliation planes in the studied core (dotted line) and the vein planes (gray). (f) Polished thin section, reflected light photomosaic (Cc: calcite, Anh: anhydrite, SS: sheared shale, St: sandstone). Inset: rose diagram of the orientation of the anhydrite-calcite veins, referred to the foliation in the gouge; dashed lines contours the number of counted segments (see auxiliary material for details of fracture counting). The black square is the area in Figure 2a.

shales with embedded veined sandstone ribbons (Figure 1d). The phase III cores have been drilled along a trajectory parallel to that of the main hole, and we consider the attitude of the main hole axis as a reference to infer an approximate orientation of the sample. Using the foliation in the shale as reference plane and assuming that its attitude is roughly parallel to the SAF plane (Figures 1d and 1e), the veins are subvertical and make an angle of 40–100° clockwise with the foliation plane (Figures 1e and 1f).

## 3. Observations

[6] The sandstone in the studied core is medium grained (<500 $\mu$m), composed of clasts of plagioclase, K-feldspar, quartz, mica and bioclasts and cemented by quartz. Pervasive macroscopic and microscopic veins in the sandstone are sealed by calcite and anhydrite; the veins crosscutting the boundary between sheared shale and sandstone are intruded by the shale (Figures 1f and 2a). The veins oriented at an acute angle to the shale foliation are extensional, while those roughly perpendicular to the shale foliation show extension with a component of sinistral shear (Figure 1f).

[7] The sheared shale is composed of illite and illite-smectite interlayers (altogether 48.9%), quartz (18.9%), albite (14.5%), K-feldspar (11.2%) and chlorite (4.9%), with minor calcite (1.1%) and pyrite (0.5%) (Rietveld XRPD quantitative analysis). The illite-smectite interlayers contain about 20% smectite. The sheared shale is foliated along clay-rich

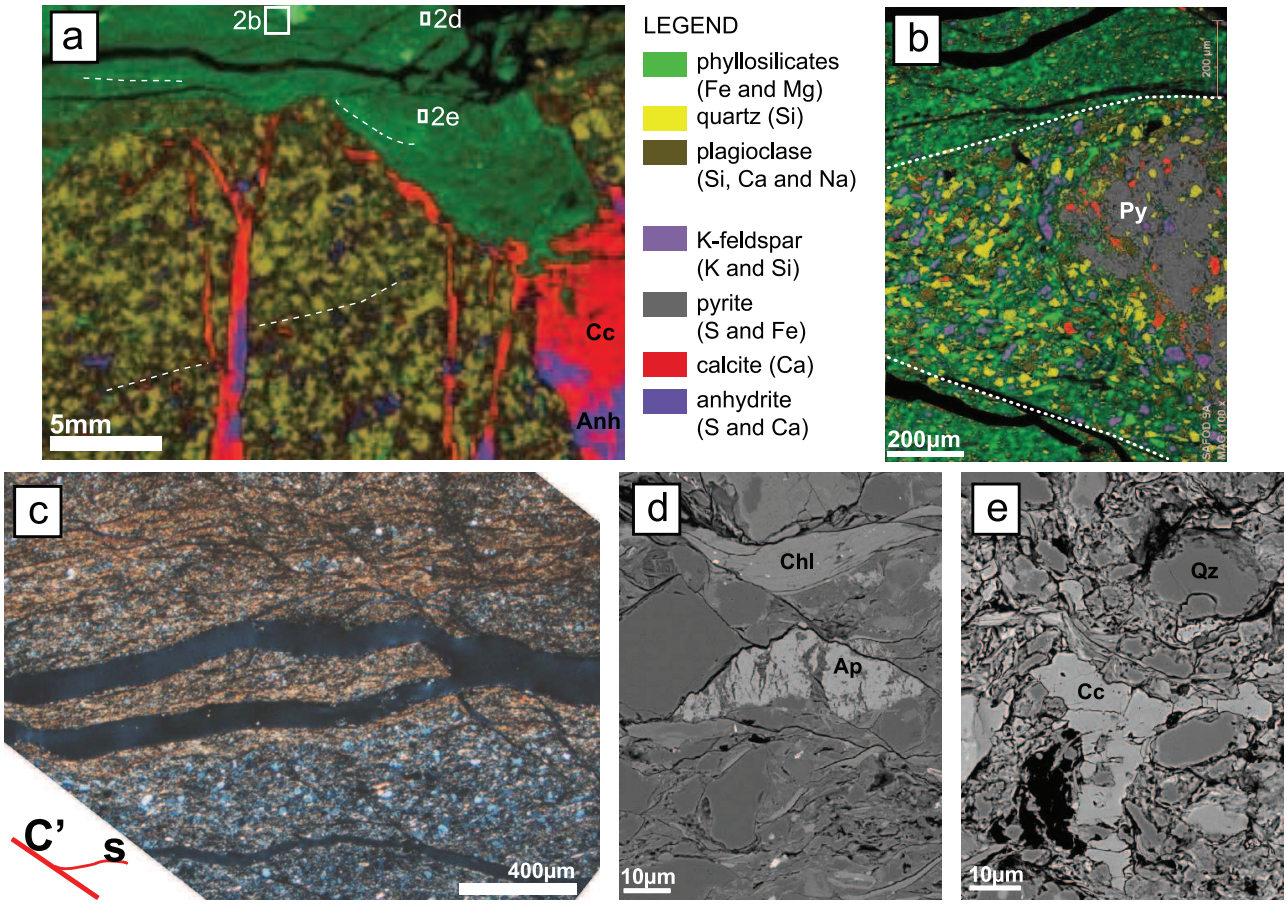


**Figure 2.** Geochemistry and microstructures. (a) Elemental chemical composition by superimposition of XRF chemical maps. Dashed lines: phyllosilicate-rich dissolution seams. (b) Detail of the elemental composition of a strain shadow around a pyrite clast (Py) within the sheared shale. Outside the strain shadow (dashed white line), there is sharp grainsize reduction, leaching of Ca and Si, and passive concentration of Fe and Mg-bearing phyllosilicates (superimposition of SEM-EDS chemical maps). (c) Foliated clay-rich shale with S-C′ foliation (optical micrograph, crossed Nicols). (d) Fractures within an apatite (Ap) clast filled by fibrous Illite-Smectite (I-S) lamellae. The S foliation is defined by a chlorite crystal (FE-SEM BSE image). (e) Blocky calcite filling the pore spaces within the shale particles from the apical part of the vein intruding the sandstone (FE-SEM BSE image).

dissolution seams, bended toward the intrusion in the veins (XRF chemical map, Figure 2a). The material within the foliation planes have smaller grain size and is depleted in Ca, Na, K, Si and enriched in Fe and Mg relative to the less deformed shale. This evolution is seen when comparing the foliation with the initial texture preserved within a strain shadow around a pyrite clast (Figure 2b). Locally the foliation shows an S-C′ texture [*Passchier and Trouw*, 2005] (Figures 2c and 2d). FE-SEM observations show that fibrous, micrometric illite-smectite lamellae have grown in strain shadows around clasts and within intragranular microcracks (Figure 2d). In the apical part of the veins (Figures 2a and 2e) intruded by randomly arranged clays and clasts from the shale layer, the pore spaces are filled by calcite (Figure 2e). The calcite and anhydrite crystals sealing the veins are mostly euhedral, forming a blocky texture [*Passchier and Trouw*, 2005], and include domains of elongated crystals (Figure 3a). Calcite shows thin and straight twins, a texture typical of deformation at temperatures below 200°C [*Ferrill et al.*, 2004]. Under the cathodoluminescence microscope, calcite has either dark or light orange luminescence. In the thick vein in Figure 2a, the calcite crystals close to the vein borders have a dark nucleus and a lighter rim and have a blocky texture. In contrast, the calcite crystals towards the vein centre have light rims alternating with dark rims and crystals are elongated with the long axis perpendicular to the vein walls (stretched-fibrous texture) (Figure 3a). In the latter texture, the associated anhydrite crystals show similar stretched-fibrous crystals associated with microcracks oriented parallel to the long axis of the light and dark luminescence rims in calcite. EBSD analysis on calcite has been performed along the vein borders (blocky calcite, Figure 3b), and towards the vein centre (elongated calcite, Figure 3c). The pole figures in blocky and elongated calcite show preferential distribution maximum density of the 'c' axes lower than 2.5 times the mean unit density (MUD), indicating a weak crystallographic preferred orientation (CPO). The blocky calcite is characterized by a weak maximum of the 'c' axes in a direction perpendicular to the vein borders. In elongated calcite, the

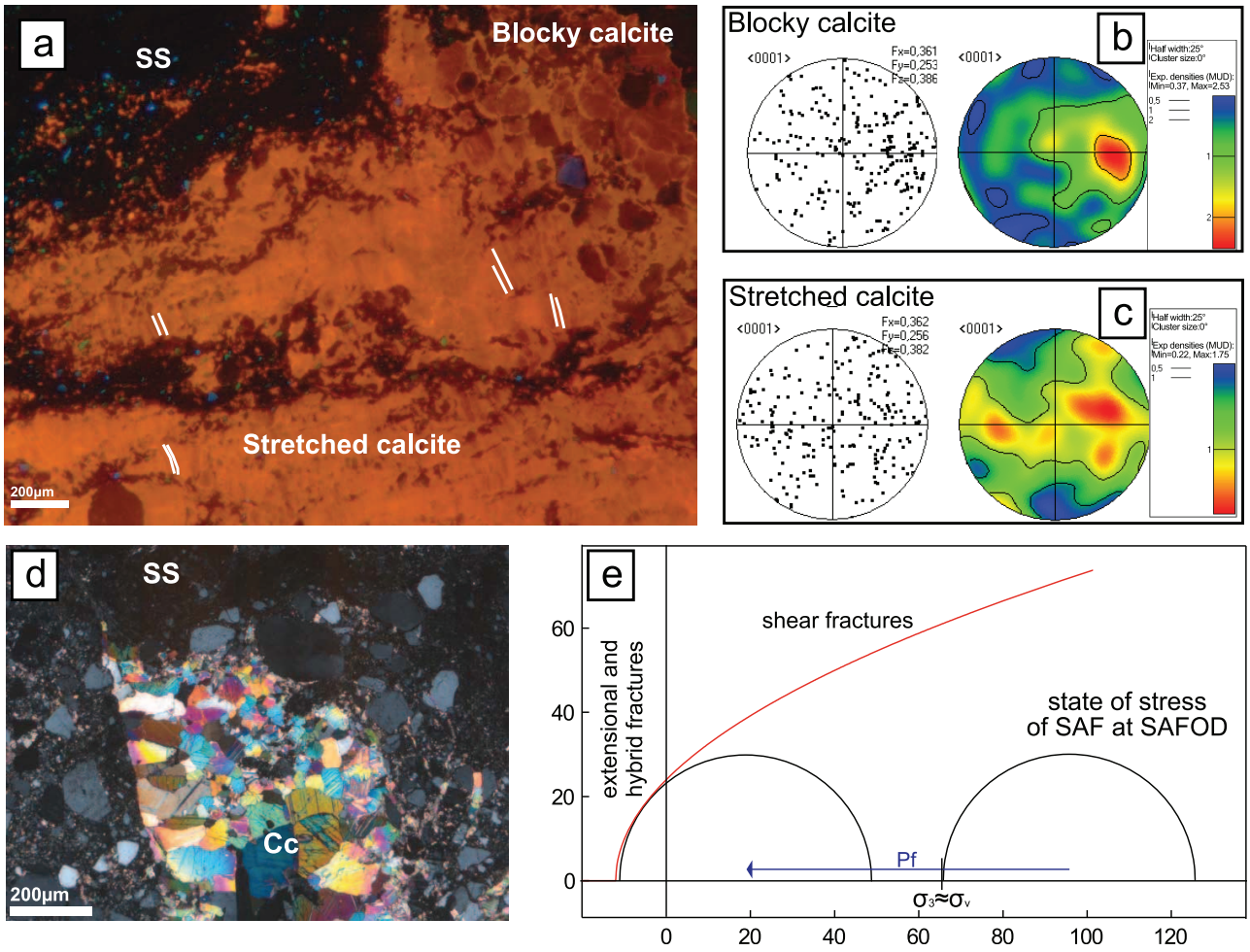


**Figure 3.** Microstructure of the calcite veins. (a) In blocky crystals close to the vein border, calcite is uniformly dark with a thin light rim; in the stretched calcite toward the vein centre, a fine scale banding of light and dark calcite is visible (CL micrograph). (b, c) EBSD data. C-axes orientation plotted in a lower hemisphere stereogram, as scattered data and contour plots; contours are expressed as multiples of mean unit density (MUD); the horizontal line in the pole figures coincides with the long axis of the CL micrograph. (d) Blocky calcite in the apical part of one of the veins, showing pervasive low temperature twinning. (e) Sketch of the Murrell-Griffith criterion of failure and the state of stress in the vicinity of the SAF [from *Hickman and Zoback*, 2004]. The conditions for extensional or hybrid fracturing are met when the least principal stress $\sigma_3$ is negative, after a negative shift due to pore pressure higher than the lithostatic value.

distribution of 'c' axes shows a minimum parallel to the vein borders, with the 'c' axes plotting within a broad girdle roughly perpendicular to the vein borders.

## 4. Discussion and Conclusions

[8] The creeping deformation within the SAF is localized within the SDZ and the CDZ. The samples we studied are from the deformed sediments at about 1.5 m from the SDZ margin, and thus the deformation structures we described cannot be rigorously related to the active deformation. The location of the microearthquakes associated to the SAF is even less constrained, since they register static stress drops (up to 120 MPa) compatible with fracturing in relatively strong rocks [*Imanishi and Ellsworth*, 2006]. Therefore, we suggest that the microearthquakes might be localized within the damaged zone, or at the boundaries between creeping zones and damage zone. Here we discuss how the deformation processes active within the siliciclastic sediments in the damage zone can cause local fluid overpressure and brittle failure.

[9] The development of a foliation in the sheared shale is associated with dissolution of quartz and feldspar clasts and growth of clay lamellae in microcracks. These processes are typical of stress driven pressure solution [*Gratier et al.*, 2009], and might cause permeability reduction due to passive concentration of clay minerals such as illite and illite-smectite, clast size reduction and pore space closure at the micrometric scale. The loss of Ca and Na and the passive enrichment in Fe and Mg along dissolution planes due to fault-perpendicular compression is a phenomenon documented at all scales in the SAF damage zone [*Schleicher et al.*, 2009; *Gratier et al.*, 2009]. Since dissolution planes are roughly perpendicular to the main compressive stress, they contribute to the development of fault-parallel permeability barriers that may separate compartments with distinct

fluid composition, as revealed by abrupt changes in real time mud gas analysis observed during drilling into the SAF [*Wiersberg and Erzinger*, 2008].

[10] Veining and dilational jogs (consistent with dextral sense of shear of the SAF) in other core sections are sealed by calcite and anhydrite, suggesting that mineral precipitation was related to the SAF activity (SAFOD, The core Atlas (version 4), 2010, available at http://www.earthscope.org/es_doc/data/safod/Core%20Photo%20Atlas%20v4.pdf). The blocky texture of calcite and the intimate intergrowth of calcite and anhydrite in the veins indicate that vein opening was faster than calcite and anhydrite growth [e.g., *Passchier and Trouw*, 2005], and mineral precipitation occurred into a free fluid in an open vein. This is supported by the weak CPO of blocky calcite with the 'c' axis perpendicular to the vein margins: after nucleation along the vein margins, calcite crystals, which are trigonal and thus anisotropic, grow faster in direction of the 'c' axis. This process would result in a weak CPO due to growth competition [*Nollet et al.*, 2005]. The intrusion of sheared shale into the veins is another indication that vein opening was sudden; disruption of foliation and calcite pore fillings within the intrusions suggest that the shale particles were mixed with fluids. The vein texture and their medium to high angle orientation to the foliation in the shale indicate that veins formed either as mode I fractures due to intrusion of pressurized shale material, or as hybrid shear – extensional [*Ramsey and Chester*, 2004] fractures. Following the Murrell-Griffith criterion of failure (Figure 3e), to form either extensional (mode I) or hybrid shear – extensional (modeI/modeII) fractures, it is necessary that the effective least principal stress is tensional: $\sigma'_3 = (\sigma_3 - P_f) < 0$. At about 2.7 km of depth, in the stress regime of the SAF, which is transitional between strike slip and reverse with $\sigma_h \approx \sigma_v$ as in the SAF, these conditions are satisfied when the fluid pressure is higher than lithostatic (Figure 3e).

[11] After sealing, the veins underwent further deformation, as suggested by twinning and stretching in calcite crystals. In elongated calcite, (1) the fine-scale alternation of light and dark luminescence rims and, (2) the 'c' axis preferentially oriented perpendicular to the vein margin (similar orientation as in the blocky grains), suggest incremental grain growth ("crack-seal", [*Ramsay*, 1980]), inheriting the orientation of the former blocky crystals (Figures 3a–3c). The change in calcite luminescence, which is influenced by traces of Fe and Mn, indicates a modification of fluid composition after the main fracturing episode.

[12] Following these observations, we propose that one of the possible mechanisms of rupture initiation in relatively "strong" rocks embedded within the damage zone of the SAF could be a transient increase of fluid pressure in isolated compartments where the circulation of fluids is limited by fault-parallel horizons consisting of insoluble minerals. Anomalies in the focal mechanisms of two M4 earthquakes in Parkfield area support a non double couple component, suggesting that some seismic ruptures might be initiated in presence of high fluid pressure and then propagate with a dominant shear component [*Johnson and Mc Evilly*, 1995]. Some of the "asperities" responsible for microearthquakes in the Parkfield segment of the SAF might thus be represented by compartments where the fluids might accumulate due to permeability reduction during compaction and pressure solution processes in clay-rich sedimentary inclusions or fault gouges [e.g., *Sleep and Blanpied*, 1992].

[13] **Acknowledgments.** We thank the HPHT INGV lab. for FE-SEM facilities (A. Cavallo, P. Scarlato). Grants: Padova University PhD scholarship (SM), CARIPARO project CD0504012134 (GDT), European Research Council Starting Grant Project 205175 (USEMS) (GDT and SAFS), INSU-C (JPG), Prin 2007BWMWM8 (RS). This material is based upon work supported by the US National Science Foundation NFS-Earthscope 0545472 (JH, GDT). We thank J. Richard, M.-L. Doan and Anne Marie Boullier for insightful discussions. The comments of D. Moore and J. Solum greatly improved the paper.

## References

Bakun, W. H., et al. (2005), Implications for prediction and hazard assessment from the 2004 Parkfield earthquake, *Nature*, *437*, 969–974, doi:10.1038/nature04067.

Boness, N., and M. D. Zoback (2006), A multi-scale study of the mechanisms controlling shear velocity anisotropy in the San Andreas Fault Observatory at Depth, *Geophysics*, *71*(5), F131–F146, doi:10.1190/1.2231107.

Brune, J. N., T. L. Henyey, and R. F. Roy (1969), Heat flow, stress, and rate of slip along the San Andreas Fault, California, *J. Geophys. Res.*, *74*, 3821–3827, doi:10.1029/JB074i015p03821.

Chéry, J., M. D. Zoback, and S. Hickman (2004), A mechanical model of the San Andreas Fault and SAFOD pilot hole stress measurements, *Geophys. Res. Lett.*, *31*, L15S13, doi:10.1029/2004GL019521.

Dreger, D., R. M. Nadeau, and A. Chung (2007), Repeating earthquake finite source models: Strong asperities revealed on the San Andreas Fault, *Geophys. Res. Lett.*, *34*, L23302, doi:10.1029/2007GL031353.

Ferrill, D. D., A. P. Morris, M. A. Evans, M. Burkhard, R. H. Groshong Jr., and C. M. Onasch (2004), Calcite twin morphology: A low temperature deformation geothermometer, *J. Struct. Geol.*, *26*, 1521–1529, doi:10.1016/j.jsg.2003.11.028.

Gratier, J. P., J. Richard, S. Mittempergher, F. Renard, M. Doan, G. Di Toro, J. Hadizadeh, and A. M. Boullier Bertrand (2009), Pressure solution as a mechanism of creep and sealing in active faults: Evidence from the SAFOD samples, *Eos Trans. AGU*, *90*(52), Fall Meet. Suppl., Abstract T21B-1800.

Hickman, S. H., and M. D. Zoback (2004), Stress orientation and magnitudes in the SAFOD pilot hole, *Geophys. Res. Lett.*, *31*, L15S12, doi:10.1029/2004GL020043.

Imanishi, K., and W. L. Ellsworth (2006), Source scaling relationships of microearthquakes at Parkfield, CA, determined using the SAFOD pilot hole seismic array, in *Earthquakes: Radiated Energy and the Physics of Earthquake Faulting*, *Geophys. Monogr. Ser.*, vol. 170, edited by R. Abercrombie et al., pp. 81–90, AGU, Washington, D. C.

Johnson, P. A., and T. V. Mc Evilly (1995), Parkfield seismicity: Fluid driven?, *J. Geophys. Res.*, *100*, 12,937–12,950, doi:10.1029/95JB00474.

Moore, D. E., and M. J. Rymer (2007), Talc-bearing serpentinite and the creeping section of the San Andreas Fault, *Nature*, *448*, 795–797, doi:10.1038/nature06064.

Nadeau, R. M., and L. R. Johnson (1998), Seismological studies at Parkfield VI: Moment release rates and estimates of source parameters for small repeating earthquakes, *Bull. Seismol. Soc. Am.*, *88*, 790–814.

Nadeau, R. M., A. Michelini, R. A. Uhrhammer, D. Dolenc, and T. V. McEvilly (2004), Detailed kinematics, structure and recurrence of micro-seismicity in the SAFOD target region, *Geophys. Res. Lett.*, *31*, L12S08, doi:10.1029/2003GL019409.

Nollet, S., J. L. Urai, P. D. Bons, and C. Hilgers (2005), Numerical simulations of polycrystal growth in veins, *J. Struct. Geol.*, *27*, 217–230, doi:10.1016/j.jsg.2004.10.003.

Passchier, C. W., and R. A. J. Trouw (2005), *Microtectonics*, 366 pp., Springer, Berlin.

Ramsay, J. G. (1980), The crack-seal mechanism of rock deformation, *Nature*, *284*, 135–139, doi:10.1038/284135a0.

Ramsey, J. M., and F. M. Chester (2004), Hybrid fracture and the transition from extension fracture to shear fracture, *Nature*, *428*, 63–66, doi:10.1038/nature02333.

Rice, J. R. (1992), Fault stress states, pore pressure distribution, and the weakness of the San Andreas Fault, in *Fault Mechanics and Transport Properties of Rocks*, edited by B. Evans and T. F. Wong, pp. 475–503, Academic, San Diego, Calif., doi:10.1016/S0074-6142(08)62835-1.

Schleicher, A. M., S. N. Tourscher, B. A. van der Pluijm, and L. N. Warr (2009), Constraints on mineralization, fluid-rock interaction, and mass transfer during faulting at 2–3 km depth from the SAFOD drill hole, *J. Geophys. Res.*, *114*, B04202, doi:10.1029/2008JB006092.

Sleep, N. H., and M. L. Blanpied (1992), Creep, compaction and the weak rheology of major faults, *Nature*, *359*, 687–692, doi:10.1038/359687a0.

Solum, J. G., S. H. Hickman, D. A. Lockner, D. E. Moore, B. A. van der Pluijm, A. Schleicher, and J. P. Evans (2006), Mineralogical characterization of protolith and fault rocks from the SAFOD main hole, *Geophys. Res. Lett.*, *33*, L21314, doi:10.1029/2006GL027285.

Titus, S. J., C. DeMets, and B. Tikoff (2006), Thirty-five-year creep rates for the creeping segment of the San Andreas Fault and the effects of the 2004 Parkfield earthquake: Constraints from alignment arrays, continuous Global Positioning System, and creepmeters, *Bull. Seismol. Soc. Am.*, *96*, S250–S268, doi:10.1785/0120050811.

Wiersberg, T., and J. Erzinger (2008), Origin and spatial distribution of gas at seismogenic depths of the San Andreas Fault from drill-mud gas analysis, *Appl. Geochem.*, *23*, 1675–1690, doi:10.1016/j.apgeochem.2008.01.012.

Zoback, M., S. Hickman, and W. Ellsworth (2010), Scientific drilling into the San Andreas Fault Zone, *Eos Trans. AGU*, *91*(22), doi:10.1029/2010EO220001.

G. Di Toro, S. Mittempergher, and R. Spiess, Dipartimento di Geoscienze, Università di Padova, Via G. Gradenigo 6, I-35131 Padova, Italy. (silvia.mittempergher@unipd.it)

J. P. Gratier, LGIT, Université Joseph Fourier – Grenoble I, BP 53, F-38041 Grenoble CEDEX 9, France.

J. Hadizadeh, Department of Geography and Geosciences, University of Louisville, 212 Lutz Hall, Louisville, KY 40292, USA.

S. A. F. Smith, Istituto Nazionale di Geofisica e Vulcanologia, Via di Vigna Murata, 605, I-00143 Roma, Italy.

Geology, published online on 21 October 2011 as doi:10.1130/G32073.1

# Aseismic sliding of active faults by pressure solution creep: Evidence from the San Andreas Fault Observatory at Depth

J.-P. Gratier[1], J. Richard[1], F. Renard[1,2], S. Mittempergher[3], M.-L. Doan[1], G. Di Toro[3,4], J. Hadizadeh[5], and A.-M. Boullier[1]
[1]ISTerre (Institut des Sciences de la Terre) Observatoire, Université Joseph Fourier Grenoble, CNRS, BP 53, Grenoble 38041, France
[2]Physics of Geological Processes, University of Oslo, 0316 Oslo, Norway
[3]Università di Padova, Via Giotto 1, Padua 35137, Italy
[4]Istituto Nazionale di Geofisica e Vulcanologia, Via di Vigna Murata 605, Rome 00143, Italy
[5]Department of Geography and Geosciences, University of Louisville, Louisville, Kentucky 40292, USA

## ABSTRACT

**Active faults in the upper crust can either slide steadily by aseismic creep, or abruptly causing earthquakes. Creep relaxes the stress and prevents large earthquakes from occurring. Identifying the mechanisms controlling creep, and their evolution with time and depth, represents a major challenge for predicting the behavior of active faults. Based on microstructural studies of rock samples collected from the San Andreas Fault Observatory at Depth (California), we propose that pressure solution creep, a pervasive deformation mechanism, can account for aseismic creep. Experimental data on minerals such as quartz and calcite are used to demonstrate that such creep mechanism can accommodate the documented 20 mm/yr aseismic displacement rate of the San Andreas fault creeping zone. We show how the interaction between fracturing and sealing controls the pressure solution rate, and discuss how such a stress-driven mass transfer process is localized along some segments of the fault.**

## INTRODUCTION AND GEOLOGICAL FRAMEWORK

Aseismic deformation is observed in active fault zones, but the mechanisms of deformation are still unclear (Scholz, 2002). Samples collected from the San Andreas Fault Observatory at Depth (SAFOD, California) allow correlation of fault rock microstructures with real-time geophysical data, and therefore provide useful information for identifying such mechanisms. Here we show that a stress-driven mass transfer process, i.e., pressure solution creep (Rutter and Mainprice, 1978), can accommodate the aseismic deformation of the San Andreas fault.

The SAFOD borehole, drilled to 3 km depth, is at the southern part of a 175-km-long creeping section of the San Andreas fault (Fig. 1A). The sliding rate is 28 mm/yr in the central part of the creeping segment, and decreases toward both northern and southern ends (Fig. 1B). The creep rate near the SAFOD site is ~20 mm/yr (Fig. 1B), as measured at the surface within a 20-m-thick fault zone (Titus et al., 2006). Such a narrow creeping zone appears to extend through the entire upper crust, coinciding with a zone of observed microseismicity (Nadeau and Dolenc, 2005). The southernmost part of the creeping section, where the creeping rate gradually falls to zero (Fig. 1B), is a zone of repeating M6 earthquakes, the most recent being the 2004 M6 Parkfield earthquake.

At the SAFOD site, the right-lateral displacement of the San Andreas fault has juxtaposed arkosic sandstones and conglomerates of the Pacific plate against the shale, siltstone, and claystone of the North American plate (Fig. 1C). Microstructural observations of the core samples show evidence of deformation across the damaged zone extending to core-parallel depths of 3150–3410 m (Zoback et al., 2010): shear zones alternate with foliated rocks more or less parallel to the San Andreas fault (Solum et al., 2006). Borehole casing deformation revealed two low-seismic-velocity, actively creeping, zones of foliated rocks (Fig. 1C): a main creeping segment (central deforming zone) at 3300.07–3302.81 m and a secondary creeping segment deforming at lower shear rate (southern deforming zone) at 3191.4–3193 m; both the central and southern deforming zones contain serpentine clasts and highly sheared siltstones (Zoback et al., 2010) without clear displacement discontinuity at their boundaries.

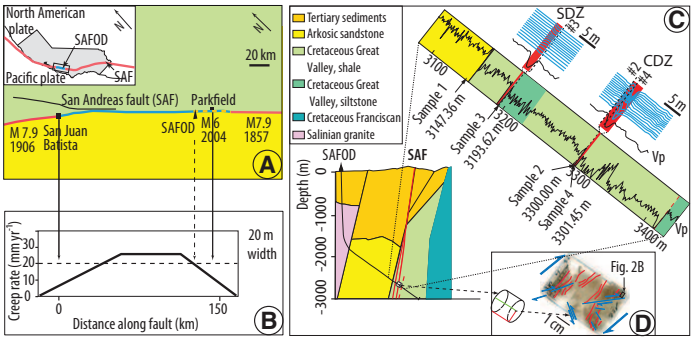


**Figure 1. A: Map view of San Andreas fault system showing creeping segment (blue line) with trace of last two M 7.9 earthquakes that currently are locked segments (red lines) and transitional zone of M6 earthquakes (dotted line); coloring corresponds to contact at 3 km depth in C. SAFOD—San Andreas Fault Observatory at Depth. B: Evolution of creep rate along creeping zone (Titus et al., 2006). C: Schematic cross section of SAFOD site, perpendicular to fault; enlargement shows P wave velocity log (Zoback et al., 2010) together with location of four described samples; two creeping faults are highlighted in red; enlargement in vicinity of these creeping zones (top right) shows casing deformation (blue lines) indicating active creep and accurate location of three of the samples. SDZ—southern deforming zone; CDZ—central deforming zone. D: Sketch of thin section (sample 2) perpendicular to foliation (red), with minor faults (blue) (location of Fig. 2B is shown).**

## EVIDENCE OF PRESSURE SOLUTION CREEP

Based on the microstructural study of samples from the SAFOD core, we infer that an important mechanism of aseismic deformation is pressure solution creep, which induces pervasive and irreversible deformation of the whole rock. This mechanism is active both in the less deformed samples collected from the damaged zone (sample 1) and in intensely deformed foliated samples of the creeping zone (sample 2) shown in Figure 1D. We show that the most highly deformed zones have the highest amount of strain accommodated by pressure solution. Evidence of pressure solution is revealed using elemental distribution maps in sample 1 (Fig. 2A). Stress-driven dissolution associated with horizontal contraction is demonstrated by the dissolution of Ca-Na feldspars at feldspar-quartz grain impingements along a pressure solution seam, whereas K, Mg, Fe, and Ti (phyllosilicates, Fe and Ti oxides, sulfurs) are passively concentrated in the same seam (Fig. 2A). Fracturing is associated with pressure solution. Contraction perpendicular to the dissolution seam, apparent from the grain shape change (Fig. 2A), was estimated to be ~10%. Since there is no evidence of redeposition in veins nearby, it may be concluded that the soluble species have been transported away from the zone of dissolution.

In sample 2, Ca, Si, and Na are depleted within the solution seams where Mg, Fe, Ti are passively concentrated (Fig. 2B). Such a pressure

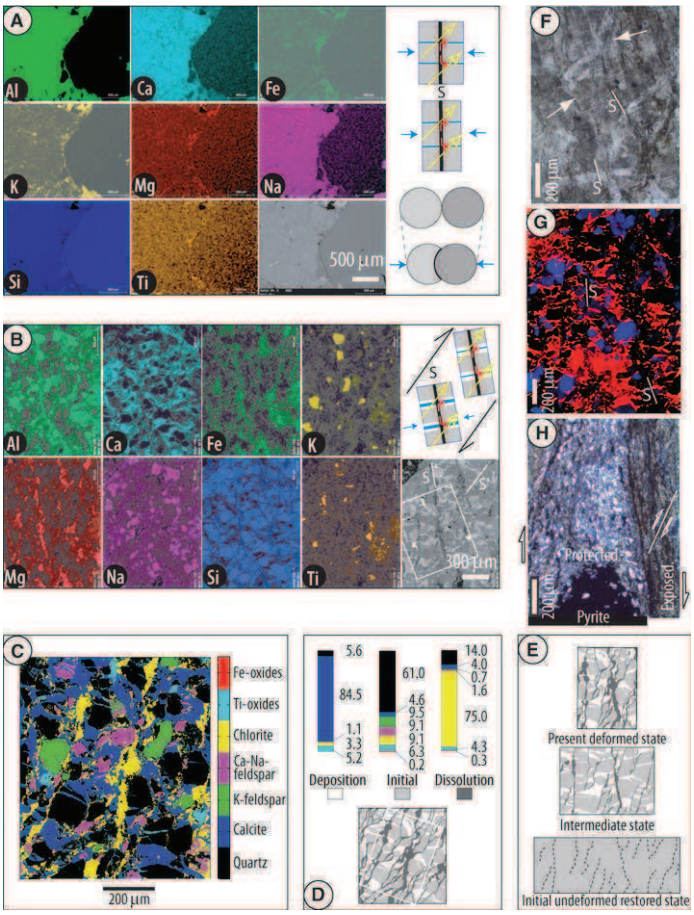


**Figure 2. Pressure solution evidence. A and B: Elements distribution from scanning electron microscopy (SEM) analyses for samples 1 and 2, respectively; brighter color indicates higher content; small sketches show diffusive mass transfer path (red arrows) from solution seams (black) (S) to fluid (blue) within vein (white) and fluid flow (yellow). C: Mineralogical distribution in white rectangle area of B (bottom right), sample 2. D: Same area as C. Top—mineral composition of deposition, initial, and dissolution zones. Bottom—areas of three zones are 27%, 58%, and 15%, respectively. E: Present deformed state (top) and restored undeformed state (bottom) of area of white rectangle of D with intermediate deformed state (middle). F: Evidence of stress dissolution of calcite (arrows) within vein with pressure solution seams (S), sample 3. G: Calcite filling of fracture network (orange) perpendicular to solution cleavage (S) (cathodoluminescence, sample 3). H: Stress shadow effect showing evidence of pressure solution grain size reduction from protected to exposed zone with quartz and feldspar depletion, sample 3. (Images A, B, F, G, H can be seen in larger view in the GSA Data Repository[1].)**

solution process leads to a foliation oriented at a high angle to the drillhole axis (Figs. 1C and 1D). In contrast to sample 1, calcite minerals in sample 2 fill a network of veins oriented perpendicular to the solution seams, consistent with an extension parallel to the foliation. Finite deformation can be calculated from mineral distribution (Fig. 2C). Three zones are distinguished (Fig. 2D): (1) a dissolution zone (with passively concentrated chlorites and Fe oxides), (2) a deposition zone (with precipitated calcite and occasional Ti oxides), and (3) an initial zone (predeformation zone composed of quartz, feldspars, and chlorites). Veins open and seal progressively (Mittempergher et al., 2011). Consequently, initial zones are dissolved at the beginning of the pressure solution process, then both initial and deposition zones are progressively dissolved (Figs. 2E and 2F). The relative mass change, $\Delta M/M_0$, is calculated using the passive concentration of insoluble minerals in the dissolution zone compared with the composition of the protected zone between solution seams (Figs. 2D and 2E) as:

$$\Delta M / M_0 = \left(I_p / I_d\right) - 1, \quad (1)$$

where $I_p$ and $I_d$ are the content in insoluble minerals in the protected and in the dissolution zone, respectively, and $M_0$ is the mass of a representative volume element before deformation. Two end members of mass transfer amount are obtained by comparing the composition of dissolution zones with the protected zones: either initial zones or both initial and deposition zones. The two calculations give about the same amounts of relative mass decrease for the dissolution zones (–88% to –90%). A mean value of contraction perpendicular to the foliation of ~60% can be calculated by taking into account the areas of the dissolution zones (Fig. 2D). A mean extension of ~50% perpendicular to the veins is evaluated from the ratio of deposition areas to initial areas (Figs. 2D and 2E). The mass decrease of each soluble mineral that shows no significant differential alteration between protected and dissolution zones can also be calculated (Gratier et al., 2003): quartz, –96%; K-feldspars, –99%; Ca-Na feldspars, –98%; calcite, –94%. Foliation as mineral segregation appears to be linked to the pressure solution creep, with an almost complete disappearance of the soluble minerals in the zones of dissolution. Mass conservation calculations comparing the amounts of dissolved Ca-Na feldspars and deposited minerals in veins show that a large proportion of calcite must come from outside the studied area, brought by episodic fluid flow (Mittempergher et al., 2011). Evidence of dextral shearing is found in thin sections cut normal to the foliation cleavage from both en echelon fractures (Fig. 1D) and crosscutting cleavages (S and S′, Fig. 2B). Consequently, the calcite vein network and the solution cleavage surfaces are consistent with a stress-driven mass transfer process that accommodates right-lateral strike-slip movement along the San Andreas fault (Fig. 2B). Similar solution cleavage–vein network texture (Fig. 3A) is recorded in samples collected near the creeping zone of the southern deforming zone (sample 3, Fig. 2G), but accommodating lower finite strain than in the central deforming zone. Pressure solution creep also develops at grain scale by diffusion-accommodated grain sliding (Fig. 3B; Ashby and Verrall, 1973) within highly sheared and foliated shale in which feldspar and quartz are depleted by the pressure solution process. This can be seen both near the southern deforming zone (sample 3, Fig. 2H) and in the middle of the central deforming zone (sample 4, Fig. 3E). Evidence of dissolution is documented at grain contacts in the SAFOD creeping zones (Schleicher et al., 2009).

## KINETICS OF PRESSURE SOLUTION CREEP

A key issue is whether pressure solution kinetics are consistent with the measured permanent fault creep rates (Titus et al., 2006). To solve this issue, we propose a model (Fig. 3) where steady-state creeping occurs within a vertical shear zone as much as 10 km deep. We use a pressure solution creep law for quartz and calcite derived from laboratory indentation experiments (Gratier et al., 2009; Zubtsov et al., 2005). The strain rate $\dot{\varepsilon}$ derived from the experimental relationship is:

$$\dot{\varepsilon} = \Delta d / \left(d\,\Delta t\right) = 8DwcV_s\left(e^{3\Delta\sigma_n V_s/RT} - 1\right)/d^3, \quad (2)$$

where $c$ is the solubility of the diffusing solid, $V_s$ is the molar volume of the stressed solid, $R$ is the gas constant, $T$ is temperature, $D$ is the diffusion constant along the stressed interface, $w$ is the thickness of the trapped fluid phase along which diffusion occurs, $t$ is time, and $\Delta\sigma_n$ is the driving stress as the difference between normal stress on a dissolution surface and the fluid pressure in the vein. In experiments, $d$ is the diam-

[1]GSA Data Repository item 2011336, Figures DR1 and DR2, is available online at www.geosociety.org/pubs/ft2011.htm, or on request from editing@geosociety.org or Documents Secretary, GSA, P.O. Box 9140, Boulder, CO 80301, USA.

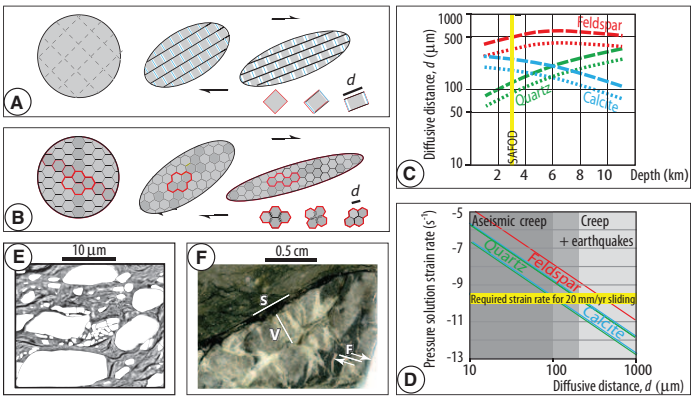


**Figure 3. Pressure solution creep mechanisms. A: Mass transfer from solution cleavage (black) to veins (white) with detail of progressive mass transfer process for given element; *d* is mean diffusion distance between veins along solution cleavage; free fluid in veins is blue. B: Diffusion-accommodated grain sliding, with detail of geometry of progressive grain sliding (Ashby and Verrall, 1973); *d* is mean diffusion distance. C: Distance of diffusive mass transfer *d* versus depth for various minerals required to accommodate 20 mm/yr horizontal displacement rate by pressure solution creep in vertical shear zone of 1 m width (dotted line, strain rate of $3.3 \times 10^{-10}$ $s^{-1}$) or 3 m width (dashed lines, strain rate of $1.1 \times 10^{-10}$ $s^{-1}$). SAFOD—San Andreas Fault Observatory at Depth. D: Pressure solution strain rate versus distance of diffusive mass transfer through entire crust for various minerals; minimum and maximum values for quartz and calcite; yellow line is required strain rate for creeping zone. E: Scanning electron microscope image of sample 4, within creeping zone of central deforming zone (CDZ), showing mixing of phyllosilicates (soft smectite, chlorite, in various grays) and soluble-rigid minerals (quartz, feldspars, calcite, serpentine, in white); crack networks (black) are linked to dewatering of smectite during sample preparation. Deformation is accommodated by grain boundary sliding, possibly by diffusion for soluble species. F: Remnant of sandstone patch deformed by pressure solution cleavage (S)–veins (V) process embedded in CDZ creeping zone, with microfaults (F) (sample 4). (Images E and F can be seen in larger view in the Data Repository [see footnote 1].)**

eter of the indenter. In nature, *d* can refer either to the spacing between fractures that corresponds to the diffusive mass transfer distance between veins along a dissolution surface (Fig. 3A), to the grain size in the case of diffusion-accommodating grain boundary sliding (Fig. 3B). Such a diffusion-controlled pressure solution creep law is likely to operate in conditions prevailing at 6–10 km, whereas for the lesser depths (2–4 km), a shift from diffusion control to reaction control is predicted (Renard et al., 1999), but only if *d* exceeds 300 μm, which is not likely here (see following). It is possible to extend the creep law for quartz obtained at 350 °C to lower temperatures within the entire upper crust by assuming an activation energy of 15 kJ/mole (Rutter and Mainprice, 1978). It is also possible to extend the creep law to other minerals such as calcite (Zubtsov et al., 2005) and feldspars by changing the solubility and molar volume parameters. Using such creep laws, with a given stress condition, we can estimate the maximum values of *d* required to accommodate a displacement rate of 20 mm/yr over a 1–3-m-thick shear zone, such as the central deforming zone (Fig. 1C). At 3 km depth, a minimum conservative value for the pressure solution driving stress is the difference between the maximum and the minimum horizontal stress ($S_{hmax}$ and $S_{hmin}$, respectively). This difference was measured to be ~60 MPa, $S_{hmin}$ being very near the overburden stress (Hickman and Zoback, 2004). The same stress value was used for the entire upper crust (Figs. 3C and 3D). With this model, we show that the maximum required distance of mass transfer at 3 km depth varies with mineral composition in the range 90–350 μm and 125–500 μm for 1 and 3 m width fault zones, respectively (Fig. 3C). These values are larger than the fracture spacing observed for samples 2 and 3 (solution cleavage–veins process; Figs. 2E–2G). They are also much larger than the observed grain sizes in the foliated zones, as in sample 3 and 4 (diffusion-accommodated grain-sliding process; Figs. 2H and 3E). Since the observed diffusion distances are smaller than a conservatively calculated *d* value, pressure solution creep can therefore easily accommodate the measured displacement rate of 20 mm/yr. The diffusion-accommodated grain-sliding process can accommodate much larger finite deformations than the solution cleavage–veins process (Ashby and Verrall, 1973). For this reason, with increasing deformation, the part of the rock deformed by the solution cleavage–veins process, which is also relevant to the most rigid part of the deformed zone, is probably progressively dilacerated and dispersed into the creeping zone (e.g., dark gray grains, Fig. 3B). Evidence of large patches of sandstone deformed by the solution cleavage–veins process can be found in the middle of the central deforming zone (sample 4, Fig. 3F). The solution cleavage–veins process appears therefore to be a transitory state of deformation, which testifies to the efficiency of the pressure solution mechanism and is probably superseded by the diffusion-accommodated grain-sliding process within the most deformed regions of creep.

## DISCUSSION AND CONCLUSION

Interaction between creep and seismic (microseismic) fracturing is an important issue. Dissolution indenter experiments show that grain-scale fracturing can drastically accelerate the displacement rate accommodated by pressure solution creep (Gratier, 2011); fracturing opens new paths for solute transport along fluid-filled fractures, decreasing the distance of diffusion, *d*. However, if the fractures are progressively sealed, this effect disappears as sealing increases the distance of mass transfer (*d*), and consequently reduces the displacement rate. At grain scale in the laboratory, such a microfracture pressure solution sealing process may be observed within no less than a few months. In nature, pressure solution fracture sealing probably takes several years or decades, depending on the spacing and the width of the fractures (Gratier, 2011). This could partially explain the effect of the A.D. 2004 M6 Parkfield earthquake on the creep rate southeast of the SAFOD site: coseismic fracturing activated afterslip creep (Freed, 2007) that progressively decreased with time as the fault healed (Li et al., 2006).

The crucial role of the diffusion distance *d* is shown in Figure 3D. When *d* is small enough (10–100 μm), steady-state pressure solution creep can accommodate the observed aseismic displacement rate of 20 mm/yr through the entire upper crust. When *d* is larger (>100 μm), pressure solution creep occurs but cannot accommodate the displacement rate and relax the stress. Consequently, small seismic ruptures occur (Fig. 3F), in turn activating pressure solution creep.

Pressure solution creep is compatible with the low heat flow measurements in the creeping section (Zoback et al., 2010), since this process does not generate significant heat. Various explanations have been proposed for the apparent low friction behavior of the creeping zone. Increases in fluid pressure may reduce the frictional resistance to sliding (Scholz, 2002), but elevated fluid pressures were not measured during drilling, although transient increases of fluid pressure may have occurred episodically in the past (Mittempergher et al., 2011). Talc minerals were found in SAFOD cuttings and should have a weakening effect (Moore and Rymer, 2007), especially if they develop a foliation (Collettini et al., 2009). However, there is as yet no evidence for the presence of continuous layers of talc at SAFOD (Holdsworth et al., 2011). Alternatively, from experiment on cuttings, or laboratory-ground samples, of San Andreas fault creeping zones, Carpenter et al. (2011) and Lockner et al. (2011) found friction values as low as 0.15–0.2, due to the presence of weak phyllosilicate as saponite. It is clear from samples of the San Andreas fault creeping zone (Fig. 3E) that the deformation is accommodated by grain boundary sliding. Friction and

diffusion may compete to accommodate such grain sliding, but it is likely that, at an imposed strain rate, the less energy-consuming process will win. Pressure solution driving forces of 10 and 0.01 MPa are enough to accommodate $10^{-10}$ $s^{-1}$ strain rate over 3 m width, with 100 and 10 µm grain size, respectively, for quartz and calcite at 6 km depth. Moreover, saponite becomes unstable above ~150 °C and is unlikely to be found deeper in the fault zone than 3.5–4 km. Consequently, as long as the deformation requires grain boundary sliding involving soluble minerals, pressure solution creep is an efficient mechanism of aseismic creep through the entire upper crust down to more than 10 km.

A final question is why, at a given time, pressure solution creep is localized along some segments of the fault. The answer may be that pressure solution creep needs specific conditions to develop at a significant rate. Soluble minerals such as feldspar, calcite, quartz (Gratier et al., 2003), and serpentine (Andreani et al., 2005) must be present with a reactive fluid phase. The distance of diffusive mass transfer (*d*) must be as small as possible. This requires very fine grained material, possibly related to intense seismic fracturing in the San Andreas fault. Soluble grains must not seal together in order to keep fast diffusive paths along solution seams (Niemeijer and Spiers, 2005). Two processes could avoid such sealing, and occur in the San Andreas fault creeping zones, i.e., passive concentration of phyllosilicates due to soluble species pressure solution depletion (Figs. 2H, 3E, and 3F) and the growth of new phyllosilicates (Holdsworth et al., 2011). In such a way, phyllosilicates get trapped around the soluble species, preventing their sealing and activating diffusive mass transfer. Under these conditions, the process is self-organized through a positive feedback process, which allows pressure solution creep process localization within some fault segments.

**ACKNOWLEDGMENTS**

We thank S. Hickman and B. Holdsworth for their suggestions on an early version, and F. Agosta, C. Colletini, and J. Imber for their comments on the final version that significantly improved the manuscript. The Grenoble team was partially supported by CNRS-INSU (Centre National de la Recherche Scientifique–Institut National des Sciences de l'Univers) natural hazards program and Agence Nationale de la Recherche ANR-09-JCJC-0011-1. Hadizadeh and Di Toro were partially supported by U.S. National Science Foundation grant EAR-0545472. Di Toro and Mittempergher were supported by a Progetti di Eccellenza Fondazione Cassa di Risparmio di Padova e Rovigo and by European Research Council Starting Grant Project 205175.

**REFERENCES CITED**

Andreani, M., Boullier, A.-M., and Gratier, J.-P., 2005, Development of schistosity by dissolution-crystallization in a Californian serpentinite gouge: Journal of Structural Geology, v. 27, p. 2256–2267, doi:10.1016/j.jsg.2005.08.004.

Ashby, M., and Verrall, R., 1973, Diffusion-accommodated flow and superplasticity: Acta Metallurgica, v. 21, p. 149–163, doi:10.1016/0001-6160(73)90057-6.

Carpenter, B.M., Marone, C., and Saffer, D.M., 2011, Weakness of the San Andrea Fault revealed by samples from the active fault zone: Nature Geoscience, v. 4, p. 251–254, doi:10.1038/ngeo1089.

Collettini, C., Niemeijer, A., Viti, C., and Marone, C., 2009, Fault zone fabric and fault weakness: Nature, v. 462, p. 907–910, doi:10.1038/nature08585.

Freed, A.M., 2007, Afterslip (and only afterslip) following the 2004 Parkfield, California, earthquake: Geophysical Research Letters, v. 34, L06312, doi:10.1029/2006GL029155.

Gratier, J.-P., 2011, Fault permeability and strength evolution related to fracturing and healing episodic processes (years to millennia): The role of pressure solution: Oil & Gas Science and Technology, v. 66, no. 3, doi:10.2516/ogst/2010014.

Gratier, J.-P., Favreau, P., and Renard, F., 2003, Modeling fluid transfer along Californian faults when integrating pressure solution crack sealing and compaction process: Journal of Geophysical Research, v. 108, no. B2, p. 28–52, doi:10.1029/2001JB000380.

Gratier, J.-P., Guiguet, R., Renard, F., Jenatton, L., and Bernard, D., 2009, A pressure solution creep law for quartz from indentation experiments: Journal of Geophysical Research, v. 114, B03403, doi:10.1029/2008JB005652.

Hickman, S., and Zoback, M., 2004, Stress orientations and magnitudes in the SAFOD pilot hole: Geophysical Research Letters, v. 31, L15S12, doi:10.1029/2004GL020043.

Holdsworth, R.E., van Diggelen, E.W.E., Spiers, C.J., de Bresser, J.H.P., Walker, R.J., and Bowen, L., 2011, Fault rocks from the SAFOD core samples: Implications for weakening at shallow depths along the San Andreas fault, California: Journal of Structural Geology, v. 33, p. 132–144, doi:10.1016/j.jsg.2010.11.010.

Li, Y.G., Chen, P., Cochran, E.S., Vidale, J.E., and Burdette, T., 2006, Seismic evidence for rock damage and healing on the San Andreas fault associated with the 2004 M 6.0 Parkfield earthquake: Seismological Society of America Bulletin, v. 96, p. S349–S363, doi:10.1785/0120050803.

Lockner, D.A., Morrow, C., Moore, D.E., and Hickman, S., 2011, Low strength of deep San Andreas fault gouge from SAFOD core: Nature, v. 472, p. 82–85, doi: 101038/Nature09927.

Mittempergher, S., Di Toro, G., Gratier, J.-P., Hadizadeh, J., Smith, S.A.F., and Spiess, R., 2011, Evidence of transient increases of fluid pressure in SAFOD phase III cores: Geophysical Research Letters, v. 38, L03301, doi:10.1029/2010GL046129.

Moore, D.E., and Rymer, M.J., 2007, Talc-bearing serpentinite and the creeping section of the San Andreas fault: Nature, v. 448, p. 795–797, doi:10.1038/nature06064.

Nadeau, R.M., and Dolenc, D., 2005, Nonvolcanic tremors deep beneath the San Andreas Fault: Science, v. 307, p. 389, doi:10.1126/science.1107142.

Niemeijer, A., and Spiers, C.-J., 2005, Influence of phyllosilicates on fault strength in the brittle-ductile transition: Insight from rock analogue experiments, *in* Bruhn, D., and Burlini, L., eds., High-strain zones: Structure and physical properties: Geological Society of London Special Publication 245, p. 303–327, doi:10.1144/GSL.SP.2005.245.01.15.

Renard, F., Park, A., Ortoleva, P., and Gratier, J.-P., 1999, An integrated model for transitional pressure solution in sandstones: Tectonophysics, v. 312, p. 97–115, doi:10.1016/S0040-1951(99)00202-4.

Rutter, E.H., and Mainprice, D.H., 1978, The effect of water on stress relaxation of faulted and unfaulted sandstones: Pure and Applied Geophysics, v. 116, p. 634–654, doi:10.1007/BF00876530.

Schleicher, A.M., Tourscher, S.N., van der Pluijm, B.A., and Warr, L.N., 2009, Constraints on mineralization, fluid-rock interaction, and mass transfer during faulting at 2–3 km depth from the SAFOD drill hole: Journal of Geophysical Research, v. 114, B04202, doi:10.1029/2008JB006092.

Scholz, C., 2002, The mechanics of earthquakes and faulting: Cambridge, Cambridge University Press, 439 p.

Solum, J.G., Hickman, S.H., Lockner, D.A., Moore, D.E., van der Pluijm, B.A., Schleicher, A.M., and Evans, J.P., 2006, Mineralogical characterization of protolith and fault rocks from the SAFOD Main Hole: Geophysical Research Letters, v. 33, L21314, doi:10.1029/2006GL027285.

Titus, S.J., DeMets, C., and Tikoff, B., 2006, Thirty-five-year creep rates for the creeping segment of the San Andreas fault and the effects of the 2004 Parkfield earthquake: Constraints from alignment arrays, continuous global positioning system, and creepmeters: Seismological Society of America Bulletin, v. 96, p. S250–S268, doi:10.1785/0120050811.

Zoback, M., Hickman, S., and Ellsworth, W., 2010, Scientific drilling into the San Andreas fault zone: Eos (Transactions, American Geophysical Union), v. 91, p. 197–199, doi:10.1029/2010EO220001.

Zubtsov, S., Renard, F., Gratier, J.-P., Dysthe, D.K., and Traskine, V., 2005, Single-contact pressure solution creep on calcite monocrystals, *in* Gapais, D., et al., eds., Deformation mechanisms, rheology and tectonics: From minerals to the lithosphere: Geological Society of London Special Publication 243, p. 81–95, doi:10.1144/GSL.SP.2005.243.01.08.

Manuscript received 14 January 2011
Revised manuscript received 31 May 2011
Manuscript accepted 9 July 2011

Printed in USA